A Thesis Submitted for the Degree of PhD at the University of Warwick

Permanent WRAP URL:

http://wrap.warwick.ac.uk/99931

Copyright and reuse:

This thesis is made available online and is protected by original copyright.

Please scroll down to view the document itself.

Please refer to the repository record for this item for information to help you to cite it.

Our policy information is available from the repository home page.

For more information, please contact the WRAP Team at: wrap@warwick.ac.uk

warwick.ac.uk/lib-publications

CMOS compatible Solidly Mounted Resonator for air quality monitoring

by

Farah Helúe Villa López

School of Engineering

University of Warwick

A thesis submitted to the University of Warwick
for the degree of Doctor of Philosophy

December 2017

CONTENTS

APPENDIX A.   MATLAB SCRIPT FOR THE ONE-DIMENSIONAL MASON MODEL

APPENDIX B.   FINITE ELEMENT MODELLING

APPENDIX C.   6-MASK FABRICATION PROCESS

APPENDIX D.   POLYMER-VAPOUR PARTITION COEFFICIENTS

APPENDIX E.   CIRCUIT DIAGRAMS

APPENDIX F.   VOC STATION HARDWARE COMPONENTS

APPENDIX G.   VIRTUAL INSTRUMENTATION

APPENDIX H.   ZNO BASED CMOS SMR DEVICES

LIST OF FIGURES

NUM.	CAPTION	PAGE

NUM.	**CAPTION**	**PAGE**

Num.	Caption	Page

LIST OF TABLES

NUM.	CAPTION	PAGE

ABBREVIATIONS

ABBREVIATION	DEFINITION
BAM	Beta attenuation monitor
BAW	Bulk acoustic wave
BTEX	Benzene, toluene, ethylbenzene, xylene
CFD	Computational fluid dynamics
CMOS	Complementary metal-oxide semiconductor
CPW	Coplanar waveguide
DI	Deionized
DRIE	Deep reactive ion etching
ELPI	Electrical low pressure impactor
EPA	United States Environmental Protection Agency
EU	European Union
FBAR	Film bulk acoustic resonator
FEM	Finite element method
FMPS	Fast mobility particle sizer
GC	Gas chromatography
GSG	Ground-signal-ground
HiTUS	High target utilisation sputtering
HSE	Health Safety Executive
IC	Integrated circuit

ABBREVIATION	DEFINITION
IDT	Interdigital transducer
IPA	Isopropanol
IR	Infrared
LCC	Leadless Chip Carrier
LO	Local oscillator
LPI	Low pressure impactor
MBL	Microsensors and Bioelectronics Laboratory
MBVD	Modified Butterworth Van Dyke
MEMS	Micro electro mechanical system
MFC	Mass flow controller
MOX	Metal oxide
MSL	Microstereolithography
OPC	Optical particle counter
PCA	Principal component analysis
PCB	Printed circuit board
PDE	Partial differential equation
PDMS	Poly(dimethylsiloxane)
PEG	Poly(ethylene glycol)
PEUT	Poly(etherurethane)
PIB	Poly(isobutylene)
PID	Photoionization detector
PM	Particulate matter
PMA	Poly(methyl acrylate)
PML	Perfectly matched layer
QCM	Quartz crystal microbalance
RF	Radio frequency
RH	Relative humidity
SAW	Surface acoustic wave
SCCM	Standard cubic centimetres per minute
SCS	Single crystal silicon
SEM	Scanning electron microscopy

ABBREVIATION	**DEFINITION**
SMD	Surface-mounted device
SMPS	Scanning mobility particle sizer
SMR	Solidly mounted resonator
SOI	Silicon-on-insulator
SXFA	Fluoroalcoholpolysiloxane
TCF	Temperature coefficient of frequency
TEOM	Tapered element oscillating microbalance
UFP	Ultrafine particle
UV	Ultraviolet
VI	Virtual instrument
VNA	Vector network analyser
VOC	Volatile organic compound
WEL	Work exposure limit
WHO	World Health Organisation

ACKNOWLEDGEMENTS

DECLARATION

This thesis is submitted to the University of Warwick in support of my application for the degree of Doctor of Philosophy. It has been composed by myself and has not been submitted in any previous application for any degree. All work presented was carried out by the author, except where otherwise indicated.

Parts of this work have been included in patent applications, published in the scientific literature and presented at international conferences, as listed below in chronological order.

PATENT

M. Cole, J.W. Gardner, **F.H. Villa-López**, S. Thomas. "Bulk acoustic wave resonator based sensor". (International PCT application, PJP/80075PCT1).

JOURNAL PAPERS

- **F. H. Villa-López,** G. Rughoobur, S. Thomas, A. J. Flewitt, M. Cole and J. W. Gardner (2016). "Design and modelling of solidly mounted resonators for low-cost particle sensing", Measurement, Science and Technology **27**(2).

- S. Thomas, M Cole, **F. H. Villa-López**, J. W. Gardner (2016). "High frequency surface acoustic wave resonator-based sensor for particulate matter detection", Sensors and Actuators A: Physical **244**, pp. 138-145.

- S. Thomas; **F.H. Villa-Lopez**; J. Theunis; J. Peters; M. Cole; J.W. Gardner (2016). "Particle sensor using solidly mounted resonators", IEEE Sensors Journal **16**(8), pp. 2282-2289.

CONFERENCE PRESENTATIONS

- S. Thomas, **F.H. Villa-Lopez**, W. Ludurczak, M. Cole and J.W. Gardner. "Design, modelling and development of low cost high frequency piezoelectric particle sensor", EMR-S 2014 Spring Meeting, Lille, France, May 2014.

- **F. H. Villa-López**, S. Thomas, M. Cole, J. W. Gardner. "Finite element modelling of particle sensors based on solidly mounted resonators", IEEE Sensors Conference 2014, Valencia, Spain, November 2014.

- **F.H. Villa-López**, S. Thomas, M. Cole and J.W. Gardner. "Particle detection using acoustic wave technology for air quality monitoring", Third Scientific Meeting COST Action TD1105 EuNetAir, Istanbul, Turkey, December 2014.

- S. Thomas**,** M. Cole, **F. H. Villa-Lopez**, J.W. Gardner, J. Peters and J. Theunis. "A low-cost acoustic microsensor based system-in-package for air quality monitoring," IEEE Sensors Conference 2016, Orlando, USA, October 2016.

- **F.H. Villa-López**, M. Cole, S. Thomas, J. W. Gardner, "Indoor air quality monitor based on solidly mounted resonators for the detection of VOCs", IEEE Sensors Conference 2017, Glasgow, UK, November 2017.

ABSTRACT

Air pollution has become a growing concern around the world. Human exposure to hazardous air pollutants is associated with a range of health problems and increased mortality. An estimated 40,000 early deaths per year are caused by the exposure to air pollutants in the UK alone, which cost over £20 billion annually to individuals and health services[1]. In this work, novel solidly mounted resonator (SMR) devices were developed for integration in a low-cost, portable air quality monitor for the real-time monitoring of particulate matter and volatile organic compounds (VOCs). Finite element models of the SMRs were developed to aid their design and simulate the response of the sensors to particles and exposure to VOCs.

For particle sensing, a SMR based unit was developed, working in a dual mode configuration. The unit was characterised inside an environmental chamber, together with commercial reference instruments, to particles of known size and composition. A detection limit of 20 µg/m^3 was found (below the safe exposure limit). To target fine particles (<2.5 µm), a virtual impactor was incorporated into the system.

For VOC detection, the SMR devices were functionalised with polymer coatings to detect acetone and toluene vapours (most common VOCs in air). A polymer drop-coating system was developed to complete this aim (polymer film thicknesses <100nm). An automated VOC test station was developed to characterise the SMR based sensors to low ppm concentrations of the target vapours (<200 ppm). The SMR devices demonstrated a limit of detection of 5 ppm to toluene and 50 ppm of acetone (well below the safe exposure limits).

A novel CMOS based SMR device, suitable for volume production and monolithic integration, was designed with an integrated microheater and CMOS acoustic mirror. The heater was included to vary the temperature of the sensing area (to enhance the sensitivity of the SMR to a particular VOC through temperature modulation or to clear particles off the surface). The fabricated device (1.9 GHz) exhibited good performance (Q_s=500), demonstrating the effectiveness of the CMOS fabricated acoustic mirror. The device developed in this work offers a potential solution to fulfil the need for a miniature, low-cost air quality monitor for personal and smart home applications.

---

[1] Royal College of Physicians (2016). "Every breath we take: the lifelong impact of air pollution". London: RCP.

CHAPTER 1

INTRODUCTION

1.1 PREFACE

In the last two decades, air pollution has become a serious issue worldwide. Hazardous substances found in the atmosphere cause not only environmental damage but are also associated with severe adverse effects on human health. Air pollution has been related to a wide range of diseases which affect millions of human lives and cost billions in health care services globally.

The spiralling health care costs have alerted governments to the need of monitoring air quality. Sensor networks have started to appear, although the substantial cost of equipment has limited their deployment to select sites. There is a growing demand for affordable personal air quality monitors which can track air quality during daily activities and provide accessible data (i.e. on a smart device). This chapter introduces the health risks of air pollution and the current policies to limit human exposure. The current state-of-the-art sensing instruments are studied in detail, with focus on volatile organic compounds and particulate matter, which are considered

extremely hazardous to human health. Lastly, the aims of this project are presented and the outline of the thesis is given.

1.2 AIR QUALITY MONITORING

Human exposure to both indoor and outdoor pollutants can have a large impact on wellbeing. A broad range of health problems, including cardiovascular and respiratory diseases, caused by the short- and long- term exposure to air pollutants have been reported in several European cities and all around the world [1-5]. Evidence of increased morbidity and mortality rates, and decreased life expectancy due to both indoor and outdoor air pollution have also been documented [6-9].

In 2012, air pollution accounted for 3.7 million deaths globally. This figure increased to 5.5 million deaths in 2013, with developing countries being the most affected [10, 11]. In the EU, indoor air pollution is estimated to have contributed to 99,000 deaths in 2012 [12]. In 2016 an estimated 40,000 deaths were attributed to the exposure to outdoor pollutants (per year) across the UK. It is estimated such deaths present an annual cost of over £20 billion to individuals and health services [12].

Indoor concentrations of airborne pollutants have been found to be two to five times higher than those found in outdoor environments [13]. This is of great concern, as in day-to-day life people spend most of their time in indoor environments [14, 15] whether at home or in a workplace, at school, in public buildings, public transport or in personal vehicles. For this reason, monitoring of indoor air quality has drawn special attention as it can strongly influence our health, wellbeing and comfort.

The quality of indoor air can also be directly affected by the outdoor air quality, i.e. outdoor air pollutants can easily enter buildings or vehicles through doors and windows (adding to the sources of indoor pollution). Therefore, monitoring of both indoor and outdoor air quality is very important. Figure 1.1 illustrates the sources of indoor air pollutants that can be encountered in a typical house.

According to their sources, air pollutants can be classified into primary or secondary pollutants. The former are those produced by a known source, either natural or anthropogenic, whereas the latter includes those pollutants formed through chemical

reactions, usually by atmospheric oxidation of some primary pollutants. The six most common ambient air pollutants and their sources are shown in Figure 1.2. The work described in this thesis is primarily focused on the detection of PM and VOCs and these are discussed in detail in the following sections.
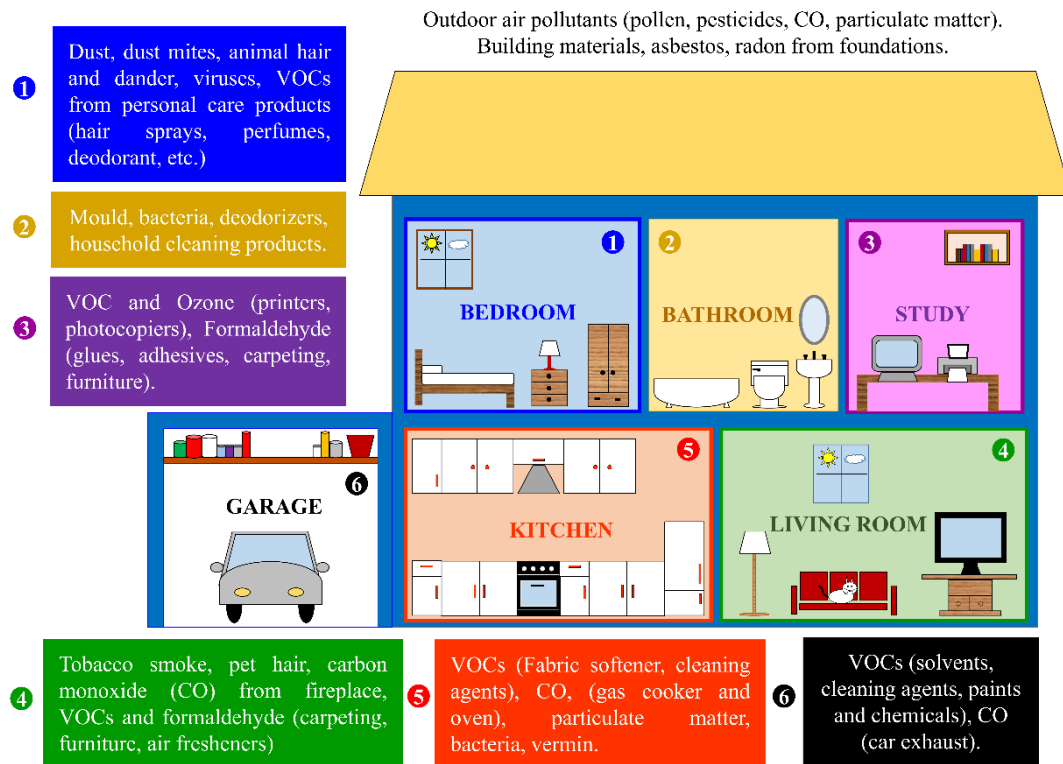
Figure 1.1 Sources of indoor air pollution in a typical household.
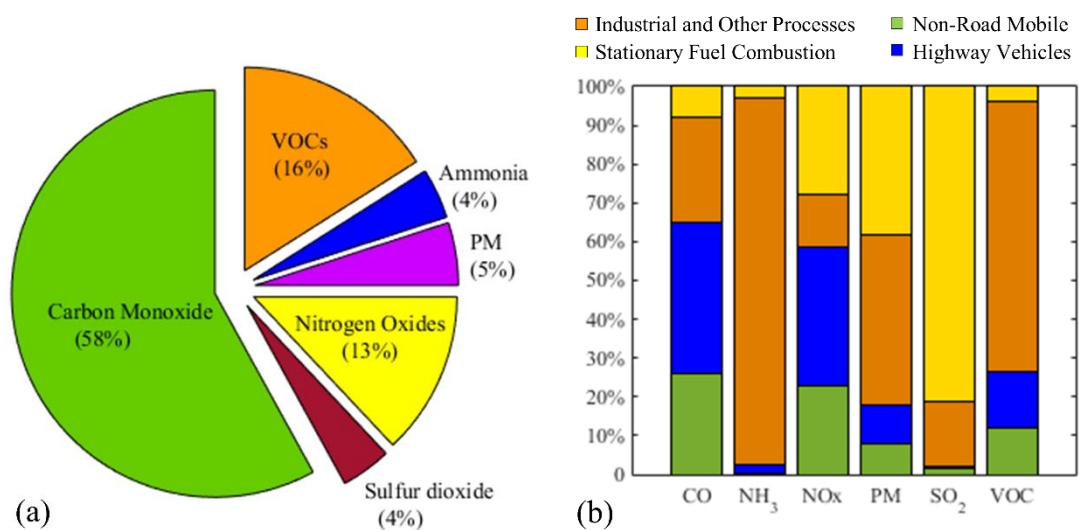
Figure 1.2 (a) Emission of air pollutants in the US (2015) and (b) their sources. Data from [16].

Aiming to gain a better understanding of the relationship between air pollutants and their associated health effects, several initiatives have been undertaken worldwide over the last 30 years, which have helped to identify the necessary actions to reduce the emission of pollutants and their harmful effects on human health [17-19]. The World Health Organisation (WHO) published the first edition of *Air Quality Guidelines for Europe* in 1987 [20]. These air quality guidelines (AQGs) are intended to provide information and offer guidance to policymakers about the health impact of air pollution and serve as the basis for establishing standards for air quality monitoring.

The WHO has regularly revised new scientific evidence on the health effects of several air pollutants resulting in the second edition of AQGs published in 2000 and a *global update* in 2006 [21, 22]. The WHO Regional Office for Europe implemented two projects in 2013, in order to review the new evidence on the effects of air pollutants on health [23, 24], More recently in 2015, a WHO expert consultation took place in order to discuss the latest available evidence for the future update of the WHO global air quality guidelines [25].

Authorities in various countries have implemented standards and regulations aiming to minimise the emission of harmful pollutants. In the EU, these standards are enforced by the European Commission directive on air quality adopted in 2008 where limit and target values for average periods of exposure are established for several pollutants [26]. In the next sections, two of the most hazardous air pollutants are introduced, i.e. particulate matter and volatile organic compounds, which are the focus of this work.

1.2.1   PARTICULATE MATTER

Particulate matter is the name given to the mixture of chemical substances in the form of very small particles, liquid and solid, that can be found suspended in the ambient air. Particle pollutants are found in a wide range of particle sizes and shapes (ranging from a few nanometres to up to 100 µm in diameter), have different chemical compositions and come from different sources. According to their size, particulate pollutants are commonly referred as PM_{10} (coarse particles with diameter equal or less than 10 µm), $PM_{2.5}$ (fine particles with aerodynamic diameter equal or less than

2.5 µm) and ultrafine particles (UFPs) with aerodynamic diameter smaller than 0.1 µm. Figure 1.3 shows a size comparison of airborne particulate matter.
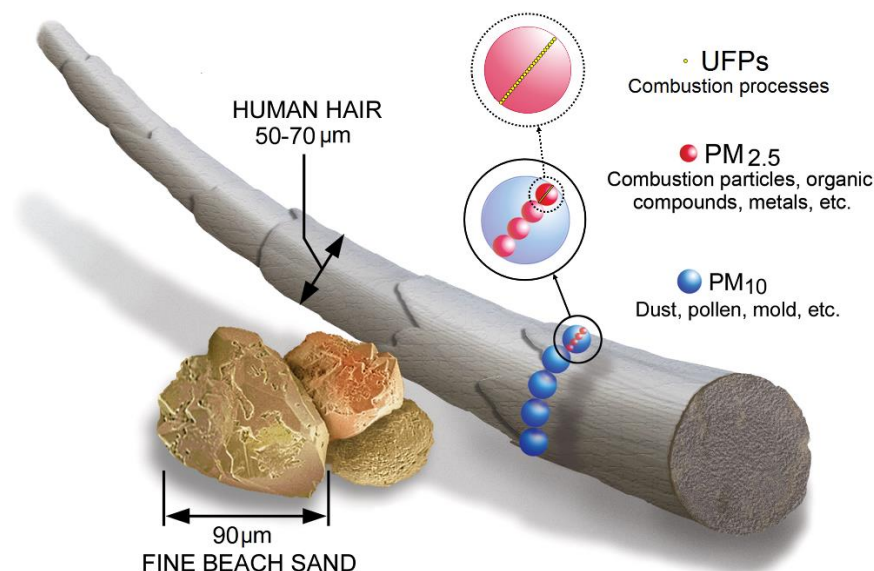
Figure 1.3 Size comparison of PM_{10}, $PM_{2.5}$ and Ultrafine particles. Adapted from [27].

Primary emission sources of PM can include road traffic, agricultural activities, industrial processes and fuel combustion. Natural PM pollution can stem from windblown dust, sea spray and volcanic activity whereas secondary PM is formed through the chemical reaction of gases present in the atmosphere such as ammonia (NH_3), sulphur dioxide (SO_2), nitrogen oxides (NO_x) and also non-methane VOCs to form particulate sulphates, nitrates and organic aerosols, respectively [28, 29].

Due to their size, particulate matter (especially $PM_{2.5}$ and UFPs) is considered greatly hazardous for human health as the finest particles can pass through the airways and penetrate deeply into the lungs as represented in Figure 1.4, where the potential penetration of airborne particles into the respiratory system is depicted.

In the past year, a vast range of clinical, epidemiological and toxicological studies concerning the health effects of human exposure to PM have been conducted [30-32]. There has been strong evidence of the impact of long-term and short-term exposure to PM pollution on mortality and morbidity [33]. Cardiovascular diseases including heart failure, abnormal heart rhythm and ischaemic heart disease have been associated with PM exposure [34-37]. Respiratory problems such as decrease of lung

capacity, risk of lung cancer and asthma have been related to PM pollution [38-41]. Other health problems including diabetes, atherosclerosis, skin diseases and impact on birth outcomes [42-46] have also been associated to PM exposure.
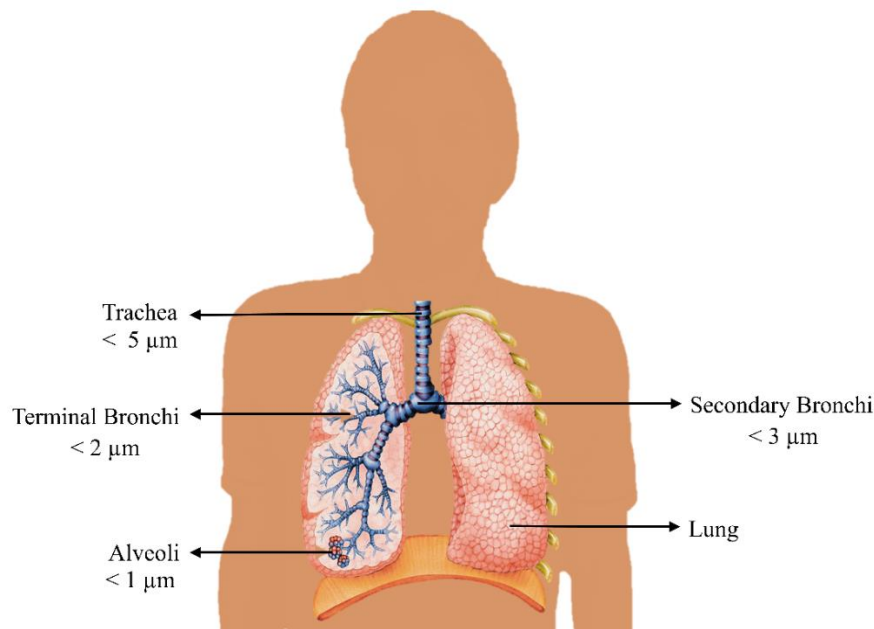
Figure 1.4 Penetration of airborne particulate matter of different sizes into the respiratory system. Adapted from [47, 48].

When looking at the review reports of the United States Environmental Protection Agency (EPA) [49] and the WHO [23], it is clear how airborne PM is impacting public health. Between the period of 2000 and 2013, pollution due to PM increased by 6% [11]. Therefore, the need to take measures to reduce air pollutants, especially PM, is clear. The WHO first published AQGs for $PM_{2.5}$ and PM_{10} in their *WHO global update 2005* and the European Commission established a PM limit and target values in the Directive 2008/50/EC [26]. Table 1.1 shows the standards and objectives for particulate matter currently enforced in the EU [26].

Table 1.1 Limit and target values for PM_{10} and $PM_{2.5}$ established by the European Commission [26].

PARTICULATE MATTER	AVERAGING PERIOD	VALUE	COMMENTS
$PM_{2.5}$	Calendar year	25 μg/m³	Target value enforced 1 January 2010
	Calendar year	20 μg/m³	Limit value to be met by 1 January 2020
PM_{10}	24 hours	50 μg/m³	Limit value enforced 1 January 2005
	Calendar year	40 μg/m³	Limit value enforced 1 January 2005

1.2.2 VOLATILE ORGANIC COMPOUNDS

Although various definitions have been used for the term *volatile organic compounds* [50-52], in general, VOCs refer to organic chemicals in liquid or solid form that easily evaporate at room temperature (therefore they are present as vapours in the atmosphere). Hundreds of compounds fall into this category. VOCs emitted from both anthropogenic and natural sources pose significant health risks. Acute effects such as headaches, dizziness, eyes, nose and skin irritation are associated with the human exposure to VOCs [53]. Other respiratory problems such as asthma and the association of VOCs with mortality have been reported [54-56].

Aromatic VOCs such as benzene, toluene, ethylbenzene and xylene (BTEX) have been found to have the most significant adverse health effects. The carcinogenicity of benzene has been evaluated and strong evidence was found to associate exposure to benzene with cancer in humans [57]. Prolonged exposure to benzene has also been linked to leukaemia in adults and children [58, 59].

Sources of VOC emissions in indoor environments include the use of household products and solvents, cigarette smoke, cooking and building materials [60-62]. Outdoor sources include industrial processes, motor vehicle exhausts and natural emissions from plants [50, 63]. Aromatic VOCs and alkanes are the most common found in outdoor and indoor environments [64].

Currently, there are regulations in the EU that establish the exposure limit to benzene at 5 µg/m^3 per calendar year. This limit value was enforced in January 2010 [26]. However, no regulations have been enforced for other VOCs. In some cases, individual member states of the EU enforce their own restrictions. For example, the Health and Safety Executive (HSE) in the United Kingdom established workplace exposure limits (WELs) for a wide range of substances and VOCs. The values for the long- and short- term exposure limits are given in Table 1.2, for the VOCs of most interest for air quality monitoring.

Table 1.2 Workplace exposure limits (UK HSE regulations) [65].

VOLATILE ORGANIC COMPOUND	LONG-TERM EXPOSURE LIMIT[1] (ppm)	SHORT-TERM EXPOSURE LIMIT[2] (ppm)
Toluene	50	100
Acetone	500	1500
Xylene	50	100
Benzene	1	-
Ethylbenzene	100	125
n-octane	300	375
Formaldehyde	2	2

[1] 8-hr TWA reference period, [2] 15-minute reference period

Table 1.3 lists the most common VOCs found indoors from a dataset of around 5000 samples. The 5 VOCs which are detected the most frequently (i.e. highest total % detect values) are shown, from a list of 300 compounds.

Table 1.3 Indoor Air Concentrations of VOCs [66, 67].

VOLATILE ORGANIC COMPOUND	TOTAL % DETECTS	50TH PERCENTILE VALUE µg/m^3 (ppb)	95TH PERCENTILE VALUE µg/m^3 (ppb)
Toluene	96.4	24 (6.37)	144 (38.21)
Acetone	94	35 (14.73)	190 (80)
Xylene	92.9	17.6 (4.05)	83.5 (19.23)
Benzene	91.1	4.7 (1.47)	29 (9.08)
Ethylbenzene	85.7	3.7 (0.85)	17 (3.92)

* 90th percentile value

1.3 SENSORS FOR AIR QUALITY MONITORING

Human exposure to volatile organic compounds and particulate matter is related to a variety of adverse health effects, as presented in section 1.1. Monitoring of the concentration levels of these harmful pollutants has become of great interest. Knowledge of the quality of the air in our surrounding environments can provide the motivation to minimise human exposure to harmful pollutants and thus prevent the associated health effects.

Several methods and techniques have been used previously for the detection of PM and VOCs. Commercial instruments for outdoor and indoor air quality monitoring are widely available. The development of low-cost, portable and wearable devices, capable of providing continuous and real-time measurements for personal air quality monitoring during everyday activities, are of particular interest. A review on the state-of-the-art instruments and technologies for PM and VOC detection are presented below.

1.3.1 SENSORS FOR PARTICULATE MATTER MONITORING

Generally, instruments used for the detection of airborne particles can be classified as samplers and monitors. The former use an air flow sample to collect particles, usually onto a filter. Particles collected are then taken to the laboratory where they can be gravimetrically analysed. Particle samplers cannot be used for real-time measurements. However, particles collected using this technique can be further analysed (physically and chemically) in the laboratory.

Particle monitors are automated particle instruments that provide real-time measurements of particle concentration. The concentration of PM in air is given in mass per unit volume, typically $\mu g/m^3$. Commercially available particle monitors are based on different measurement methods. Table 1.4 shows a comparison of common techniques used for particle measurements.

The Tapered element oscillating microbalance (TEOM) analyser uses an oscillating element on which particles in a sample air are collected. The change of the oscillating frequency of the microbalance element is related to the mass of particles on

its surface. In turn, this is related to the concentration of PM. The instruments can only measure one diameter of particles at a time, which is defined by an inlet filter.

Beta attenuation monitors (BAM) are based on the absorption of β radiation by airborne particles. A cycling ribbon filter moves in between a β radiation source and the detector. When a sample air is drawn through the filter, airborne particles are loaded onto the ribbon. The loaded particles cause an attenuation of the beta rays which is related to the total mass of PM.

Low pressure impactors (LPIs) and electrical low pressure impactors (ELPIs) both use impactors to separate particles in air by their size. These operate on a principle based on inertia. Air, containing particles, is drawn into impactors which have a structure consisting of sharp changes in flow direction. The small particles which are able to stay in the air flow channel, follow the sharp changes in flow path. The larger particles leave the flow path, and impact into a collection plate. The flow rate and structure of the channels in the device determine the cut-off diameters between the particle sizes.

LPIs are not suitable for real-time monitoring. They typically use a series of impactor stages ('cascade impactor') to categorise the particles by size. The collection plates are weighed after each measurement to calculate the mass concentration present. ELPIs operate on a similar basis, although real-time measurements can be achieved. The particles are charged when they enter the system, before they are separated using a cascade impactor, as used in a LPI. The electrical charge carried by particles that are collected after each stage can be measured. The charge measured is proportional to the number concentration of the particles collected.

Scanning mobility particle sizer (SMPS) instruments measure particle size distribution and concentration using differential mobility analysis. An electric field is created inside the instrument, which causes the particles to drift according to their electrical mobility. The mobility distribution is analysed, from which particle size can be calculated.

Electrical mobility is also used in fast mobility particle sizer (FMPS) systems to measure particle number and concentration. In these systems, particles are charged

when they enter the unit. A high-voltage electrode is located in the centre of the system, surround by a series of electrometers. As the particles approach the electrode, they are repelled towards the electrometers. The mobility distribution can be analysed, by considering the location on the electrometers that the particles reach (a particle with lower electrical mobility will land lower on the electrometers).

Table 1.4 Comparison of techniques used for particle measurements [68-71].

METHOD	REAL TIME	MEASURED PARAMETER	SIZE RANGE (µm)	DETECTION LIMIT	ADVANTAGES	DISADVANTAGES
Filter based sampler	×	Mass concentration	Depends on filter size	10 µg/m^3	▪ Simple and reliable ▪ Possible physical and chemical analysis of particles	▪ Time consuming ▪ High operating cost ▪ 24hr averaging time
TEOM	✓		2.5-10	1.5 µg/m^3	▪ Fast response time (0.5s). ▪ Greater precision than filter sampler	▪ Filter may need changing at high concentrations. ▪ High capital cost
LPI	×	Mass concentration and size distribution	0.03-10	-	▪ Reliable ▪ Large size range	▪ Potential loss of particles at low pressures.
ELPI	✓		0.07-10	1000/cm^3	▪ Robust	▪ Wide channel plates may affect the result
SMPS	×	Number concentration and size distribution	0.025-1	100/cm^3	▪ Measures small particles ▪ No particle shape assumptions.	▪ Not suitable for large sized particles. ▪ Slow scanning time (>16s)
FMPS	✓		0.056-0.56	1000/cm^3	▪ Fast response time (1 second) ▪ High flow rate (10 L/min)	▪ Lower accuracy than SMPS
BAM	✓	Mass concentration	2.5-10	1 µg/m^3	▪ Suitable for real-time data with short time resolution (<1 hr)	▪ Needs a radioactive source
Optical (scattering)	✓	Particle number and size distribution	0.25-32	0.1 µg/m^3	▪ Good response time (6s) ▪ Insensitive to vibrations	▪ Sensitive to ambient pressure changes.

Optical methods are the most commonly used for particle detection, counting and particle size measurements. These methods can be based on different principles

such as light scattering, light absorption and light attenuation. Optical particle counters (OPCs) use a light source (typically a laser) and a detector. Light is scattered by the airborne particles passing through the beam light and this scattered light is detected. Pulses of scattered light determine the particle number whereas the particle size is determined by the intensity of the light.

Industrial instruments commonly used for PM monitoring in outdoor environments (example photographs shown in Figure 1.5) are bulky, heavy and expensive (cost range from $20,000 to $30,000 USD depending on options and accessories required) [72]. Furthermore, they cannot provide personal and real-time information about the quality of the air in our surrounding environment as they are often placed only in strategic open locations (monitoring points) such as the ones used in the national air quality monitoring networks across Europe and the UK [29]. In the UK, particulate matter monitoring stations are commonly located in either 'kerbside' (within 1 m from a busy road) or 'urban centre' (e.g. away from roads, in a pedestrian precinct) sites.

Unlike these instruments, indoor PM monitors are compact and lightweight. They are usually placed on a bench or table and used to assess the air quality inside buildings such as homes, offices, schools or laboratories (cleanrooms) providing more accessible, real-time information of the indoor air we breathe. The majority of indoor PM monitors available in the market are optical based such as the DC1100 (Dylos Corporation) or the Speck^{TM} fine particulate matter monitor. Other mass-based instruments such as cascade impactors are also available. These instruments are relatively affordable (<$500), but they are still too costly for mass distribution and for use in the general population as personal monitors.

Portable monitors are those that can be carried. Handheld devices usually fall into this category. Handheld devices provide a more convenient way for monitoring personal exposure to airborne particles. They are especially useful to localise PM pollution sources. These devices are battery powered and small enough to fit in one hand (to be carried around in the field). Even though handheld devices can be used as mobile instruments, they are not categorised as personal monitors. Personal monitors are wearable devices, small enough to fit in a pocket.

(a)

Partisol™ 2000i Air Sampler (Thermo Scientific Inc.) mounted on optional stand. Dimensions: 37.1 cm (D) x 47.0 cm (W) x 77.2 cm (H), Weight: 37.2 kg. [73]

(b)

TEOM™ 1405 Continuous Ambient Particulate Monitor (Thermo Scientific Inc.). Dimensions: 48.3 cm (D) x 43.2 cm (W) x 75.0 cm (H), Weight: 18 kg. [74]

(c)

BAM-1020 Continuous Particulate Monitor (Enviro Technology Services plc). Dimensions: 40.0 cm (D) x 43 cm (W) x 31.0 cm (H), Weight: 24.5 kg. [75]

(d)

GRIMM EDM164 (GRIMM Aerosol Technik GmbH). Dimensions: 20.0 cm (D) x 40.0 cm (W) x 40.0cm (H), Weight: 12 kg. [76]

Figure 1.5 Example of commercial particle samplers and monitors based on different measurement principles: (a) Gravimetric particle sampler, (b) TEOM analyser, (c) Beta attenuation monitor, (d) Optical particle counter.

A wearable optical based particle monitor has been recently introduced by TZOA (TZOA Enviro-Tracker). This device is still under research and development and is currently only available to pre-order [77]. Table 1.5 presents a comparison of commercially available portable devices for PM monitoring. Examples of these instruments are presented in Figure 1.6. Most of these instruments are optical based.

(a)

(b)
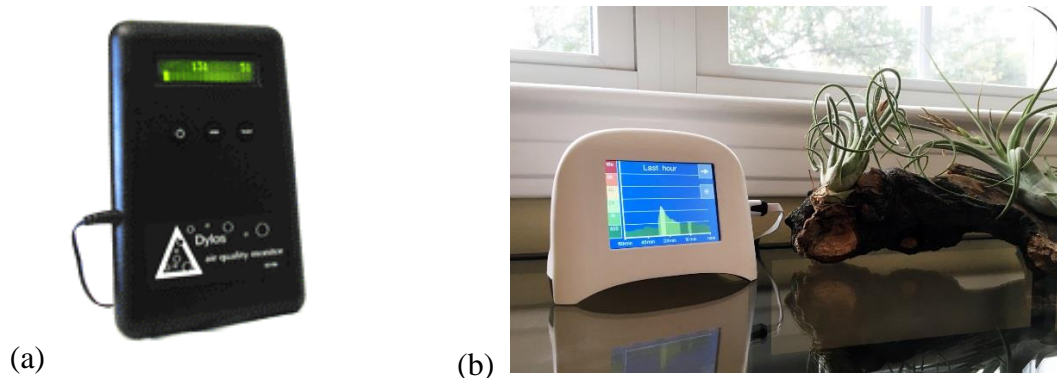
Indoor air quality monitors: (a) DC 1100 Air quality monitor (Dylos Corporation). (b) Speck^{TM}. Dimensions: 9.4 cm (D) x 11.4 cm(W) x 8.9 cm (H). Weight: 164.4g. [78, 79]

(c)

(d)

(e)

Handheld portable particle monitors: (c) DustTrak^{TM} II Aerosol Monitor 8532 (TSI Inc.). Dimensions: 12.5 cm x 12.1 cm x 31.6 cm. Weight: 1.3 kg. (d) GT-321 Handheld Particle counter (Met One Instruments, Inc.). Dimensions: 9.3 cm (W) x 5.1 cm (D) x 15.9 cm (H). Weight: 0.79 kg. (e) Fluke 985 Particle Counter (Fluke Inc.) Dimensions: 27.2 cm x 9.9 cm x 5.3 cm. Weight: 0.68 kg. [80-82]

OPC-N2 Particle Monitor (Alphasense Ltd). [83]

PM2.5 Sensor Module DN7C3CA007 (Sharp Corporation). [84]

Personal Cascade Impactor 290 Series (Tisch Environmental).

Figure 1.6 Commercially available portable and handheld particle monitors.

Table 1.5 . Comparison of representative commercially available portable particle monitors.

Operating Principle	Device	Dimensions and Weight	Current Consumption	Flow Rate	Target Particles	Measurement Range	Advantages	Disadvantages
Light scattering	DC1100-Pro (Dylos Corporation)	3 x 4.5 x 7 in 2.5 lb	400 mA	1.08 L/min	PM2.5 PM10	-	Digital display and serial communication	Poor limit of detection for a particle counter
	DN7C3CA007 (Sharp Corporation)	53 x 40 x 21 mm, 53 g	80 mA	-	PM2.5	25 to 500 µg/m^3	Low cost and lightweight	Analog output that requires external circuit
	OPC-N2 (Alphasense, Ltd.)	75 x 63.5 x 60 mm, 105 g	175 mA	1.2 L/min	0.38 -17 µm	-	Similar performance to state-of-art monitors	SPI interface required
Light absorption	Microaeth® AE51	117 x 66 x 38 mm, 280 g	500 mA	100 mL/min	Black carbon	0-5 µg/m^3 (24 hours)	Good measurement resolution (0.001 µm/m^3)	High current consumption
	Sootscan™ Model OT21	127 x 305 x 356 mm 4.5 kg	-	16.7 L/min	Black carbon	0-18 µg/m^3 (24 hours)	Non-destructive analysis. Further analysis can be performed	Relatively heavy and bulky
Cascade impactor	SE298 Model 290 Marple	86 x 56 x 41 mm, 200 g	-	2 L/min	0.52 – 21.3 µm	-	Particles are collected for later chemical analysis	No real -time measurements
TEOM sensor	PDM3700	171.5 x 82.6 x 243.1 mm 2 kg	-	2.2 L/min	Dust (mining applications)	0-200 mg/m^3	Battery powered	Filter needs daily replacement
Diffusion charging	Nanotracer	165 x 95 mm 750 g	-	0.3-0.4 L/min	10-300 nm	0 - 10^6 particles/cm^3	Minimal maintenance requirements. Silent operation	Limited environmental operating conditions

Optical Devices   Mass-based   Other

Over time, researchers have sought the development of low-cost, personal PM instruments. These particle sensors have been proposed based on a variety of operating principles, using different readout techniques and implementing filters or virtual impactors (VI) to classify the particles. Representative examples of these approaches are presented in Table 1.6. A virtual impactor is a device that separates particles from an air flow into two airstreams, according to their aerodynamic diameter (different sized particles have different inertia). Particles with sizes above a specified cut-off diameter follow the minor flow channel while particles smaller than the cut-off diameter are collected at the major flow channel.

Table 1.6 A summary of approaches for the development of personal instruments for the detection of airborne particles.

OPERATING PRINCIPLE	DESCRIPTION	REF.
Corona discharge	Particles become charged when passing through a corona discharge region. The current produced due to the flow of charged particles in the system is related to the concentration of particles.	[85]
Gravimetric or mass sensors	Measurement of the change in the resonance frequency of the device to determine the mass of aerosol particles.	
	Thermally actuated MEMS resonators	[86-88]
	Thin film piezoelectric on silicon resonators	[89, 90]
	Silicon resonant cantilevers	[91-98]
	Acoustic devices	[99-101]
Paddle-type silicon cantilever	Dust particles are attracted by applying an electrostatic field to the electrode and particle mass is measured as a change in the oscillation phase.	[102]
MEMS electrometer	Operating principle similar to a vibrating reed electrometer. Use of MEMS vibrating capacitance to detect small currents from ionized particles.	[103]

Of all the approaches listed above, the greatest progress towards a personal monitor has been achieved using silicon resonant cantilevers. In particular, the collaboration between the Institute of Semiconductor Technology (IHT) and the Fraunhofer-Wilhelm-Klauditz-Institut in Braunsweig, Germany has led to the

development of sensors for the detection of airborne nanoparticles. In these devices, a Wheatstone bridge configuration is used for signal readout.

The research group have carried out different experimental set-ups. For example, in one article Wasisto *et al.* describe an experiment where the cantilever was operated using its fundamental mode with an aerosol sampler, based on the dielectrophoresis method for trapping the particles [93]. The study of cantilevers operated in the second resonant mode has also been reported [96] and the integration of heating resistors and electrostatic sampling was analysed [92]. Further work has been reported [95, 97, 104] and has led to the development of a portable cantilever-based airborne nanoparticle detector [98], following a previous work reported by Merzch *et al.* [91].

As an alternative approach, acoustic wave technology has also been proposed for the detection of micro-sized particles. Acoustic wave devices such as quartz crystal microbalance (QCM) and surface acoustic wave (SAW) devices have been investigated as mass sensors for particle sensing. The total mass of particles deposited on the sensing area of these devices is measured as a shift in their resonance frequency. This is further discussed in section 0.

1.3.2   SENSORS FOR THE DETECTION OF VOCS

Several technologies based on different physical or chemical effects are used for the detection of gases and vapours. In the last few years, researchers have focused on the development of low-cost, low-power and small gas sensors capable of fast-response and accurate detection of VOCs. A comparison between available technologies is presented in Table 1.7.

Gas chromatography (GC) is a well-known and common technique for measuring gas concentrations in mixtures. GC is an analytical method mainly used in the laboratory for the quantitative and qualitative analysis of volatile organic compounds. Even though this technology has shown an excellent performance with high precision, sensitivity and selectivity for the detection of VOCs [105], gas chromatographs are considerably bulky, slow and costly [106]. Although some efforts

have been made towards the miniaturization of these instruments [107, 108], further work is required in this field.

Electrochemical sensors consist of a diffusion barrier, a sensing electrode and a counter electrode separated by an electrolyte. The gas diffuses through the membrane reaching the sensing electrode surface, where it is oxidized or reduced, generating a current flow. These sensors are basically electrochemical cells that can operate in amperometric or potentiometric mode. Electrochemical sensors are primary used for the detection of oxygen (O_2) and toxic gases such as carbon monoxide (CO) and hydrogen sulphide (H_2S). They offer an affordable solution for VOC detection. However, due to their short life span, susceptibility to poisoning and bulky design [109] their use as air quality monitors is limited.

Metal oxide semiconductor (MOS) gas sensors make use of semiconductor materials, usually metal oxides (MOX) such as tin oxide (SnO_2), titanium dioxide (TiO_2) or tungsten trioxide (WO_3) and a heating element such as a resistive filament or micro-hotplate. The conductivity of the sensing material changes due to the interaction between its surface and the target gas. The sensitivity of MOX sensors mainly depend on the sensing material, its thickness and the operating temperature [106]. Traditional MOX sensors have high power consumption (>200 mW) and exhibit cross sensitivities [110, 111] limiting their use in portable and wearable devices for air quality monitoring. However, recent developments have proved the use of WO_3 based sensors with low power consumption (<65 mW) and limited cross sensitivity for the detection of NO_2 [112].

Photoionization detectors (PID) are the gold standard for the detection of VOCs. This type of sensors can detect volatile organic compounds at very low concentrations (ppb levels) with fast response time (only a few seconds) and good sensitivity [113] . PIDs use an ultraviolet (UV) light source and two electrodes. The UV light ionizes the vapour molecules, resulting in a measured ion current proportional to the vapour concentration. The UV source is basically a lamp which emits UV light with a certain wavelength determined by the type of gas in the lamp. Only vapours with ionization potential equal or lower than the lamp output energy can be detected. Lamps with 10.6 eV (krypton gas, magnesium fluoride windows) are the

most widely used in PIDs as they can detect a variety of compounds and have a long life span (~6000 hours) [113]. PID sensors, however, have limited selectivity and usually correction factors need to be applied for specific VOCs [114].

Optical gas sensors are based on the optical absorption of a gas at a specific wavelength. In particular, non-dispersive infrared (NDIR) sensors can detect gases with unique infrared (IR) absorption. NDIR sensors mainly consist of a IR radiation source, an IR detector and a path (gas chamber) between the IR source and the detector. These sensors benefit from selectivity by using wavelength filters when a specific gas is absorbed over a specific wavelength range. Unlike other gas sensor technologies, optical sensors work on a physical absorption process, offering very fast response (<1 second), reduced drift and high gas specificity [115]. However, restriction on their miniaturization comes from the need for the IR radiation to travel a long distance (e.g. 10 cm) through the sample gas.

A list of commercial VOC sensors is given in Table 1.8. This list is not exhaustive; however, it summarises the current standard of commercially available sensors. There is no defined standard for product data sheets, and as such manufacturers often choose not to disclose performance details of their sensors (i.e. limit of detection etc.).

Acoustic wave devices are also used for VOC detection. This is accomplished by applying a selective coating on the sensing area of the device. These sensors are highly sensitive, low cost and have fast response times. However, they exhibit limited selectivity and susceptibility to noise [106]. A review of acoustic devices for VOC detection is presented in Chapter 2.

Based on the review of all the available sensor technologies, a device based on an acoustic wave resonator is preferred for use in this work. Acoustic sensors offer performance advantages compared to other techniques, such as: miniaturisation, long lifetime, high sensitivity, low power-consumption and low-cost. The project aims listed below summarise the steps needed to realise an acoustic sensor for this air quality monitoring application.

Table 1.7 A review of gas sensing technologies for the detection of VOCs. [106, 113, 116-118]

GAS SENSING TECHNOLOGY	ADVANTAGES	DISADVANTAGES
Gas chromatography (GC)	▪ Excellent separation performance ▪ High precision, sensitivity, selectivity and reproducibility.	▪ Expensive ▪ Bulky, difficult in miniaturization. ▪ Long response time
Electrochemical sensors	▪ Short response time ▪ High accuracy ▪ Wide range of detection ▪ Low cost	▪ Primary sensitive to toxic gases and O_2 (not for VOCs) ▪ Short life span ▪ Bulky design ▪ Susceptibility to poisoning
Metal Oxide sensors (MOX)	▪ Fast response ▪ Affordable solution ▪ Wide range of target gases ▪ High sensitivity to combustible gases (methane, propane) ▪ Compact ▪ Long life span	▪ Relatively low sensitivity ▪ Sensitive to environmental effects (humidity) ▪ High power consumption ▪ Exhibit Cross-sensitivity
Photoionization detector (PID)	▪ Gold standard for VOC detection ▪ High sensitivity ▪ Fast response time ▪ Long lifetime (depending on lamp used) ▪ Wide range of target gases	▪ Low selectivity (correction factors needed) ▪ Require periodic cleaning and calibration.
Non-dispersive infrared sensors (NDIR)	▪ High sensitivity ▪ Very fast response time ▪ High gas specificity ▪ Reduced drift ▪ Minimal maintenance and calibration	▪ High cost ▪ Sensitive to environmental effects (humidity) ▪ Difficult miniaturization
Acoustic Wave Sensors	▪ Long lifetime ▪ High sensitivity ▪ Low cost ▪ Low power consumption ▪ Small footprint ▪ Fast response time ▪ Can be used for wireless applications	▪ Sensitive to environmental effects (temperature, humidity) ▪ Limited selectivity ▪ Susceptible to noise

Table 1.8 Commercial devices for the detection of volatile organic compounds.

DEVICE	SENSOR TYPE	DETECTION RANGE	RESOLUTION	LIMIT OF DETECTION	RESPONSE TIME	LIFE SPAN	TARGET VOC
TGS 2620-C00 Figaro, Inc.	MOS	50 – 5000 ppm	-	-	-	-	Alcohol, Solvent vapours
MiCS-5914 SGX Sensortech	MOS	10 – 500 ppm	-	-	-	-	Ethanol
GM-502B Winsen Electronics	MOS	10 – 500 ppm 10 – 100 ppm	-	-	-	-	Alcohol Formaldehyde
PID-A12 Alphasense, Ltd.	PID	1 ppb – 50 ppm	50 ppb	1 ppb	< 3 s	Lamp life 5000 hrs	VOCs with ionisation potentials <10.6 eV
piD-TECH 045-018 Mocon Baseline	PID	15 ppb – 60 ppm	-	15 ppb	-	-	VOCs with ionisation potentials <10 eV
IRM-AT Methane, Alphasense Ltd.	NDIR	0 – 2.5 %	< 400 ppm	< 500 ppm	< 40 s	> 3 years	Methane
NDIR CH4 Wuhan Cubic	NDIR	0 – 5 %	0.01 %	-	< 25 s	> 5 years	Methane
FECS44-100 Figaro, Inc.	EC	0 – 100 ppm	1 ppm	-	< 60 s	> 2 years	Ammonia
Sensoric NH3 3E 500 SE	EC	0 – 500 ppm	-	-	< 90 s	> 2 years	Ammonia

1.4   AIMS OF THE PROJECT

Large size, complexity, high fabrication costs and portability limitations are the major problems found in many of the current technologies used for air quality monitoring. The target of this project is to fulfil the need for an affordable and portable air quality monitoring system, for the detection of particulate matter and volatile organic compounds. The aim of this work is to develop a miniature, low-cost sensor with low power consumption, which is CMOS compatible and capable of high volume manufacturing and monolithic integration with CMOS circuitry.

The work in this thesis mainly focuses on the development of the sensing element (a solidly mounted resonator) for its future integration within a monolithic system as a personal air quality monitor and communication/integration within a smartphone. The objectives of this research are summarised as follows:

- IMPLEMENT AN ANALYTICAL MODEL AND DEVELOP FINITE ELEMENT MODELS OF A SOLIDLY MOUNTED RESONATOR.
  To design a device with optimal performance for sensing applications (VOC, particles) the device parameters must be investigated. The device should be able to detect fine particles (<10 µm diameter) and VOCs in low concentrations (ppm levels). Simulation results will be used to verify the resonant frequency, ensure the device will work within manufacturing tolerances and estimate sensitivity (3D model required).

- DESIGN, FABRICATE AND DEVELOP HIGH FREQUENCY SOLIDLY MOUNTED RESONATORS.
  The resonators will be designed and manufactured using standard microfabrication processes. The devices will need to be characterised and tested to investigate their suitability for the detection of fine particles and volatile organic compounds.

- DESIGN A DISCRETE SENSING UNIT FOR PARTICLE SENSING.
  For low-cost air quality monitoring, a portable sensing unit is required which can be interfaced to a computer (i.e. no specialist equipment needed). The unit needs to have low power consumption (able to be battery powered) and function without

sensitivity to temperature or humidity. The unit must be able to detect particles which are hazardous to health (<10 µm diameter).

- DESIGN AN AUTOMATED TESTING APPARATUS FOR EXPOSING THE DEVICE TO VOCs.
  To be able to be used in air quality monitoring applications, the solidly mounted resonator should be capable of detecting VOCs within their safe exposure limits. A testing rig is needed to generate controlled low concentration of the VOCs and produce step changes of gas concentrations.

- CHARACTERISE THE SOLIDLY MOUNTED RESONATORS TO THE EXPOSURE OF ORGANIC VAPOURS AND PARTICULATE MATTER.
  To verify the functionality of the device to low concentration of VOCs (generated on the testing apparatus) and fine particulate matter deposited on the sensor surface.

- DESIGN A CMOS COMPATIBLE SOLIDLY MOUNTED RESONATOR.
  To develop a low-cost and low power personal air quality monitor with improved performance, the device must be capable of being fabricated within a standard CMOS process together with the integrated CMOS circuitry. The device must have a long-life span (being able to clean the sensing surface after particles become deposited) and improved sensitivity of VOCs.

1.5 THESIS OUTLINE

This thesis describes the design, development and characterisation of solidly mounted acoustic resonators for air quality monitoring. Chapter 1 introduces the sources of indoor air pollutants and their associated health hazards. Air quality guidelines and safe exposure limits of air pollutants currently enforced in the European Union are discussed. The state-of-the-art technologies for the detection of particulate matter and volatile organic compounds are reviewed.

Chapter 2 covers background information on acoustic wave technology (principle of operation and wave propagation). The chapter also includes an overview on surface and bulk acoustic wave devices and a comparison between both technologies and their sensing applications, with more emphasis on bulk acoustic

devices. Additionally, performance metrics, driving circuitry and CMOS integration of these devices are discussed.

Chapter 3 discusses the design considerations of the devices and describes the implementation of analytical and finite element models to evaluate their performance prior to fabrication. The layout design of the devices is also presented.

Chapter 4 details the fabrication process of the designed devices. The devices are characterised and their temperature and humidity dependence is investigated. These results are compared to the simulated results obtained in Chapter 3.

Chapter 5 describes the use of the fabricated devices for particle sensing applications. The devices are characterised with fine particles of known size and composition and results are compared to finite element simulations. The development of a discrete particle sensing unit is presented. Interface circuitry is designed so that the system can operate in a dual mode configuration. Experimental results from an environmental chamber are presented. Further improvements to this unit are described with the development of a hybrid sensor system that includes an active air sampler and a module to separate particles by size.

Chapter 6 covers characterisation of the SMRs to the exposure of organic vapours. The partition coefficients of selected polymer-vapour pairs are investigated. The SMR devices are coated with a polymer film using two polymer deposition methods (spray and drop coating). The development of an automated VOC test station capable of delivering concentrations in the ppb levels is presented and experimental results of polymer-coated devices are presented to the exposure of two different analytes (acetone and toluene).

Chapter 7 describes the design, modelling and characterisation of a novel CMOS based SMR with an embedded single crystal silicon micro heater. The acoustic mirror and heater were fabricated in a standard SOI CMOS process, that will allow high volume production and on-chip integration. Thermal simulations of the heater and CMOS acoustic mirror performance are presented. Experimental results of particle sensing are shown.

Chapter 8 gives an overall discussion of the results and reviews the aims of the project. Further work on the development of a monolithic system is discussed, including the possible integration with a smart device.

1.6 REFERENCES

[1]   Carugno, M., Consonni, D., Randi, G., Catelan, D., Grisotto, L., Bertazzi, P. A., Biggeri, A. and Baccini, M. (2016). "Air pollution exposure, cause-specific deaths and hospitalizations in a highly polluted Italian region", *Environmental Research*. **147**: 415-424.

[2]   Alves, C. A., Scotto, M. G. and Freitas, M. d. C. (2010). "Air pollution and emergency admissions for cardiorespiratory diseases in Lisbon (Portugal)", *Química Nova*. **33**: 337-344.

[3]   Phung, D., Hien, T. T., Linh, H. N., Luong, L. M. T., Morawska, L., Chu, C., Binh, N. D. and Thai, P. K. (2016). "Air pollution and risk of respiratory and cardiovascular hospitalizations in the most populous city in Vietnam", *Science of The Total Environment*. **557–558**: 322-330.

[4]   Rodopoulou, S., Samoli, E., Chalbot, M.-C. G. and Kavouras, I. G. (2015). "Air pollution and cardiovascular and respiratory emergency visits in Central Arkansas: A time-series analysis", *Science of The Total Environment*. **536**: 872-879.

[5]   Dai, X., He, X., Zhou, Z., Chen, J., Wei, S., Chen, R., Yang, B., Feng, W., Shan, A., Wu, T. and Guo, H. (2015). "Short-term effects of air pollution on out-of-hospital cardiac arrest in Shenzhen, China", *International Journal of Cardiology*. **192**: 56-60.

[6]   Çapraz, Ö., Efe, B. and Deniz, A. (2016). "Study on the association between air pollution and mortality in İstanbul, 2007–2012", *Atmospheric Pollution Research*. **7**(1): 147-154.

[7]   Bentayeb, M., Wagner, V., Stempfelet, M., Zins, M., Goldberg, M., Pascal, M., Larrieu, S., Beaudeau, P., Cassadou, S., Eilstein, D., Filleul, L., Le Tertre, A.,

Medina, S., Pascal, L., Prouvost, H*., et al.* (2015). "Association between long-term exposure to air pollution and mortality in France: A 25-year follow-up study", *Environment International*. **85**: 5-14.

[8]   Lu, F., Zhou, L., Xu, Y., Zheng, T., Guo, Y., Wellenius, G. A., Bassig, B. A., Chen, X., Wang, H. and Zheng, X. (2015). "Short-term effects of air pollution on daily mortality and years of life lost in Nanjing, China", *Science of The Total Environment*. **536**: 123-129.

[9]   Mentese, S., Mirici, N. A., Otkun, M. T., Bakar, C., Palaz, E., Tasdibi, D., Cevizci, S. and Cotuker, O. (2015). "Association between respiratory health and indoor air pollution exposure in Canakkale, Turkey", *Building and Environment*. **93, Part 1**: 72-83.

[10]   World Health Organisation (WHO) (2012). "Burden of disease from ambient air pollution for 2012".

[11]   Forouzanfar, M. H., Alexander, L., Anderson, H. R., Bachman, V. F., Biryukov, S., Brauer, M., Burnett, R., Casey, D., Coates, M. M., Cohen, A., Delwiche, K., Estep, K., Frostad, J. J., Kc, A., Kyu, H. H*., et al.* (2015). "Global, regional, and national comparative risk assessment of 79 behavioural, environmental and occupational, and metabolic risks or clusters of risks in 188 countries, 1990-2013: a systematic analysis for the global burden of disease study 2013", *The Lancet*. **386**(10010): 2287-2323.

[12]   Royal College of Physicians. (2016). "Every breath we take: the lifelong impact of air pollution". Report of a working party. London: RCP

[13]   US Environmental Protection Agency. Why indoor air quality is important to schools. Last updated: 17th February 2016, Accessed on 13th September 2016; Available from: https://www.epa.gov/iaq-schools/why-indoor-air-quality-important-schools.

[14]   Klepeis, N. E., Nelson, W. C., Ott, W. R., Robinson, J. P., Tsang, A. M., Switzer, P., Behar, J. V., Hern, S. C. and Engelmann, W. H. (2001). "The National Human Activity Pattern Survey (NHAPS): a resource for assessing

exposure to environmental pollutants", *J Expo Anal Environ Epidemiol*. **11**(3): 231-252.

[15] Gligorovski, S. and Weschler, C. J. (2013). "The oxidative capacity of indoor atmospheres", *Environmental Science & Technology*. **47**(24): 13905-13906.

[16] EPA and Agency, U. E. P. 2016. Our Nation's air: Status and trends through 2015. Last Updated: 21st July 2016, Accessed: 08 May 2017; Available from: https://gispub.epa.gov/air/trendsreport/2016/.

[17] European Commission (2001). "Communication from the commission. The Clean Air for Europe (CAFE) programme: Towards a thematic strategy for air quality".

[18] (2011). "Public Health and Air Pollution in Asia (PAPA): Coordinated studies of short-term exposure to air pollution and daily mortality in two Indian cities". Research Report 157, Health Effects Institute. Boston, MA.

[19] Pascal, M., Corso, M., Chanel, O., Declercq, C., Badaloni, C., Cesaroni, G., Henschel, S., Meister, K., Haluza, D., Martin-Olmedo, P. and Medina, S. (2013). "Assessing the public health impacts of urban air pollution in 25 European cities: Results of the Aphekom project", *Science of The Total Environment*. **449**: 390-400.

[20] World Health Organisation (WHO) Regional Office for Europe (1987). "Air quality guidelines for Europe".

[21] World Health Organisation (WHO) Regional Office for Europe (2000). "Air quality guidelines for Europe, Second edition".

[22] World Health Organisation (WHO) Regional Office for Europe (2006). "Air quality guidelines global update 2005".

[23] World Health Organisation (WHO) Regional Office for Europe (2013). "Review of evidence on health aspects of fair pollution – REVIHAAP Project".

[24] World Health Organisation (WHO) Regional Office for Europe (2013). "Health risks of air pollution in Europe –HRAPIE project".

[25] World Health Organisation (WHO) Regional Office for Europe (2016). "WHO Expert Consultation: Available evidence for the future update of the WHO Global Air Quality Guidelines (AQGs)".

[26] (2008). "DIRECTIVE 2008/50/EC of the European Parliament and of the Council of 21 May 2008 on ambient air quality and cleaner air for Europe", *Official Journal of the European Union*. **51**.

[27] US Environmental Protection Agency (EPA). Particulate Matter (PM) basics. Last Updated: 1st July 2016, Accessed on 12th September 2016; Available from: https://www.epa.gov/pm-pollution/particulate-matter-pm-basics.

[28] CAFE Working Group on Particulate Matter (2004). "Second position paper on particulate matter ".

[29] (2005). "Particulate Matter in the United Kingdom". Department for the Environment, Food and Rural Affairs (DEFRA).

[30] Rückerl, R., Schneider, A., Breitner, S., Cyrys, J. and Peters, A. (2011). "Health effects of particulate air pollution: A review of epidemiological evidence", *Inhalation Toxicology*. **23**(10): 555-592.

[31] Martinelli, N., Olivieri, O. and Girelli, D. (2013). "Air particulate matter and cardiovascular disease: A narrative review", *European Journal of Internal Medicine*. **24**(4): 295-302.

[32] Kim, K.-H., Kabir, E. and Kabir, S. (2015). "A review on the human health impact of airborne particulate matter", *Environment International*. **74**: 136-143.

[33] Yorifuji, T., Kashima, S. and Doi, H. (2016). "Acute exposure to fine and coarse particulate matter and infant mortality in Tokyo, Japan (2002–2013)", *Science of The Total Environment*. **551–552**: 66-72.

[34] Pope, C. A., Burnett, R. T., Thurston, G. D., Thun, M. J., Calle, E. E., Krewski, D. and Godleski, J. J. (2004). "Cardiovascular mortality and long-term exposure to particulate air pollution: epidemiological evidence of general pathophysiological pathways of disease", *Circulation*. **109**(1): 71-77.

[35] Chang, C.-C., Chen, P.-S. and Yang, C.-Y. (2015). "Short-term effects of fine particulate air pollution on hospital admissions for cardiovascular diseases: A case-crossover study in a tropical city", *Journal of Toxicology and Environmental Health, Part A*. **78**(4): 267-277.

[36] Zhang, L.-w., Chen, X., Xue, X.-d., Sun, M., Han, B., Li, C.-p., Ma, J., Yu, H., Sun, Z.-r., Zhao, L.-j., Zhao, B.-x., Liu, Y.-m., Chen, J., Wang, P. P., Bai, Z.-p.*, et al.* (2014). "Long-term exposure to high particulate matter pollution and cardiovascular mortality: A 12-year cohort study in four cities in northern China", *Environment International*. **62**: 41-47.

[37] Chiu, H.-F., Peng, C.-Y., Wu, T.-N. and Yang, C.-Y. (2013). "Short-term effects of fine particulate air pollution on ischemic heart disease hospitalizations in Taipei: A case-crossover study ", *Aerosol and Air Quality Research*. **13**: 1563-1569.

[38] Raaschou-Nielsen, O., Beelen, R., Wang, M., Hoek, G., Andersen, Z. J., Hoffmann, B., Stafoggia, M., Samoli, E., Weinmayr, G., Dimakopoulou, K., Nieuwenhuijsen, M., Xun, W. W., Fischer, P., Eriksen, K. T., Sørensen, M.*, et al.* (2016). "Particulate matter air pollution components and risk for lung cancer", *Environment International*. **87**: 66-73.

[39] César, A. C. G., Nascimento, L. F. C., Mantovani, K. C. C. and Pompeo Vieira, L. C. (2016). "Fine particulate matter estimated by mathematical model and hospitalizations for pneumonia and asthma in children", *Revista Paulista de Pediatria (English Edition)*. **34**(1): 18-23.

[40] Qiu, H., Yu, I. T.-s., Tian, L., Wang, X., Tse, L. A., Tam, W. and Wong, T. W. (2012). "Effects of coarse particulate matter on emergency hospital admissions

for respiratory diseases: A time-series analysis in Hong Kong", *Environmental Health Perspectives*. **120**(4): 572-576.

[41]   Jang, A.-S. (2012). "Particulate Air Pollutants and Respiratory Diseases " in *Air pollution - A comprehensive perspective*, InTech.

[42]   Hansen, A. B., Ravnskjær, L., Loft, S., Andersen, K. K., Bräuner, E. V., Baastrup, R., Yao, C., Ketzel, M., Becker, T., Brandt, J., Hertel, O. and Andersen, Z. J. (2016). "Long-term exposure to fine particulate matter and incidence of diabetes in the Danish Nurse Cohort", *Environment International*. **91**: 243-250.

[43]   Sun, X., Luo, X., Zhao, C., Zhang, B., Tao, J., Yang, Z., Ma, W. and Liu, T. (2016). "The associations between birth weight and exposure to fine particulate matter (PM2.5) and its chemical constituents during pregnancy: A meta-analysis", *Environmental Pollution*. **211**: 38-47.

[44]   Kim, K. E., Cho, D. and Park, H. J. (2016). "Air pollution and skin diseases: Adverse effects of airborne particulate matter on various skin diseases", *Life Sciences*. **152**: 126-134.

[45]   Shah, P. S. and Balkhair, T. (2011). "Air pollution and birth outcomes: A systematic review", *Environment International*. **37**(2): 498-516.

[46]   Brook, R. D. and Rajagopalan, S. (2010). "Particulate matter air pollution and atherosclerosis", *Current Atherosclerosis Reports*. **12**(5): 291-300.

[47]   Horwell, C. and Donaldson, K. US Geological Survey Volcano Hazards Program. Respiratory Effects. Last Update: 14th December 2015, Accessed on 12 September 2016; Available from: https://volcanoes.usgs.gov/volcanic_ash/respiratory_effects.html.

[48]   Piano per la Salute della provicnia di Modena, 2001. Inquinamento atmosferico e polveri. Accessed on 12th September 2016; Available from: http://www.ausl.mo.it/pps/approf/07/07_02.html.

[49]   United States Environmental Protection Agency (EPA) (2009). "Integrated science assessment for particulate matter ".

[50]   Derwent, R. G. (1995). "Sources, distributions, and fates of VOCs in the atmosphere" in *Volatile Organic Compounds in the Atmosphere*, R. E. Hester and R. M. Harrison, Editors, The Royal Society of Chemistry, 1-16.

[51]   (1999). "COUNCIL DIRECTIVE 1999/13/EC of 11 March 1999 on the limitation of emissions of volatile organic compounds due to the use of organic solvents in certain activities and installations", *Official Journal of the European Communities*.

[52]   (2004). "DIRECTIVE 2004/42/CE of the European Parliament and of the council of 21 April 2004 on the limitation of emissions of volatile organic compounds due to the use of organic solvents in certain paints and varnishes and vehicle refinishing products and amending Directive 1999/13/EC", *Official Journal of the European Union*.

[53]   Rumchev, K., Brown, H. and Spickett, J. (2007). "Volatile organic compounds: Do they present a risk to our health? ", *Reviews on Environmental Health*. **22**(1): 39-55.

[54]   Rumchev, K., Spickett, J., Bulsara, M., Phillips, M. and Stick, S. (2004). "Association of domestic exposure to volatile organic compounds with asthma in young children", *Thorax*. **59**(9): 746-751.

[55]   Arif, A. A. and Shah, S. M. (2007). "Association between personal exposure to volatile organic compounds and asthma among US adult population", *International Archives of Occupational and Environmental Health*. **80**(8): 711-719.

[56]   Cakmak, S., Dales, R. E., Liu, L., Kauri, L. M., Lemieux, C. L., Hebbern, C. and Zhu, J. (2014). "Residential exposure to volatile organic compounds and lung function: Results from a population-based cross-sectional survey", *Environmental Pollution*. **194**: 145-151.

[57]   International Agency for Research on Cancer (IARC) (2012). "Chemical agents and related occupations Volume 100F: A review of human carcinogens".

[58]   Snyder, R. (2012). "Leukemia and benzene", *International Journal of Environmental Research and Public Health*. **9**(8): 2875-2893.

[59]   Vinceti, M., Rothman, K. J., Crespi, C. M., Sterni, A., Cherubini, A., Guerra, L., Maffeis, G., Ferretti, E., Fabbi, S., Teggi, S., Consonni, D., De Girolamo, G., Meggiato, A., Palazzi, G., Paolucci, P*., et al.* (2012). "Leukemia risk in children exposed to benzene and PM10 from vehicular traffic: a case–control study in an Italian population", *European Journal of Epidemiology*. **27**(10): 781-790.

[60]   Chin, J. Y., Godwin, C., Parker, E., Robins, T., Lewis, T., Harbin, P. and Batterman, S. (2014). "Levels and sources of volatile organic compounds in homes of children with asthma", *Indoor Air*. **24**(4): 403-415.

[61]   Ayoko, G. A. (2009). "Volatile organic ingredients in household and consumer products" in *Organic Indoor Air Pollutants*, Wiley-VCH Verlag GmbH & Co. KGaA, 347-372.

[62]   Huang, Y., Ho, S. S. H., Ho, K. F., Lee, S. C., Yu, J. Z. and Louie, P. K. K. (2011). "Characteristics and health impacts of VOCs and carbonyls associated with residential cooking activities in Hong Kong", *Journal of Hazardous Materials*. **186**(1): 344-351.

[63]   Rad, H. D., Babaei, A. A., Goudarzi, G., Angali, K. A., Ramezani, Z. and Mohammadi, M. M. (2014). "Levels and sources of BTEX in ambient air of Ahvaz metropolitan city", *Air Quality, Atmosphere & Health*. **7**(4): 515-524.

[64]   Massolo, L., Rehwagen, M., Porta, A., Ronco, A., Herbarth, O. and Mueller, A. (2010). "Indoor–outdoor distribution and risk assessment of volatile organic compounds in the atmosphere of industrial and urban areas", *Environmental Toxicology*. **25**(4): 339-349.

[65]   Health and Safety Executive (HSE) (2013). "EH40/2005 Workplace exposure limits".

[66]   U.S. Environmental Protection Agency (2011). "Background indoor air concentrations of volatile organic compounds in North American residences (1990–2005): A compilation of statistics for assessing vapor intrusion".

[67]   (2013). "AGÖF guidance values for volatile organic compounds in indoor air".

[68]   Amaral, S., de Carvalho, J., Costa, M. and Pinheiro, C. (2015). "An overview of particulate matter measurement instruments", *Atmosphere*. **6**(9): 1327.

[69]   Weingartner, E., Burtscher, H., Hüglin, C. and Ehara, K. (2011). "Semi-continuous mass measurement" in *Aerosol Measurement*, John Wiley & Sons, Inc., 255-268.

[70]   Njuguna, J., Pielichowski, K. and Zhu, H. (2014). "Health and environmental safety of nanomaterials". Cambridge,UK: Woodhead Publishing Limited.

[71]   Nussbaumer, T., Czasch, C., Klippel, N., Johansson, L. and Tullin, C. 2008. "Particulate emissions from biomass combustion in IEA countries". Zurich, Austria

[72]   Kelly, K. E., Whitaker, J., Petty, A., Widmer, C., Dybwad, A., Sleeth, D., Martin, R. and Butterfield, A. (2017). "Ambient and laboratory evaluation of a low-cost particulate matter sensor", *Environmental Pollution*. **221**: 491-500.

[73]   Partisol 2000i Air Sampler/Partisol 2000i-D dichotomous air sampler. Instruction manual Thermo Fisher Scientific Inc., 2015.

[74]   TEOM 1405 ambient particulate monitor. Product specifications, Thermo Scientific, 2010.

[75]   BAM-1020 continuous particulate monitor. Product datasheet, Enviro Technology Services plc,

[76]   GRIMM EDM164 industrial enviro check specifications, GRIMM Aerosol Technik, 2016.

[77]   TZOA. Last Updated: 20 October 2014, Accessed on: 24th October 2016; Available from: http://www.tzoa.com/#homepage.

[78]   DC1100 air quality monitor. Last Updated: 22 August 2007, Accessed on: 21st October 2016; Available from: http://www.dylosproducts.com/ornodcairqum.html.

[79]   2015. Speck technical specifications. Accesed on: 21st October 2016; Available from: https://www.specksensor.com/support/tech-specs.

[80]   DUSTTRAK™ II aerosol monitors models 8530, 8530EP and 8532. Last Updated: 4 April 2012, Accessed on: 21st October 2016; Available from: http://www.tsi.com/uploadedFiles/_Site_Root/Products/Literature/Spec_Sheets/DustTrak-II-6001987_UK-A4-web.pdf.

[81]   GT-321 handheld particle counter. Last Updated: 26 March 2006, Accessed on: 21st October 2016; Available from: http://www.metone.com/docs/gt321_datasheet.pdf.

[82]   Fluke 985 particle counter. Last Updated: 1 May 2012, Accessed on: 21st October 2016; Available from: http://en-us.fluke.com/products/hvac-iaq-tools/fluke-985-hvac-iaq.html#techspecs.

[83]   OPC-N2 particle monitor. Last Updated: 1 May 2015, Accessed on: 21st October 2016; Available from: http://www.alphasense.com/WEB1213/wp-content/uploads/2015/05/OPC-N2.pdf.

[84]   PM2.5 sensor module /temperature and humidity sensor. Accessed on: 21st October 2016; Available from: http://www.sharp-world.com/products/device/lineup/selection/pdf/rf_pm_th201609_e.pdf.

[85]   Lim, H. H., Park, D., Maeng, J. Y., Hwang, J. and Kim, Y. J. (2006). "MEMS based integrated particle detection chip for real time environmental monitoring", *19th IEEE International Conference on Micro Electro Mechanical Systems (MEMS)* Istanbul, Turkeypp. 62-65.

[86]   Hajjam, A., Wilson, J. C., Rahafrooz, A. and Pourkamali, S. (2010). "Detection and mass measurement of individual air-borne particles using high frequency micromechanical resonators", *IEEE Sensors*. pp. 2000-2004.

[87]   Hajjam, A., Wilson, J. C., Rahafrooz, A. and Pourkamali, S. (2010). "Fabrication and characterization of resonant aerosol particle mass sensors", *Proceedings of The IEEE 23rd International Conference on Micro Electro Mechanical Systems (MEMS)*. pp. 863-866.

[88]   Mehdizadeh, E., Wilson, J. C., Hajjam, A., Rahafrooz, A. and Pourkamali, S. (2013). "Aerosol impactor with embedded MEMS resonant mass balance for real-time particulate mass concentration monitoring", *The 17th International Conference on Solid-State Sensors, Actuators and Microsystems (TRANSDUCERS) & Eurosensors XXVII*. Barcelona,Spainpp. 661-664.

[89]   Harrington, B. P., Abdolvand, R., Hajjam, A., Wilson, J. C. and Pourkamali, S. (2010). "Thin-film piezoelectric-on-silicon particle mass sensors", *IEEE International Frequency Control Symposium (FCS)*. Newport Beach, CApp. 238-241.

[90]   Mehdizadeh, E., Kumar, V., Pourkamali, S., Gonzales, J. and Abdolvand, R. (2013). "A two-stage aerosol impactor with embedded MEMS resonant mass balances for particulate size segregation and mass concentration monitoring", *IEEE Sensors Conference*. Baltimore, MDpp. 1-4.

[91]   Merzsch, S., Wasisto, H. S., Waag, A., Kirsch, I., Uhde, E., Salthammer, T. and Peiner, E. (2011). "Low-weight electrostatic sampler for airborne nanoparticles", *IEEE Sensors Conference*. Limerick, Irelandpp. 1177-1180.

[92]   Wasisto, H. S., Doering, L., Merzsch, S., Waag, A., Uhde, E. and Peiner, E. (2011). "Self-exciting and self-sensing resonant cantilever sensors for improved monitoring of airborne nanoparticles exposure", *IEEE Sensors*. pp. 728-731.

[93]   Wasisto, H. S., Merzsch, S., Stranz, A., Waag, A., Kirsch, I., Uhde, E., Salthammer, T. and Peiner, E. (2011). "A resonant cantilever sensor for

monitoring airborne nanoparticles", *16th International Solid-State Sensors, Actuators and Microsystems Conference (TRANSDUCERS)* Beijing, Chinapp. 1116-1119.

[94] Wasisto, H. S., Merzsch, S., Stranz, A., Waag, A., Uhde, E., Salthammer, T. and Peiner, E. (2013). "Silicon nanowire resonators for aerosol nanoparticle mass sensing", *Proceedings of the 8th IEEE International Conference onNano/Micro Engineered and Molecular Systems* pp. 506-509.

[95] Wasisto, H. S., Merzsch, S., Stranz, A., Waag, A., Uhde, E., Salthammer, T. and Peiner, E. (2012). "Femtogram mass measurement of airborne engineered nanoparticles using silicon nanopillar resonators", *Procedia Engineering*. **47**(0): 289-292.

[96] Wasisto, H. S., Merzsch, S., Waag, A., Kirsch, I., Uhde, E., Salthammer, T. and Peiner, E. (2011). "Enhanced airborne nanoparticles mass sensing using a high-mode resonant silicon cantilever sensor", *IEEE Sensors*. pp. 736-739.

[97] Wasisto, H. S., Merzsch, S., Waag, A., Uhde, E., Salthammer, T. and Peiner, E. (2013). "Airborne engineered nanoparticle mass sensor based on a silicon resonant cantilever", *Sensors and Actuators B: Chemical*. **180**(0): 77-89.

[98] Wasisto, H. S., Merzsch, S., Waag, A., Uhde, E., Salthammer, T. and Peiner, E. (2013). "Portable cantilever-based airborne nanoparticle detector", *Sensors and Actuators B: Chemical*. **187**(0): 118-127.

[99] Liang, D., Shih, W.-P., Chen, C.-S. and Dai, C.-A. (2010). "A miniature system for separating aerosol particles and measuring mass concentrations", *Sensors*. **10**(4): 3641-3654.

[100] Stanley, S. M., McHale, G., Newton, M. I., Percival, C. J. and Evans, C. R. (2005). "An EP-SAW for measurements of particulate matter in ambient air", *Nondestructive Testing and Evaluation*. **20**(1): 3-7.

[101] Black, J. P., Elium, A., White, R. M., Apte, M. G., Gundel, L. A. and Cambie, R. (2007). "MEMS-enabled miniaturized particulate matter monitor employing

1.6 GHz aluminum nitride thin-film bulk acoustic wave resonator (FBAR) and thermophoretic precipitator", *IEEE Ultrasonics Symposium*. New York, NY pp. 476-479.

[102] Park, B., Hong, J. and Lee, S.-B. (2009). "Real-time detection of airborne dust particles using paddle-type silicon cantilevers", *Journal of Vacuum Science & Technology B*. **27**(6): 3120-3124.

[103] Jaramillo, G., Buffa, C., Mo, L., Brechtel, F. J., Langfelder, G. and Horsley, D. A. (2013). "MEMS electrometer with femtoampere resolution for aerosol particulate measurements", *IEEE Sensors Journal*. **13**(8): 2993-3000.

[104] Wasisto, H. S., Merzsch, S., Stranz, A., Waag, A., Uhde, E., Salthammer, T. and Peiner, E. (2013). "Silicon nanowire resonators for aerosol nanoparticle mass sensing", *8th IEEE International Conference on Nano/Micro Engineered and Molecular Systems (NEMS)*. Suzhou, Chinapp. 506-509.

[105] Dewulf, J., Van Langenhove, H. and Wittmann, G. (2002). "Analysis of volatile organic compounds using gas chromatography", *TrAC Trends in Analytical Chemistry*. **21**(9–10): 637-646.

[106] Lakkis, S., Younes, R., Alayli, Y. and Sawan, M. (2014). "Review of recent trends in gas sensing technologies and their miniaturization potential", *Sensor Review*. **34**(1): 24-35.

[107] Radadia, A. D., Salehi-Khojin, A., Masel, R. I. and Shannon, M. A. (2010). "The effect of microcolumn geometry on the performance of micro-gas chromatography columns for chip scale gas analyzers", *Sensors and Actuators B: Chemical*. **150**(1): 456-464.

[108] Sun, J. H., Cui, D. F., Chen, X., Zhang, L. L., Cai, H. Y. and Li, H. (2013). "A micro gas chromatography column with a micro thermal conductivity detector for volatile organic compound analysis", *The Review of scientific instruments*. **84**(2): 025001.

[109] Piedrahita, R., Xiang, Y., Masson, N., Ortega, J., Collier, A., Jiang, Y., Li, K., Dick, R. P., Lv, Q., Hannigan, M. and Shang, L. (2014). "The next generation of low-cost personal air quality sensors for quantitative exposure monitoring", *Atmos. Meas. Tech.* **7**(10): 3325-3336.

[110] Fine, G. F., Cavanagh, L. M., Afonja, A. and Binions, R. (2010). "Metal Oxide semi-conductor gas sensors in environmental monitoring", *Sensors*. **10**(6).

[111] Ho, C. K., Itamura, M. T., Kelley, M. and Hughes, R. C. 2001. "Review of chemical sensors for in-situ monitoring of volatile contaminants". Albuquerque, New Mexico

[112] Urasinska-Wojcik, B., Vincent, T. A., Chowdhury, M. F. and Gardner, J. W. (2017). "Ultrasensitive WO3 gas sensors for NO2 detection in air and low oxygen environment", *Sensors and Actuators B: Chemical*. **239**: 1051-1059.

[113] Chou, J. (2000). "Photoionization detectors" in *Hazardous gas monitors: A practical guide to selection, operation and application*, McGraw-Hill: New York, 73-81.

[114] RAE Systems Inc. (2013). "The PID handbook. Theory and applications of direct-reading photoionizatoin detectors". Available from: http://www.raesystems.com/sites/default/files/content/resources/pid_handbook_1002-02.pdf

[115] Hodgkinson, J. and Tatam, R. P. (2013). "Optical gas sensing: A review", *Measurement Science and Technology*. **24**: 59.

[116] Liu, X., Cheng, S., Liu, H., Hu, S., Zhang, D. and Ning, H. (2012). "A survey on gas sensing technology ", *Sensors*. **12**: 9635-9665.

[117] Yunusa, Z., Hamidon, M. N., Kaiser, A. and Awang, Z. (2014). "Gas sensors: A review ", *Sensors & Transducers*. **168**(4): 61-75.

[118] Ho, C., Lindgren, E., Rawlinson, K., McGrath, L. and Wright, J. (2003). "Development of a surface acoustic wave sensor for in-situ monitoring of volatile organic compounds", *Sensors*. **3**(7): 236.

CHAPTER 2

ACOUSTIC WAVE TECHNOLOGY

2.1 INTRODUCTION

The various sensing technologies available for air quality monitors were introduced in Chapter 1. In this project, acoustic wave technology is employed for the development of an air quality sensor. This chapter introduces this technology by reviewing the generation of acoustic waves and their propagation modes in piezoelectric materials. The two main types of acoustic waves, i.e. surface acoustic waves (SAW) and bulk acoustic waves (BAW), are discussed. Acoustic devices using these wave modes are introduced and their performance metrics are reviewed. A detailed comparison between SAW and BAW based devices is presented.

General applications of acoustic wave devices are discussed with focus of sensing applications. In particular, a review on acoustic devices used for particle sensing and VOC detection is presented. For an acoustic device to be used in a real-time, portable sensing application, the system must have reasonable power

requirements and not need bulky laboratory equipment. Driving circuitry for the acoustic devices is introduced (oscillator topologies), which enables sensor read-out without the need for specialist instruments.

Driving circuitry constructed from discrete components is adequate for small-scale testing, although for mass-production, circuitry implemented in CMOS technologies is required. For a low cost, low power sensor system the acoustic device must be integrated with the circuitry on the same substrate. In this chapter, the different approaches of integrating complementary metal oxide semiconductor circuits with microelectromechanical systems are introduced and the current art of monolithic integration of BAW devices is discussed.

2.2 THE PIEZOELECTRIC EFFECT

The operating principle of acoustic wave devices is based on the piezoelectric effect. Piezoelectricity was first observed by the Curie brothers in 1880 [1] and refers to the property of some crystals to generate an electrical displacement when mechanical stress is applied (direct piezoelectric effect) or vice versa: to experience a mechanical deformation when an electrical field is applied (inverse piezoelectric effect).

The coupling between the electrical field and mechanical displacement is described by the piezoelectric constitutive equations shown below in their stress-charge form [2]:

$$T_i = c_{ij}{}^E S_j - e_{ij} E_j \tag{2.1}$$

$$D_i = \varepsilon_{ij}{}^S E_j + e_{ij} S_j \tag{2.2}$$

where T_i, c_{ij}, S_j, e_{ij}, E_j, D_i and E_{ij} are the stress components, the stiffness constants, the strain components, the piezoelectric stress constants, the electric field components, the electrical displacement components and the permittivity constants, respectively. The superscripts *E* and *S* denote that the constants are measured at a constant electric field and constant strain, respectively.

For a crystal structure to exhibit piezoelectric properties, the structure must have no centre of symmetry. Among the 32 classes of crystalline materials (categorised according to number of rotational axes and reflection planes), 20 classes are non-centrosymmetric.

Single crystals such as quartz, lithium niobate and lithium tantalate exhibit piezoelectricity as a result of their crystalline structure. These materials can be natural (e.g. quartz) or man-made (e.g. lithium niobate). Different angles of cut, with respect to the crystallographic axis, are possible due to the anisotropic structure of these crystals. Thus, various types of acoustic wave modes can be generated, and the crystals can be used at a range of frequencies [3].

Man-made piezoelectric materials include piezoceramic materials (such as lead zirconate titanate or barium titanate) and piezopolymer materials (such as polyvinylidene difluoride, PVDF). For this application, only piezoelectric materials capable of being deposited as thin films are considered (i.e. PZT, AlN and ZnO). AlN and ZnO are Wurtzite crystals, which have hexagonal structures, as shown in Figure 2.1.
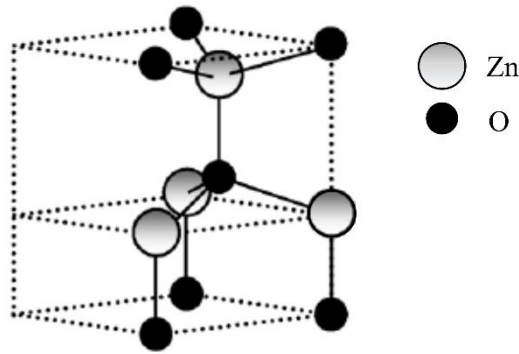
Figure 2.1 Representation of the hexagonal Wurtzite unit cell as found in zinc oxide [4].

The stress-strain relation for hexagonal wurtzite crystals is shown in (2.3). The corresponding values for ZnO and AlN are given in Table 2.1. The number of unique piezoelectric constants decreases as crystal symmetry increases [2]. For hexagonal crystals, there are a total of five independent elastic constants due to the degree of symmetry.

$$
\begin{pmatrix} \sigma_{xx} \\ \sigma_{yy} \\ \sigma_{zz} \\ \sigma_{yz} \\ \sigma_{zx} \\ \sigma_{xy} \end{pmatrix} = \begin{pmatrix} C_{11} & C_{12} & C_{13} & 0 & 0 & 0 \\ C_{12} & C_{11} & C_{13} & 0 & 0 & 0 \\ C_{13} & C_{13} & C_{33} & 0 & 0 & 0 \\ 0 & 0 & 0 & C_{44} & 0 & 0 \\ 0 & 0 & 0 & 0 & C_{44} & 0 \\ 0 & 0 & 0 & 0 & 0 & \dfrac{C_{11}\text{-}C_{12}}{2} \end{pmatrix} \begin{pmatrix} \varepsilon_{xx} \\ \varepsilon_{yy} \\ \varepsilon_{zz} \\ \varepsilon_{yz} \\ \varepsilon_{zx} \\ \varepsilon_{xy} \end{pmatrix} \tag{2.3}
$$

Table 2.1 Elastic stiffness coefficients (GPa) for ZnO and AlN.

	C_{11}	C_{12}	C_{13}	C_{33}	C_{44}	C_{66}	REF.
ZnO	210	121	105	211	42.5	44.3	[4]
AlN	396	137	108	373	116	129.5	[5]

Given an understanding of the material crystal structure, acoustic sensors can be designed for different applications, depending of the type of waves required. In the next section, the propagation of acoustic waves generated in the piezoelectric materials is discussed.

2.3 ACOUSTIC WAVES PROPAGATION

Acoustic waves are disturbances within a medium caused by an excitation source. As they propagate, the energy is transferred along the elastic medium (gas, liquid or solid) in the form of oscillation or vibration [6]. The propagation speed of the wave depends on the mechanical properties of the medium.

Two main types of acoustic waves can be generated in a piezoelectric material, when an electric voltage is applied, namely Surface Acoustic Waves (SAW) and Bulk Acoustic Waves (BAW). As the name suggests, the main difference is the way in which the acoustic waves propagate through the piezoelectric material.

Depending on the orientation of the piezoelectric crystal, different types of acoustic waves can be generated as depicted in Figure 2.2. Longitudinal and shear (transverse) waves have particle displacements that are parallel and normal to the direction of wave propagation, respectively. In Rayleigh waves, surface particles move in elliptical paths, with two distinctive particle displacement components: longitudinal

and vertical shear. Other types of waves include Lamb and Love waves which are well documented in publications by Ballentine [2], Rosenbaum [7] and Auld [8].
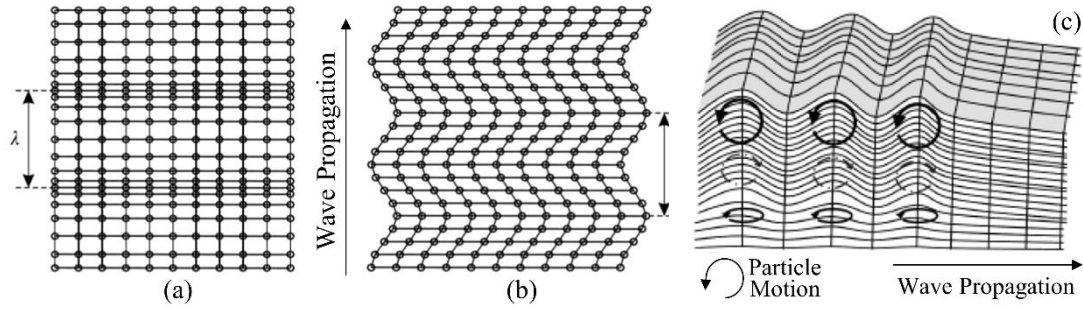
Figure 2.2 Representation of the particle displacement of (a) longitudinal, (b) shear and (c) Rayleigh waves. [9, 10]

An important design criterion for acoustic wave based sensors is the careful selection of the mode of acoustic wave. This dictates the efficiency of the devices for a given sensing application (gas or liquid media) which will be discussed in section 0. For example, longitudinal waves are suitable for use in gaseous media but not suitable for liquid applications (they become attenuated). A comparison of the operation of the different types of waves according to their mode is presented by Gardner *et al.* [3]. The next two sections discuss the devices that utilise SAW and BAW waves for various applications. All these devices fundamentally operate through the use of piezoelectric materials.

2.4   SURFACE ACOUSTIC WAVE DEVICES

Surface acoustic wave devices consist of a piezoelectric substrate on which metallic interdigital transducers (IDTs) are patterned using a photolithography process. An IDT is formed by two comb-shaped electrodes [3] with periodically spaced fingers. In SAW devices, acoustic waves propagate along the surface of the substrate. For the case of Rayleigh waves, the most commonly used wave mode, their wave motion extends below the piezoelectric surface, to a depth of approximately one wavelength [2].

SAW devices can be classified into delay line and resonator configurations. A SAW delay line is depicted in Figure 2.3. An electrical signal applied to the input IDT generates an acoustic wave which propagates along the surface until it reaches the

output IDT. Here, mechanical to electrical conversion takes place (direct piezoelectric effect) and an output electrical signal is generated.
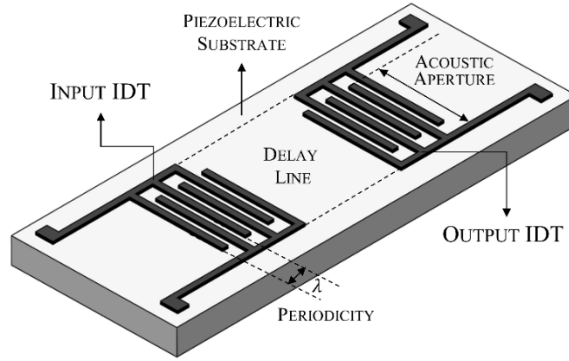
Figure 2.3 Structure of a SAW delay line device.

The resonant frequency of the device is mainly determined by the periodicity of the IDT as per equation (2.4), along with other geometric parameters such as the acoustic aperture and number of finger pairs.

$$f_o = \frac{v}{\lambda}$$ (2.4)

where v is the acoustic velocity of the piezoelectric material, λ is the wavelength (periodicity) and f_o is the fundamental resonant frequency. Typical operating frequencies of SAW devices range between 30 MHz and 1 GHz [3]. For frequencies above 2 GHz, the IDTs become difficult to manufacture given the fine dimensions required, when in general, mask accuracy is limited to 0.25 µm.

A two-port SAW resonator (SAWR) is shown in Figure 2.4a. The operating principle is the same as the delay line configuration but it incorporates additional reflector gratings. These reflectors aid the reflecting and confining of the wave between the IDTs to reduce acoustic losses [10]. The one-port configuration (shown in Figure 2.4b) employs a single IDT to both generate and receive the acoustic wave.

Commonly used piezoelectric substrate materials for SAW devices are Quartz, Lithium Niobate ($LiNbO_3$) and Lithium Tantalate ($LiTaO_3$). Depending on their crystal cut and orientation, shear horizontal (SH) or Rayleigh waves can be excited. Relevant characteristics of different cuts of these materials are presented in [3, 11, 12]. The temperature coefficient (TC) of a piezoelectric material describes the relation

between a change in temperature and the consequent change in a physical property of the material (e.g. elastic constant values, acoustic velocity).

One of the most relevant properties of quartz crystal is that its TC value is dependent on the cut angle of the crystal. ST-cut quartz (42°-Y cut angle) has a TC of 0 ppm/°C (material properties are not dependant on temperature) and thus, it is attractive for sensing applications to eliminate temperature effects, that will influence the sensor readings.
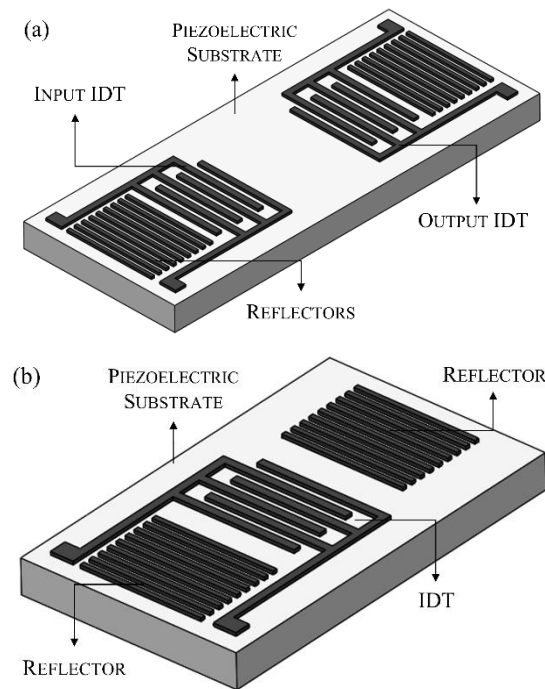
Figure 2.4 Schematic of (a) Two-port and (b) One-port SAW resonators.

2.5   BULK ACOUSTIC WAVE DEVICES

The basic configuration of a BAW resonator is shown in Figure 2.5. It comprises of a piezoelectric material sandwiched between two metal electrodes. Applying an electrical signal between the electrodes generates an acoustic wave that propagates through the bulk of the piezoelectric material. Due to the reflection of the wave at the surfaces of the electrodes in contact with air, a standing wave is formed inside the piezoelectric layer.

The fundamental resonant frequency is determined by the thickness, d, of the piezoelectric layer and the acoustic velocity, v, of the material by [13, 14]:

$$f_o = \frac{v}{2d} \tag{2.5}$$

Thus, at the fundamental resonant frequency, the thickness of the piezoelectric layer is half the wavelength of the acoustic wave (see equation (2.4)).
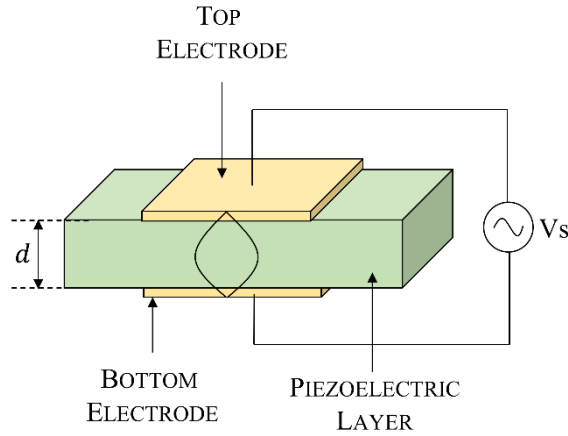
Figure 2.5 BAW resonator configuration and wave propagation.

Although equation (2.5) provides a good approximation of the fundamental frequency, the characteristics of the electrodes (i.e. thickness, density) influence the resonant frequency of the device [14, 15]. Thus, this will be considered during the design process, as described in Chapter 3.

2.5.1 QUARTZ CRYSTAL MICROBALANCE

Quartz crystal microbalance (QCM) is the most widely known BAW resonator [11]. They are formed by an AT-cut quartz crystal (36° YX cut), usually disk-shaped, with patterned metal electrodes on both sides. An electrical signal applied across the electrodes produces standing shear waves (thus they are also referred as thickness shear mode (TSM) resonator). A photograph of a commercial QCM device is shown in Figure 2.6.

Figure 2.6 Photograph of commercial QCM device (10 MHz).

The Sauerbrey equation describes the effects of mass loading on the resonant frequency of a quartz crystal, given as [16]:

$$\Delta f = \frac{2f_o{}^2}{\sqrt{\mu\rho}} \cdot \frac{\Delta m}{A} \tag{2.6}$$

where Δf is the change in resonant frequency, f_o the fundamental resonant frequency, μ the elastic constant, ρ the density, Δm the mass load and A is the area. The addition of a uniform mass, of thickness d, in contact with the surface of the device causes a shift in the resonant frequency of the crystal with mass sensitivity defined as [17]:

$$S_m = \frac{A\Delta f}{\Delta m} = -\frac{f_o}{\rho d} \tag{2.7}$$

The thinner the quartz crystal, the higher the resonant frequency of the device and therefore, the higher the sensitivity that can be attained [17].

For their use in sensing applications, acoustic devices operating at high frequencies (>1 GHz) are desired, as the sensitivity is directly proportional to the frequency of operation. The operating frequencies of QCM devices is limited by the mechanically achievable thickness of the quartz crystal [18] (limited to ~50 µm). Thin quartz crystals are very fragile and difficult to handle, thus QCMs typically can only operate at frequencies in the range of 5-30 MHz [11]. SAW devices are limited to operate at frequencies up to 2 GHz due to the fine pitch required for the IDTs

(~0.25 µm), which become difficult to pattern. These manufacturing limitations clearly restrict the sensitivity of QCM and SAW devices. Thin film BAW acoustic resonators, capable of operating at high frequencies (2-5 GHz), were developed to overcome the restrictions of QCM and SAWs. In the next section, the operation of these resonators is discussed.

2.5.2 THIN FILM BULK ACOUSTIC RESONATORS

Thin film technology and modern micromachining techniques have made possible the development of bulk acoustic wave devices working at high frequencies, typically in the range of 2-5 GHz [19-21]. Thin film bulk acoustic resonators consist of a thin piezoelectric layer (deposited by various methods such as sputtering, up to a maximum 6 µm thick) sandwiched between two metal electrodes and fabricated on top of a carrier substrate, typically silicon. To prevent wave dissipation into the substrate and obtain high quality factors, acoustic isolation must be provided.

Depending on the way in which the acoustic energy in confined within the resonator structure, two different types of thin film BAW resonators can be identified, namely free-standing Film Bulk Acoustic Resonator (FBAR) and Solidly Mounted Resonator (SMR), depicted in Figure 2.7.
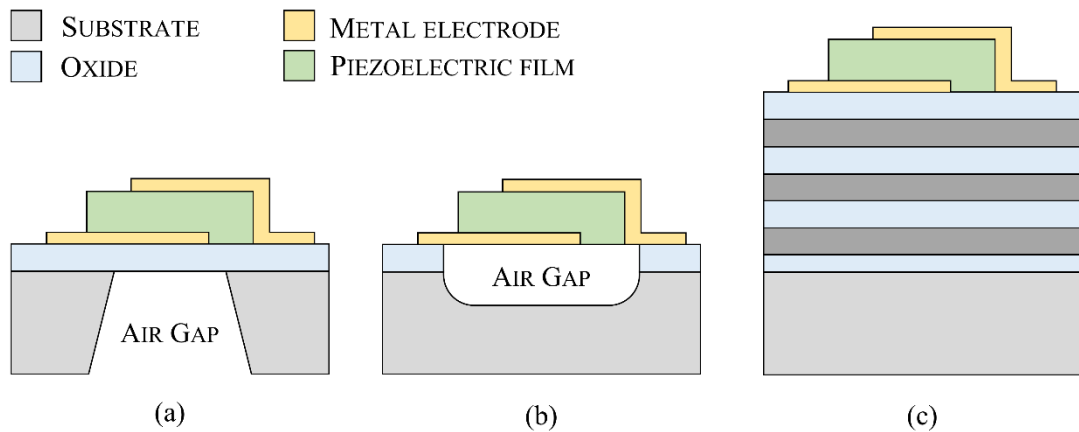
Figure 2.7 Structure of thin film BAW resonators (a) membrane FBAR, (b) air-gap FBAR and (c) SMR. Figures are not to scale.

First reported in 1980 by three independent groups, [13, 22, 23], FBAR devices take advantage of the low acoustic impedance of air to provide acoustic isolation to

the substrate. An air gap is created between the substrate and the resonator structure either by bulk micromachining (membrane FBAR) or surface micromachining (air-gap FBAR).

The very first SMR concept was proposed by Newell in 1965 [24] who described the use of quarter wavelength layers with large impedance ratios to isolate the resonator from the substrate (avoiding the need of micromachining an air gap). Decades later, Lakin *et al.* [25] demonstrated a SMR device for wireless systems applications.

Solidly mounted resonators make use of an acoustic mirror formed by alternating layers of low and high acoustic impedance materials. The impedance mismatching of these layers reflects the acoustic energy back to the resonator structure preventing energy leakage. The operation and design of solidly mounted resonators (including the acoustic mirror) are discussed in detail in Chapter 3.

To be able to assess the advantages and disadvantages of the different types of devices (SAW, FBAR and SMR), the methods of measuring performance of the devices must be understood. A detailed comparison is given in section 2.7. The performance criteria for acoustic devices is described in section 2.6.

2.6 PERFORMANCE METRICS

2.6.1 QUALITY FACTOR

One of the key performance parameters for bulk acoustic waves resonators is the quality factor. This performance metric indicates how well the acoustic energy is confined within the resonator. The fundamental definition of the Q factor relates the total energy stored in the resonator and the power dissipated per cycle as [26]:

$$Q = \omega \cdot \frac{\text{Energy Stored}}{\text{Power dissipated}} \tag{2.8}$$

A BAW resonator with high quality factor is desirable as this means that the energy is efficiently trapped in the resonator structure and thus low energy losses are present in the system. Energy dissipation in BAW devices can steam from different

loss mechanisms such as Ohmic losses in the electrodes and contacts, mechanical losses due to laterally leaking waves (spurious modes) and viscous damping [27-29].

For the suppression of spurious modes two methods are commonly reported in the literature [28, 30, 31]. The first method, apodization, involves the careful design of the top electrode of the resonator, to avoid parallel sides on the active area (also, the angle between any two sides must not be near 90°) [32]. This entails that none of the edge points on the active area have the same lateral resonator path (different path lengths will be possible from all the points). Thus, a large number of broader peaks are created, giving the effect of a smoother pass band (a reduction compared to the sharp spurious modes) [33].

The second method was proposed by Kaitila, in order to prevent the spurious modes from being excited, as opposed to apodization, which only reduces their effect [30]. The method suggests adding a border region at the edge of the active area. The border must match the boundary conditions for homogenous excitation in the active area [28]. This has the effect of removing the lateral wave vector components, and leaves only the main mode to couple electromechanically [33]. This method is preferred as it can be used to reduce the losses due to the lateral modes (thereby increasing the Q factor of the device), unlike apodization, which reduces the spurious modes, but does not greatly improve performance.

In the case of SMRs, another primary loss mechanism should be taken into account, namely the acoustic energy dissipation to the substrate. This is discussed in the following chapter. In short, appropriate design of the acoustic mirror is necessary to ensure these losses are minimised and to obtain a high Q factor.

The Q factor is an important parameter in characterising oscillators and resonators that must be measured carefully. Several methods of determining the Q factor of a resonator have been proposed [34]. These methods aim to overcome the frequency dependent additive noise and measurement noise that make calculation of the Q factor very sensitive and susceptible to spurious results [18].

One of the most commonly used practical techniques involves using the phase derivative method to extract the Q factor from the impedance measured of the BAW

device. Equation (2.9) shows the Q factor calculation, where ϕ represents the admittance or impedance phase [35].

$$Q = \frac{1}{2}f_s \left| \frac{d\phi}{df} \right|_{f=f_s}$$

(2.9)

The most accessible method is often termed the 3dB method [36]. This method uses the S_{21} parameter against frequency data, which is usually smoothed or filtered to reduce the sensitivity to noise. The points where the magnitude of the S_{21} response falls to -3 dB either side of the centre resonant frequency are measured. The Q factor is then calculated by dividing the difference between the two -3 dB points by the resonant frequency [37]. To overcome the measurement noise affecting the accurate determination of BAW resonator Q factors it was proposed the raw data be fitted to a model curve prior to calculating the -3 dB points [18]. However, this method is not suited to resonators that have spurious ripple and non-ideal loss, which are common artefacts in BAW devices.

A complementary method of measuring the performance of acoustic devices, the electromechanical coupling coefficient, is discussed below. A well optimised design will consider both parameters (Q factor and electromechanical coupling coefficient).

2.6.2   ELECTROMECHANICAL COUPLING COEFFICIENT

The electromechanical coupling coefficient, k^2, measures how efficiently the electrical energy is converted to mechanical energy in piezoelectric materials, it is expressed as:

$$k^2 = \frac{\text{stored mechanical energy}}{\text{applied electrical energy}}$$

(2.10)

The electromechanical coupling coefficient is a piezoelectric material property dependant on the piezoelectric and elastic parameters of the material. For the longitudinal mode, it can be expressed as [19]:

$$k^2 = \frac{e_{33}^2}{c_{33}^D \varepsilon_{33}^S} \tag{2.11}$$

where e_{33} is the elastic constant, c_{33}^D is the elastic stiffness at constant electric displacement and ε_{33}^S is the dielectric permittivity.

The overall mechanical-to-electrical conversion efficiency of the entire resonator structure (not only of the piezoelectric layer) is given by the effective electromechanical coupling coefficient, k_{eff}^2 determined by [9]:

$$k_{eff}^2 = \frac{\pi}{2} \cdot \frac{f_s}{f_p} \cdot \cot\left(\frac{\pi}{2} \cdot \frac{f_s}{f_p}\right) \tag{2.12}$$

where f_s and f_p are the series and parallel resonant frequency, respectively. In practice, the effective coupling coefficient is approximated as:

$$k_{eff}^2 = \frac{\pi^2}{4} \cdot \frac{f_s}{f_p} \cdot \left(\frac{f_p - f_s}{f_p}\right) \tag{2.13}$$

The electromechanical coupling coefficient, k^2, and the effective electromechanical coupling coefficient, k_{eff}^2, have usually different values. While the former only depends on the piezoelectric material parameters, the latter is influenced by the properties of other materials used in the electrodes and additional losses in the entire structure such as the lateral spurious modes.

2.7 COMPARISON BETWEEN ACOUSTIC TECHNOLOGIES

In this section, a comparison between SAW and thin film BAW technologies is presented, followed by a review of the two types of BAW resonators (FBAR and SMR).

2.7.1 COMPARISON BETWEEN BAW AND SAW TECHNOLOGIES

FREQUENCY OF OPERATION. In SAW devices, the frequency of operation is limited by the achievable IDT pitch and finger width. Commercially devices are in the range of

500 MHz to 1 GHz [3] although a limit of 2.5 GHz could be achieved with finger width of 0.25 µm [18].

Typical operating frequencies of commercial BAW devices are in the range of 2 - 5GHz [19], however devices working at frequencies up to 20 GHz can be obtained with piezoelectric films as thin as 220 nm [38].

SIZE. The footprint of BAWs is about 3 to 5 times smaller than that of SAWs. Miniature BAWs allow their integration in mobile communication devices.

PERFORMANCE. BAW devices exhibit higher Q values in the high frequency range (>2 GHz), have smaller Ohmic losses of the electrodes compared to that of the IDTs in SAWs and demonstrate better temperature coefficients of frequency (TCFs) than SAW at -20 ppm/°C and -45 ppm/°C, respectively. [18, 39, 40].

MANUFACTURING. BAW devices can be fabricated on any substrate. Silicon substrates are usually preferred due to their low cost, availability and good thermal properties. Standard IC equipment, readily available in CMOS foundries can be employed for the processing of BAW devices. This makes the devices suitable for monolithic integration and low cost, high-volume production [41].

SAW devices usually only require a one-mask photolithography process and the deposition of only two materials. In contrast, BAW devices require more fabrication steps involving the deposition of several layers and the use of up to ten photolithography masks, increasing the total manufacturing time and cost [18, 34].

In the case of SAW design, the resonant frequency is determined by the parameters of the IDTs, which can be modified in the mask design. A single wafer can contain multiple SAW designs of different operating frequencies. For BAW devices, the frequency is determined by the thicknesses of the layers. As the layer thickness is fixed across a wafer, only devices working at the same frequency can be fabricated at a time. When BAW devices are manufactured, accurate control of the thicknesses of the layers is needed and so there is room for fabrication inaccuracies between wafer to wafer. [39]

POWER HANDLING. Due to their parallel plate geometry, BAW filters can have better power handling capabilities compared to SAW devices [18, 40].

PACKAGING. BAW devices use microcaping packaging technology, allowing packaging in a few steps using batch processing (wafer-level packaging) [40, 41]. Conversely, SAW devices use hermetic packages, to prevent humidity damaging the IDTs [42]. Often, flip chip technology is used with LTCC packages, that can be sealed with a lid [40]. Packaging represents the biggest cost for SAW devices.

2.7.2 COMPARISON BETWEEN **FBAR** AND **SMR** TECHNOLOGIES

ELECTROMECHANICAL COUPLING COEFFICIENT. Compared to SMRs, FBAR devices exhibit k_{eff}^2 values ~0.4% higher than SMRs [40]. The air-electrode interface yields excellent reflectivity at any frequency [41] and is more effective at trapping the acoustic energy [18]. However, the reflectivity of the acoustic mirror in SMRs is a function of frequency and thus can be tailored to eliminate harmonics [41].

TEMPERATURE COEFFICIENT OF FREQUENCY. In SMRs, the use of SiO_2 layers in the acoustic mirror (with positive TCF) helps compensate for the negative TCF of the other layers in the structure. Thus, SMRs have lower TCFs (-20 ppm/°C) compared to FBARs (-30 ppm/°C) [18].

SOURCES OF LOSSES. Both FBARs and SMRs suffer from three main loss mechanisms (losses due to lateral modes, Ohmic losses and scattering losses). However, additional losses are present in SMR devices related to the energy leaking through the acoustic mirror. Therefore, higher Q values are observed in FBAR devices [40].

DESIGN. Unlike SMR devices, the design of FBAR devices is more straight forward. The performance of FBARs is only dependent on the process. A one-dimensional model can suffice for their design. On the other hand, the design of SMRs becomes more complicated, and often 2D models are required for the design of the acoustic mirror. At the same time however, this provides flexibility in the design, which helps optimize the device [18].

MANUFACTURING. Both FBAR and SMR devices can be manufactured upon any substrate. Silicon is usually the substrate of choice due its near-unlimited availability, low cost and excellent thermal properties [41] (it is widely used in IC processes). All processes required for the fabrication of BAW devices are CMOS compatible, in terms of thermal budget and contamination issues. Thus, BAW devices can be manufactured in a standard CMOS foundry, using existing IC equipment and infrastructure [41]. This CMOS compatibility makes BAW devices suitable to be integrated with the circuitry fabricated in a CMOS process. However, the fabrication of the BAW device itself is performed only in a post-CMOS process, as discussed in section 2.11.

HANDLING. FBAR devices are very fragile (due to the cavity formed to isolate the device) and so they should be handled with care. They are prone to mechanical damage during dicing and packaging [18]. On the other hand, SMRs are mechanically more robust [41].

2.8 APPLICATIONS

Electro-acoustic devices became popular in many technical applications during the 1980s, particularly SAW devices for use in commercial products in the telecommunications area (in the range of 100 MHz to a few GHz) [43]. After serving the mobile communications market for more than 20 years, the need of technology capable to meet the very stringent power requirements and electrical specifications for applications at frequencies above 3 GHz led to the development of BAW devices, with the first commercial BAW filters introduced in 2001 [40, 42].

RF applications of FBAR devices such as filters and duplexers have overcome the limitations of SAW and ceramic technologies and can nowadays be manufactured at competitive prices using standard IC manufacturing processes [21]. A comparison between BAW and SAW technologies was presented in section 2.7.

With the advances in mobile technology, there has been a surge in demand for low power, low cost sensors and transducers for portable consumer electronics. The RF MEMS market has shown a staggering growth over the last decade. It is estimated that in just five years (2010 to 2015) the RF MEMS market grew from a global worth of $359 Million to $1.1 Billion [44, 45].

In particular, the market for BAW filters has enjoyed a huge growth since 2011. This is largely due to increased reliance on a wide range of wireless technologies (e.g. WiFi, Bluetooth, 3G, 4G networks) in mobile communications. Smartphones usually use BAW filters to isolate the signals from each other. BAW technology delivers excellent performance at the GHz frequencies needed for mobile applications. The market for BAW filters dominates the RF MEMS market share (~90%), as shown in Figure 2.8. The market is set to exponentially grow to almost $2.5 Billion by 2019 [46].
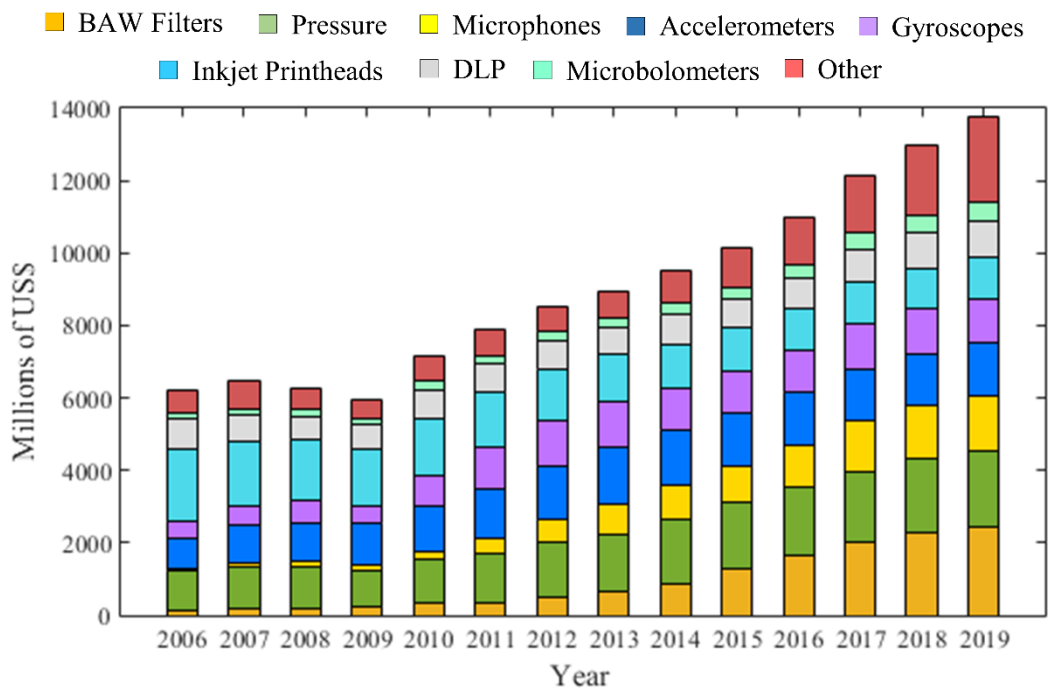
Figure 2.8 Total MEMS Market by Device.

2.8.1   SENSING APPLICATIONS

Although SAW and BAW devices have been used extensively in the telecommunications industry, acoustic devices are also widely used in sensing applications. SAW sensors have been used for the last 4 decades, and in the last 20 years they have matured from a popular research area to a strong commercial market. Today there is still great interest in SAW devices in the acoustic sensors research field, due to their low-cost, small size and good sensitivity [47].

The sensing mechanism of acoustic devices relies on a change in the properties of the propagating wave (frequency, amplitude, phase or velocity) caused by the interaction with the environment [2]. Acoustic devices are sensitive to physical properties (mechanical or electrical) occurring at their surface (e.g. mass loading, viscosity or conductivity) [48].

For their use in sensing applications, acoustic devices are commonly used in an oscillator circuit. Perturbations induced by the physical property being measured are related to a change in the oscillation frequency. However, it is important to consider any external disturbances to the device such as changes in temperature, humidity and pressure which will produce undesirable changes not directly related to the property of interest.

A popular method to eliminate common mode interference is the use of a dual oscillator configuration as depicted in Figure 2.9 [49, 50]. This method uses a differential principle implemented using a mixing circuit. One acoustic device is used as the reference element while the second acts as the sensing element. The reference and sensing oscillator frequencies are mixed in a heterodyne process. A low pass filter is used to output only the differential frequency. In this way, any frequency changes measured from the differential output will be solely due to the property being measured.
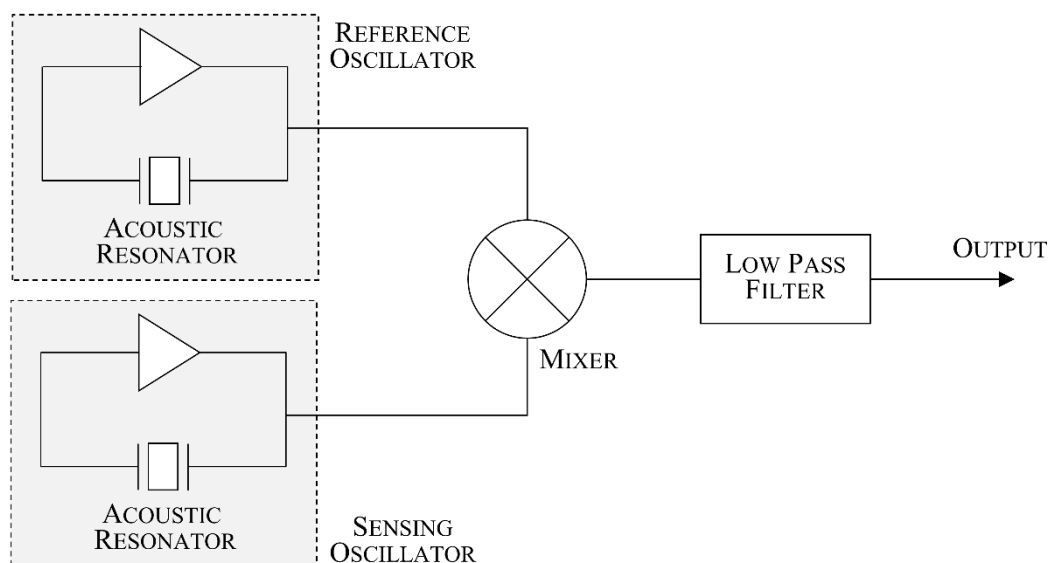
Figure 2.9 Block diagram of dual oscillator configuration and mixing circuitry.

Table 2.2 Example of sensing applications of acoustic wave devices.

SENSING APPLICATION	EXAMPLE
Pressure and Temperature sensors	▪ Two-port SAW resonators on ST-cut quartz by Benetti *et al.* [51]. ▪ Quartz thickness shear mode sensor for downhole pressure measurements [52]. ▪ Aluminium Nitride and Zinc oxide-based FBARs for simultaneous measurement of pressure and temperature by Chiu *et al*. [53] and He *et al*. [54].
Chemical vapour sensors	▪ An array of four polymer-coated SAW resonators for pheromone detection. [55] ▪ Chemical sensor based on a Thin Film Bulk Acoustic Resonator using a thin film of Pd as chemically interactive membrane [56] ▪ Vapour phase detection of odorant molecules based on Solidly Mounted Resonator [57].
Humidity sensors	▪ Surface acoustic wave sensor using polyvinyl-alcohol film demonstrated by Penza *et al.* [58] ▪ Quartz crystal microbalance based on nanodiamond sensing films [59]. ▪ Zinc oxide-based FBAR devices with hygroscopic polymeric materials [60]. ▪ Graphene oxide coated FBAR device driven by Pierce oscillator by Xuan *et al.* [61]
Gravimetric or mass sensors	▪ Zinc oxide based film bulk acoustic resonator reported by Lin *et al.* [62] with a mass sensitivity 3654 Hz·cm^2/ng. ▪ A surface acoustic wave resonator for the detection of fine particles [63]. ▪ A system for measuring particle mass concentration based on quartz crystal microbalance [64].
Biosensing and Liquid phase sensors	▪ QCM based sensor for the detection of *Escherichia coli*. [65] ▪ Two-port SH-SAW Resonator [66] and SH-SAW in a delay line configuration [67] on 36° YX LiTaO3 piezoelectric substrate for the discrimination between liquids of basic tastes. ▪ Solidly Mounted Resonators operating in shear mode for liquid sensor applications [68, 69].

Sensing applications of acoustic devices are very wide-ranging. These devices have been used, for example, as gravimetric, temperature, pressure and humidity sensors. If functionalised with selective coatings, they can also serve as chemical sensors [11] in both gas and liquid phases (depending of propagation mode, to be explained in section 0). This has made them very attractive for biosensing applications [43, 70]. Several works have reported the use of acoustic wave devices in a variety of sensing applications. Representative examples are compiled in Table 2.2 above.

2.8.2 COUPLING TO GASES, SOLIDS AND LIQUIDS

Thin film BAW resonators can operate in longitudinal or shear mode. In the case of wurtzite piezoelectric materials, the mode of operation is determined by the direction of the applied electric field relative to the c-axis orientation.

BAW resonators are typically operated in the longitudinal mode, also referred as thickness extensional mode (TEM) [71]. The c-axis orientation of the deposited thin films together with the standard BAW configuration best support this mode [41]. Longitudinal waves are excited when the electric field is applied parallel to the c-axis.

BAW devices can also operate in the thickness shear mode (TSM). TSM waves can be excited in BAW devices by applying an electric field perpendicular to the c-axis of the piezoelectric material. This can be accomplished in two different ways: (1) deposition of c-axis inclined piezoelectric layers [70, 72, 73] or (2) lateral field excitation (LFE) [71, 74].

Several different techniques have been proposed to deposit the tilted layers and promising results have been reported in the literature [73, 75]. However, these techniques are confined to use in research laboratories, as the controlled directional deposition process required to create uniformly tilted c-axis grains is not possible when using industrial main-stream manufacturing [76].

The second way of achieving a TSM resonator involves patterning coplanar electrodes on the top surface of the piezoelectric material. With this method higher Q values can be obtained because the electrodes are not directly in the path of the acoustic wave [74].

For gaseous and solid phase sensing applications, BAW resonators are mainly operated in the longitudinal mode. In gas sensing applications, these devices are functionalised with a selective coating, which absorbs the gas or vapour changing the mass loading of the resonator, as will be explained in more detail in section 6.2.

For in-liquid sensing applications, however, a BAW device operating in the thickness shear mode is desirable. The longitudinal mode is not appropriate for liquid phase applications due to energy dissipation into the liquid which can result in a decrease of the quality factor of the resonator of about 95% [77]. Conversely, shear waves do not produce compressional motion into liquids [72] resulting in lower attenuation of the acoustic energy. Thus, shear mode resonators are preferred for biosensing applications.

2.8.3 PARTICLE SENSING

Acoustic wave devices, particularly QCMs and SAWs, have been previously proposed for particle detection. The sensitivity of these devices, however, is limited by their operating frequency. In an early work by Chuan [78], QCM devices coated with an adhesive layer were used within an impactor instrument for the mass measurement of particles. Trying to improve the sensitivity of this instrument, Bowers and Chuan developed a particulate mass sensing instrument based on a commercial delay line SAW device and a SAW resonator [79, 80].

In a more recent work conducted at the National Taiwan University, two QCM devices were used together with two virtual impactors (VIs) for the measurement of particle mass and size distribution at a time [64]. Delay line SAW devices were used with electrostatic precipitators for PM measurements in the work by Stanley [81]. Recent work at the University of Warwick focused on the development of a particle sensor consisting of two SAW resonators working at a frequency of 262 MHz and associated to interface circuitry for the detection of micro sized particles [63, 82], finding a relationship between particle size and mass sensitivity.

Researchers at the University of California, USA worked on the development of a particulate matter monitor based on a thin film bulk acoustic resonator (FBAR) as the mass sensitive element [83]. They proposed the use of thermophoresis for the

deposition of the particles onto the FBAR device and used a thermofluidic interconnect for the air sample flow. Further improvements were made to this first prototype by the same research group including the addition of an air-based microfluidic circuit and incorporation of a miniature air sampler and VI [84, 85]. A much higher sensitivity was observed for these devices compared to the previously mentioned works employing QCMs and SAW devices as summarised in Table 2.3.

Table 2.3 Comparison of mass sensitivities of reported acoustic wave devices for particle detection.

ACOUSTIC DEVICE	RESONANT FREQUENCY	SENSITIVITY	LIMIT OF DETECTION	TEST PARTICLES	NOTES	REF.
QCM	~ 5MHz	0.288 Hz/ng	> 3.47 ng	Silicon dioxide (0.5 -8 µm)	Coated with thin photoresist.	[86]
QCM	10 MHz	0.7 Hz/ng	3 ng	Aerosol particles	Coated with an adhesive layer.	[79, 80]
QCM	~12 MHz	-	Minimum mass detected: 0.83 µg	Acrylic particles	Device coated with hydrogel	[64]
SAW love wave	125 MHz	0.2 m°m^3/s·µg	Concentration range: 0-400 µg/m^3	PM2.5, PM10 generated from burning candle /soldering iron	Silica guiding layer. Phase shift measurements	[87]
SAW delay line	158 MHz	266 Hz/ng	-	Aerosol particles	-	[79]
SAW resonator	200 MHz	904 Hz/ng	3 pg	Monodisperse olive oil aerosol particles	Mass sensitivity dependant on mass location on the device.	[80]
SAW resonator	262 MHz	275 Hz/ng	0.2 ng	Gold particles diameter 0.75 µm	Mass sensitivity dependant on particle size	[63]
FBAR	1.6 GHz	2.5 Hz per µg/m^3	1 pg 18 µg/m^3	Environmental Tabaco smoke from cigarette	Thermophoresis used for particle deposition.	[83]

2.8.4 VOC SENSING

VOC sensing with acoustic devices is usually accomplished by coating the device with a thin sensitive layer. Several works have been published for the detection of VOCs using QCM and SAW based sensor technologies. Extensive reviews of these works can be found in the literature [88, 89]. In this section, a brief review regarding the use of thin film BAW resonators for VOC detection is presented. Table 2.4 gives representative examples of such devices.

For their application in air quality monitoring, VOC sensors based on BAW resonators should be capable of detecting the maximum safe exposure limits of the target vapour (given in Table 1.2). Thus, the sensitivity and limit of detection of these sensors are very important factors to consider.

Thin polymer coatings (of a few hundreds of nanometres) applied to the sensing area of the BAW resonators is the most common method to detect gases and vapours using FBARs. However, alternative approaches have been proposed such as the use of the piezoelectric layer itself as sensitive layer [90].

Table 2.4 Examples of BAW devices used for VOC detection.

ACOUSTIC DEVICE	SENSING LAYER	TARGET VAPOUR	SENSITIVITY / DETECTION LIMIT	NOTES	REF.
ZnO based FBAR 1.7 GHz	Not disclosed	Benzene Ethanol Formaldehyde	2500 Hz/ppm 84 Hz/ppm 5067 Hz/ppm	The use of a microheater for the reference oscillator is proposed.	[91]
ZnO based FBAR 1.4 GHz	-	Acetone Ethanol	4 ppm LOD 6ppm LOD	ZnO thin film of the resonator used as sensing layer	[90]
AlN based SMR 8 GHz	PMMA	Acetone	900 m^2/kg	-	[92]
ZnO based SMR 2 GHz	PVDF	DMMP Vapour (10-50 ppm)	718 kHz/ppm	-	[93]
ZnO based SMR 1.44 GHz	PDMS	Toluene (1000ppm – 7000ppm)	7.29 Hz/ppm 60 ppm LOD	Low concentration of the vapour not tested	[94]
AlN based SMR 2.5 GHz	20-80 nm PMMA	Acetone	300-700 Hz/ppm	Different sensitivities according to polymer thickness	[95]

For acoustic devices to be used in real-time, low cost applications, read-out circuitry must be developed. Bulky and expensive instruments (i.e. network analysers) are suitable only for laboratory characterisation and require highly qualified operators. The next section introduces the electronic circuitry used to drive acoustic resonators and measure the response of these devices.

2.9 DRIVING CIRCUITRY

Three main methods can be used for measuring the response of piezoelectric resonators, namely amplitude, phase and frequency measurements [48]. In this work, a frequency measurement system using an oscillator circuit will be used as it provides a simple yet accurate, compact and inexpensive solution for sensing applications [3]. An overview of oscillators for this implementation is presented here.

A basic feedback oscillator is shown in Figure 2.10. It consists of an RF amplifier of voltage gain $A(j\omega)$ with its output fed back into the input signal in a positive feedback loop. The loop gain around the feedback loop is given by $A\beta$, where $\beta(j\omega)$ is the transfer function describing the feedback network, in this case the acoustic resonator, which determines the oscillation frequency.
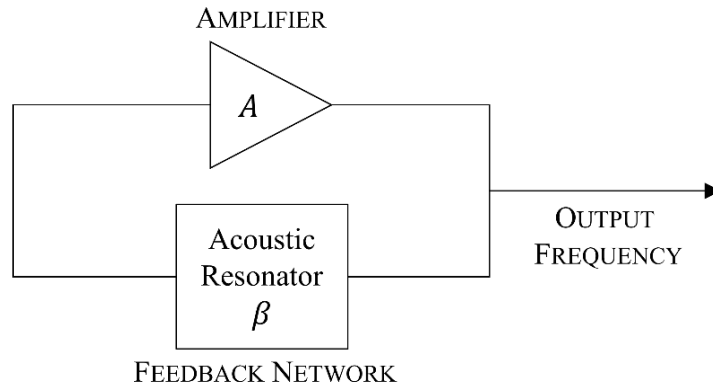
Figure 2.10 Basic form of feedback oscillator.

For oscillations to be sustained, the Barkhausen criterion must be met. The criterion states the loop gain must equal unity and the phase shift around the loop must be zero or a multiple of 360°. In most cases the amplifier provides a 180° phase shift and thus the acoustic resonator must provide an additional phase shift of $180° \pm n360°$, where n is an integer, as stated in equation (2.15). The amplifier gain must provide sufficient gain to overcome the insertion losses of the resonator and meet criteria (2.14).

$$|A\beta| = 1 \tag{2.14}$$

$$\angle A\beta = \pm n360° \tag{2.15}$$

2.9.1 OSCILLATOR CONFIGURATIONS

Most widely used crystal oscillators are the Colpitts and Pierce oscillators, depicted in Figure 2.11 in a transistor-based implementation. Both oscillators (as well as the Clapp oscillator) have similar configurations, with the main difference being the grounding location.
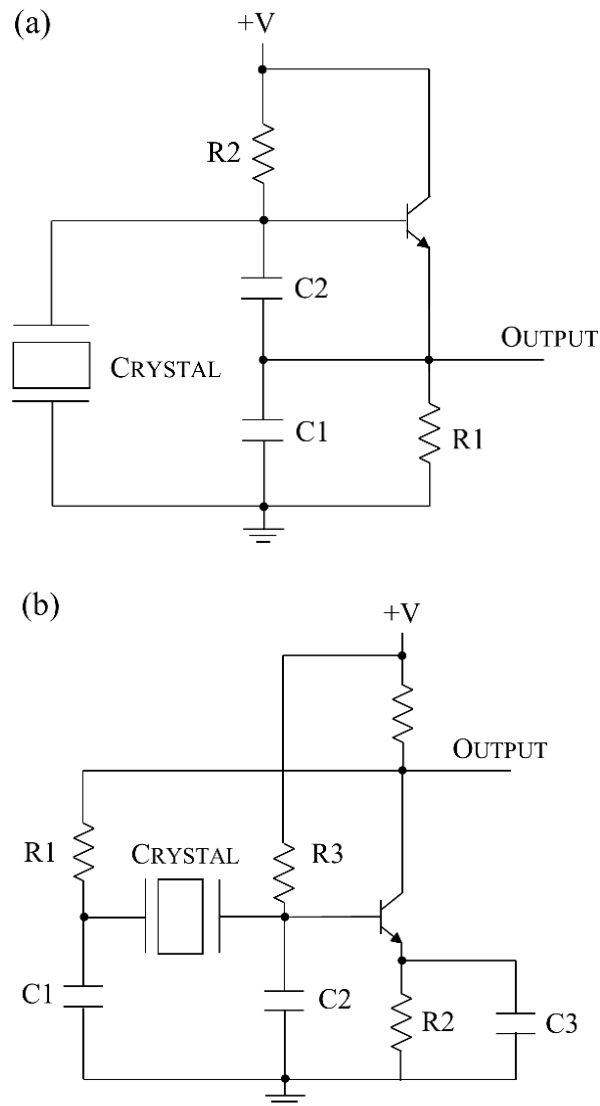
Figure 2.11 Common implementations of (a) Colpitts and (b) Pierce crystal oscillator using transistors. [96]

The Colpitts oscillator is a parallel resonant circuit, where the resonator behaves as an inductor. Although simple in appearance, its operation is complex and careful selection of the components should be made. If non-optimal values are used,

parasitics will dominate the oscillating frequency. It offers fair stability up to low Megahertz range and very low power consumption [96]. However, due to low impedance of the static capacitance of the resonators at high frequencies (~600 MHz), sufficient negative resistance is required to maintain oscillation [97, 98]. Operation of Colpitts oscillators at high frequencies are rarely reported in the literature due to their complex and inflexible design which must be carefully tailored to a specific device.

2.9.2 PIERCE OSCILLATOR

Due to its simplicity, the most desirable and commonly used oscillator configuration is the Pierce oscillator [99]. For acoustic resonators operating at high frequencies (>500 MHz), the Pierce oscillator configuration (shown in Figure 2.12 for implementation with an inverting amplifier) is usually preferred as less parasitic effects are introduced to the system [100]. This provides good frequency stability and large output at low power level [96] with only a few components. Furthermore, this oscillator configuration can be easily implemented in CMOS technology, for the development of a miniature, low power system with the advantage of no inductors required (which would increase the overall die size of an IC).
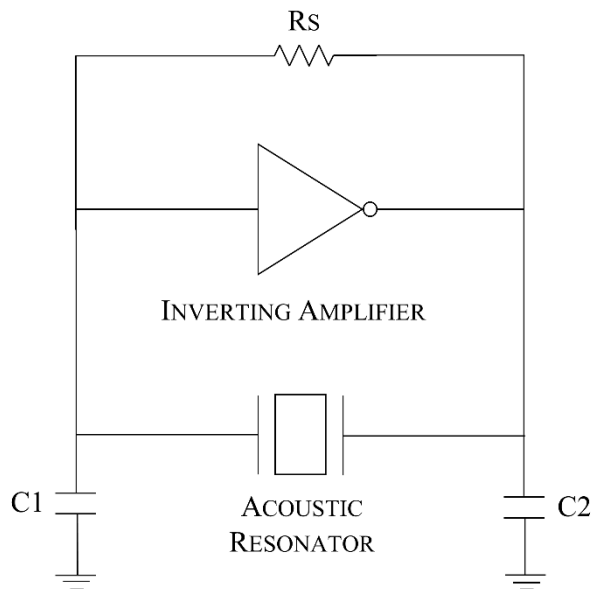
Figure 2.12 Pierce Oscillator topology.

As opposed to the Colpitts configuration, the Pierce oscillator is a series resonant circuit, where the acoustic resonator is resistive. The total phase shift around

the loop is 360°. An inverting amplifier provides a 180° phase shift and loop gain to sustain oscillation. The acoustic resonator, C1 and C2 form the feedback network providing the additional 180° phase shift to meet the Barkhausen criteria. The resonator determines the oscillation frequency (near series resonance). Rs is a biasing resistor for the inverting amplifier. In this work a transistor-based Pierce type oscillator was designed to drive the acoustic resonators. Details on this design are presented in Chapter 6.

2.9.3 CMOS IMPLEMENTATION

Electronic circuitry implemented with discrete components has been used to drive BAW devices in the research field, where the use of discrete components benefits from high design flexibility. [61, 101, 102]. These are transistor-based oscillators implemented on a printed circuit board (PCB) using SMD components, to which the BAW device is interfaced, usually via wire bonding. The use of discrete components allows rapid deployment, testing and great design flexibility of the circuitry. However, discrete circuits are not suitable for low-cost volume manufacturing, they can exhibit reliability issues (associated with the soldering and bonding process) and they can have a large footprint.

Compared to these conventional discrete solutions, the implementation of BAW driving electronics in CMOS technology not only can improve the oscillator performance (and included signal processing circuitry) but can significantly reduce the overall die size and manufacturing costs (for mass production). Integration of BAW devices with IC's has allowed the development of miniature, low-power systems that are extensively used in the RF communication technologies, and can be used for the development of low-cost sensing devices.

When designing an oscillator circuit, particularly for sensing applications, the performance characteristics of the oscillator (i.e. frequency stability) should be carefully considered. They can significantly impact the overall performance of the sensor system (limit of detection). Frequency stability is commonly measured in terms of the oscillator phase noise, which refers to phase fluctuations in the nominal oscillator frequency.

Phase noise is characterised in the frequency domain and measured as the ratio of the output power, P_s, at the oscillator frequency, ω_0, to the noise power, P_n, considering a unit bandwidth at an offset, $\Delta\omega$, from the frequency of oscillation [103]. Phase noise can be measured from the output spectrum of the oscillator, obtained with a spectrum analyser. As an example, Figure 2.13 shows the implementation of a CMOS Pierce oscillator, together with the measured output spectrum and phase noise analysis as reported by Johnston *et al.* [104]. Table 2.5 reviews BAW based oscillators implemented in CMOS technologies and their performance parameters, as reported in the literature.
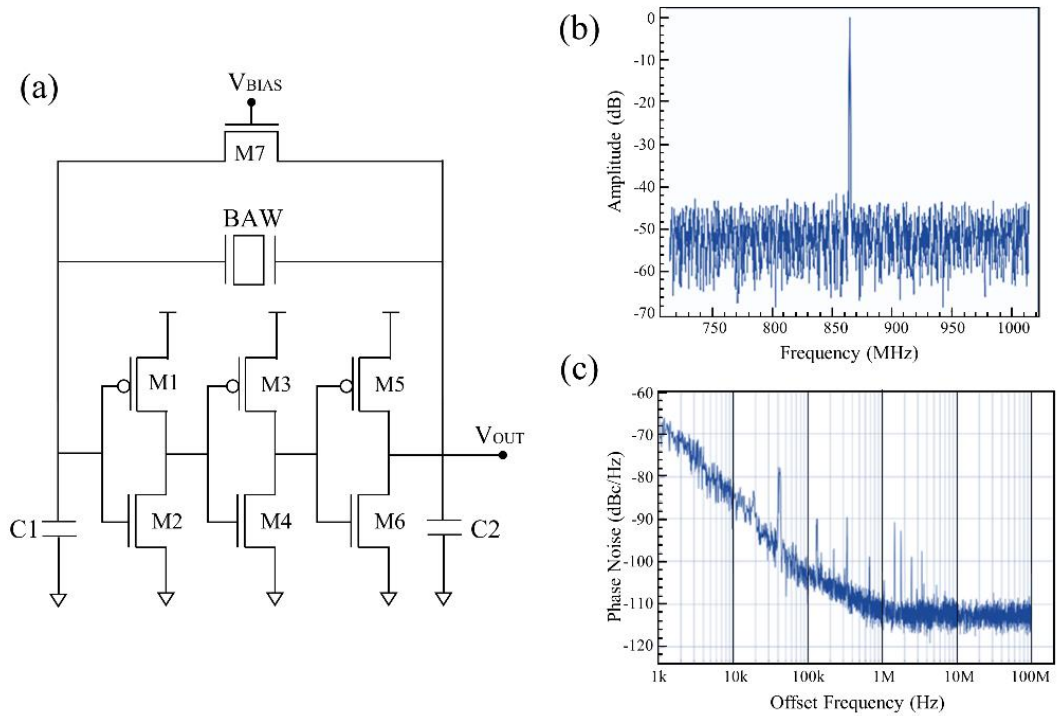
Figure 2.13 (a) Pierce oscillator implemented in CMOS technology, (b) the output spectrum and (c) the phase noise measurement. Adapted from [104]. Oscillator resonance frequency at 864.54 MHz and phase noise level of -104 dBc/Hz at an offset of 100 kHz.

The integrated circuitry (implemented in CMOS technology) must be interfaced to the BAW devices. This BAW-CMOS integration can be performed in several ways and successful developments have been reported in the literature. In section 2.10 the general approaches to integrating CMOS and microelectromechanical systems (MEMS) are discussed, which are, in principle, also applicable to BAW devices. Section 2.11 reviews the state-of-the-art of integrating BAW devices (i.e. FBARs and SMRs) with the CMOS circuitry.

Table 2.5 Comparison of BAW based oscillators found in the literature.

BAW RESONATOR	OSCILLATOR TOPOLOGY	CMOS TECHNOLOGY	OPERATING FREQUENCY	PHASE NOISE (dBc/Hz)	POWER	REF
AlN based FBAR	Colpitts	0.35 µm CMOS	604 MHz	-149 at 100 kHz	5.3 mW	[105]
AlN based FBAR	Colpitts	0.35 µm BiCMOS	5.46 GHz	-121 at 100 kHz	-	[106]
AlN based FBAR	Colpitts	90 nm CMOS	6.3 GHz	-110 at 1 MHz	475 µW	[107]
AlN based FBAR	Pierce	0.18 µm CMOS	1.9 GHz	-120 at 100 kHz	300 µW	[108]
AlN based FBAR	Pierce	0.13 µm CMOS	1.9 GHz	-120 at 100 kHz	89 µW	[109]
AlN based FBAR	Pierce	0.25 µm CMOS	1.6 GHz	-102 at 10 kHz	4 mW	[83]
ZnO based SMR	Pierce	0.18 µm RF CMOS	864.5 MHz	-104 at 100 kHz	-	[110]
AlN based SMR	Differential	65 nm CMOS	2.5 GHz	-130 at 100 kHz	1.2 mW	[111]
AlN based SMR	Differential	65 nm CMOS	2.11 GHz	-124 at 100 kHz	50 µW	[112]
AlN based SMR	Butler	Qubic4+ BiCMOS	2 GHz	-120 at 100 kHz	-	[113]

2.10   CMOS INTEGRATION OF MEMS

Interface circuitry for the operation of microelectromechanical systems (MEMS) can be realised through integrated circuits (ICs), fabricated in CMOS technologies, as discussed in the previous section. The integration of MEMS and IC components in a single chip enables the miniaturisation of sensors, actuators and transducers with the advantages of low power consumption, low cost, increased reliability, reduction of parasitic effects and improved performance compared to the use of discrete components.

Commercial MEMS products (gyroscopes, accelerometers, pressure sensors, microphones, BAW filters, etc.) are usually interfaced with CMOS circuitry and packaged together in a single chip. This MEMS-IC integration enables the development of a complete sensor system that can be used in more complex electronic

modules with applications in a broad range of areas such as healthcare, automotive, aerospace, environmental and wireless communications.

Integration and packaging of MEMS and ICs can be realised following two main approaches: (1) hybrid integration and (2) monolithic integration. The selection of an integration method can be performed based on general considerations such as device complexity, field of application, performance requirements and manufacturing costs [114, 115]. These integration methods are detailed below.

2.10.1   HYBRID INTEGRATION

In hybrid integration, MEMS and ICs are manufactured on separate substrates using independent fabrication processes. While ICs are fabricated in CMOS foundries, MEMS are commonly manufactured with standard microfabrication technologies. MEMS and IC dies (either bare or packaged) are mounted together on a common substrate (laminate platform, ceramic package), and are interfaced using wire bonding or flip chip technologies (other interconnections methods can be used such as quilt packaging [116]).

Hybrid integration can be realised in a 2D (side-by-side) or 3D (stacked) arrangement. Two-dimensional hybrid integrated systems (depicted in Figure 2.14a) are known as *multi-chip modules* (MCM). MEMS and ICs are horizontally placed next to each other on the carrier substrate and interfaced to one another and to the package. If the dies are arranged vertically (in a stacked configuration), a *system-in-a-package* (SiP) is obtained. This 'three-dimensional' arrangement is depicted in Figure 2.14b.
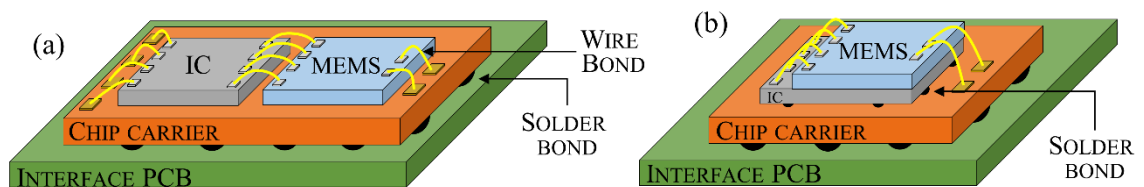
Figure 2.14 Hybrid MEMS-IC integration: (a) multi-chip module (2D integration) and (b) system-in-a-package (3D integration) interconnected via wire bonding and flip chip. Figures are not to scale.

This hybrid integration approach allows high design flexibility (devices can be tested, modified or redesigned independently) and rapid development at reasonable fabrication costs [115]. However, the need of external interconnections (bond wires, solder bumps) adds parasitic capacitance and resistance that can attenuate the signals and deteriorate the performance of the system [117]. In terms of physical size, the footprint and thickness of the system can significantly increase (as two separate devices must be placed side by size or stacked). Figure 2.15 shows an example of a hybrid system of two BAW devices (developed in this work) interfaced to an ASIC chip. Devices are placed side-by-side in a LTCC package (6 mm × 6mm) and interconnected via wire bonding.
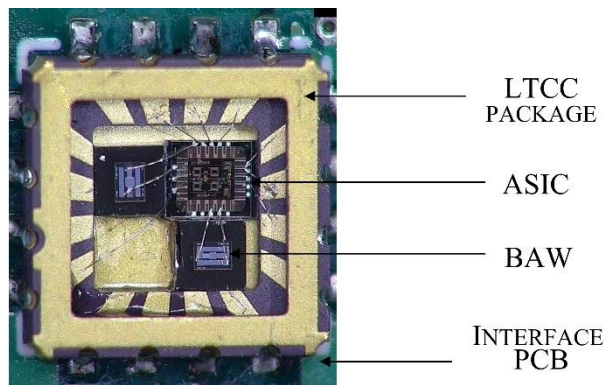
Figure 2.15 Photograph of an example hybrid SMR based sensor system working in dual configuration, showing ASIC chip and two SMR devices, developed in this work. Overall dimensions are 6 mm × 6 mm.

2.10.2   MONOLITHIC INTEGRATION

MEMS are monolithically integrated with the CMOS circuitry when both MEMS and ICs are fabricated on a single substrate. These systems are commonly referred as *system-on-chip* (SoC). This integration approach allows further miniaturisation (small footprint and low thickness) and improved performance, compared to hybrid systems. However, systems are more complex and only allow for low flexibility in the design procedure. In terms of performance, monolithic systems have the advantages of increased reliability and reduced parasitic capacitance (no external interconnections are required), power consumption and noise levels [117]. Furthermore, packaging of the systems is less complex (it can be performed at wafer level) yielding to reduced fabrication, packaging and testing costs [115].

Monolithic integration can be realised in three different ways according to the sequence in which the CMOS circuity and the MEMS structures are processed. These approaches are referred as: (a) pre-CMOS (MEMS process takes place before the CMOS process, (b) inter-CMOS (MEMS are processed during the CMOS process) and (c) post-CMOS (MEMS processing after the CMOS process). These approaches are discussed in more detail below. As an example, Figure 2.16 depicts the post-CMOS monolithic integration of a BAW device above the IC electronics.
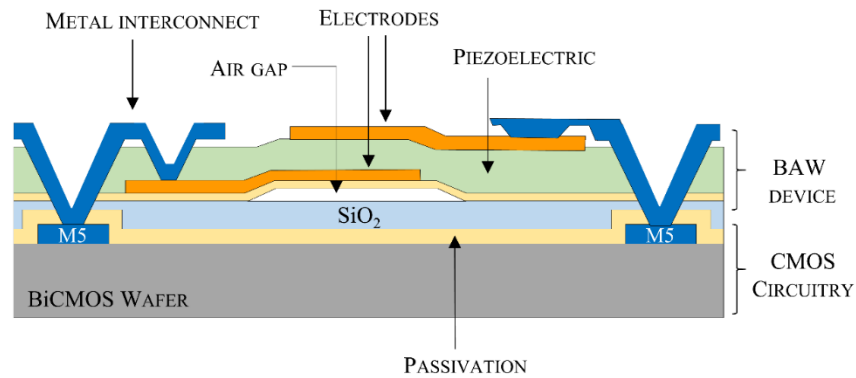
Figure 2.16 Monolithic MEMS-IC integration: A cross-section of a BAW device integrated above the CMOS circuitry. Adapted from [118].

2.10.2.1 PRE-CMOS INTEGRATION

In the monolithic integration of MEMS and CMOS circuitry using a pre-CMOS process (also termed 'MEMS-first'), MEMS structures are fabricated prior to the CMOS process. In this approach, no tight constraints exist in terms of thermal budget (amount of thermal energy transferred to the wafer, related to the high temperatures processes used and their duration). For the processing of MEMS (very high thermal budgets up to 1100 °C are possible). Using such high temperature material processes allows for the fabrication of high performance MEMS [115] (e.g. stress release of thick polysilicon layers can be achieved at high temperatures). However, CMOS foundries do not accept pre-processed wafers, unless they meet strict entry-requirements (i.e. high surface planarity and contamination-free), which require careful wafer preparation. Thus, pre-CMOS integration is usually only performed at a commercial level, where the process can be completed in-house provided IC processing capabilities are available.

A representative example of a pre-CMOS integration process is the M^3EMS technology developed by Sandia National Laboratories (Albuquerque, USA) [119]. In this process, a polysilicon microstructure is manufactured in a trench (formed by wet etching into the bulk silicon) with a deposited nitride layer at the bottom. Polysilicon studs are also formed to provide contact between the CMOS metal layers and the MEMS device. After forming the polysilicon microstructures, the trench is refilled with oxide and planarized using chemical-mechanical polishing (CMP). Subsequently, the structure is annealed to release stress and sealed with a nitride membrane. The wafer is then ready to use within a standard CMOS process. MEMS structures have been successfully fabricated using this M^3EMS process, e.g. the inertial sensors reported by Allen *et al.* [120] and the resonant accelerometer by Seshia *et al.* [121].

2.10.2.2 INTER-CMOS INTEGRATION

In the inter-CMOS approach, also referred as interleaved, intra or intermediate-CMOS, the CMOS processing steps are interrupted to perform additional deposition of polysilicon layers or micromachining process, to form the MEMS structures. Thus, the polysilicon structures are formed before the CMOS back-end processing (formation of interconnect metallization). In this way, the deposition of polysilicon and annealing are compatible with the process (with the annealing process limited up to 900 °C so that doping profiles of the front-end CMOS process are not affected) [119].

Examples of available commercial devices fabricated with this inter-CMOS approach are capacitive pressure sensors by Infineon Technologies (Neubiberg, Germany) and accelerometers by Analog Devices (Norwood, USA) [114]. Scheiter *et al.* described the fabrication of a pressure sensor, fabricated in a BiCMOS process technology following these inter-CMOS processing steps [122].

Inter-CMOS monolithic integration requires access to a custom CMOS production line, where both the fabrication and micromachining can be performed. This requirement is commonly not available in CMOS foundries, that are unlikely to admit back into their line pre-processed wafers with post-micromachining steps. This, together with the high associated costs, limits the utility of this processing technology [115, 119].

2.10.2.3 POST-CMOS INTEGRATION

Post-CMOS integration of MEMS (also called MEMS-last processing) refers to the approach in which the MEMS structures are fabricated only after the CMOS process has been completed. Post-CMOS integration offers high flexibility, short development cycles and low cost processing [114, 115]. In this approach, CMOS circuitry can be fabricated at any CMOS foundry and MEMS structures subsequently manufactured at dedicated MEMS facilities (standard CMOS production lines and MEMS infrastructure are used, with no special requirements, as opposed to the pre-CMOS and inter-CMOS integration).

Fabrication processes following the CMOS process steps are limited by the overall thermal budget, which is determined by the metallization layer and the doping profiles of transistors (the maximum process temperature for standard Al metallization process is ~450 °C [119]), also limiting the materials of choice for the MEMS structures [115]. Deposition processes such as PECVD, sputtering, electroplating and wet/dry bulk and surface micromachining can be used during post-CMOS integration. However, high temperature deposition processes (e.g. LPCVD deposition of polysilicon) and annealing, which require temperatures above 600 °C, are incompatible [119]. Careful design of the post-CMOS integration of MEMS is required (considering the thermal budget) to avoid damage to the CMOS circuitry (affecting the doping profiles).

Post-CMOS integration can be realised following either an additive technique (MEMS are manufactured on top of the CMOS substrate) or subtractive method (MEMS are formed by machining the CMOS substrate). The former technique is more elaborate as it usually requires a greater number of processing steps to build the MEMS structure. These two methods are described below.

Post-CMOS integration, where the MEMS structures are fabricated on top of the CMOS substrate, is accomplished by adding and patterning layers of materials on top of the finished CMOS wafer, after which surface micromachining techniques are used to release the MEMS structure. In this approach, a good surface planarity of the CMOS substrate and good electrical and mechanical contact are required [119]. Furthermore, MEMS materials and sacrificial layer must be compatible with the

CMOS substrate, in terms of thermal budget and etching selectivity. This approach allows integration on the MEMS structure on top of the CMOS circuitry, which reduces the die area and allows further miniaturisation of the system.

Subtractive post-CMOS integration is accomplished by means of bulk micromachining of the CMOS substrate to create a cavity. This approach is widely used for the fabrication of piezo resistive pressure sensors, membranes and cantilevers. The silicon substrate is commonly back-etched by anisotropic wet etching with KOH (time controlled or using an etch stop layer). Dry etching methods and front-side etching can also be used in this approach. A review of several approaches to realise this subtractive technique is presented by Fischer *et al.* [115] and examples of CMOS-MEMS devices fabricated using these approaches are summarised by Hongwei Qu [114].

In summary, there is a need of miniature devices capable of being manufactured at very low cost in volume production. The integration of MEMS with integrated circuits, (fabricated in CMOS technology) allows miniaturisation of microsystems with improved performance, which can be used in more complex electronic systems. Several approaches can be implemented for the integration of MEMS and CMOS circuitry, with two main categories: hybrid and monolithic integration. Selection of a MEMS-IC integration approach is driven by performance requirements and costs.

Hybrid solutions consist of MEMS and IC's fabricated in separate substrates and interfaced via wire bonding or flip chip technology. This method allows for high design flexibility at the expense of larger footprints and deterioration of the system performance (due to the use of external interconnections). On the other hand, monolithic integration eliminates the need of external interconnections (both MEMS and ICs are fabricated in the same substrate), thus devices with improved performance and miniature size can be manufactured at low cost. This integration approach, however, involves complex design with low flexibility.

2.11 CMOS-BAW INTEGRATION

Advances in wireless communication technologies and the growing demand for personal devices (mobile phones, smart wearables) have generated a need for low power, low-cost and miniature components suitable to be used together with integrated circuits (ICs).

BAW devices emerged as alternative of SAW and ceramic devices in the communications area, where they are extensively used as antenna filters in mobile phones. The limitations for the IC integration of ceramic and SAW filters (size, packaging, costs) lead to the development of BAW filters. Their small footprint (<1 mm^2) and compatibility with silicon technologies allow for IC integration and miniaturisation of RF modules, offering high performance at reduced size. The potential use of this technology for sensing applications was soon recognised, making the development of BAW devices and their integration with CMOS circuitry of great interest in the research and commercial community.

Thin film BAW devices are, however, especially susceptible to noise due to their high operating frequencies. Short interconnections between the BAW device and the driving circuitry can considerably reduce parasitics and noise, allowing improved functionality of the system. Hybrid integration of thin film BAW devices has helped minimising the parasitic effects (associated with long wires/tracks used in discrete implementations) and significantly reducing the overall size of the system (as devices are placed in close proximity to the IC).

Several approaches have been proposed to integrate thin film BAW devices with the active CMOS circuitry in a hybrid configuration. Augustiniak *et al.* reported on a 0.13 µm CMOS chip interfaced to a SMR substrate via flip chip bonding (implementation shown in Figure 2.17a) for use in gravimetric liquid applications [123]. Similar to this approach, Vanhelmont *et al.* made use of flip chip technology to attach both the CMOS chip (fabricated in a BiCMOS process) and the SMR device onto a common carrier substrate (with overall size 2.8 mm $\times$2 mm) [113].
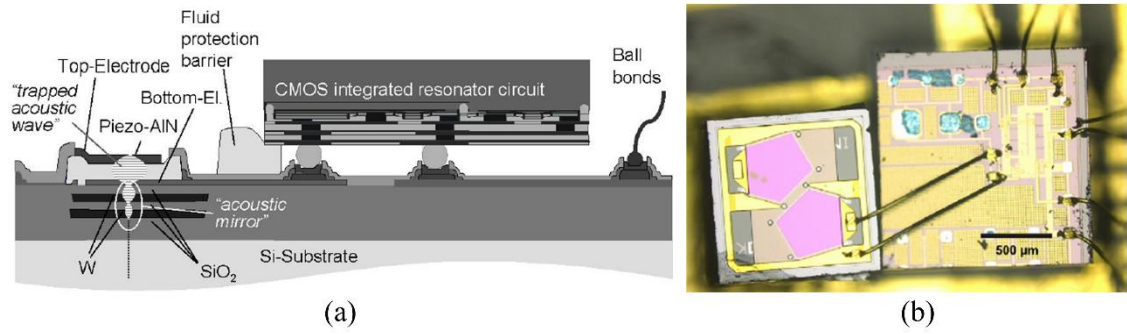
Figure 2.17 Hybrid BAW-CMOS implementations (a) using flip chip technology [123] and (b) wire bonding interconnections [84].

Other approaches used wire bonding to interconnect the CMOS circuitry and the BAW device. As an example, Elbrecht *et al.* reported on a hybrid BAW based RF filter packaged together with the active circuitry in a low-cost laminate package with overall dimensions of 3 mm × 3 mm [124]. Similarly, Chee *et al.* interfaced a FBAR device (1.9 GHz) to the CMOS die, onto a test board using two short bond wires to interconnect them (entire system was 1.7 mm × 0.8 mm in size). Figure 2.17b shows the hybrid integrated system developed by Paprotny *et al.* [84]. In this implementation, a 0.25 μm CMOS process was used for the IC, which was interfaced to a FBAR device via wire bonding.

Even though hybrid BAW systems demonstrated improved performance at reduced size (compared to discrete implementations), the need of external interconnections to interface two separate substrates make this implementation unsuitable for low cost production. Other disadvantages include the increased overall size of the system (dies are placed side by side) and additional parasitic inductance introduced by the external interconnections.

Further attempts to miniaturize these systems while maintaining a low production cost without compromising performance, has led to the monolithic integration of BAW devices and ICs. Fabrication processes used in the manufacture of BAW devices (e.g. magnetron sputtering) do not require any high temperature process, making them compatible with CMOS processes. Thus, BAW devices can be realised in conventional CMOS foundries, provided the materials used (metals for the electrodes) are also compatible with the CMOS substrate, in terms of thermal budgets [41, 124]. Although the possibility to monolithically integrate thin film BAW devices

was identified at an early stage of the development of this technology, there are very few reports of this being implemented in the literature.

The state-of-the-art monolithic integration of thin film BAW devices is realised following a post-CMOS processing approach. Both electronic circuitry and BAW device are fabricated on a single substrate. The integrated circuitry is manufactured first in a standard CMOS process, which is followed by the fabrication of the BAW device on the same substrate. CMOS integration of both FBAR and SMR devices have been proposed and demonstrated in the literature [110, 118, 124-130]. Two different approaches have been mainly implemented for BAW monolithic integration: (1) the IC and BAW devices are integrated side-by-side in the same substrate or (2) the BAW device is fabricated above the IC substrate. These two integration alternatives are depicted in Figure 2.18 for both FBAR and SMR devices.
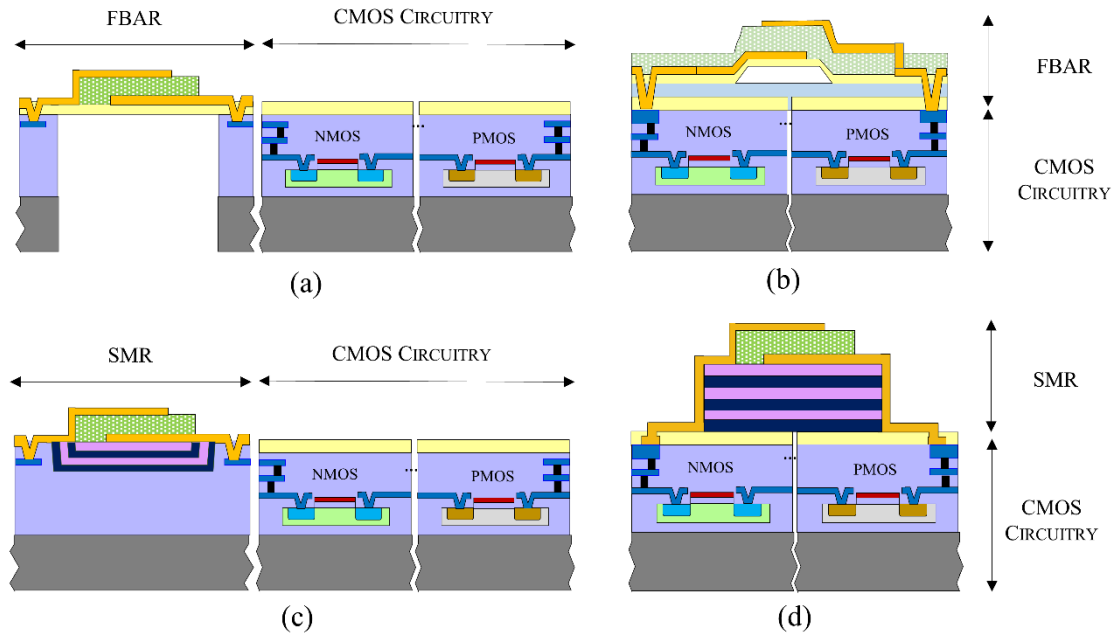
Figure 2.18 Approaches of CMOS Integration of BAW devices: in (a) and (c) FBAR and SMR devices are fabricated in a post-CMOS process aside the CMOS circuitry. FBAR and SMR integration above the IC is depicted in (b) and (d). This implementation is also realised in a post-CMOS process [110, 118, 124-130].

The following points must be considered for the integration of BAW devices with the CMOS circuitry on the same substrate [131]: (1) A higher number of lithography steps are required for the fabrication of the integrated system (processing steps for the IC plus those for the BAW); (2) the manufacturing yield of the joint

process is lower compared to the yield obtained from separate processes; (3) the integration may result in increased manufacturing costs if the BAW device (with a small footprint) is combined with a large IC; and (4) as with any monolithically integrated system, the design flexibility is reduced.

An example of the implementation shown in Figure 2.18a is the integrated FBAR filter based on an on-off keying receiver reported by Fang *et al.* [129], where a bulk micromachining process was used to release the FBAR structure (dry etching of the Si substrate). Alternatively, the use of surface micromachining has also been proposed by Dunn *et al.* [126]. Compared to this approach, the monolithic integration of a FBAR device above the IC (first implemented by Dubois *et al.* [118], and depicted in Figure 2.18b) allows further miniaturisation (and thus further cost reduction) of the integrated system.

To realise the configuration shown in Figure 2.18b, an air gap, to provide isolation to the resonator structure, must be created by surface micromachining. Air gap FBARs, however, are fragile and should be handled with care during dicing and packaging. On the positive side, interconnecting the FBAR and the IC is easier, compared to the configuration in Figure 2.18d, as the distance between the top electrode and the top metal of the IC is considerably reduced.

As discussed in section 2.7.2, SMR devices exhibit better power handling capabilities, lower TCFs and are mechanically more robust compared to FBAR devices. This has driven the interest to develop monolithically integrated SMR devices. Elbrecht *et al.* [124] first described a process that combined a RF bipolar process with the fabrication of a SMR device, as depicted in Figure 2.18c. In this process, an additional silicon nitride layer is embedded within the oxide layers of the CMOS process. This nitride layer acts as an etch stop during the formation of a cavity (etching of the oxide) where the acoustic mirror is embedded. In this way, the face level of the FBAR top electrode and the CMOS top layer is minimised but at the expense of increased die area.

Another approach for the CMOS-SMR integration has been implemented and used in mass sensing applications by Tukkiniemi *et al.*[130] and Johnston *et al.* [132], depicted in Figure 2.18d. The SMR device is built above the CMOS substrate in a post-

CMOS process and interconnections are created to the top metal layer of the CMOS process. This configuration offers the advantage of reduced die size, but significantly increases the thickness of the device and distance between the SMR-IC interconnections. Furthermore, post-fabrication of the SMR device requires the deposition of several layers and use of a large number of photolithography masks (5 to 10), which increases the manufacturing time and cost, and can considerably decrease the manufacturing yield.

2.12 CONCLUSIONS

Acoustic wave devices, working on the principle of piezoelectricity, have been extensively used in the telecommunications industry for several decades. In the sensing area, they have matured from a research field to a strong commercial market (i.e. QCM and SAW devices). A variety of piezoelectric materials can be used to realise acoustic wave devices (e.g. quartz, lithium niobate, aluminium nitride, polyvinylidene fluoride). These materials exhibit different properties (e.g. propagation velocity, temperature dependence) and according to their cut and orientation, different modes of acoustic waves can be generated (e.g. longitudinal, transverse, Rayleigh). Transverse (shear) waves are preferred for in-liquid applications as they do not propagate in liquids and only experience minimum attenuation, compared to longitudinal waves. For gas and solid phase applications, devices working in the longitudinal mode are suitable.

The sensing mechanism of these devices is based on the change in the properties of the propagating waves (amplitude, phase, velocity) and their sensing applications are extensive (e.g. pressure, temperature, humidity, mass and biosensors). In particular, applications of acoustic wave devices for particle sensing and VOC detection were reviewed in detail. QCM and SAW devices have been reported extensively for such applications. However, their operating frequency is limited (up to 30 MHz for QCMs and to 2 GHz for SAWs), thus limiting their sensitivity.

FBARs and SMRs have several advantages compared to SAWs and QCMs (smaller footprint, higher operation frequencies in the range of 2-5 GHz, higher sensitivity, better power handling, higher Q values, better TCFs) but in terms of

manufacturing, more fabrication steps and micromachining are required. Several reports on the use of these devices for VOC detection were reviewed but only a limited number of publications are available on their use in particle sensing.

Although the frequency response of acoustic devices can be measured using specialist equipment (i.e. network analyser), these instruments are only suitable for laboratory testing as they are bulky, expensive and require highly trained personnel. For use in a portable, low-cost and low power air quality monitor, electronic circuitry is required to drive the acoustic devices and measure the sensor response. Driving the acoustic devices with oscillator circuits (e.g. Colpitts and Pierce oscillator topologies) provide an inexpensive and accurate solution for sensing applications. However, careful design of the circuitry is required to provide good frequency stability and reduce parasitic effects.

Discrete driving circuitry is not suitable for low-cost, mass production. The implementation of such circuitry in CMOS technology allows for low-cost, volume manufacturing, reduced chip size and improved performance. The CMOS compatibility of FBARs and SMRs makes it possible to monolithically integrate these devices. Approaches to integrate these devices with the CMOS circuitry in the same substrate have been demonstrated, based on a post-CMOS integration approach.

Due to their mechanical robustness, increased power handling and higher design flexibility, monolithic integration of SMR devices has been given special interest in both telecommunications and sensing research areas. Current state-of-the-art SMR-CMOS integration requires the deposition and patterning of a number of layers (a minimum of four) for the reflector stack, which significantly increases the distance between the SMR-IC interconnections, and increases the fabrication time and associated costs.

From the background research on acoustic devices, the high frequency (high sensitive) BAW devices are suitable for sensing VOC at low concentrations and detection of fine particles. Specifically, in this work SMR devices will be utilised, as they offer the best performance (in terms of Q-factor, power handling and TCF) and are mechanically robust. In this work, an SMR device for air quality monitoring applications will be fabricated. The next chapter discusses the first steps in the design

process of the SMR design, including the design parameters and modelling techniques. Finite element models are developed and simulations results presented, also taking into account temperature effects on the device.

2.13 REFERENCES

[1] Ballato, A. (1995). "Piezoelectricity: old effect, new thrusts", *IEEE Transactions on Ultrasonics, Ferroelectrics, and Frequency Control*. **42**(5): 916-926.

[2] Ballentine, D. S., White, R. M., Martin, S. J., Ricco, A. J., Zellers, E. T., Frye, G. C. and Wohltjen, H. (1997). "Acoustic wave sensors: theory, design and physico-chemical applications", Academic Press. San Diego.

[3] Gardner, J. W., Varadan, V.K., and Awadelkarim, O.O. (2001). "Microsensors, MEMS, and smart devices", John Wiley & Sons Ltd.

[4] Morkoç, H. and Özgür, Ü. (2009). "General properties of ZnO" in *Zinc Oxide*, Wiley-VCH Verlag GmbH & Co. KGaA, 1-76.

[5] Hanada, T. (2009). "Basic properties of ZnO, GaN, and related materials" in *Oxide and Nitride Semiconductors: Processing, Properties, and Applications*, Takafumi Yao and Soon-Ku Hong, Editors, Springer Berlin Heidelberg: Berlin, Heidelberg, 1-19.

[6] Campanella, H. (2010). "Acoustic microresonator technologies" in *Acoustic Wave and Electromechanical Resonators : Concept to Key Applications*, Artech House: Norwood.

[7] Rosenbaum, J. (1988). "Bulk acoustic wave theory and devices". Norwood, MA: Artech House.

[8] Auld, B. A. (1990). "Acoustic fields and waves in solids". Malabar, Fla.: R.E. Krieger.

[9] Hashimoto, K.-Y. and Wrobel, S. M. (2009). "RF bulk acoustic wave filters for communications". Norwood, US: Artech House Books.

[10]   Campanella, H. (2010). "Acoustic wave and electromechanical resonators: concept to key applications". Norwood, MA: Artech House.

[11]   Drafts, B. (2001). "Acoustic wave technology sensors", *IEEE Transactions on Microwave Theory and Techniques*. **49**(4): 795-802.

[12]   Wolff, U., Dickert, F. L., Fischerauer, G. K., Greibl, W. and Ruppel, C. C. W. (2001). "SAW sensors for harsh environments", *IEEE Sensors Journal*. **1**(1): 4-13.

[13]   Lakin, K. M. and Wang, J. S. (1980). "UHF composite bulk wave resonators", *1980 Ultrasonics Symposium*. pp. 834-837.

[14]   Loebl, H. P., Metzmacher, C., Milsom, R. F., Lok, P., van Straten, F. and Tuinhout, A. (2004). "RF bulk acoustic wave resonators and filters", *Journal of Electroceramics*. **12**(1): 109-118.

[15]   Perez-Sanchez, G. F. and Morales-Acevedo, A. (2009). "Design of bulk acoustic wave resonators based on ZnO for filter applications", *6th International Conference on Electrical Engineering, Computing Science and Automatic Control*. pp. 1-6.

[16]   Sauerbrey, G. (1959). "Verwendung von schwingquarzen zur wägung dünner schichten und zur mikrowägung", *Zeitschrift für Physik* **155**: 206-222.

[17]   White, R. M. (1998). "Acoustic sensors for physical, chemical and biochemical applications", *Proceedings of the IEEE International Frequency Control Symposium*. pp. 587-594.

[18]   Bi, F. Z. and Barber, B. P. (2008). "Bulk acoustic wave RF technology", *IEEE Microwave Magazine*. **9**(5): 65-80.

[19]   Lanz, R. and Muralt, P. (2005). "Bandpass filters for 8 GHz using solidly mounted bulk acoustic wave resonators", *IEEE Transactions on Ultrasonics, Ferroelectrics and Frequency Control*. **52**(6): 938-948.

[20]   Nishihara, T., Yokoyama, T., Miyashita, T. and Satoh, Y. (2002). "High performance and miniature thin film bulk acoustic wave filters for 5 GHz", *Proceedings of the IEEE Ultrasonics Symposium* pp. 969-972.

[21]   Fattinger, G. G., Kaitila, J., Aigner, R. and Nessler, W. (2003). "Thin film bulk acoustic wave devices for applications at 5.2 GHz", *IEEE Symposium on Ultrasonics, 2003*. pp. 174-177.

[22]   Grudkowski, T. W., Black, J. F., Reeder, T. M., Cullen, D. E. and Wagner, R. A. (1980). "Fundamental mode VHF/UHF bulk acoustic wave resonators and filters on silicon", *1980 Ultrasonics Symposium*. pp. 829-833.

[23]   Kiyoshi, N., Hiromasa, S. and Hiroshi, S. (1981). "A piezoelectric composite resonator consisting of a ZnO film on an anisotropically etched silicon substrate", *Japanese Journal of Applied Physics*. **20**(S3): 111.

[24]   Newell, W. E. (1965). "Face-mounted piezoelectric resonators", *Proceedings of the IEEE*. **53**(6): 575-581.

[25]   Lakin, K. M., Kline, G. R. and McCarron, K. T. (1995). "Development of miniature filters for wireless applications", *IEEE Transactions on Microwave Theory and Techniques*. **43**(12): 2933-2939.

[26]   Drozd, J. M. and Joines, W. T. (1996). "Determining Q using S parameter data", *IEEE Transactions on Microwave Theory and Techniques*. **44**(11): 2123-2127.

[27]   Thalhammer, R. and Aigner, R. (2005). "Energy loss mechanisms in SMR-type BAW devices", *IEEE MTT-S International Microwave Symposium Digest, 2005*. pp. 4.

[28]   Thalhammer, R., Kaitila, J., Zieglmeier, S. and Elbrecht, L. (2006). "Spurious mode suppression in BAW resonators", *IEEE Ultrasonics Symposium*. pp. 456-459.

[29]   Enjamuri, S., Amsanpally, A. and Raju, K. C. J. (2012). "Optimization and analysis of piezoelectric and electrode materials' thickness effects on the

performance of film bulk acoustic resonator", *1st International Symposium on Physics and Technology of Sensors (ISPTS)*. pp. 185-188.

[30]   Kaitila, J., Ylilammi, M., Ella, J. and Aigner, R. (2003). "Spurious resonance free bulk acoustic wave resonators", *2003 IEEE Symposium on Ultrasonics*. pp. 84-87.

[31]   Fattinger, G. G., Marksteiner, S., Kaitila, J. and Aigner, R. (2005). "Optimization of acoustic dispersion for high performance thin film BAW resonators", *IEEE Ultrasonics Symposium* pp. 1175-1178.

[32]   Ruby, R., Larson, J., Feng, C. and Fazzio, S. (2005). "The effect of perimeter geometry on FBAR resonator electrical performance", *IEEE MTT-S International Microwave Symposium Digest, 2005*. pp. 4.

[33]   Link, A., Schmidhammer, E., Heinze, H., Mayer, M., Bader, B. and Weigel, R. (2006). "Appropriate methods to suppress spurious FBAR modes in volume production", *2006 IEEE MTT-S International Microwave Symposium Digest*. pp. 394-397.

[34]   Ruby, R. (2007). "11E-2 Review and comparison of bulk acoustic wave FBAR, SMR technology", *2007 IEEE Ultrasonics Symposium Proceedings*. pp. 1029-1040.

[35]   Garcia-Gancedo, L., Pedros, J., Iborra, E., Clement, M., Olivares, J., Capilla, J., Luo, J. K., Milne, W. I. and Flewitt, A. J. (2012). "Experimental comparison of FBARs and SMRs responsitivities to mass loadings", *IEEE International Ultrasonics Symposium (IUS)* pp. 1545-1548.

[36]   Petersan, P. J. and Anlage, S. M. (1998). "Measurement of resonant frequency and quality factor of microwave resonators: Comparison of methods", *Journal of Applied Physics*. **84**(6): 3392-3402.

[37]   Coakley, K. J., Splett, J. D., Janezic, M. D. and Kaiser, R. F. (2003). "Estimation of Q-factors and resonant frequencies", *IEEE Transactions on Microwave Theory and Techniques*. **51**(3): 862-868.

[38]   Lakin, K. M., Belsick, J. R., McDonald, J. P., McCarron, K. T. and Andrus, C. W. (2002). "Bulk acoustic wave resonators and filters for applications above 2 GHz", *2002 IEEE MTT-S International Microwave Symposium Digest* pp. 1487-1490.

[39]   Yoshio, S., Tokihiro, N., Tsuyoshi, Y., Masanori, U. and Tsutomu, M. (2005). "Development of piezoelectric thin film resonator and its impact on future wireless communication systems", *Japanese Journal of Applied Physics*. **44**(5R): 2883.

[40]   Ruby, R. (2004). "FBAR - from technology development to production ", *2nd International Symposium on Acoustic Wave Devices fro Future Mobile Communication Systems*. pp. 135-139.

[41]   Aigner, R. (2004). "Volume manufacturing of BAW-filters in CMOS fab", *2nd International Symposium on Acoustic Wave Devices for Future Mobile Communication Systems*. pp. 129-134.

[42]   Aigner, R. (2008). "SAW and BAW technologies for RF filter applications: A review of the relative strengths and weaknesses", *2008 IEEE Ultrasonics Symposium*. pp. 582-589.

[43]   Länge, K., Rapp, B. E. and Rapp, M. (2008). "Surface acoustic wave biosensors: a review", *Analytical and Bioanalytical Chemistry*. **391**(5): 1509-1519.

[44]   Mounier, E. (2012). "MEMS markets and applications", *Second Workshop on Design, Control and Software Implementation for Distributed MEMS*. Besancon, France pp.

[45]   Yole Development. 2016. "Status of the MEMS Industry".

[46]   Johnson, C., *MEMS market: ups and ppstarts*, in *EE Times*. 2015, AspenCore.

[47]   Vellekoop, M. J. (1998). "Acoustic wave sensors and their technology", *Ultrasonics*. **36**(1): 7-14.

[48]   Grate, J. W., Martin, S. J. and White, R. M. (1993). "Acoustic wave microsensors", *Analytical Chemistry*. **65**(21): 940A-948A.

[49]   Vellekoop, M. J., Nieuwkoop, E., Haartsan, J. C. and Venema, A. (1987). "A monolithic SAW physical-electronic system for sensors", *IEEE Ultrasonics Symposium*. pp. 641-644.

[50]   Benes, E., Groschl, M., Seifert, F. and Pohl, A. (1997). "Comparison between BAW and SAW sensor principles", *Proceedings of International Frequency Control Symposium*. pp. 5-20.

[51]   Benetti, M., Cannata, D., Di Pietrantonio, F., Marchiori, C., Persichetti, P. and Verona, E. (2008). "Pressure sensor based on surface acoustic wave resonators", *IEEE Sensors*. pp. 1024-1027.

[52]   Clayton, L. D. and EerNisse, E. P. (1998). "Quartz thickness-shear mode pressure sensor design for enhanced sensitivity", *IEEE Transactions on Ultrasonics, Ferroelectrics and Frequency Control*. **45**(5): 1196-1203.

[53]   Chiu, K.-H., Chen, H.-R. and Huang, S. R.-S. (2007). "High-performance film bulk acoustic wave pressure and temperature sensors", *Japanese Journal of Applied Physics*. **46**(4A): 1392-1397.

[54]   He, X. L., Garcia-Gancedo, L., Jin, P.C., Zhou, J., Wang, W.B., Dong, S.R., Luo, J.K., Flewitt, A.J., and Milne, W.I. (2012). "Film bulk acoustic resonator pressure sensor with self temperature reference", *Journal of Micromechanics and Microengineering*. **22**(12).

[55]   Thomas, S., Leon, S. L. T., Rácz, Z., Cole, M. and Gardner, J. W. (2012). "Design and implementation of a high-frequency surface acoustic wave sensor array for pheromone detection in an insect-inspired infochemical communication system", *14th International Meeting on Chemical Sensors*. Nuremberg, Germanypp. 11-14.

[56]   Benetti, M., Cannata, D., Damico, A., Di Pietrantonio, F., Foglietti, V. and Verona, E. (2004). "Thin film bulk acoustic wave resonator (TFBAR) gas sensor", *Ultrasonics Symposium, 2004 IEEE*. pp. 1581-1584.

[57]   Cannata, D., Benetti, M., Verona, E., Varriale, A., Staiano, M., D'Auria, S. and Di Pietrantonio, F. (2012). "Odorant detection via solidly mounted resonator biosensor", *IEEE International Ultrasonics Symposium* pp. 1537-1540.

[58]   Penza, M. and Anisimkin, V. I. (1999). "Surface acoustic wave humidity sensor using polyvinyl-alcohol film", *Sensors and Actuators A: Physical*. **76**(1–3): 162-166.

[59]   Yao, Y., Chen, X., Ma, W. and Ling, W. (2014). "Quartz crystal microbalance humidity sensors based on nanodiamond sensing films", *IEEE Transactions on Nanotechnology*. **13**(2): 386-393.

[60]   Ashley, G. M., Kirby, P. B., Butler, T. P., Whatmore, R. and Luo, J. K. (2010). "Chemically sensitized thin-film bulk acoustic wave resonators as humidity sensors", *Journal of The Electrochemical Society*. **157**(12): J419-J424.

[61]   Xuan, W., Cole, M., Julia, W. G., Thomas, S., Villa-López, F.-H., Wang, X., Dong, S. and Luo, J. (2017). "A film bulk acoustic resonator oscillator based humidity sensor with graphene oxide as the sensitive layer", *Journal of Micromechanics and Microengineering*. **27**(5): 055017.

[62]   Lin, R.-C., Chen, Y.-C., Chang, W.-T., Cheng, C.-C. and Kao, K.-S. (2008). "Highly sensitive mass sensor using film bulk acoustic resonator", *Sensors and Actuators A: Physical*. **147**(2): 425-429.

[63]   Thomas, S., Cole, M., Villa-López, F. H. and Gardner, J. W. (2016). "High frequency surface acoustic wave resonator-based sensor for particulate matter detection", *Sensors and Actuators A: Physical*. **244**: 138-145.

[64]   Liang, D., Shih, W.-P., Chen, C.-S. and Dai, C.-A. (2010). "A miniature system for separating aerosol particles and measuring mass concentrations", *Sensors*. **10**(4): 3641-3654.

[65] Vo Ke Thanh, N., Dang Giang, N., Hoang Phuong Uyen, N., Van Man, T., Thi Khoa My, N., Trong Phat, H., Quang Vinh, L., Thanh Dat, H. and Thi Ngoc Lien, T. (2014). "Quartz crystal microbalance (QCM) as biosensor for the detecting of Escherichia coli O157:H7", *Advances in Natural Sciences: Nanoscience and Nanotechnology*. **5**(4): 045004.

[66] Cole, M., Leonte, I. I., Gardner, J. W. and Hesketh, P. (2008). "Identification of taste solutions and their binary mixtures using SH-SAW resonator-based taste sensor", *IEEE Sensors Conference*. pp. 1556-1559.

[67] Sehra, G., Cole, M. and Gardner, J. W. (2004). "Miniature taste sensing system based on dual SH-SAW sensor device: an electronic tongue", *Sensors and Actuators B: Chemical*. **103**(1–2): 233-239.

[68] Sharma, G., Liljeholm, L., Enlund, J., Bjurström, J., Katardjiev, I. and Hjort, K. (2010). "Fabrication and characterization of a shear mode AlN solidly mounted resonator-silicone microfluidic system for in-liquid sensor applications", *Sensors and Actuators A: Physical*. **159**(1): 111-116.

[69] Link, M., Weber, J., Schreiter, M., Wersing, W., Elmazria, O. and Alnot, P. (2007). "Sensing characteristics of high-frequency shear mode resonators in glycerol solutions", *Sensors and Actuators B: Chemical*. **121**(2): 372-378.

[70] Weber, J., Albers, W. M., Tuppurainen, J., Link, M., Gabl, R., Wersing, W. and Schreiter, M. (2006). "Shear mode FBARs as highly sensitive liquid biosensors", *Sensors and Actuators A: Physical*. **128**(1): 84-88.

[71] Chen, D., Wang, J., Li, D., Xu, Y. and Li, Z. (2011). "Solidly mounted resonators operated in thickness shear mode based on c-axis oriented AlN films", *Sensors and Actuators A: Physical*. **165**(2): 379-384.

[72] Wingqvist, G., Bjurström, J., Liljeholm, L., Yantchev, V. and Katardjiev, I. (2007). "Shear mode AlN thin film electro-acoustic resonant sensor operation in viscous media", *Sensors and Actuators B: Chemical*. **123**(1): 466-473.

[73] Link, M., Schreiter, M., Weber, J., Primig, R., Pitzer, D. and Gabl, R. (2006). "Solidly mounted ZnO shear mode film bulk acoustic resonators for sensing applications in liquids", *IEEE Transactions on Ultrasonics, Ferroelectrics, and Frequency Control*. **53**(2): 492-496.

[74] Corso, C. D., Dickherber, A. and Hunt, W. D. (2007). "Lateral field excitation of thickness shear mode waves in a thin film ZnO solidly mounted resonator", *Journal of Applied Physics*. **101**(5): 054514.

[75] Bjurstrom, J., Wingqvist, G. and Katardjiev, I. (2006). "Synthesis of textured thin piezoelectric AlN films with a nonzero C-axis mean tilt for the fabrication of shear mode resonators", *IEEE Transactions on Ultrasonics, Ferroelectrics, and Frequency Control*. **53**(11): 2095-2100.

[76] DeMiguel-Ramos, M. (2015). "High sensitivity biosensors based on shear mode AlN resonators for in liquid operation", PhD. Universidad Politecnica de Madrid, Madrid, Spain.

[77] Hao, Z., Mong, S. M., Eun Sok, K., Charles, E. M. and Mark, E. T. (2005). "A film bulk acoustic resonator in liquid environments", *Journal of Micromechanics and Microengineering*. **15**(10): 1911.

[78] Chuan, R. L. (1970). "An instrument for the direct measurement of particulate mass", *Journal of Aerosol Science*. **1**(2): 111-113.

[79] Bowers, W. D. and Chuan, R. L. (1989). "Surface acoustic-wave piezoelectric crystal aerosol mass microbalance", *Review of Scientific Instruments*. **60**(7): 1297-1302.

[80] Bowers, W. D., Chuan, R. L. and Duong, T. M. (1991). "A 200 MHz surface acoustic wave resonator mass microbalance", *Review of Scientific Instruments*. **62**(6): 1624-1629.

[81] Stanley, S. M., McHale, G., Newton, M. I., Percival, C. J. and Evans, C. R. (2005). "An EP-SAW for measurements of particulate matter in ambient air", *Nondestructive Testing and Evaluation*. **20**(1): 3-7.

[82]   Thomas, S., Racz, Z., Cole, M. and Gardner, J. W. (2013). "Dual high-frequency surface acoustic wave resonator for ultrafine particle sensing", *IEEE Sensors Conference 2013*. pp. 1-4.

[83]   Black, J. P., Elium, A., White, R. M., Apte, M. G., Gundel, L. A. and Cambie, R. (2007). "MEMS-enabled miniaturized particulate matter monitor employing 1.6 GHz aluminum nitride thin-film bulk acoustic wave resonator (FBAR) and thermophoretic precipitator", *IEEE Ultrasonics Symposium*. New York, NY pp. 476-479.

[84]   Paprotny, I., Doering, F., Solomon, P. A., White, R. M. and Gundel, L. A. (2013). "Microfabricated air-microfluidic sensor for personal monitoring of airborne particulate matter: Design, fabrication, and experimental results", *Sensors and Actuators A: Physical*. **201**(0): 506-516.

[85]   Paprotny, I., Doering, F. and White, R. M. (2010). "MEMS particulate matter (PM) monitor for cellular deployment", *IEEE Sensors Conference*. pp. 2435-2440.

[86]   Zhao, J., Liu, M., Liang, L., Wang, W. and Xie, J. (2016). "Airborne particulate matter classification and concentration detection based on 3D printed virtual impactor and quartz crystal microbalance sensor", *Sensors and Actuators A: Physical*. **238**: 379-388.

[87]   Djoumi, L., Blondeau-Patissier, V., Vanotti, M., Appert-Collin, J.-C., Thomas, D. and Fertier, L. (2016). "Surface acoustic wave sensors for PM2.5 and PM10 concentration", *Procedia Engineering*. **168**: 696-699.

[88]   Vashist, S. K. and Vashist, P. (2011). "Recent advances in quartz crystal microbalance-based sensors", *Journal of Sensors*. **2011**: 13.

[89]   Devkota, J., Ohodnicki, P. and Greve, D. (2017). "SAW sensors for chemical vapors and gases", *Sensors*. **17**(4): 801.

[90] Qiu, X., Tang, R., Zhu, J., Yu, H., Oiler, J. and Wang, Z. (2010). "Acetone sensor based on Film Bulk Acoustic Resonator", *2010 IEEE Sensors*. pp. 1546-1549.

[91] Heon-Min, L., Hong-Teuk, K., Hyung-Kyu, C., Hee-Chul, L., Hyung-Ki, H., Don-Hee, L., Joung-Uk, B. and Euisik, Y. (2006). "A Highly-Sensitive Differential-Mode Microchemical Sensor Using TFBARs with On-Chip Microheater for Volatile Organic Compound (VOC) Detection", *19th IEEE International Conference on Micro Electro Mechanical Systems*. pp. 490-493.

[92] Rey-Mermet, S., Lanz, R. and Muralt, P. (2006). "Bulk acoustic wave resonator operating at 8GHz for gravimetric sensing of organic films", *Sensors and Actuators B: Chemical*. **114**(2): 681-686.

[93] Da, C., Jingjing, W., Dehua, L., Yijian, L., Hongwei, S. and Qixin, L. (2011). "A poly(vinylidene fluoride)-coated ZnO film bulk acoustic resonator for nerve gas detection", *Journal of Micromechanics and Microengineering*. **21**(8): 085017.

[94] Johnston, M. L., Edrees, H., Kymissis, I. and Shepard, K. L. (2012). "Integrated VOC vapor sensing on FBAR-CMOS array", *2012 IEEE 25th International Conference on Micro Electro Mechanical Systems (MEMS)*. pp. 846-849.

[95] Wang, J. and Chen, D. (2013). "Investigation of polymer-coated film bulk acoustic wave resonator for acetone vapor detection", *2013 IEEE International Conference on Green Computing and Communications and IEEE Internet of Things and IEEE Cyber, Physical and Social Computing*. pp. 1680-1684.

[96] Matthys, R. J. (1992). "Crystal oscillator circuits". Malabar,Florida: Krieger publishing company.

[97] Matsuoka, J., Sato, T. and Ohshima, T. (2003). "A circuit for high frequency crystal oscillators", *Proceedings of the IEEE International Frequency Control Symposium and PDA Exhibition Jointly with the 17th European Frequency and Time Forum*. pp. 569-574.

[98]   Nomura, N., Aoyagi, Y. and Sekine, Y. (2005). "1 [GHz] high frequency Colpitts oscillator", *Proceedings of the 2005 IEEE International Frequency Control Symposium and Exposition, 2005*. pp. 4.

[99]   Gonzalez, G. (2006). "Foundations of oscillator circuit design". Artech House.

[100]   Glas, A. 2001. "Comparison between negative impedance oscillator (Colpitz oscillator) and feedback oscillator (Pierce structure). App.: Note #13".

[101]   Zhang, X., Xu, W., Abbaspour-Tamijani, A. and Chae, J. (2009). "Thermal analysis and characterization of a high Q film bulk acoustic resonator (FBAR) as biosensors in liquids", *2009 IEEE 22nd International Conference on Micro Electro Mechanical Systems*. pp. 939-942.

[102]   Brederlow, R., Zauner, S., Scholtz, A. L., Aufinger, K., Simburger, W., Paulus, C., Martin, A., Fritz, M., Timme, H. J., Heiss, H., Marksteiner, S., Elbrecht, L., Aigner, R. and Thewes, R. (2003). "Biochemical sensors based on bulk acoustic wave resonators", *IEEE International Electron Devices Meeting 2003*. pp. 32.7.1-32.7.3.

[103]   Razavi, B. (1996). "A study of phase noise in CMOS oscillators", *IEEE Journal of Solid-State Circuits*. **31**(3): 331-343.

[104]   Johnston, M. L., Kymissis, I. and Shepard, K. L. (2009). "An array of monolithic FBAR-CMOS oscillators for mass-sensing applictions", *Solid-State Sensors, Actuators and Microsystems Conference*. pp. 1626-1629.

[105]   Pang, W., Ruby, R. C., Parker, R., Fisher, P. W., Unkrich, M. A. and Larson, J. D. (2008). "A temperature-stable film bulk acoustic wave oscillator", *IEEE Electron Device Letters*. **29**(4): 315-318.

[106]   Aissi, M., Tournier, E., Dubois, M. A., Billard, C., Ziad, H. and Plana, R. (2006). "A 5 GHz above-IC FBAR low phase noise balanced oscillator", *IEEE Radio Frequency Integrated Circuits (RFIC) Symposium*. pp. 4 pp.-28.

[107] ElBarkouky, M., Wambacq, P. and Rolain, Y. (2007). "A low-power 6.3 GHz FBAR overtone-based oscillator in 90 nm CMOS technology", *Ph.D Research in Microelectronics and Electronics Conference*. pp. 61-64.

[108] Otis, B. P. and Rabaey, J. M. (2003). "A 300-µW 1.9-GHz CMOS oscillator utilizing micromachined resonators", *IEEE Journal of Solid-State Circuits*. **38**(7): 1271-1274.

[109] Chee, Y. H., Niknejad, A. M. and Rabaey, J. (2005). "A sub-100 uW 1.9-GHz CMOS oscillator using FBAR resonator", *IEEE Radio Frequency integrated Circuits (RFIC) Symposium - Digest of Papers*. pp. 123-126.

[110] Johnston, M. L., Kymissis, I. and Shepard, K. L. (2010). "FBAR-CMOS oscillator array for mass-sensing applications", *IEEE Sensors Journal*. **10**(6): 1042-1047.

[111] Dossou, S., Joblot, S., Petit, D. and Ancey, P. (2008). "A 2.5 GHz low phase noise oscillator design in 65nm CMOS technology with reduced current consumption", *2008 IEEE International Conference on Electron Devices and Solid-State Circuits*. pp. 1-4.

[112] Dossou, S., Abele, N., Cesar, E., Ancey, P., Carpentier, J. F., Vincent, P. and Fournier, J. M. (2008). "60µW SMR BAW oscillator designed in 65nm CMOS technology", *IEEE International Symposium on Circuits and Systems,* . pp. 1456-1459.

[113] Vanhelmont, F., Philippe, P., Jansman, A. B. M., Milsom, R. F., Ruigrok, J. J. M. and Oruk, A. (2006). "A 2 GHz reference oscillator incorporating a temperature compensated BAW resonator", *IEEE Ultrasonics Symposium*. pp. 333-336.

[114] Qu, H. (2016). "CMOS MEMS fabrication technologies and devices", *Micromachines*. **7**(1): 14.

[115] Fischer, A. C., Forsberg, F., Lapisa, M., Bleiker, S. J., Stemme, G., Roxhed, N. and Niklaus, F. (2015). "Integrating MEMS and ICs", *Microsystems & Nanoengineering*. **1**.

[116] Bernstein, G. H., Qing, L., Zhuowen, S. and Fay, P. (2005). "Quilt packaging: a new paradigm for interchip communication", *7th Electronic Packaging Technology Conference*. pp. 6.

[117] Pustan, M. and Rymuza, Z. (2007). "Comparative studies of advantages of integrated monolithic versus hybrid microsystems" in *Recent Advances in Mechatronics*, Springer Berlin Heidelberg: Berlin, Heidelberg, 521-525.

[118] Dubois, M. A., Billard, C., Muller, C., Parat, G. and Vincent, P. (2005). "Integration of high-Q BAW resonators and filters above IC", *ISSCC. 2005 IEEE International Digest of Technical Papers. Solid-State Circuits Conference, 2005*. pp. 392-606.

[119] Brand, O. (2008). "Fabrication Technology" in *CMOS—MEMS*, Wiley-VCH Verlag GmbH, 1-67.

[120] Allen, J. J., Kinney, R. D., Sarsfield, J., Daily, M. R., Ellis, J. R., Smith, J. H., Montague, S., Howe, R. T., Boser, B. E., Horowitz, R., Pisano, A. P., Lemkin, M. A., Clark, W. A. and Juneau, C. T. (1998). "Integrated micro-electro-mechanical sensor development for inertial applications", *IEEE Position Location and Navigation Symposium*. pp. 9-16.

[121] Seshia, A. A., Palaniapan, M., Roessig, T. A., Howe, R. T., Gooch, R. W., Schimert, T. R. and Montague, S. (2002). "A vacuum packaged surface micromachined resonant accelerometer", *Journal of Microelectromechanical Systems*. **11**(6): 784-793.

[122] Scheiter, T., Kapels, H., Oppermann, K. G., Steger, M., Hierold, C., Werner, W. M. and Timme, H. J. (1998). "Full integration of a pressure-sensor system into a standard BiCMOS process", *Sensors and Actuators A: Physical*. **67**(1): 211-214.

[123] Augustyniak, M., Weber, W., Beer, G., Mulatz, H., Elbrecht, L., Timme, H. J., Tiebout, M., Simburger, W., Paulus, C., Eversmann, B., Schmitt-Landsiedel, D., Thewes, R. and Brederlow, R. (2007). "An integrated gravimetric FBAR circuit for operation in liquids using a flip-chip extended 0.1um CMOS technology", *2007 IEEE International Solid-State Circuits Conference. Digest of Technical Papers*. pp. 392-610.

[124] Elbrecht, L., Aigner, R., Lin, C. I. and Timme, H. J. (2004). "Integration of bulk acoustic wave filters: concepts and trends", *2004 IEEE MTT-S International Microwave Symposium Digest*. pp. 395-398.

[125] Satoh, H., Suzuki, H., Takahashi, C., Narahara, C. and Ebata, Y. (1987). "A 400MHz one-chip oscillator using an air-gap type thin film resonator", *IEEE 1987 Ultrasonics Symposium*. pp. 363-368.

[126] Dunn, W. C., Liaw, H. M., Ristic, L. and Raymond M. Roop, *Monolithic circuit with integrated bulk structure resonator*, United States Patent, Editor. 1993: United States.

[127] Fazzio, R. S. and Dungan, T. E., *Monolithic vertical integration of an acoustic resonator and electronic circuitry*. 2007, United States Patents.

[128] Po-Hsun, S., Chi-Ming, F., Pei-Zen, C., Yung-Chung, C. and Pei-Yen, C. (2004). "The method for integrating FBAR with circuitry on CMOS chip", *IEEE International Frequency Control Symposium and Exposition,* . pp. 562-565.

[129] Fang, C. M., Chen, P. Y., Chin, Y. C., Lin, Y. T., Wang, X. Y., Lu, S. S. and Chang, P. Z. (2007). "Design and microfabrication of innovated FBAW filters based on an OOK receiver using 0.18um CMOS technology", *2007 2nd IEEE International Conference on Nano/Micro Engineered and Molecular Systems*. pp. 390-395.

[130] Tukkiniemi, K., Rantala, A., Nirschl, M., Pitzer, D., Huber, T. and Schreiter, M. (2009). "Fully integrated FBAR sensor matrix for mass detection", *Procedia Chemistry*. **1**(1): 1051-1054.

[131]   Aigner, R. (2003). "High performance RF-filters suitable for above IC integration: film bulk-acoustic- resonators (FBAR) on silicon", *Proceedings of the IEEE 2003 Custom Integrated Circuits Conference, 2003*. pp. 141-146.

[132]   Johnston, M., Shepard, K. and Kymissis, I., *Monolithic FBAR-cmos structure such as for mass sensing*. 2012: United States Patent.

CHAPTER 3

DESIGN AND MODELLING OF SOLIDLY MOUNTED RESONATORS

3.1 INTRODUCTION

In Chapter 2, the theoretical background of acoustic wave devices and their use in sensor applications were introduced. This chapter details the complete development process of a SMR for air quality monitoring, starting from the basic design considerations and the different modelling techniques used for BAW resonator design. Analytical and finite element models are implemented to aid the design process. Simulation results are presented and used to evaluate the performance of the acoustic mirror, the frequency response of the devices and their temperature dependency of frequency.

Preliminary layout designs of the devices are described. These devices will be used as the initial platform, towards developing a CMOS based SMR. Thus, the SMRs were designed considering CMOS compatibility.

3.1.1   PIEZOELECTRIC THIN FILMS

The sensitivity of acoustic wave based sensors is directly proportional to the frequency of operation of the devices. Therefore, acoustic devices operating in the GHz range are desirable for use in sensing applications. The maximum operating frequency of QCMs is limited by the mechanically achievable minimum thickness of the quartz piezoelectric crystal [1], and the maximum resonant frequency of SAWs is limited by the manufacturability of the IDTs. Thanks to the use of thin film technology (deposition of thin films of materials <100 µm), devices working at higher resonant frequencies (in the GHz range) can be fabricated (FBAR and SMR devices), and thus highly sensitive sensors based on these devices can be developed.

Widely used piezoelectric materials for the development of thin film BAW resonators are aluminium nitride (AlN), zinc oxide (ZnO) and lead zirconium titanate (PZT) with a hexagonal wurtzite crystal structure and well known thin film deposition processes (e.g. magnetron sputtering) [2-5]. The relevant physical properties of these piezoelectric materials are given in Table 3.1. Although not used in thin film devices, and not a CMOS compatible material, properties of quartz are also given for comparison.

Table 3.1 Properties of commonly used piezoelectric materials for BAW devices [6-15].

MATERIAL	AlN	ZnO	PZT	Quartz (ST cut)
Longitudinal acoustic velocity (m/s)	10400	6350	5400	3158
Piezoelectric coupling coefficient (%)	6.5	8.5	25	0.16
Temperature coefficient of frequency (ppm/°C)	-25	-60	-	0
Dielectric constant	10.4	10.9	350	4.4
Density (kg/m^3)	3270	5680	7550	2650
Attenuation at 1 GHz (dB/µS)	~5	8.3	400-2100	3.1

PZT is a very good candidate for thin film BAW devices, with a high coupling coefficient and a high dielectric constant. However, it exhibits high acoustic attenuation at frequencies above 1 GHz, which leads to high insertion losses. Thus, it is commonly preferred only for low frequency, broadband applications [10, 16].

ZnO exhibits a higher piezoelectric coupling coefficient (+24%) compared to AlN. However, its temperature dependency of frequency is a factor of 2.4 greater. Compared to AlN, thinner ZnO films are required for a given frequency due to its lower acoustic velocity. In terms of manufacturability, ZnO is CMOS compatible in terms of thermal budget and can be used in a post-CMOS process. However, ZnO is not compatible within CMOS facilities as Zn decreases minority carrier lifetimes in silicon. Thus, ZnO based BAW devices are unlikely to transfer into high volume production or on-chip integration [17, 18]. Furthermore, ZnO is chemically not very stable, which can cause reliability problems in humid environments [19].

Even though the electromechanical coupling coefficient of ZnO is slightly higher than that of AlN, the high electrical resistivity, low density, lower temperature coefficient of frequency (TCF), high thermal conductivity and its compatibility with standard integrated circuits fabrication technologies makes AlN more commonly preferred over ZnO [20]. AlN provides the best compromise between performance and manufacturability [19]. Indeed, AlN is used in most commercially available BAW devices operating in the GHz range [20].

Regardless of the piezoelectric material used, the performance of a device is directly affected by the quality of the films deposited (e.g. uniformity). High quality piezoelectric films are desired in order to obtain BAW resonators with high quality factors [16]. Poorly grown films with high density grains and impurities will scatter the acoustic waves [21]. The deposition of high quality piezoelectric thin films for their application in BAW devices is a wide research field on its own. Several studies have been carried out to investigate these deposition techniques [6, 22, 23]. The deposition of AlN and ZnO thin films by sputtering have been demonstrated to provide the performance required for high frequency applications [24, 25].

3.1.2   ACOUSTIC MIRROR

The quality factor of BAW resonators not only depends on the quality of the piezoelectric layers but also on the effective confinement of the acoustic energy within the resonator [16]. In SMR devices, acoustic isolation to the substrate is achieved by means of the so-called acoustic mirror, also commonly referred as reflector stack or Bragg reflector due to its analogy with optics.

The acoustic mirror is formed by alternating layers of low and high acoustic impedance materials with thicknesses equal to quarter-wavelength ($\lambda/4$) of the fundamental frequency. This configuration was first proposed by Newell [26]. The impedance mismatching between these layers causes a large portion of the acoustic energy to be reflected at each interface of the stack thus preventing energy leakage to the substrate as depicted in Figure 3.1.
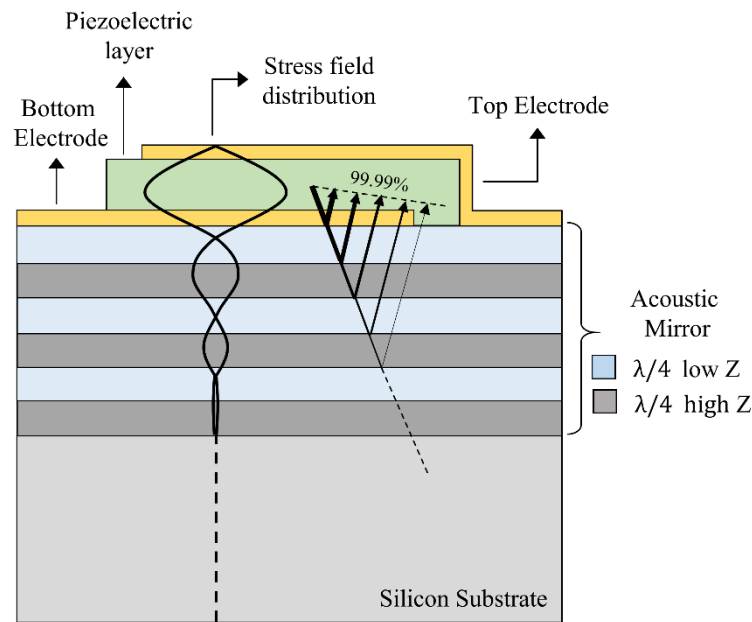
Figure 3.1 Structure of the acoustic mirror and stress field distribution in the SMR.

The effective confinement of the acoustic energy mainly depends on the impedance ratio mismatch of the materials and the number of layers used. The larger the impedance ratio, the better the performance of the reflector. Well-designed acoustic mirrors are capable of confining practically all the energy, achieving a reflectivity of at least 99.98% [19]. Depending on the materials used, maximum

reflectivity can be achieved with a total of only 4 layers, as in the case of W/SiO$_2$ (impedance ratio of ~8). An acoustic mirror formed by Al/SiO$_2$ (impedance ratio of ~1.3), would require >10 layers to achieve a good reflectivity.

Common material combinations used for the reflector stack in SMR devices are W/SiO$_2$ [27] and Mo/SiO$_2$ [28, 29] due to their high acoustic impedance ratio of 8 and 5, respectively. Other material combinations such as ZnO/Pt [30] have been proposed, which make use of the same piezoelectric material to form the mirror, thus simplifying the fabrication process. A detailed discussion on the design and selection of materials for the acoustic mirror in this work is presented in section 3.3.2.

The most common acoustic mirror configuration uses a low acoustic impedance material for the top layer of the reflector stack with the piezoelectric film thickness at half-wavelength (λ/2). This configuration not only has shown larger Q values and coupling coefficients [31] but also helps to temperature-compensate the BAW device, if materials with positive temperature coefficients are used for the top layer such as SiO$_2$ [32]. Temperature compensation of SMR devices is further discussed in section 3.1.4.

The implementation of fully insulating and fully conductive acoustic mirrors has been proposed [33-36]. Fully conductive reflectors have shown improved performance thanks to the reduced Ohmic losses [37]. On the other hand, fully dielectric reflectors can be useful in filter applications to avoid crosstalk between devices in the same substrate [38] and reduce parasitics between the electrodes and the upper metal layer [39]. However, unlike fully insulating structures, reflector stacks including metal layers have better power handling capabilities due to the increased heat conductivity through the reflector [17, 37].

3.1.3   ELECTRODES

Materials used for the electrodes in SMRs have an effect in the performance characteristics of the device. By using electrode materials with high acoustic impedance, high effective coupling coefficients can be obtained. The larger the impedance mismatch between the electrode and the piezoelectric materials, the better

the acoustic energy is confined in the resonator [21, 40]. However, other properties such as density and electrical conductivity need to be considered.

The electrical resistivity of thin metal films (<200 nm) of high acoustic impedance materials can be up to two times higher than the corresponding bulk resistivities [17]. Metals such as aluminium and gold do not experience this effect, with comparable resistivity values in thin film and bulk forms. Increased resistivity lead to electrical losses and degradation of the Q factor in SMRs [21, 41]. Thus, metals with low resistivity are preferred to reduce the resistive losses.

The use of thick electrodes and materials of high conductivity can minimise the series electrical loss and improve the Q factor [20]. However, there is a compromise between the electrode thickness and mechanical losses (i.e. thicker electrodes increase the mass load on the resonator). In order to minimise this mass loading effect, materials with low densities are required [41, 42]. A trade-off between metal density, acoustic impedance and conductivity is required.

Figure 3.2 shows a comparison between the density, acoustic impedance and electrical resistivity values of common metals. Metals such as platinum (Pt), tungsten (W) and iridium (Ir) have advantageous high acoustic impedances, but come with the disadvantage of high density. On the other hand, aluminium (Al) offers good conductivity and low density, but has low acoustic impedance.
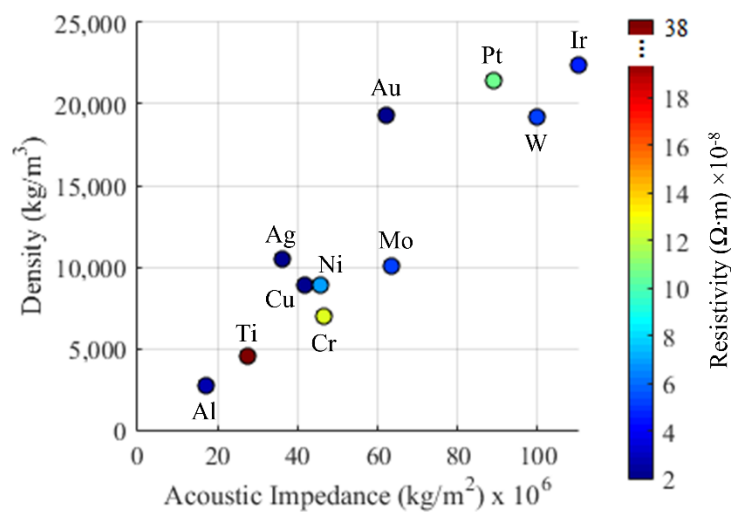
Figure 3.2 Comparison of mechanical and electrical properties of commonly used electrode materials in SMR devices. Material data from [43].

Considering the important properties for resonator design, molybdenum (Mo) offers a favourable compromise of low density, high acoustic impedance and adequate conductivity. Therefore, Mo is a popular choice for electrode material in the literature [44, 45]. Other materials for the electrodes such as ruthenium (Ru), carbon nanotubes (CNT) and iridium (Ir) have also been investigated [46, 47].

The material used for the bottom electrode plays an important role in the quality of the piezoelectric layer. The bottom electrode acts as a seeding layer for the piezoelectric material, where its surface roughness influences the growth of high quality piezoelectric film. Materials such as Ir and Mo have been reported to produce high quality AlN piezoelectric films [48, 49].

The geometry and surface area of the electrodes do not affect the resonant frequency of the device [50]. However, the total surface of the active area (overlap of top and bottom electrodes) can directly impact the attenuation of the device. An increase in the surface area of the electrode results in an increase of S-parameter values [10, 51]. Furthermore, the use of certain geometries of the electrodes (e.g. non-parallel side edges) have been proposed for the suppression of spurious lateral modes [52, 53].

3.1.4 TEMPERATURE COMPENSATION

Temperature dependence of the resonant frequency in SMRs is attributed to the change with temperature of the mechanical and electrical properties of the materials, in particular to the thermal variations of the elastic constants which are directly related to a change in acoustic velocity and the resulting change in resonant frequency.

Unlike ST-cut quartz substrates frequently used in SAW devices (with a TCF of 0 ppm/°C), the piezoelectric thin films commonly used in BAW resonators (AlN and ZnO), have negative and relatively high TCFs as shown in Table 3.1 (p. 98).

Compensation of the temperature variations in SMRs can be achieved by adding a layer of a positive TCF material such as SiO_2 close to the piezolayer [32]. Several ways of implementing these composite configurations have been proposed and are used in temperature compensated SMRs [32, 54, 55]. However, these methods can

affect the performance of the devices, degrading their electromechanical coupling coefficient and Q factor [56].

The influence of the entire SMR structure in the total TCF of the device has been also investigated. The electrodes and the two uppermost layers of the reflectors have been found to have the most significant effect and an adjustment to the thickness of these two layers can be done in order to achieve a temperature compensated device with better performance characteristics [57].

In the use of acoustic wave devices for sensing applications, a common method to supress the temperature effects (and other common mode interferences such as humidity and pressure) is the use of a dual mode configuration, where two identical devices are used, one of them acting as the sensing channel and the other as a reference device [58]. This method will be employed in this work for the development of SMR based sensors.

3.2 MODELLING OF SOLIDLY MOUNTED RESONATORS

3.2.1 ONE-DIMENSIONAL MASON MODEL

The Mason electromechanical equivalent circuit for piezoelectric crystals [59] is commonly used for the analysis of piezoelectric resonators in thickness mode [29, 36, 60, 61]. The piezoelectric layer is represented as a three-port network with one electric port and two mechanical ports. An ideal transformer is used to take into account the electro-acoustic interaction. This is a one-dimensional analytical model, which together with the transmission line theory can be employed to model BAW devices.

Figure 3.3 shows the equivalent circuit representation of an SMR device based on the Mason model. The piezoelectric film is a three-port component while all other material layers of the SMR structure (acoustic mirror layers and electrodes) are represented as cascaded two-port networks. At one end (left), the surface of the top electrode in contact with air is modelled as a mechanical short while the reflector stack (right) is terminated with the impedance of the substrate.
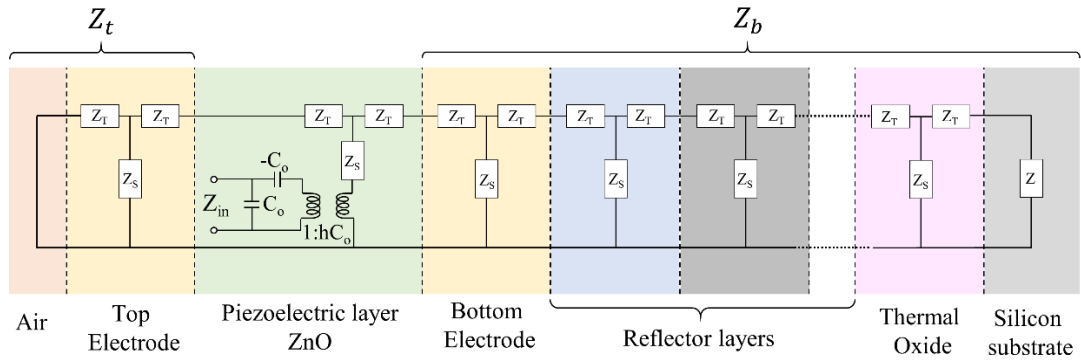
Figure 3.3 Equivalent circuit representation of the Solidly Mounted Resonator according to the Mason model.

The parameters of the Mason equivalent model shown in Figure 3.3 are defined as follows:

$$Z_T = jZ_L \ \tan(\theta/2) \tag{3.1}$$

$$Z_S = \frac{-jZ_L}{\sin \theta} \tag{3.2}$$

$$C_o = \frac{\varepsilon_{33}A}{d_p} \tag{3.3}$$

$$h = \frac{e_{33}}{\varepsilon_{33}} \tag{3.4}$$

Z_T and Z_S are given in terms of the mechanical impedance $Z_L = A\rho v$, where A is the active area of the SMR, ρ is the density of the material (for each layer) and v is the acoustic velocity of the material. $\theta = kd$ is the total phase across the line section. For each layer of thickness d, the corresponding propagation coefficient k is defined as $k = \omega/v$, where ω is the angular frequency. C_o is the parallel capacitance given by the relationship between the permittivity of the piezoelectric material, ε_{33}, the thickness of the piezoelectric layer, d_p, and the active area, A. h is a constant given by the ratio between piezoelectric strain constant, e_{33}, and the permittivity.

The impedance Z_{in} at the electrical port has been derived by Lakin [62] and can be expressed as:

$$Z_{in} = \frac{1}{j\omega C_o}\left[1 - K^2\frac{\tan\phi}{\phi}\cdot\frac{(z_b + z_t)\cos^2\phi + j\sin 2\phi}{(z_b + z_t)\cos 2\phi + j(z_b z_t + 1)\sin 2\phi}\right] \tag{3.5}$$

where $\phi = (kd_p)/2$ is the half phase across the piezoelectric layer. z_b and z_t are the acoustic impedances at the boundaries of the piezoelectric layer (Z_b and Z_t as shown in Figure 3.3), normalised to the acoustic impedance of the piezolayer (Z_p). K^2 is the piezoelectric coupling coefficient given by:

$$K^2 = \frac{\frac{e_{33}^2}{\varepsilon_{33}c_{33}}}{1 + \frac{c_{33}}{\varepsilon_{33}}} \tag{3.6}$$

where c_{33} is the elastic constant of the piezoelectric material.

The acoustic impedances Z_b and Z_t at the boundaries (bottom and top) of the piezolayer can be found by using transmission line theory. Each of these layers is uniquely defined and the ABCD parameters of the resulting two-port networks are specified by a 2×2 transfer matrix as shown below:

$$\begin{bmatrix} A & B \\ C & D \end{bmatrix} = \begin{bmatrix} 1 + \dfrac{Z_T}{Z_S} & 2Z_T + \dfrac{Z_T^2}{Z_S} \\ \dfrac{1}{Z_S} & 1 + \dfrac{Z_T}{Z_S} \end{bmatrix} \tag{3.7}$$

where Z_T and Z_S are defined in equations (3.1) and (3.2). This allows for a cascaded network by multiplying each of the matrices of the boundary layers [63].

At the top electrode interface in contact with air, the acoustic impedance is close to zero. In the case of the top electrode being formed by only one metal layer, the impedance at the top boundary can be given by:

$$Z_T = jZ_{TE}\tan\theta \tag{3.8}$$

where Z_{TE} is the acoustic impedance of the top electrode material.

The acoustic impedance of the bottom boundary can be used to calculate the transmissivity of the acoustic mirror as follows [64]:

$$T_{(dB)} = 10 \log(1 - |R|^2) \tag{3.9}$$

where R is the reflectivity of the acoustic mirror given by:

$$R = \frac{Z_p - Z_b}{Z_p + Z_b} \tag{3.10}$$

The quality factor of the reflector stack can be described in terms of the transmittance by considering the energy transmitted through the reflector as lost, in this way the Q-factor of the acoustic mirror can be given as [65]:

$$Q_{reflector} = \frac{2\pi}{T} \tag{3.11}$$

In order to estimate the resonant frequency of the SMR devices as well as the performance of the reflector stack for the longitudinal waves, equations (3.5) - (3.10) were implemented in a script using Matlab® R2015a. This model aided the design of the SMR devices throughout this work. An example of the Matlab script is given in Appendix A.

3.2.2 FINITE ELEMENT MODEL

The vast majority of engineering phenomena are boundary value problems expressed by partial differential equations (PDEs). For complex geometries with different materials, analytical solutions cannot be obtained for the entire problem domain. The finite element method (FEM) discretises the problem by dividing the domain into smaller parts (finite elements) connected with nodes. The PDEs are approximated with algebraic equations that can be solved for each element and then put back together to find an approximate numerical solution for the entire domain.

Commercial software is available to perform finite element analysis. The typical procedure when using these software packages consists of (1) defining the geometry domain, material properties, boundary conditions, physics and mesh (pre-processing), (2) the computation of the numerical analysis (processing), and (3) analysis and display of the obtained results (post-processing).

In this work, the Acoustic Module of COMSOL Multiphysics® v4.4 [66] was employed to perform the finite element analysis of the designed solidly mounted resonators. The interaction between electrical potential and mechanical displacement is solved using the piezoelectric interface (*pzd*) according to the piezoelectric constitutive equations (2.1) and (2.2) in the stress-charge form. Both 2D and 3D finite element models of the resonators were developed. The geometries of the developed models are shown in Figure 3.4 below.
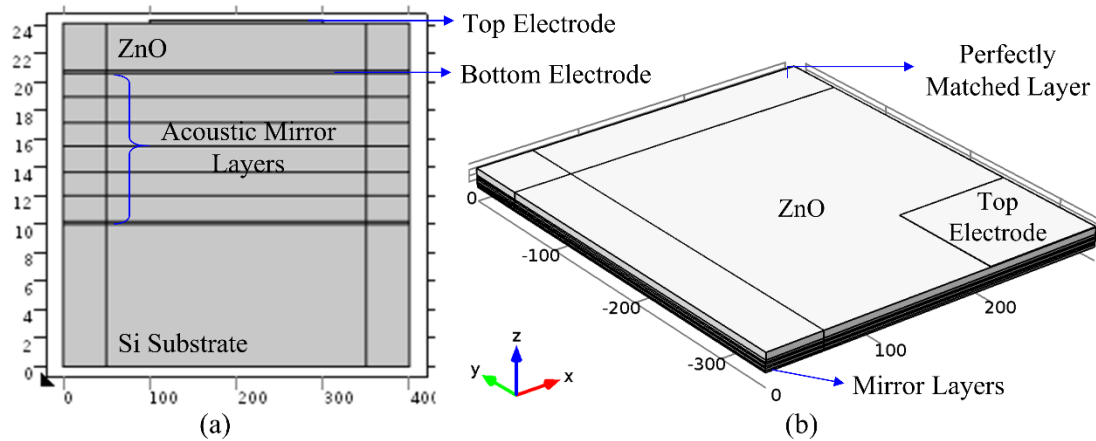
Figure 3.4 Geometry of the (a) two-dimensional and (b) three-dimensional finite element model of the SMR

The 2D model used the plane strain assumption where the out of plane thickness is defined [67]. In order to reduce computation time, the 3D model consisted of only a quarter of the complete structure of the SMR by taking advantage of the symmetry of the device. Perfectly matched layers (PMLs) were used to account for the absorption of the elastic waves at the boundaries. Further details on the implementation of the FEM models are given in Appendix B.

The developed FEM models were used to evaluate the resonant frequency of the SMRs, the displacement profile of the mechanical waves and the temperature dependence of frequency. The results obtained are presented in the following sections. Sensitivity to the deposition of fine particles and the absorption of volatile organic compounds was also evaluated with the FEM models and will be discussed in Chapters 5 and Chapter 6, respectively.

3.2.3 MODIFIED BUTTERWORTH VAN DYKE MODEL

The Butterworth Van Dyke (BVD) model is an equivalent electrical circuit for BAW resonators in the fundamental mode [68-70]. Due to its simplicity, this lumped element model is widely used for circuit design purposes to model the frequency behaviour of the resonator with the aid of circuit simulation software.

Larson *et al.* [71] modified the BVD model to take into account acoustic losses in the piezoelectric layer. The modified Butterworth Van Dyke (MBVD) model is shown in Figure 3.5, it is formed by two branches: R_m, C_m and L_m form the motional arm representing the mechanical resonance. R_o and C_o form the static arm.
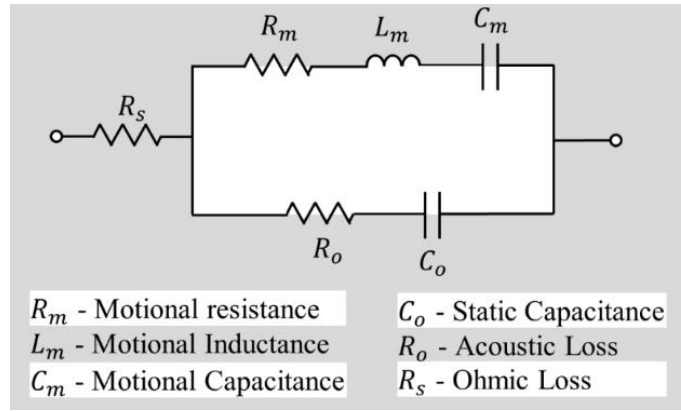
Figure 3.5 Modified Butterworth Van Dyke (MBVD) model for a BAW resonator.

R_o represents the acoustic losses while C_o is the electrical plate capacitance formed by the resonator structure given as:

$$C_0 = \frac{\varepsilon A}{d} \tag{3.12}$$

where ε is the piezoelectric permittivity, A is the active area and d is the piezoelectric thickness. The electrical resistance of the electrodes is represented by R_s.

The series and parallel resonant frequencies and the corresponding quality factors can be expressed in terms of these lumped elements by [72, 73]:

$$f_s = \frac{1}{2\pi \sqrt{L_m C_m}} \tag{3.13}$$

$$f_p = f_s \sqrt{1 + \frac{C_m}{C_o}} \qquad (3.14)$$

$$Q_s = \frac{1}{2\pi f_s \, C_m R_m} \qquad (3.15)$$

$$Q_p = Q_s \sqrt{1 + \frac{C_m}{C_o}} \qquad (3.16)$$

The series resonance is set by the LC circuit of the motional arm and occurs when the capacitive and inductive reactance have the same magnitude cancelling their effects (minimum impedance). The parallel resonance is set by the capacitance of the static arm C_0 with C_m and L_m. In this work, the MBVD model of the fabricated SMR devices was extracted and used in the design on the driving circuitry, as will be discussed in Chapter 6.

3.3   DESIGN AND SIMULATION OF SMRS FOR SENSING APPLICATIONS

A 1D Mason model was used to evaluate the performance of the acoustic reflector and the frequency behaviour of the designed SMRs. While the one dimensional model can provide a very good estimation of the resonant frequency of the SMRs and the reflectivity of the acoustic mirror, it does not take into account the lateral energy leakage at the edges of the device [1]. The 2D and 3D FEM models developed in COMSOL Multiphysics® were helpful to compute these spurious modes. However, the computation time and computer memory usage had to be considered when selecting the number of dimensions and mesh elements for efficient simulations [74].

3.3.1   DESIGN PARAMETERS

Solidly mounted resonators were designed to operate in the longitudinal mode for use in mass sensing applications (particle sensing and VOC detection). For these applications, lateral field excitation or tilting of the piezoelectric crystal are not required.

Acoustic devices (thin film BAW resonators) operating at frequencies between 1 GHz and 2 GHz are the most commonly reported for sensing applications (see Table

2.4). These devices provide an excellent compromise between improved sensitivity and the increased presence of parasitic capacitance. High frequency signals are more susceptible to noise and parasitic effects. The interface electronic circuitry for these signals requires careful design to ensure improved stability, which directly affects the sensitivity and limit of detection of a sensing system.

In this work, two different devices were designed to operate at the fundamental frequencies of 870 MHz and 1.5 GHz, both below the 2 GHz bound. The lower frequency resonator was developed to provide a test module which could be trialled with different interface circuit designs, to find a suitable oscillator circuit for use at high frequency. Furthermore, to aid the development of initial interface circuits, reduced parasitic capacitances (associated to lower frequency devices) were preferred.

For the two operating frequencies, devices with two different electrode materials were designed: aluminium (Al) because of its low density and good conductivity to reduce mass loading effects, and gold (Au/Cr) due its high acoustic impedance. Both top and bottom electrodes used the same material and thickness. For the SMRs with gold electrodes, a seed layer of chrome was used for improved adhesion, with negligible effects. The electrodes are either 200 nm Al electrodes or Au/Cr electrodes in a ratio of 10:1.

Zinc oxide was selected as the piezoelectric material in this work, with two main advantages: (1) the high-quality and low-stress of the ZnO thin film layers (achieved when deposition is performed at room temperature) and (2) the thinner piezoelectric film required for the 870 MHz design (~3.65 µm compared to ~6.6 µm required for AlN). A thicker layer would considerably increase the total deposition processing time and induce more stress in the films.

For the design of the acoustic mirror, a combination of metal and insulating layers was selected (as this is the configuration that will be later used in the design of a CMOS based acoustic mirror, presented in Chapter 7). Table 3.2 gives the materials and properties used in the design of the SMRs. Table 3.3 summarises the final design parameters. The design procedure of the device (acoustic mirror, electrodes) is explained in detail in the following sections.

Table 3.2 Material properties used for the modelling of the SMRs.

MATERIAL	DENSITY (kg/m³)	ACOUSTIC VELOCITY (m/s)
Si	2330	8320
Mo	10200	6340
W	19350	5210
SiO$_2$	2070	5710
Al	2700	6450
Cr	7150	6630
Au	19300	3430
ZnO	5680	6370

ZnO properties: elastic constant $c_{33} = 211$ GPa, piezoelectric constant $e_{33} = 1.32$ C/m², dielectric constant = 10.2.

Table 3.3 Final thicknesses of the layers for the SMR designs.

MATERIAL	THICKNESS	
	DESIGN 870 MHz	DESIGN 1.5 GHz
Mo	1.82 µm	1.05 µm
W	1.53 µm	887 nm
SiO$_2$	1.65 µm	995 nm
Al	200 nm	200 nm
ZnO	3.35 µm	1.85 µm
Cr	10 nm	10 nm
Au	100 nm	100 nm
ZnO	2.85 µm	1.35 µm

3.3.2   ACOUSTIC MIRROR DESIGN

In the development of a SMR device, careful design and accurate deposition of the acoustic mirror layers is fundamental to achieve high quality factors at the desired operating frequency. Typical Q factors of SMR devices are in the range of 500 to 800 compared to FBAR devices, which exhibit Q values of about 2000 [64]. The lower Q values of SMRs is attributed to the acoustic energy leaking into the substrate.

A wide range of materials can be employed in the implementation of the acoustic mirror in SMR devices. As mentioned before, a large ratio of high to low acoustic impedance materials is preferred to maximize the wave reflection, thus requiring less number of layers to form the reflector. The combination of W/SiO$_2$, with an impedance ratio of nearly eight, has been shown to be very efficient as only a total of four layers are required to obtain good reflectivity [75].

The acoustic mirror layers in this work were designed with a $\lambda/4$ thickness. During the design procedure, several material pairs were considered for this implementation. The relevant properties of these materials are shown in Table 3.4. Materials were chosen to achieve the maximum wave reflection with a minimum number of layer pairs. Furthermore, only CMOS compatible metals were considered and chosen as the high acoustic impedance material.

Table 3.4 Properties of the materials considered for the implementation of the quarter wavelength acoustic mirror and the required thicknesses for the design frequencies.

MATERIAL	DENSITY (kg/m^3)	ACOUSTIC VELOCITY (m/s)	ACOUSTIC IMPEDANCE (kg/m^{2}s) $\times 10^6$	$\lambda/4$ 870 MHz (nm)	$\lambda/4$ 1500 MHz (nm)
Mo	10200	6280	65	1804	1046
W	19350	5210	101	1497	868
Al	2700	6450	17.1	1853	1075
Ti	4505	6260	27.3	1798	1073
Pt	21500	4080	87.7	1172	680
SiO$_2$	2170	5540	13.1	1591	923
ZnO	5680	6330	35.6	1818	1055

For selected combinations of material pairs, simulations were performed using the 1D Mason model, assuming a silicon substrate of 500 µm thickness, an aluminium bottom electrode of 200 nm and an active area of 0.04 mm^2. Results from these simulations are shown in Figure 3.6, where the transmittance and bandwidth of the acoustic mirrors are shown (for longitudinal waves) for a total of 4 and 6 layers.

The transmittance of the acoustic mirror formed by two pairs of W/SiO$_2$ was found to be -33 dB which corresponds to a reflection coefficient of 0.99974. This reflector performs extremely well considering that it is formed by only 4 layers. For the Pt/SiO$_2$ and Mo/SiO$_2$ acoustic mirrors with 4 layers, the reflections are 99.958% and 99.859%, respectively. All other material combinations were not considered as even with 6 layers they perform poorly (more than three layer pairs would have to be deposited in order to achieve good reflection, making the fabrication process more complex).

In general, it was observed that the acoustic mirror structures formed by a total of 6 layers exhibited higher reflectivity (+40%) but narrower bandwidth (-20%) compared to the structures with only 4 layers (shown in Figure 3.6c). Although high reflectivity is the main parameter in the design of an acoustic mirror (for optimum confinement of the acoustic energy within the resonator), wider bandwidth can result advantageous. A significant variation of the piezoelectric layer thickness (during fabrication), will produce a significant shift of the designed resonant frequency of the device. In this case, an acoustic mirror with a wide bandwidth can still confine the energy efficiently.
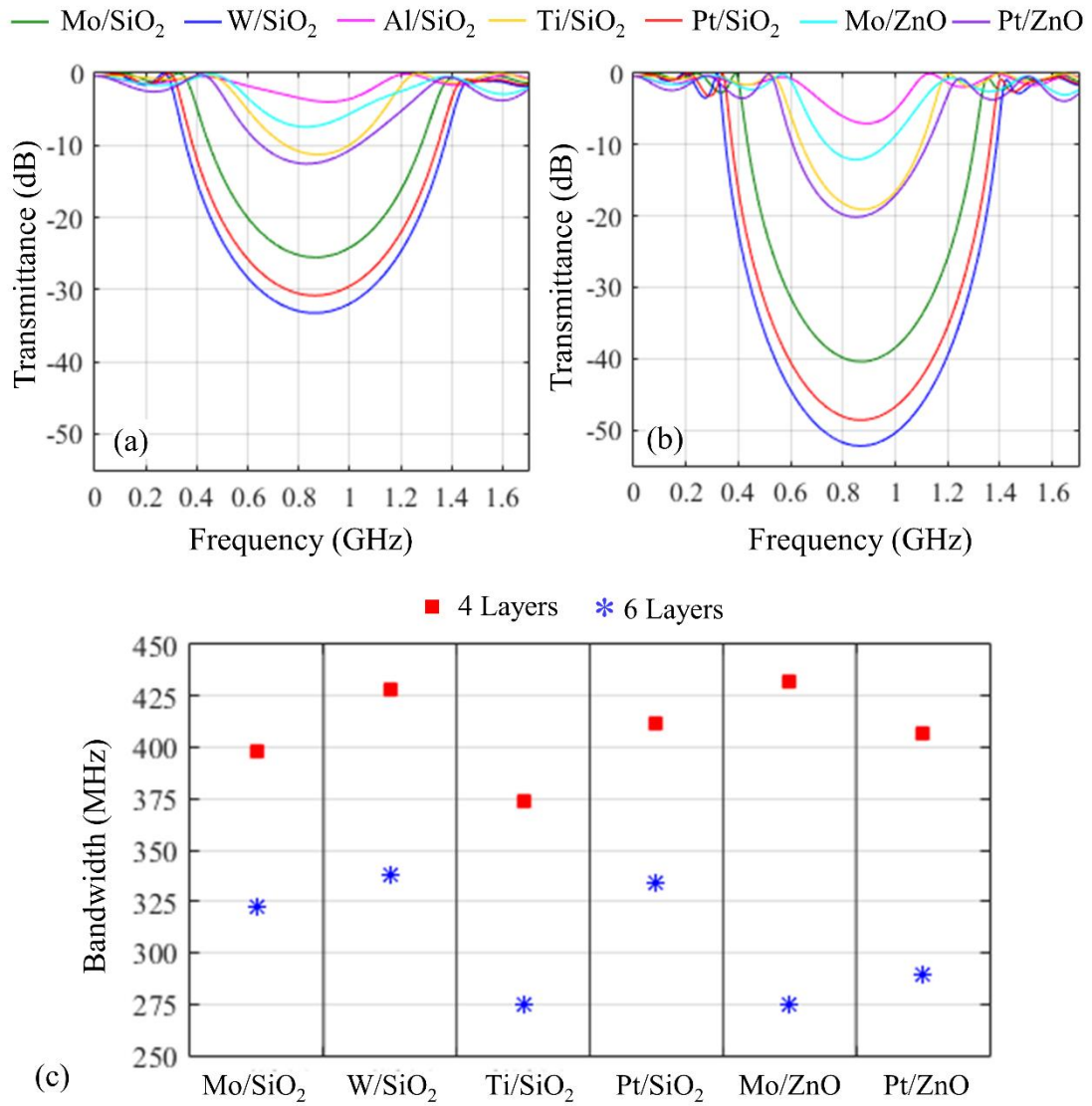
Figure 3.6 Simulated transmittance of different $\lambda/4$ acoustic mirrors for longitudinal waves at 870 MHz with (a) 4 layers and (b) 6 layers using the one-dimensional model and (c) the corresponding bandwidths.

The selected material combinations for the acoustic reflector in this work were W/SiO_2 and Mo/SiO_2. On one hand, tungsten and molybdenum were chosen as the high acoustic impedance layer due to their acoustic velocity and CMOS compatibility. On the other hand, silicon dioxide was selected as the low acoustic impedance layer due to its low density, low acoustic velocity and positive temperature coefficient, to help with the temperature compensation of the resonator [76].

For comparison, the transmittance of a $\lambda/4$ acoustic mirror with three pairs of Mo/SiO$_2$ and two pairs of W/SiO$_2$ is shown in Figure 3.7 for both SMR design frequencies of 870 MHz and 1.5 GHz.

(a)   (b)
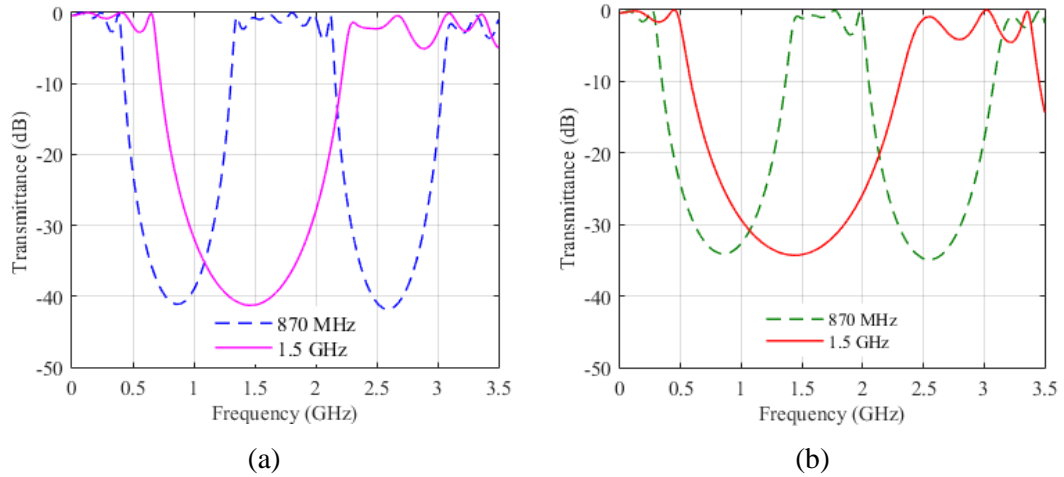
Figure 3.7 Simulated longitudinal waves transmittance of the acoustic reflector consisting of (a) three pairs of Mo/SiO$_2$ and (b) two pairs of W/SiO$_2$ based on the one-dimensional model.

As expected, the Mo/SiO$_2$ reflector showed a slightly higher (+20%) reflectivity at the desired frequencies (due the larger number of layers used). However, all these reflector structures exhibited low transmittance at the desired centre frequencies. Additionally, a wider bandwidth was observed for the 1.5 GHz design in both designs (Mo/SiO$_2$ and W/SiO$_2$).

In this work, the Mo/SiO$_2$ layers were selected due to the good adhesion properties of these materials and the lower density of Mo, compared to W. SMR devices with a Mo/SiO$_2$ acoustic mirror were further simulated to analyse their frequency response and study the effect of the piezoelectric layer thickness.

For a Mo/SiO$_2$ reflector with 4 layers, the simulated transmittance is -25.53 dB which is just below the minimum calculated transmittance for a Q=2000 (-25.5 dB). For improved performance, a Mo/SiO$_2$ acoustic mirror with a total of 6 layers was preferred, giving a very low transmittance of -40.42 dB which corresponds to a reflection coefficient of 0.9999, thus confining practically all the acoustic energy.

To further evaluate the performance of the designed acoustic mirror, simulations were obtained from the 2D finite element model. The standing wave

amplitude was plotted as a function of depth into the SMR [40] and the vertical displacement profile was obtained for the longitudinal wave as shown in Figure 3.8. As observed, the amplitude of the standing wave reduces at each interface with no considerable energy leaking into substrate, hence achieving optimal reflection of the longitudinal waves.
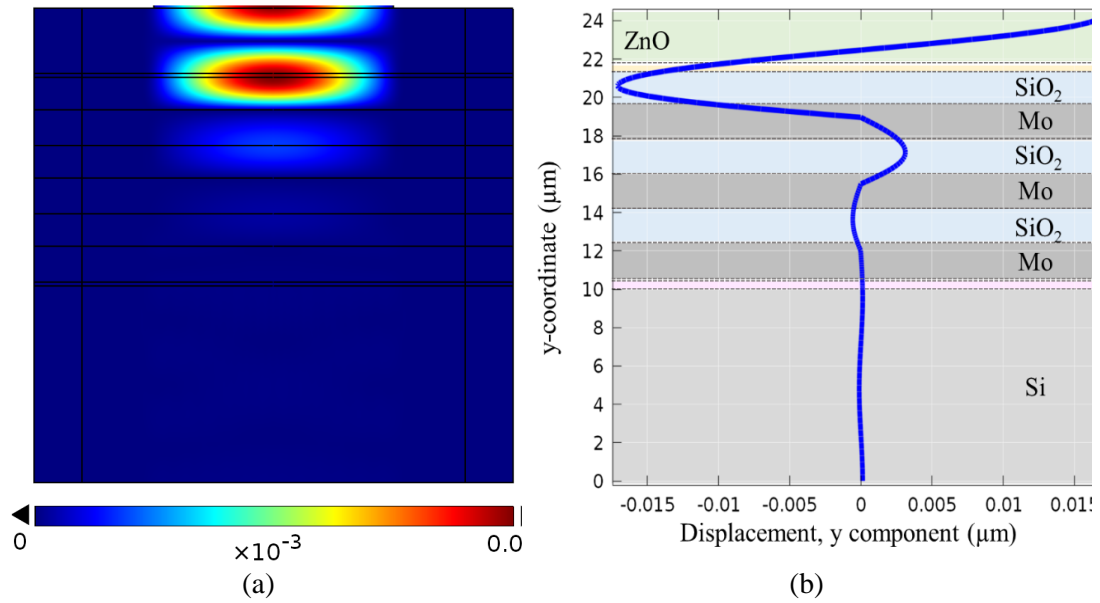
Figure 3.8 (a) Displacement profile for the longitudinal wave at resonant frequency and (b) y-displacement at the cross section of the device.

It is important to note that in the conventional quarter-wavelength design used in this work, any shear waves generated in the device will be poorly reflected at the designed frequency (as shown in Figure 3.9). These shear waves will be transmitted through the reflector [77], leaking into the substrate and thus, limiting the Q-factor of the devices. This arises from the fact that the propagation velocity of shear waves is roughly half the velocity of the longitudinal waves, making the thickness of the reflector layers about $\lambda/2$ for the shear mode [64, 78].

Optimization of the acoustic mirror structure (thicknesses of the layers) has been proposed to reflect both longitudinal and shear waves effectively to obtain resonators with high quality factors (Q>1000) [65, 79-81]. However, these optimisation procedures usually require the reflector layers near the resonator (piezoelectric and electrodes) to be thicker compared to the $\lambda/4$ approach, giving place to asymmetric structures. This compromises the piezoelectric coupling of the device

as a large portion of the acoustic energy (stress field) resides outside the piezoelectric film [17]. In this work, a conventional $\lambda/4$ approach is used in the design procedure of the SMR devices due to trade-off between simplicity and effective reflection of the acoustic energy.
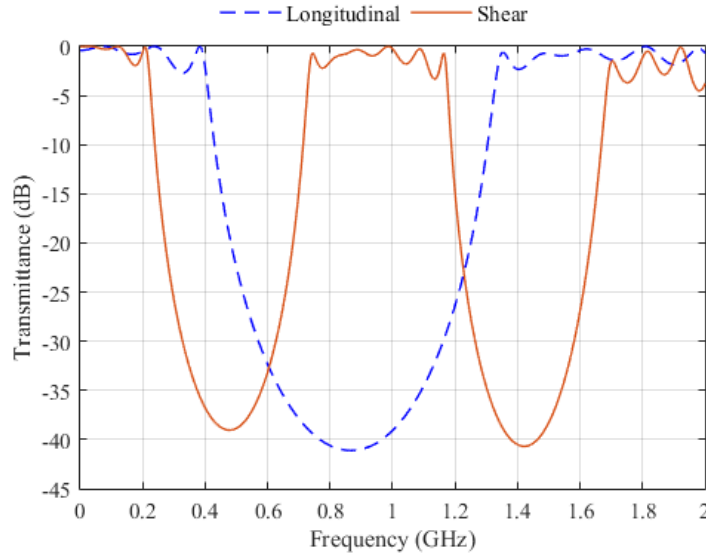
Figure 3.9 Longitudinal and shear wave transmittance of the designed Mo/SiO$_2$ acoustic mirror for the fundamental frequency at 870 MHz.

3.3.3   FREQUENCY RESPONSE SIMULATIONS

The Mason model is a one-dimensional model where the lateral dimension of the resonator is considered infinite. For a sufficiently large BAW device, the resonant frequencies can be precisely predicted by a 1D model [74]. However, the model cannot be used to study spurious modes in the SMR caused by laterally standing waves, as the finite lateral dimensions are not considered. A two-dimensional (or three-dimensional) model is needed to this aim [1].

Figure 3.10 shows the simulated impedance curves of the designed SMRs obtained with the 1D Mason model over a large range of frequencies. The fundamental modes can be observed at 872 MHz and 1.49 GHz which are very close to the design frequencies. Second harmonics at 2.68 GHz and 4.5 GHz are observed for each of the designs, respectively.

To compare the results obtained with the Mason model, the 2D and 3D FEM models developed in COMSOL® were used to compute the frequency response of the

designed SMRs. The resulting curves are shown in Figure 3.11 compared to that obtained with the 1D model.
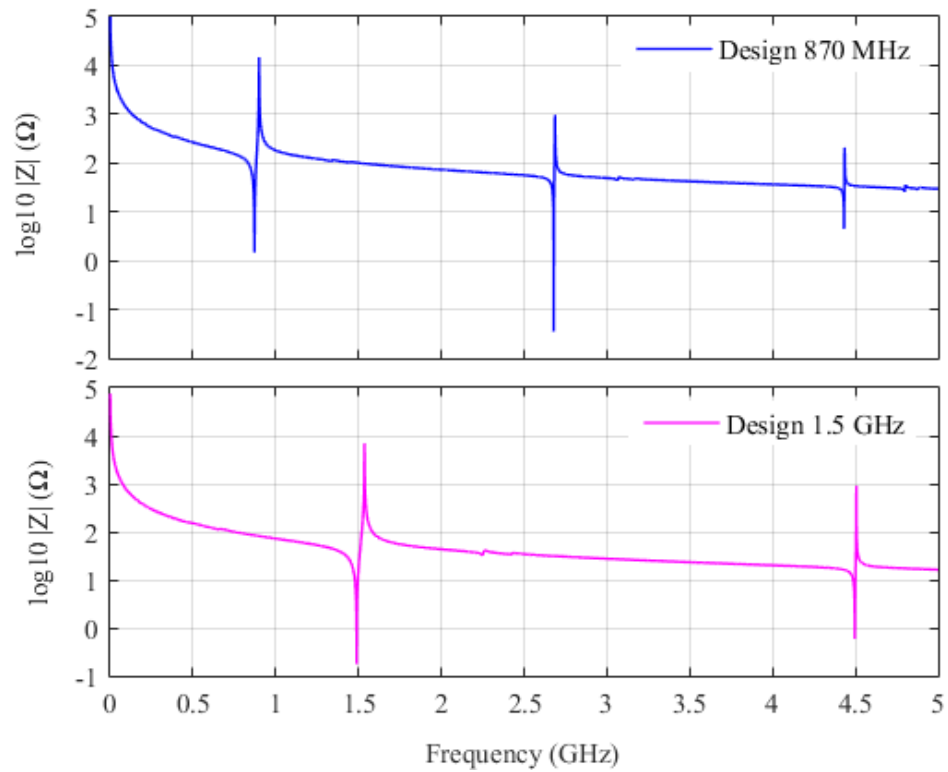
Figure 3.10 Simulated frequency response of the Mo/SiO$_2$ based SMRs with designed frequencies at 870 MHz and 1.5 GHz and aluminium electrodes for the longitudinal mode obtained using the 1D model.
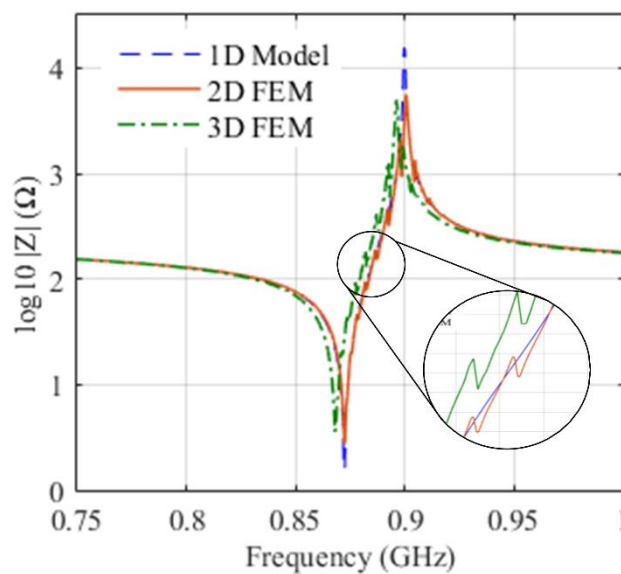
Figure 3.11 Comparison of the 1D analytical model and the 2D and 3D FEM models of the frequency response of the SMR design at 870 MHz with Al electrodes.

A good agreement was observed between all three models in terms of impedance values and resonant frequencies. However, the spurious modes were only apparent in the FEM simulations. These spurious modes originate from the lateral plate waves in the device. Suppression of these modes could be accomplished by appropriate design of the border region of the structure [82].

When comparing the simulations results obtained from the 2D and 3D models, no significant differences were observed. The spurious modes were predicted by both models and the resonant frequencies were very close at 869 MHz and 872 MHz with the 2D and 3D model, respectively. As the 3D model requires considerably longer computation times (by a factor of 20 times), frequency response simulations presented hereafter were obtained using only the 1D and 2D models, unless otherwise stated.

The impedance curves for all four SMR designs are shown in Figure 3.12. In the case of the 870 MHz design, devices with Au/Cr electrodes demonstrated a lower resonant frequency (-1%), while in the 1.5 GHz design a +0.5% variation was observed. These variations are minimal and within the range of the designed frequencies at ~870 MHz and ~1.5 GHz. Again, good correlation between the 1D and 2D models was observed. Spurious modes were present in both waveforms but less apparent on the 1.5 GHz design, which are enlarged in the inset.

From the simulated impedance curves, the series and parallel resonance frequencies were extracted. The quality factors were calculated using the phase derivative method of equation (2.9) and the effective coupling coefficients were evaluated from equation (2.13). These values are summarised in Table 3.5 for all four SMR designs.

The effective electromechanical coupling factor is greater for the SMR devices using Au/Cr electrodes (100nm/10nm) while the quality factors are slightly higher for the devices with Al electrodes (200 nm). This can be attributed to the high acoustic impedance of gold (effects of Cr are negligible due to high acoustic impedance) and the low density and good conductivity of Al, respectively. Quality factors at the series resonance demonstrated higher values than at the parallel resonant frequency as a result of laterally propagating waves [81].

(a)

(b)
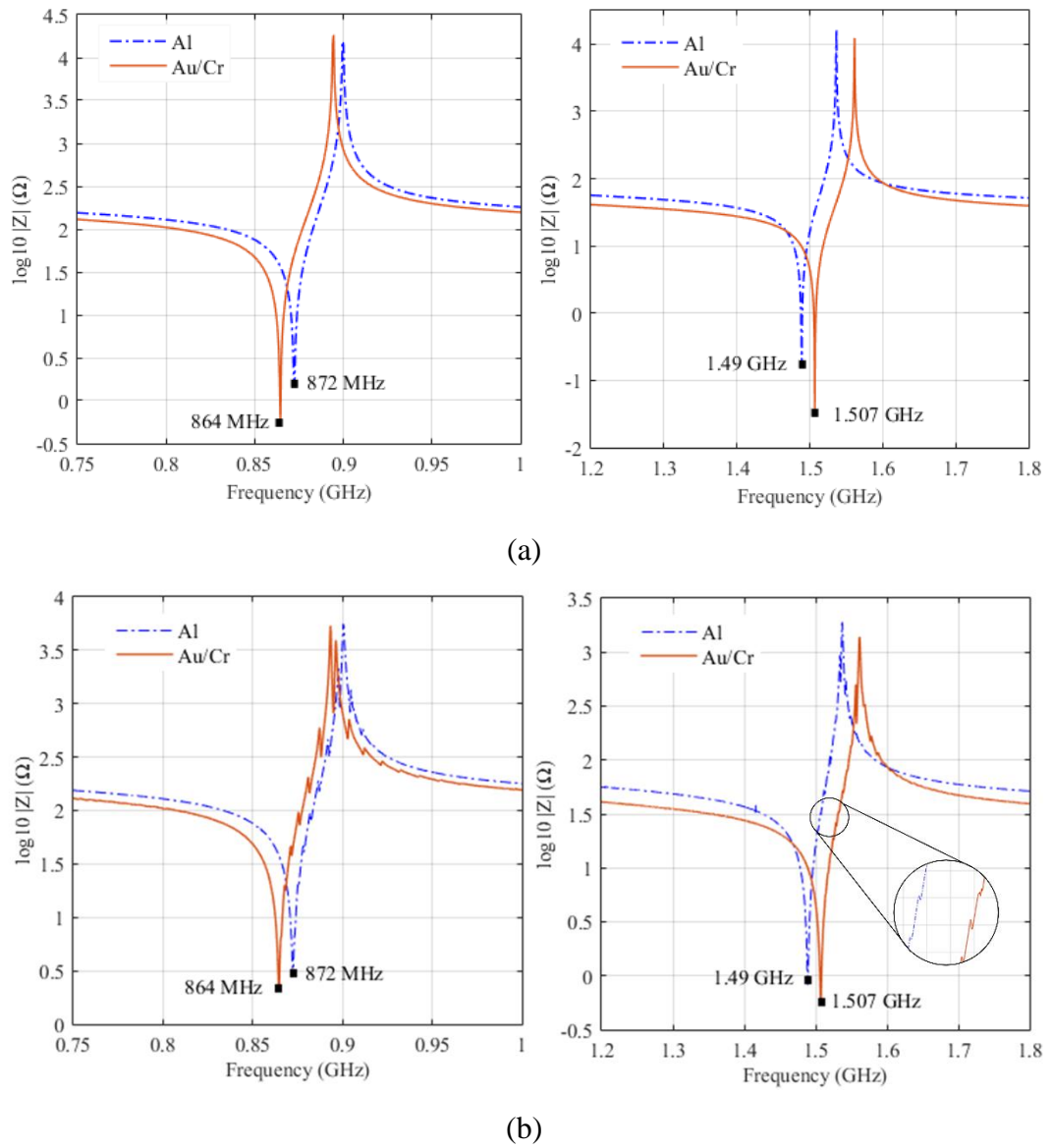
Figure 3.12 Simulated electrical behaviour of the designed SMRs obtained using (a) the 1D and (b) 2D FEM model.

Table 3.5 Calculated k_{eff}^2 and Q factor for series and parallel frequencies obtained from the 2D FEM simulation data.

	SMR DESIGN	f_s	f_p	Q_s	Q_p	k_{eff}^2
870 MHz	Al Electrodes	872.4 MHz	900.5 MHz	639	467	6.14 %
	Au/Cr Electrodes	864.6 MHz	893.3 MHz	632	453	6.32 %
1.5 GHz	Al Electrodes	1.49 GHz	1.53 GHz	622	524	6.18 %
	Au/Cr Electrodes	1.5 GHz	1.56 GHz	627	434	6.86 %

3.3.4   TEMPERATURE EFFECTS

Temperature stability is a very important factor to consider when using acoustic wave devices in sensing applications. For the application of this work, changes in the environmental temperature is likely to be very significant. If the air quality monitor is located outside, the ambient temperature would have diurnal and seasonal variations (-10°C to -50°C). These temperature variations have a significant effect on the resonant frequency of the SMR, which can be larger than the frequency shift caused by the physical parameter under investigation. In order to ensure accurate sensor output measurements, thermal variations should be monitored and the temperature effects taken into account in the final sensor readings.

Temperature dependence of the resonant frequency in BAW devices can be measured in terms of the temperature coefficient of frequency defined as [83]:

$$\text{TCF} = \frac{1}{f_o} \cdot \frac{\Delta f}{\Delta T} \times 10^6 \ \ (\text{ppm/°C}) \tag{3.17}$$

where f_o is the fundamental resonant frequency and Δf is the change in frequency due to the temperature change ΔT. Piezoelectric thin films used in BAW resonators have negative and relatively high TCFs (see Table 3.1, p.98). For sensing applications, it is desirable that the total TCF of the BAW device is low, to reduce frequency variations due to temperature. The total TCF of an SMR can strongly depend on the two uppermost layers of the acoustic reflector [57].

Simulations were performed in COMSOL Multiphysics® to investigate the TCF of the designed devices. In order to account for temperature variations in the FEM model, temperature-dependant material properties were added, namely the thermal expansion coefficients and the thermal coefficients of the elastic constants [84, 85]. A frequency response analysis was again performed with a parametric sweep of temperature from 25°C to 155°C in steps of 10°C. The computed frequency shifts of the series and parallel resonant frequencies as a function of the temperature are shown in Figure 3.13 for the fundamental longitudinal mode.

With rising temperature, the acoustic velocity of the longitudinal waves drops due to the decrease in the elastic constants of ZnO. This together with the effect of thermal expansion leads to a decrease in the resonant frequency of the device. A negative linear variation of both the series and parallel resonant frequencies was observed.

From the obtained results, the TCFs of the designed devices were extracted using equation (3.17). The TCF of the series resonance for the 870 MHz design with Al electrodes was calculated as -33.2 ppm/°C, while the SMR with Au/Cr electrodes exhibited a TCF of -34.7 ppm/°C. For the 1.5 GHz design, TCFs of -31.9 ppm/°C and -37.1 ppm/°C were obtained for the devices with Al and Au/Cr electrodes, respectively. A summary of the computed TCFs is given in Table 3.6.
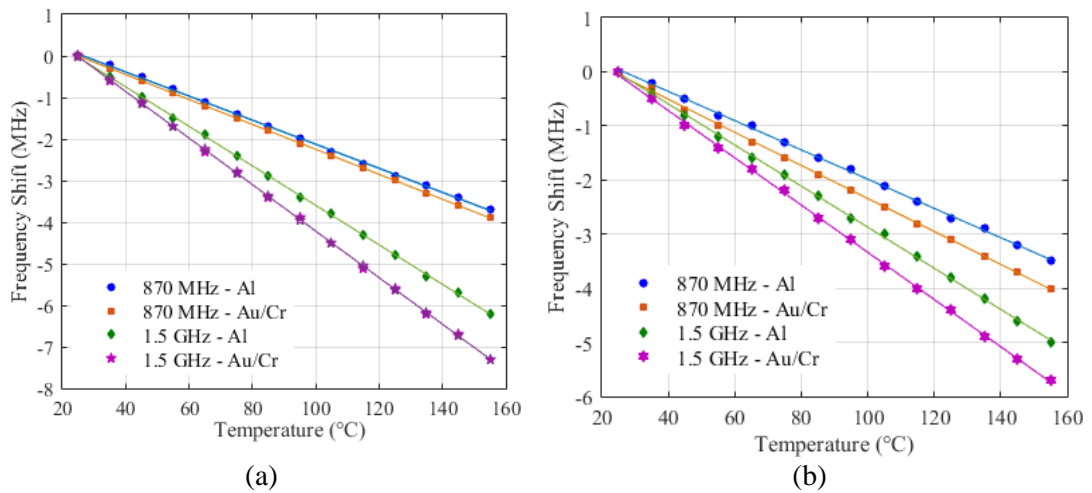
Figure 3.13 Simulated resonant frequency shifts as a function of temperature of the designed SMRs for (a) the series resonant frequency and (b) the parallel resonant frequency. Linear fits are also shown.

The series resonant frequency simulations demonstrated the 1.5 GHz devices exhibit a notably higher TCF (+15%) compared to the 870 MHz resonators. For the parallel resonance, the frequency shifts are similar for both the 870 MHz and 1.5 GHz devices. The highest frequency shifts are found for the series resonant frequency of the 1.5 GHz devices with Au/Cr.

In a report by Pinkett and Hunt [86], the TCF was noted of 6 fabricated devices when the temperature was varied from -50 to 175°C. The series TCF was found to increase for half the devices and decrease for the other half, demonstrating the variance

of the TCF due to temperature is reliant on material properties. Manufacturing tolerances and the minute variation in material properties have an effect.

Table 3.6 Simulated temperature coefficient of frequency for the series and parallel resonant frequencies of the designed SMR devices.

DESIGN	SMR DESIGN	TCF (f_s) (ppm/°C)	TCF (f_p) (ppm/°C)
870 MHz	Al Electrodes	-33.2	-30
	Au/Cr Electrodes	-34.7	-34.2
1.5 GHz	Al Electrodes	-31.9	-24.7
	Au/Cr Electrodes	-37.1	-27.9

3.4   LAYOUT DESIGN OF THE SMR DEVICES

The layout design of the SMRs consisted of six main patterns of the top and bottom electrodes as shown in Figure 3.14. Different dimensions were used for the active area giving a total of 25 different SMR designs. All layout designs had a square surface area of the top and bottom electrodes with dimensions varying from 125 µm to 250 µm in the case of design (a), and between 250 µm and 400 µm for designs (b) to (d). Designs (e) and (f) had both an active area of 390 µm. The footprint for all the designs was 1.5 mm × 1.5 mm.

Different dimensions of the active area were implemented. For particle detection, a larger surface area may be desirable in order to provide a sufficient region where the particles can be accumulated in relation to the particle size under analysis. Furthermore, the effect of the size of the sensing area on the performance of the device can also be evaluated.

For the electrical characterisation of the SMRs, a planar transmission line structure was incorporated, when possible. The top electrode was integrated within a short coplanar waveguide (CPW) for the connection to the measurement system. The use of CPWs reduces parasitic effects arising from bond wires and provides a ground-signal-ground (GSG) configuration for a convenient method of making contact with the device, enabling on-wafer measurements [10].
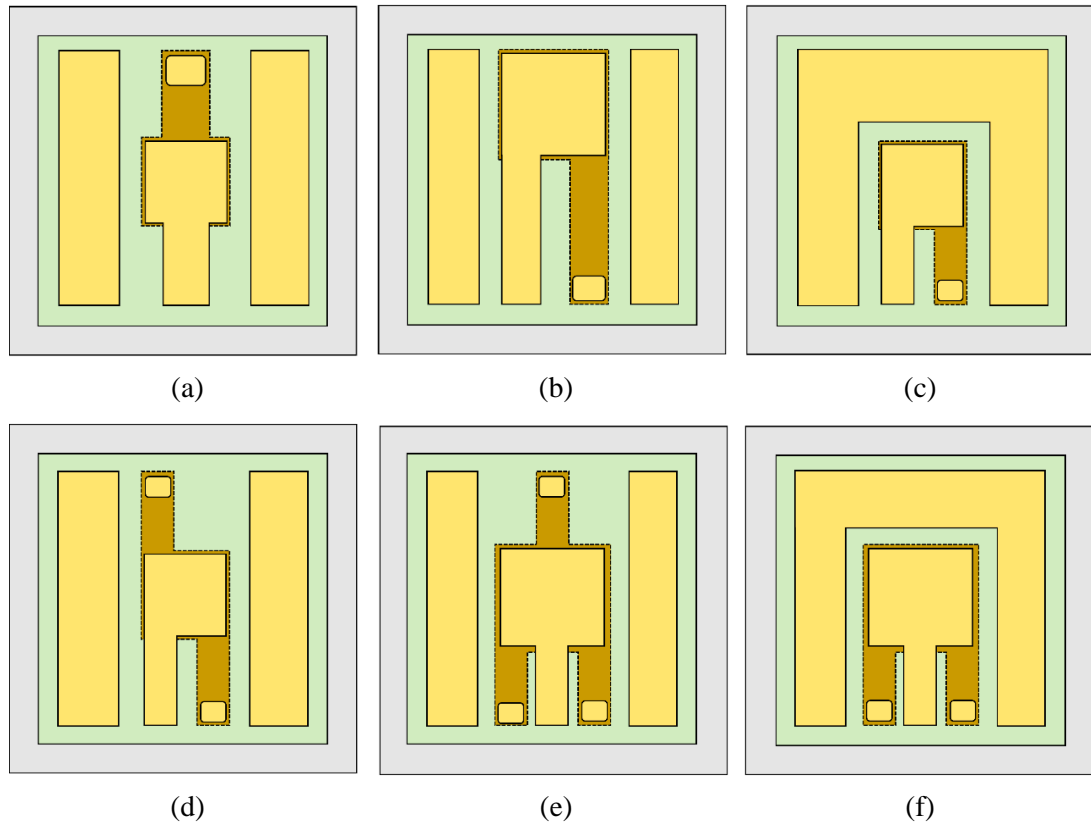
Figure 3.14 Basic SMR design layouts of top and bottom electrodes with incorporated transmission lines.

The coplanar waveguide (CPW) was designed for a characteristic impedance of approximately 50 Ω to match the impedance of the measurement equipment, cables and connectors. The characteristic impedance of the CPW is determined by its dimensions and the properties of the substrate. Careful design of the CPW is needed to obtain the desired characteristic impedance. To avoid diminishing the performance of the resonators, extension tracks from the top and bottom electrodes (and transmission lines) are kept as short as possible (~200 µm). Long extension tracks can add considerable parasitic capacitance that results in a decrease of the electromechanical coupling coefficient and the quality factor of the device [17], especially when using metal layers underneath (for the acoustic mirror). Using such short extensions was feasible as extending the pad contacts away from the sensing area is not essential for the intended applications in this work.

A FEM model can aid the design of the CPW. This would be helpful as the capacitance created between the metal layer of the acoustic reflector needs to be

considered. Such capacitance could be avoided or minimised by using all insulating acoustic reflectors [39]. In this work, however, metal/insulating reflectors are preferred as a first approach towards the construction of a CMOS acoustic mirror, where the metal layers and insulating layers (SiO_2) of a CMOS process must be used.

The CPW was designed using the expressions derived from conformal mapping techniques [87], for a characteristic impedance of 50 Ω. Even though the CPW lies on the piezoelectric layer, the dimensions of the CPW in this work were calculated for a high resistivity silicon substrate, considering that the thickness of the ZnO layer is negligible compared to the Si substrate, it has a very similar dielectric constant (ε_r=10.2 compared to ε_r=11.2) and the lines are very short.

Opening vias through the piezoelectric layer were included in all the layouts to provide access to the bottom electrode. Designs were labelled in the form 'MBLxxx' where MBL stands for Microsensors and Bioelectronics Laboratory and xxx is a three-digit number assigned to the device. The development of photolithography masks, required for the fabrication of these devices, is presented in the following chapter. As designed, these devices will be fabricated using both Al and Au/Cr electrodes. A summary of the designs is presented in Table 3.7.

Table 3.7 Summary of SMR design layouts specifying active area dimensions.

ID LABEL	BASIC DESIGN LAYOUT	ACTIVE AREA DIMENSION (µm)
MBL000	(a)	125
MBL002	(a)	150
MBL003	(a)	200
MBL004	(a)	250
MBL005	(a)*	125
MBL006	(a)*	150
MBL007	(a)*	200
MBL008	(a)*	250
MBL009	(b)	250
MBL020	(b)	400
MBL022	(b)*	250
MBL023	(b)*	400
MBL024	(c)	250

ID LABEL	BASIC DESIGN LAYOUT	ACTIVE AREA DIMENSION (µm)
MBL025	(c)	400
MBL026	(c)	250
MBL027	(c)	400
MBL028	(c)*	250
MBL029	(c)*	400
MBL030	(d)	250
MBL032	(d)	400
MBL033	(d)	250
MBL034	(d)	400
MBL035	(e)	390
MBL036	(f)	390
MBL037	(a)	175

*Extensions were added to enlarge terminations of the ground planes and electrode extensions to ease bonding of the devices.

3.5 CONCLUSIONS

This chapter detailed the design procedure for SMR devices, to be used in air quality monitoring applications (i.e. particle sensing and VOC detection). To aid the design of these resonators, considerations regarding material properties (piezoelectric films, electrodes, acoustic mirror) were presented and the modelling techniques for BAW devices were reviewed.

A 1D Mason equivalent model for the SMR was implemented in a Matlab script. This model aided the design of the device (frequency response) and the acoustic mirror (transmittance simulations). Finite element models were developed to analyse the temperature dependency of frequency of the devices. A comparison of the simulation results using these modelling techniques was presented.

Frequency simulations are in good agreement across the models (impedance curves and resonant frequencies). However, lateral spurious modes could only be predicted with the FEM models, as they consider the finite dimensions of the device. Computation times for the 1D analytical model were 12 times faster, compared to the 2D FEM model. Thus, the Mason model was mainly used through this work for frequency response simulations.

SMR devices were designed for two different resonant frequencies (870 MHz and 1.5 GHz) to work in the longitudinal mode, for gravimetric sensing. These frequencies were selected based on the required thickness of the piezoelectric layer. These devices are a first generation of SMRs, designed for their manufacture by standard microfabrication techniques, but considerations were taken at this stage towards their implementation of CMOS based devices at a later stage.

The structure of the acoustic mirror was formed by metal and insulating layers (this configuration must be used in a CMOS based device). The final design of the acoustic mirror was formed by three pairs of alternating Mo/SiO_2 layers, obtaining a reflectivity of 99.99%. For the electrode materials, Al and Au/Cr electrodes were chosen. Al provides good conductivity and low density; whereas Au/Cr exhibits a high acoustic impedance (Cr was used as an adhesion layer). For the piezoelectric layer, ZnO was used to obtain high-quality, low stress films, for the required thicknesses.

Performance characteristics of the SMR designs were extracted from the 2D FEM model, with simulated Q factors of ~640 and electromechanical coupling coefficients of ~6.2%. Temperature stability of the devices was evaluated, with TCFs values of about -34 ppm/°C. However, manufacturing tolerances and variations in the properties of the deposited materials are likely to create discrepancies between the simulated and experimental data.

The layout design of the devices included coplanar wave guides, designed for a characteristic impedance of 50 Ω. These CPWs enable characterisation of the device, using standard GSG configuration probes. Six main layout designs of the top and bottom electrodes were realised with dimensions of the active area (overlap between bottom and top electrode) ranging from 125 µm to 400 µm. The overall area of SMR design was 2.25 mm^2.

In the next chapter, the fabrication and characterisation of the devices designed in this chapter are presented. The effects of temperature and humidity variation on the resonant frequency of the SMRs are experimentally tested.

3.6 REFERENCES

[1]   Bi, F. Z. and Barber, B. P. (2008). "Bulk acoustic wave RF technology", *IEEE Microwave Magazine*. **9**(5): 65-80.

[2]   Damiani, L. R. and Mansano, R. D. (2012). "Zinc oxide thin films deposited by magnetron sputtering with various oxygen/argon concentrations", *Journal of Physics: Conference Series*. **370**(1): 012019.

[3]   Mishin, S., Marx, D. R., Sylvia, B., Lughi, V., Turner, K. L. and Clarke, D. R. (2003). "Sputtered AlN thin films on Si and electrodes for MEMS resonators: relationship between surface quality microstructure and film properties", *Ultrasonics, 2003 IEEE Symposium on*. pp. 2028-2032 Vol.2.

[4]   Alrashdan, M. H. S., Hamzah, A. A., Majlis, B. Y. and Aziz, M. F. (2014). "Aluminum nitride thin film deposition using DC sputtering", *2014 IEEE*

International Conference on Semiconductor Electronics (ICSE2014). pp. 72-75.

[5]   Muralt, P. (2000). "PZT thin films for microsensors and actuators: Where do we stand?", *IEEE Transactions on Ultrasonics, Ferroelectrics, and Frequency Control.* **47**(4): 903-915.

[6]   Dubois, M.-A. and Muralt, P. (1999). "Properties of aluminum nitride thin films for piezoelectric transducers and microwave filter applications", *Applied Physics Letters.* **74**(20): 3032-3034.

[7]   Lakin, K. M. (1999). "Thin film resonators and filters", *1999 IEEE Ultrasonics Symposium. Proceedings. International Symposium (Cat. No.99CH37027).* pp. 895-906 vol.2.

[8]   Crisler, D. F., Cupal, J. J. and Moore, A. R. (1968). "Dielectric, piezoelectric, and electromechanical coupling constants of zinc oxide crystals", *Proceedings of the IEEE.* **56**(2): 225-226.

[9]   Lobl, H. P., Klee, M., Wunnicke, O., Kiewitt, R., Dekker, R. and Pelt, E. V. (1999). "Piezo-electric AlN and PZT films for micro-electronic applications", *1999 IEEE Ultrasonics Symposium. Proceedings. International Symposium (Cat. No.99CH37027).* pp. 1031-1036 vol.2.

[10]   Su, Q. X., Kirby, P., Komuro, E., Imura, M., Qi, Z. and Whatmore, R. (2001). "Thin-film bulk acoustic resonators and filters using ZnO and lead-zirconium-titanate thin films", *Microwave Theory and Techniques, IEEE Transactions on.* **49**(4): 769-778.

[11]   Suzuki, Y., Fujiwara, T. and Sato, K., *Surface acoustic wave device.* 1997, Untied States Patent.

[12]   Larson, J. D., Gilbert, S. R. and Baomin, X. (2004). "PZT material properties at UHF and microwave frequencies derived from FBAR measurements", *IEEE Ultrasonics Symposium, 2004.* pp. 173-177 Vol.1.

[13]   Campanella, H. (2010). "Acoustic wave and electromechanical resonators: concept to key applications". Norwood, MA: Artech House.

[14]   Gardner, J. W., Varadan, V.K., and Awadelkarim, O.O. (2001). "Microsensors, MEMS, and smart devices", John Wiley & Sons Ltd.

[15]   Drafts, B. (2001). "Acoustic wave technology sensors", *IEEE Transactions on Microwave Theory and Techniques*. **49**(4): 795-802.

[16]   Löbl, H. P., Klee, M., Milsom, R., Dekker, R., Metzmacher, C., Brand, W. and Lok, P. (2001). "Materials for bulk acoustic wave (BAW) resonators and filters", *Journal of the European Ceramic Society*. **21**(15): 2633-2640.

[17]   Hashimoto, K.-Y. and Wrobel, S. M. (2009). "RF bulk acoustic wave filters for communications". Norwood, US: Artech House Books.

[18]   Ruby, R. (2004). "FBAR - from technology development to production ", *2nd International Symposium on Acoustic Wave Devices fro Future Mobile Communication Systems*. pp. 135-139.

[19]   Aigner, R. (2004). "Volume manufacturing of BAW-filters in CMOS fab", *2nd International Symposium on Acoustic Wave Devices for Future Mobile Communication Systems*. pp. 129-134.

[20]   Ruby, R. (2007). "11E-2 Review and comparison of bulk acoustic wave FBAR, SMR technology", *2007 IEEE Ultrasonics Symposium Proceedings*. pp. 1029-1040.

[21]   Lee, S.-H., Yoon, K. H. and Lee, J.-K. (2002). "Influence of electrode configurations on the quality factor and piezoelectric coupling constant of solidly mounted bulk acoustic wave resonators", *Journal of Applied Physics*. **92**(7): 4062-4069.

[22]   Yoshino, Y. (2009). "Piezoelectric thin films and their applications for electronics", *Journal of Applied Physics*. **105**(6): 061623.

[23]   Loebl, H. P., Klee, M., Metzmacher, C., Brand, W., Milsom, R. and Lok, P. (2003). "Piezoelectric thin AlN films for bulk acoustic wave (BAW) resonators", *Materials Chemistry and Physics*. **79**(2–3): 143-146.

[24]   García-Gancedo, L., Pedrós, J., Zhu, Z., Flewitt, A. J., Milne, W. I., Luo, J. K. and Ford, C. J. B. (2012). "Room-temperature remote-plasma sputtering of c-axis oriented zinc oxide thin films", *Journal of Applied Physics*. **112**(1): 014907.

[25]   Clement, M., Olivares, J., Iborra, E., González-Castilla, S., Rimmer, N. and Rastogi, A. (2009). "AlN films sputtered on iridium electrodes for bulk acoustic wave resonators", *Thin Solid Films*. **517**(16): 4673-4678.

[26]   Newell, W. E. (1965). "Face-mounted piezoelectric resonators", *Proceedings of the IEEE*. **53**(6): 575-581.

[27]   Kim, S.-H., Kim, J.-H., Park, H.-D. and Yoon, G. (2001). "AlN-based film bulk acoustic resonator devices with W/SiO2 multilayers reflector for rf bandpass filter application", *Journal of Vacuum Science & Technology B*. **19**(4): 1164-1168.

[28]   Norling, M., Enlund, J., Gevorgian, S. and Katardjiev, I. (2006). "A 2 GHz oscillator based on a solidly mounted thin film bulk acoustic wave resonator", *International Microwave Symposium Digest*. pp. 1813-1816.

[29]   García-Gancedo, L., Pedrós, J., Iborra, E., Clement, M., Zhao, X. B., Olivares, J., Capilla, J., Luo, J. K., Lu, J. R., Milne, W. I. and Flewitt, A. J. (2013). "Direct comparison of the gravimetric responsivities of ZnO-based FBARs and SMRs", *Sensors and Actuators B: Chemical*. **183**(0): 136-143.

[30]   Yan, Z., Zhou, X. Y., Pang, G. K. H., Zhang, T., Liu, W. L., Cheng, J. G., Song, Z. T., Feng, S. L., Lai, L. H., Chen, J. Z. and Wang, Y. (2007). "ZnO-based film bulk acoustic resonator for high sensitivity biosensor applications", *Applied Physics Letters*. **90**(14).

[31] Kanbara, H., Kobayashi, H. and Nakamura, K. (2000). "Analysis of Piezoelectric Thin Film Resonators with Acoustic Quarter-Wave Multilayers", *Japanese Journal of Applied Physics*. **39**(5B): 3049-3053.

[32] Lakin, K. M., McCarron, K. T. and McDonald, J. F. (2000). "Temperature compensated bulk acoustic thin film resonators", *2000 IEEE Ultrasonics Symposium. Proceedings. An International Symposium (Cat. No.00CH37121).* pp. 855-858 vol.1.

[33] Dubois, M. A., Muralt, P., Matsumoto, H. and Plessky, V. (1998). "Solidly mounted resonator based on aluminum nitride thin film", *IEEE Ultrasonics Symposium*. pp. 909-912.

[34] Lanz, R. and Muralt, P. (2005). "Bandpass filters for 8 GHz using solidly mounted bulk acoustic wave resonators", *IEEE Transactions on Ultrasonics, Ferroelectrics and Frequency Control*. **52**(6): 938-948.

[35] Wei, C. L., Chen, Y. C., Cheng, C. C. and Kuo-Sheng, K. (2008). "Solidly mounted resonators consisting of a molybdenum and titanium Bragg reflector", *Applied Physics A*. **90**(3): 501-506.

[36] Cannatà, D., Benetti, M., Di Pietrantonio, F., Verona, E., Palla-Papavlu, A., Dinca, V., Dinescu, M. and Lippert, T. (2012). "Nerve agent simulant detection by solidly mounted resonators (SMRs) polymer coated using laser induced forward transfer (LIFT) technique", *Sensors and Actuators B: Chemical*. **173**: 32-39.

[37] Enlund, J., Martin, D., Yantchev, V. and Katardjiev, I. (2008). "Solidly mounted thin film electro-acoustic resonator utilizing a conductive Bragg reflector", *Sensors and Actuators A: Physical*. **141**(2): 598-602.

[38] Capilla, J., Olivares, J., Clement, M., Sangrador, J., Iborra, E., Felmetsger, V. and Devos, A. (2011). "Ta2O5/SiO2 insulating acoustic mirrors for AlN-based X-band BAW resonators", *2011 IEEE International Ultrasonics Symposium (IUS)*. pp. 1704-1707.

[39] DeMiguel-Ramos, M., Mirea, T., Olivares, J., Clement, M., Sangrador, J., Iborra, E. and Barba, M. (2014). "Influence of the electrical extensions in AlN-BAW resonators for in-liquid biosensors", *2014 European Frequency and Time Forum (EFTF)*. pp. 301-304.

[40] Lakin, K. M. B., J.; McDonald, J. F.; McCarron, K.T. (2001). "Improved bulk wave resonator coupling coefficient for wide bandwidth filters", *IEEE Ultrasonics Symposium*. pp. 827-831

[41] Perez-Sanchez, G. F. and Morales-Acevedo, A. (2009). "Design of bulk acoustic wave resonators based on ZnO for filter applications", *6th International Conference on Electrical Engineering, Computing Science and Automatic Control*. pp. 1-6.

[42] Enjamuri, S., Amsanpally, A. and Raju, K. C. J. (2012). "Optimization and analysis of piezoelectric and electrode materials' thickness effects on the performance of film bulk acoustic resonator", *1st International Symposium on Physics and Technology of Sensors (ISPTS)*. pp. 185-188.

[43] Jiles, D. C. (2007). "Introduction to the Principles of Materials Evaluation". Boca Raton , FL: CRC Press Taylor and Francis Group.

[44] Nam, K., Park, Y., Ha, B., Shim, D. and Song, I. (2005). "Piezoelectric Properties of Aluminum Nitride for Thin Film Bulk Acoustic Wave Resonator", *Journal of the Korean Physical Society*. **47**: S309-S312.

[45] Ruby, R. C., Bradley, P., Oshmyansky, Y., Chien, A. and Larson, J. D. (2001). "Thin film bulk wave acoustic resonators (FBAR) for wireless applications", *2001 IEEE Ultrasonics Symposium. Proceedings. An International Symposium (Cat. No.01CH37263)*. pp. 813-821 vol.1.

[46] García-Gancedo, L., Iborra, E., Clement, M., Olivares, J., Zhu, Z., Flewitt, A. J., Milne, W. I., Ashley, G. M., Luo, J. K., Zhao, X. B. and Lu, J. R. (2011). "Solidly mounted resonators with carbon nanotube electrodes for biosensing applications", *2011 Joint Conference of the IEEE International Frequency*

Control and the European Frequency and Time Forum (FCS) Proceedings. pp. 1-5.

[47]   Yokoyama, T., Nishihara, T., Taniguchi, S., Iwaki, M., Satoh, Y., Ueda, M. and Miyashita, T. (2004). "New electrode material for low-loss and high-Q FBAR filters", *IEEE Ultrasonics Symposium, 2004*. pp. 429-432 Vol.1.

[48]   Lee, J.-B., Jung, J.-P., Lee, M.-H. and Park, J.-S. (2004). "Effects of bottom electrodes on the orientation of AlN films and the frequency responses of resonators in AlN-based FBARs", *Thin Solid Films*. **447–448**: 610-614.

[49]   Iborra, E., Clement, M., Olivares, J., Sangrador, J., Rimmer, N. and Rastogi, A. (2007). "7E-6 Aluminum Nitride Bulk Acoustic Wave Devices with Iridium Bottom Electrodes", *2007 IEEE Ultrasonics Symposium Proceedings*. pp. 616-619.

[50]   Salgar, S., Guntae, K., Dae-Hyun, H. and Kim, B. (2002). "Modeling and simulation of the thin film bulk acoustic resonator", *Frequency Control Symposium and PDA Exhibition, 2002. IEEE International*. pp. 40-44.

[51]   Mai, L., Do, N. H., Hoang, T. A., Tran, V. S., Pham, L. P. B., Thi, T. T. N. and Le, H. N. (2009). "Thermal techniques to improve ZnO-based FBAR devices characteristics", *2009 International Conference on Advanced Technologies for Communications*. pp. 183-186.

[52]   Rosen, D., Bjurstrom, J. and Katardjiev, I. (2005). "Suppression of spurious lateral modes in thickness-excited FBAR resonators", *IEEE Transactions on Ultrasonics, Ferroelectrics, and Frequency Control*. **52**(7): 1189-1192.

[53]   Ruby, R., Larson, J., Feng, C. and Fazzio, S. (2005). "The effect of perimeter geometry on FBAR resonator electrical performance", *IEEE MTT-S International Microwave Symposium Digest, 2005*. pp. 4.

[54]   Vanhelmont, F., Philippe, P., Jansman, A. B. M., Milsom, R. F., Ruigrok, J. J. M. and Oruk, A. (2006). "A 2 GHz reference oscillator incorporating a

temperature compensated BAW resonator", *IEEE Ultrasonics Symposium*. pp. 333-336.

[55]   Allah, M. A., Kaitila, J., Thalhammer, R., Weber, W. and Schmitt-Landsiedel, D. (2009). "Temperature compensated solidly mounted resonators with thin SiO2 layers", *IEEE International Ultrasonics Symposium (IUS)*. pp. 859-862.

[56]   Allah, M. A., Kaitila, J., Thalhammer, R., Weber, W. and Schmitt-Landsiedel, D. (2009). "Temperature compensated solidly mounted bulk acoustic wave resonators with optimum piezoelectric coupling coefficient", *IEEE International Electron Devices Meeting (IEDM),*. pp. 1-4.

[57]   DeMiguel-Ramos, M., Olivares, J., Mirea, T., Clement, M., Iborra, E., Rughoobur, G., Garcia-Gancedo, L., Flewitt, A. J. and Milne, W. I. (2014). "The influence of acoustic reflectors on the temperature coefficient of frequency of solidly mounted resonators", *2014 IEEE International Ultrasonics Symposium*. pp. 1472-1475.

[58]   Jeutter, D., Josse, F., Johnson, M., Wenzel, M., Hossenlopp, J. and Cernosek, R. (2005). "Design of a portable guided SH-SAW chemical sensor system for liquid environments", *Proceedings of the 2005 IEEE International Frequency Control Symposium and Exposition,*. pp. 59-68.

[59]   Mason, M. P. (1948). "Electromechanical Transducers and Wave Filters". Second Edition ed. Princeton,New Jersey: D. Van Nostrand Company, Inc.

[60]   Po-Hsun, S., Chi-Ming, F., Pei-Zen, C., Yung-Chung, C. and Pei-Yen, C. (2004). "The method for integrating FBAR with circuitry on CMOS chip", *IEEE International Frequency Control Symposium and Exposition, *. pp. 562-565.

[61]   Nakamura, K. and Kanbara, H. (1998). "Theoretical analysis of a piezoelectric thin film resonator with acoustic quarter-wave multilayers", *IEEE International Frequency Control Symposium*. pp. 876-881.

[62]   Lakin, K. M., Kline, G. R. and McCarron, K. T. (1993). "High-Q microwave acoustic resonators and filters", *IEEE Transactions on Microwave Theory and Techniques*. **41**(12): 2139-2146.

[63]   Sittig, E. K. (1969). "Effects of Bonding and Electrode Layers on the Transmission Parameters of Piezoelectric Transducers Used in Ultrasonic Digital Delay Lines", *IEEE Transactions on Sonics and Ultrasonics*. **16**(1): 2-9.

[64]   Marksteiner, S., Kaitila, J., Fattinger, G. G. and Aigner, R. (2005). "Optimization of acoustic mirrors for solidly mounted BAW resonators", *IEEE Ultrasonics Symposium*. pp. 329-332.

[65]   Jose, S. (2011). "Reflector Stack Optimization for Bulk Acoustic Wave Resonators", PhD Thesis. Univeristy of Twente, Enschede, The Netherlands.

[66]   *COMSOL Multiphysics® v.4.4.* COMSOL AB, Stockholm, Sweden.

[67]   COMSOL 2013. "Acoustics Module User's Guide ".

[68]   Butterworth, S. (1914). "On Electrically-maintained Vibrations", *Proceedings of the Physical Society of London*. **27**(1): 410.

[69]   Butterworth, S. (1913). "On a Null Method of Testing Vibration Galvanometers", *Proceedings of the Physical Society of London*. **26**(1): 264.

[70]   Dyke, K. S. V. (1928). "The Piezo-Electric Resonator and Its Equivalent Network", *Proceedings of the Institute of Radio Engineers*. **16**(6): 742-764.

[71]   Larson, J. D., III, Bradley, R. C., Wartenberg, S. and Ruby, R. C. (2000). "Modified Butterworth-Van Dyke circuit for FBAR resonators and automated measurement system", *IEEE Ultrasonics Symposium*. pp. 863-868

[72]   Chatras, M., Bila, S., Giraud, S., Catherinot, L., Fan, J., Cros, D., Aubourg, M., Flament, A., Frapp, A., Stefanelli, B., Kaiser, A., Cathelin, A., Baptiste, J., Reinhardt, A., Leyssenne, L*., et al.* (2013). "Modeling and Design of BAW Resonators and Filters for Integration in a UMTS Transmitter".

[73]   Lakin, K. M. (1992). "Modeling of thin film resonators and filters", *1992 IEEE MTT-S Microwave Symposium Digest*. pp. 149-152 vol.1.

[74]   Thalhammer, R. K. and Larson, J. D. (2016). "Finite-Element Analysis of Bulk-Acoustic-Wave Devices: A Review of Model Setup and Applications", *IEEE Transactions on Ultrasonics, Ferroelectrics, and Frequency Control*. **63**(10): 1624-1635.

[75]   Johnston, M. L., Kymissis, I. and Shepard, K. L. (2010). "FBAR-CMOS oscillator array for mass-sensing applications", *IEEE Sensors Journal*. **10**(6): 1042-1047.

[76]   Lakin, K. M., McCarron, K. T., McDonald, J. F. and Belsick, J. (2001). "Temperature coefficient and ageing of BAW composite materials", *IEEE International Frequency Control Symposium and PDA Exhibition*. pp. 605-608.

[77]   Kaitila, J. (2007). "Review of Wave Propagation in BAW Thin Film Devices - Progress and Prospects", *2007 IEEE Ultrasonics Symposium*. New York, NYpp. 120-129.

[78]   Fattinger, G. G., Marksteiner, S., Kaitila, J. and Aigner, R. (2005). "Optimization of acoustic dispersion for high performance thin film BAW resonators", *IEEE Ultrasonics Symposium* pp. 1175-1178.

[79]   Jose, S., Hueting, R. J. E. and Jansman, A. B. M. (2010). "Acoustic dispersion of solidly mounted resonators with an optimized reflector stack for dual wave reflection", *IEEE Ultrasonics Symposium (IUS)*. pp. 291-294.

[80]   Jose, S., Jansman, A. B. M. and Hueting, R. J. E. (2009). "A design procedure for an acoustic mirror providing dual reflection of longitudinal and shear waves in Solidly Mounted BAW Resonators (SMRs)", *IEEE International Ultrasonics Symposium (IUS)*. pp. 2111-2114.

[81]   Thalhammer, R. and Aigner, R. (2005). "Energy loss mechanisms in SMR-type BAW devices", *IEEE MTT-S International Microwave Symposium Digest, 2005*. pp. 4.

[82]   Kaitila, J., Ylilammi, M., Ella, J. and Aigner, R. (2003). "Spurious resonance free bulk acoustic wave resonators", *2003 IEEE Symposium on Ultrasonics*. pp. 84-87.

[83]   He, X. L., Garcia-Gancedo, L., Jin, P.C., Zhou, J., Wang, W.B., Dong, S.R., Luo, J.K., Flewitt, A.J., and Milne, W.I. (2012). "Film bulk acoustic resonator pressure sensor with self temperature reference", *Journal of Micromechanics and Microengineering*. **22**(12).

[84]   Nakahata, H., Hachigo, A., Higaki, K., Fujii, S., Shikata, S. and Fujimori, N. (1995). "Theoretical study on SAW characteristics of layered structures including a diamond layer", *IEEE Transactions on Ultrasonics, Ferroelectrics, and Frequency Control*. **42**(3): 362-375.

[85]   Ohta, S., Nakamura, K., Doi, A. and Ishida, Y. (2003). "Temperature characteristics of solidly mounted piezoelectric thin film resonators", *2003 IEEE Symposium on Ultrasonics*. pp. 2011-2015.

[86]   Pinkett, S. L., Hunt, W. D., Barber, B. P. and Gammel, P. L. (2001). "Temperature characteristics of ZnO-based thin film bulk acoustic wave resonators", *2001 IEEE Ultrasonics Symposium. Proceedings. An International Symposium (Cat. No.01CH37263)*. pp. 823-826 vol.1.

[87]   Simons, R. N. (2001). "Coplanar Waveguide Circuits, Components, and Systems". New York: John Wiley & Sons, Inc.

CHAPTER 4

FABRICATION AND CHARACTERISATION OF SOLIDLY MOUNTED RESONATORS

4.1 INTRODUCTION

In this chapter, the fabrication process of the solidly mounted resonators designed in Chapter 3, is described. Standard microfabrication techniques were employed for the fabrication using a three-mask photolithography process. The mask design and process parameters are discussed.

Electrical characterisation of the devices is presented and their performance parameters are extracted (Q factor, k_{eff}^2). The manufacturing tolerances of the layer thicknesses are investigated. Frequency dependence on ambient effects (temperature and humidity) is also characterised and experimental results are compared to the simulation results presented in Chapter 3. The fabricated devices are the fundamental

elements for the development of an air quality sensor and the basis towards the development of a CMOS compatible acoustic device.

4.2   FABRICATION OF THE SOLIDLY MOUNTED RESONATORS[2]

Fabrication of the ZnO based SMRs was performed in collaboration with the University of Cambridge (UK). It took place at the Centre for Advanced Photonics and Electronics (CAPE), University of Cambridge.

Table 4.1 summarizes the material thicknesses for fabrication as designed in Chapter 3. Originally, a 6-mask photolithography process was proposed for the fabrication of these devices, for which a total of six masks were designed and manufactured. However, the actual fabrication was simplified to a 3-mask fabrication process. Thus, only the 3-mask process is presented in this chapter. The complete 6-mask fabrication process is discussed in Appendix C. It was designed to provide acoustic isolation to individual devices through the patterning of the reflector layers in order to avoid cross-talking between devices on the same substrate.

Table 4.1 Designed thicknesses of the thin films for the fabrication of the ZnO based SMR devices working at 870 MHz and 1.5 GHz.

SMR WITH ALUMINIUM ELECTRODES

MATERIAL	THICKNESS	
	870 MHz	1.5 GHz
SiO$_2$	1.65 μm	995 nm
Mo	1.82 μm	1.05 μm
Al	200 nm	200 nm
ZnO	3.35 μm	1.85 μm

SMR WITH GOLD ELECTRODES

MATERIAL	THICKNESS	
	870 MHz	1.5 GHz
SiO$_2$	1.65 μm	995 nm
Mo	1.82 μm	1.05 μm
Au/Cr	100/10 nm	100/10 nm
ZnO	2.85 μm	1.35 μm

4.2.1   DESIGN OF THE PHOTOMASKS

The lithographic photomasks were designed in Tanner EDA layout Editor (L- Edit v15.1). Finalised mask designs were submitted for manufacture as GDSII files. The

---

[2] The work presented in this section was performed in collaboration with Mr Girish Rughoobur, PhD student at the University of Cambridge.

photomasks were fabricated on a 5" by 5" mask plate (0.060" thick) in Soda Lime glass with chrome coating (JD Photo Tools, UK) at super high resolution (128k dpi or 5 dots/µm) and a critical dimension of 15 microns, offering an affordable solution yet good quality features are achieved (features as small as 5 µm). The specifications (polarity and view side) for each photomask and the type of photoresist used during lithography are given in Table 4.2.

Table 4.2 Specifications of the photomasks for the lithography process.

MASK ID	POLARITY	VIEW SIDE	TYPE OF RESIST	DESCRIPTION
BOT	Darkfield	Right read Chrome down	Positive	Patterning of bottom electrode
TOP	Darkfield	Right read Chrome down	Positive	Patterning of top electrode
PIE	Darkfield	Right read Chrome down	Negative	Patterning of piezoelectric thin film

Each mask was identified with a three-character abbreviation as shown above. The layout of the mask was designed for a patterning area of a 4-inch wafer and included a total of six alignment marks. All 25 different SMR layout designs were arranged in a 5×5 array with four devices of each design (as shown in Figure 4.1). This array acted as a "reticule" that was repeated across the patterning area of the mask. In this way, SMR designs were distributed across the wafer and could be tested from different locations within the wafer. It is likely that variations of the thickness and material properties will exist between locations of the dies, influencing the resonant frequency and electrical characteristic of the devices [1].

The device ID number, the electrode material, the piezoelectric material and the design date were patterned in the top mask layer. This helped to clearly identify the devices at a later stage (looking under the microscope). Dicing guide marks were incorporated in the TOP mask which were employed during mechanical sawing, and alignment marks were also included. Polarity of the masks was not critical as an image reversal resist was used (AZ5214E).
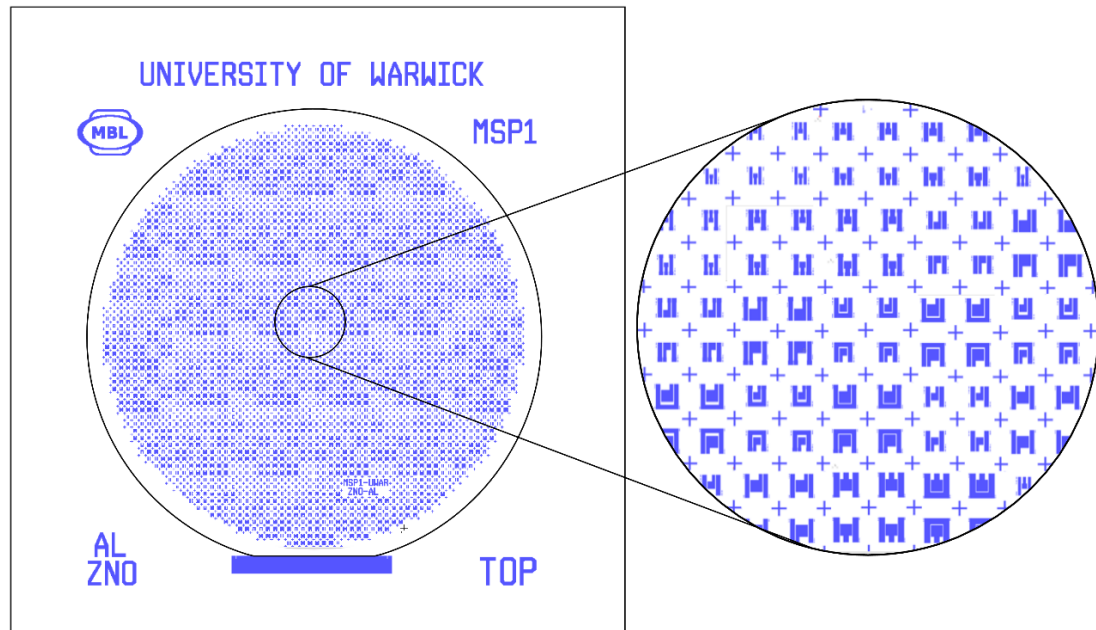
Figure 4.1 Layout design of the top mask showing distribution of the SMR designs within the patterning area.

4.2.2 THREE-MASK FABRICATION PROCESS

The 3-mask fabrication process (depicted in Figure 4.2) consisted on the following steps:

1. SUBSTRATE CLEANING. Double-side polished, 4- inch, 525 µm thick (+/- 25µm), p-type silicon wafers with crystallographic orientation (100) and 200 nm thermal oxide on both sides were purchased from Si-Mat (Germany). Cleaning of the substrate, to remove any contaminants, consisted on soaking the wafer in acetone, followed by isopropanol (IPA) and then flushing with deionized (DI) water. Finally, the wafer was dried in nitrogen and baked at 125 °C for 3 minutes.

2. DEPOSITION OF THE REFLECTOR LAYERS. A total of three layers of Mo and three layers of SiO_2 were alternately sputtered on the silicon substrate using a high target utilisation sputtering (HiTUS S500) system. As the system can accommodate several targets at a time, deposition of the reflector layers can be performed without breaking the vacuum in the system or removing the sample, resulting in better adhesion between the layers.

3. DEPOSITION AND PATTERNING OF BOTTOM ELECTRODE. The bottom electrode (200 nm Al or 100/10 nm Au/Cr) was deposited on top of the acoustic mirror layers and patterned using a standard lift-off photolithography process. The aluminium layer was deposited using sputtering while the chrome/gold layers were thermally evaporated.

4. DEPOSITION OF PIEZOELECTRIC LAYER. The ZnO layer was reactively sputtered at room temperature from a zinc target using an Ar/O_2 mixture in the HiTUS system [2]. This results in high quality ZnO films with excellent c-axis orientation, smooth surface and low stress [3] to obtain high quality resonators.

5. DEPOSITION AND PATTERNING OF TOP ELECTRODE. The top electrode is patterned in a second lift-off process in a similar way as the bottom electrode using the same materials, thicknesses and deposition methods.

6. PATTERNING OF PIEZOELECTRIC LAYER. In order to provide electrical contact to the bottom electrode, the ZnO film was patterned and via holes etched through it in a wet etching process using a 2% glacial acetic acid and phosphoric acid solution at room temperature with at etching rate of ~1.2 µm/min.

7. DEPOSITION OF PASSIVATION LAYER. To protect devices from environmental factors and scratching during the dicing process, a passivation layer (photoresist) was deposited over the entire wafer. This passivation needed to be completely removed before characterisation of the devices.

8. WAFER DICING. Processed wafers were diced using a mechanical saw. With this process, thinner and cleaner separation lines were achieved.

a) Wafer cleaning

b) Alternating sputtering of three Mo layers and three SiO$_2$ layers.

c) Photoresist coating and soft bake.

d) Exposure of photoresist using mask **BOT**, development and hard bake.

e) Evaporation of the bottom electrode material (Al or Au/Cr).

f) Bottom electrode lift-off.

g) Sputtering of ZnO piezoelectric layer.

h) Photoresist coating and soft bake.

i) Exposure of photoresist using mask **TOP,** development and hard bake.

j) Evaporation of the top electrode material (Al or Au/Cr).

k) Top electrode lift-off.

l) Photoresist coating and soft bake

m) Exposure of photoresist using mask **PIE**, development and hard bake.

n) Etching of piezoelectric ZnO and photoresist removal.

o) Wafer dicing using mechanical saw.

Figure 4.2 Three mask fabrication process used in the fabrication of the designed SMR devices.

Sputtering targets used in the HiTUS system are 4-inch in diameter and 6 mm thick. For the photolithography processes, an EVG620 Mask aligner was used. Lithography processes are accomplished using a thin photoresist (AZ5214E with ~1.6 µm thickness). The deposition parameters of the materials used in the fabrication of the SMRs are summarised in Table 4.3.

Table 4.3 Deposition and etching parameters of SMR materials.

PARAMETER	ZnO	Mo	SiO$_2$
DEPOSITION METHOD	RF reactive sputtering (HiTUS)	RF sputtering (HiTUS system)	RF reactive sputtering (HiTUS)
TARGET	Zn 99.999% (Kurt J. Lesker Ltd)	Mo 99.999% (Pi-Kem Ltd)	Si 99.999% (Testbourne Ltd)
BASE PRESSURE (mbar) $\times 10^6$	< 2	< 2	< 2
LAUNCH POWER (W)	1000	1500	1000
TARGET POWER (W)	800	1300	800
Ar FLOW RATE (sccm)	55	60	55
O$_2$ FLOW RATE (sccm)	41	0	8
DEPOSITION RATE (nm/min)	19	29	~23
ETCHING METHOD	Wet etching	-	-
ETCHANT	H$_3$PO$_4$ and glacial acetic solution at 2% volume	-	-
ETCHING RATE (nm/min)	~1200	-	-

*Aluminium electrodes were deposited using DC magnetron sputtering from an Al target with 99.99% purity. A base pressure of 1 x10^{-5} mbar is used. Ar flow rate is set to 31 sccm and a sputtering pressure of 3×10^{-3} mbar is used.

Two batches of SMR devices were produced in the period of July – December 2014 with a total of 12 wafers fabricated, each containing about 2500 individual SMRs and approximately 100 samples of each SMR design.

The first batch consisted of a total of 8 wafers: four wafers of the 1.5 GHz design (two wafers with Al electrodes and two with Au/Cr electrodes) and four wafers of the 870 MHz design (again, two with Al electrodes and two with Au/Cr electrodes).
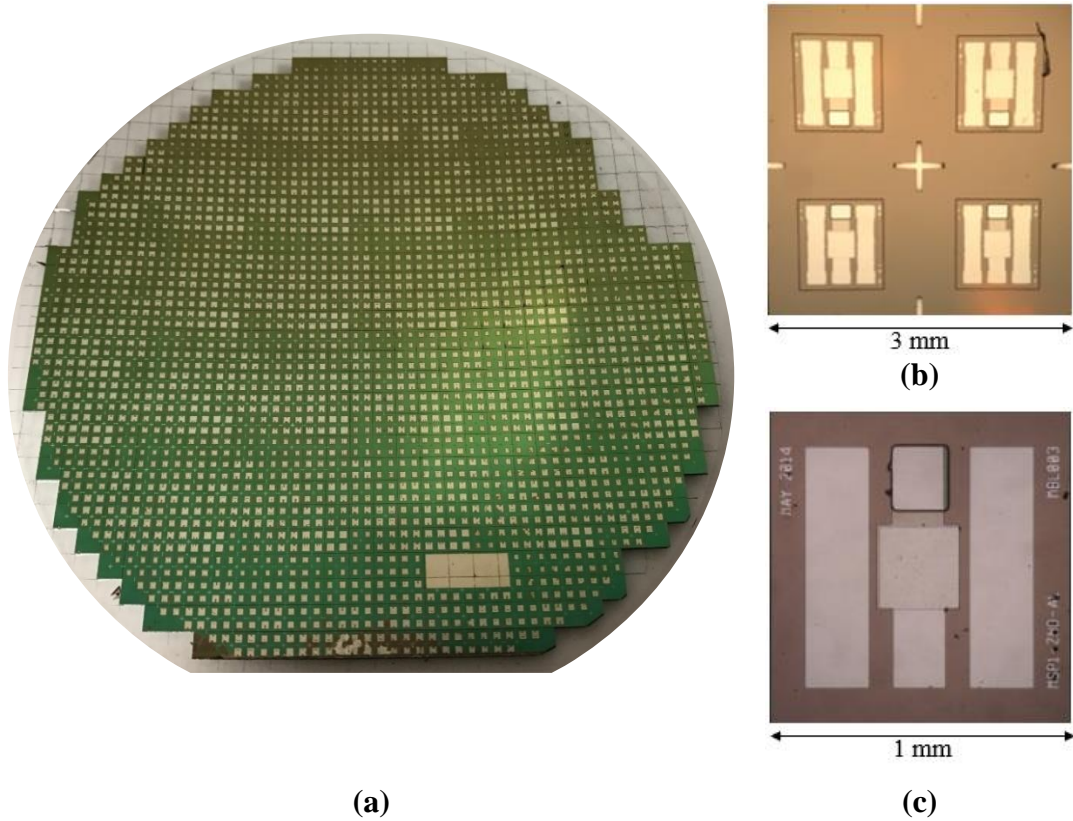
Figure 4.3 (a) Photograph of a patterned 4" SMR wafer, (b) die with four devices and (c) top view of single SMR with Al electrodes.

To ease handling of the devices, the first batch of wafers were diced into groups of 4 devices (arrays of 2×2), obtaining a total of ~700 square dies of 3 mm, each array containing devices of the exact same SMR design. Problems were experienced during the dicing process of the 870 MHz wafers as devices were delaminating. This was attributed to the poor adhesion of the thick layers of the SMR structure, required for the designed frequency. To tackle this issue, two of the 870 MHz wafers were coated with the thick photoresist (instead of the thin one used previously) obtaining better results. An example of fabricated devices is shown in Figure 4.3.

4.2.3 FABRICATION OUTPUT

Thicknesses of the deposited reflector layers were estimated from SEM images of the cross section of the acoustic mirrors. The ZnO layer and electrodes were measured with a stylus profiler (Ambios XP-100). The thicknesses of the reflector layers (summarised in Figure 4.4) varied by up to 19% compared with the designed values. However, they were within an acceptable range due to the broad bandwidth of the reflector.
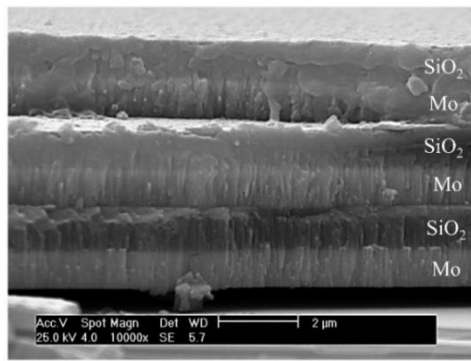
LAYER	870 MHz	1.5 GHz
SiO_2	1.39 (-0.26)	0.95 (-0.05)
Mo	1.87 (+0.05)	1.07 (+0.02)
ZnO (Al)	2.96 (-0.39)	1.49 (-0.36)
ZnO (Au)	2.55 (-0.30)	1.12 (-0.23)

(variation from design) µm

(a)
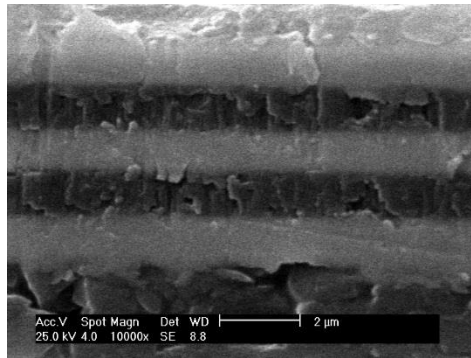
LAYER	870 MHz	1.5 GHz
SiO_2	1.52 (-0.13)	0.97 (-0.03)
Mo	1.75 (-0.07)	1.02 (-0.03)
ZnO (Al)	3.12 (-0.23)	2.19 (+0.34)
ZnO (Au)	3.92 (+1.07)	1.59 (+0.24)

(variation from design) µm

(b)

Figure 4.4 SEM image of deposited reflector layers and measured thicknesses for devices of (a) the first batch and (b) the second batch.

The thickness of the piezoelectric layer is more critical. Small variations of the designed thickness (±5%) significantly shift the resonant frequency of the devices. Given the measured thicknesses (variation of up to 13% for the Al 870 MHz design), the resonant frequencies of the fabricated devices were expected to differ from the designed values.

The second batch of devices consisted of 4 wafers (one wafer of each frequency design and electrode materials). Substantial improvements were made in the fabrication procedure as listed below:

- To improve uniformity of the layers, wafers were sputtered one by one in the HiTUS system (as opposed to the first batch were two wafers were sputtered at a time).

- Sputtering times were increased, as it was observed that the ZnO and Mo deposition rates decreased to 15 nm/min and 24 nm/min, respectively which explains the thinner layers obtained in the previous batch.

- Thick photoresist coating was used in all four wafers to prevent delamination of the devices during dicing, particularly for the 870 MHz design.

- The seed layer of chrome was increased to a thickness of 18 nm to improve adhesion of the gold electrode. Gold electrodes from the 1st batch were found to be peeling off during wire bonding.

- Wafers were diced in individual SMR devices with resulting SMR dies of dimension 1.5 mm×1.5 mm, avoiding crosstalk between devices and significantly reducing the overall size of the chip.

Although targeted thicknesses were not achieved in this second run (thickness error of up to 7% for Al devices), they are closer to the designed values (compared to the first batch). Thus, resonant frequencies are expected to be close to the design values. Moreover, higher quality and uniformity of the deposited piezoelectric film is expected across the wafer (not characterised) thanks to the improvements in the fabrication procedure. New 1D simulations were performed to evaluate these variations in the resonant frequency. Results are presented and compared to the experimental measurements in the following section.

4.3 ELECTRICAL CHARACTERISATION OF FABRICATED DEVICES

Scattering parameters of fabricated SMRs were measured using a vector network analyser (Agilent E5071B). A full 2-port calibration was performed prior the

measurements to account for any system errors including coaxial cables and connectors. Figure 4.5 shows a comparison between the designed, predicted and measured S11 magnitudes of MBL003 devices from the first batch.
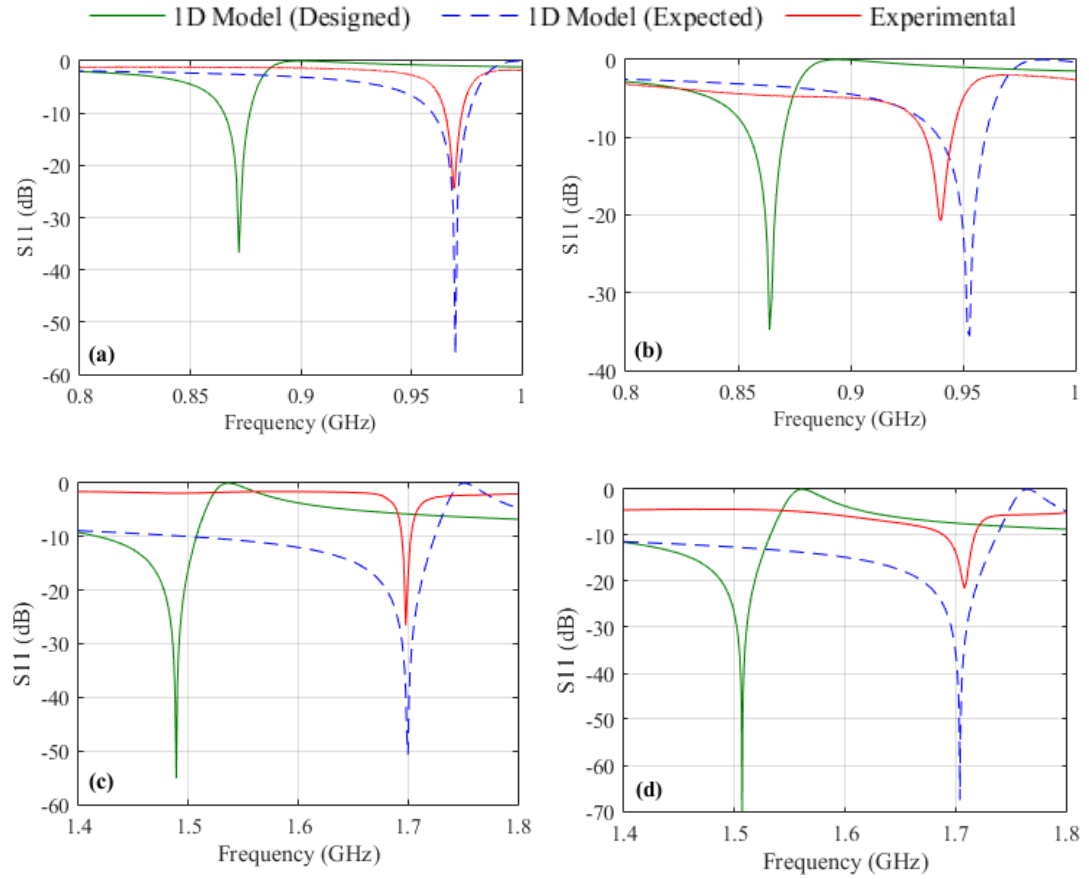
Figure 4.5 S11 parameter for 1st batch designs: (a) 870 MHz, Al electrodes; (b) 870 MHz, Au electrodes; (c) 1.5 GHz, Al electrodes; (d) 1.5 GHz, Au electrodes.

Series resonant frequencies at 970 MHz, 940 MHz, 1.7 GHz and 1.72 GHz were measured for the SMR designs at 870 MHz (Al), 870 MHz (Au/Cr), 1.5 GHz (Al) and 1.5 GHz (Au/Cr), respectively. As expected, a shift in the designed frequencies is observed due to manufacturing tolerances. The 1D model was considered sufficient to perform this comparison being the resonant frequency the property of interest. The S11 magnitude, however, is much smaller and wider for the measured response attributed to material properties, i.e. surface roughness of the layers. Devices from the second batch resonated at 900 MHz, 740 MHz, 1.2 GHz and 1.4 GHz, respectively with series resonant frequencies closer to the designed values.

Devices from the first and second batch had comparable electrical performance. For the 870 MHz design with aluminium electrodes, series and parallel frequencies were measured at 972 MHz and 992 MHz, respectively with extracted quality factor $Q_s = 140$ and electromechanical coupling coefficient of 4.13% for the first batch. Devices of the second batch resonated at 900 MHz (series) and 912 MHz (parallel) with a quality factor of 170 and effective electromechanical coupling coefficient of 2.6%.
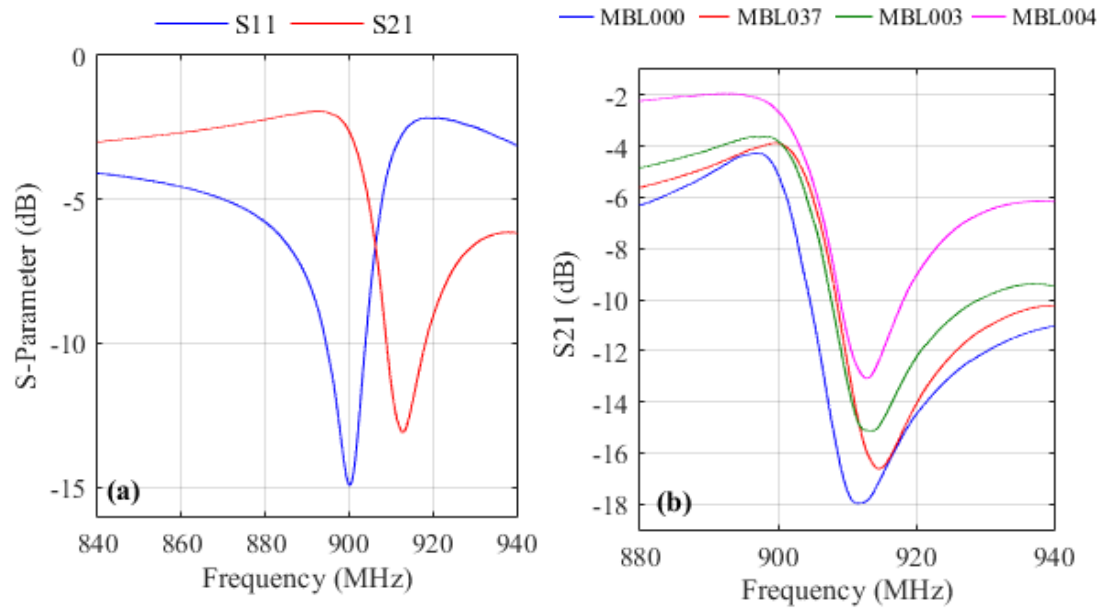
Figure 4.6 Scattering parameters of devices from the second batch (a) 900 MHz Al electrodes and (b) devices with different sensing area dimension.

SMR devices with square active area ranging from 125 µm to 250 µm were designed and fabricated (refer to section 3.4). The S21 parameters of these devices are shown in Figure 4.6b. As the active area of the device increases, the resonator static capacitance increases as per equation (3.12) leading to an increase of S21 values.

Although devices from the first and second batch exhibited similar performance, devices from the second batch (1.5 × 1.5 mm) were preferred for the experimental work (presented in the following sections), due to their compact size (which allowed the necessary interface circuitry to be smaller). In particular, the 900 MHz device with aluminium electrodes (MBL003) was used, unless otherwise stated. These devices were further characterised, to study the frequency dependency on

ambient effects (variations of temperature and humidity), as presented in the next section.

4.4 AMBIENT EFFECTS

Characterisation of the SMR devices was carried out to evaluate the effects of environmental variations (temperature and humidity) on their frequency response. Devices were first tested in single ended output to observe their temperature dependence and later tested in differential output to demonstrate a method of correcting for ambient variations.

4.4.1 TEMPERATURE EFFECTS

To characterise temperature dependency of the SMRs, the resonant frequencies of the devices were measured over a wide range of temperatures (30°C – 90°C), and the corresponding TCFs were extracted for the series and parallel resonant frequencies.

The SMR was placed inside a universal heating oven (UNP 200, Memmert GmbH) where it was exposed to controlled temperatures (30°C – 90°C). A temperature and humidity sensor (BME280, Bosch) was placed near the device. Series and parallel resonant frequencies were monitored with the VNA, controlled via serial communication. A LabVIEW virtual instrument was developed to control the network analyser, and to log these data together with the temperature sensor readings. Obtained results are shown in Figure 4.7a.

Both series and parallel resonant frequencies decreased with temperature rise. The extracted TCFs are -55 ppm/°C and -49 ppm/°C for the series and parallel resonant frequency, respectively. Experimental results agree with simulations performed in section 3.3.4 where the parallel TCF was lower than that for the series frequency. However, measured TCFs are slightly higher (+38%) compared to the simulations. This can be due to the parasitics induced by the measurement setup (bond wires and coaxial cables).
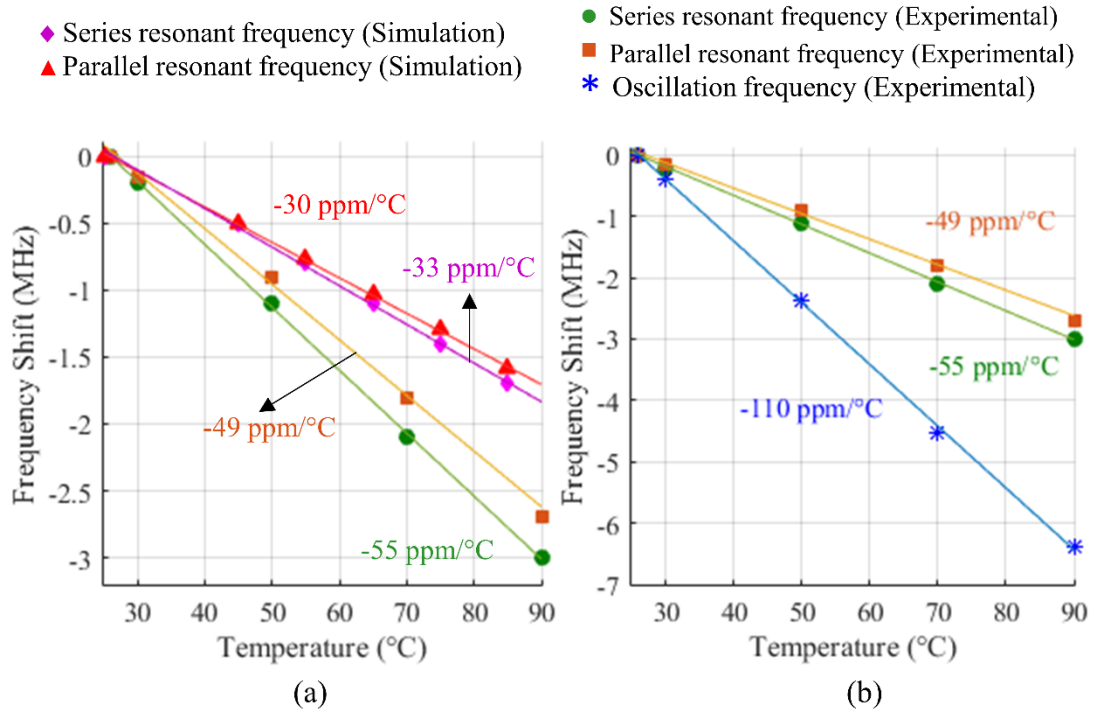
Figure 4.7 (a) Comparison between experimental and simulated (FEM model) temperature coefficients of the series and parallel frequencies. (b) Comparison of experimental TCFs of the series, parallel and oscillation frequency of fabricated SMRs.

The TCF of the SMR provides a good insight into the temperature stability of the device itself. For sensing applications, however, it is more useful to analyse the temperature coefficient of oscillation frequency (TCF$_{osc}$) of the integrated system [4]. In addition to the resonator itself, the oscillation frequency is also controlled by temperature dependant components in the circuitry (transistors, capacitors) and parasitics in the system arising from wire-bonding and interconnections [5, 6]. Careful design of the integrated system (SMR and readout circuitry) can result in low TCFs values. Design considerations for such a system have been proposed in [5].

Temperature dependence of the readout circuitry (oscillator and mixing circuit are presented in section 6.5) was characterised as above. The temperature sensor (BME280) was located near the sensing system, and the overall temperature of the oven (30L volume) was recorded, together with the sensing system output signal.

To test the TCF of an individual SMR with associated circuitry, an external RF signal (Agilent 8648C) was fed to the LO input of the mixer and used as an environmentally isolated reference signal. The second signal originated from the SMR

wire-bonded onto the Pierce oscillator. In this way, any frequency changes measured are only due to temperature dependency of the SMR and circuit with no contributions of any other effects. Results are presented in Figure 4.8 for two different SMRs.
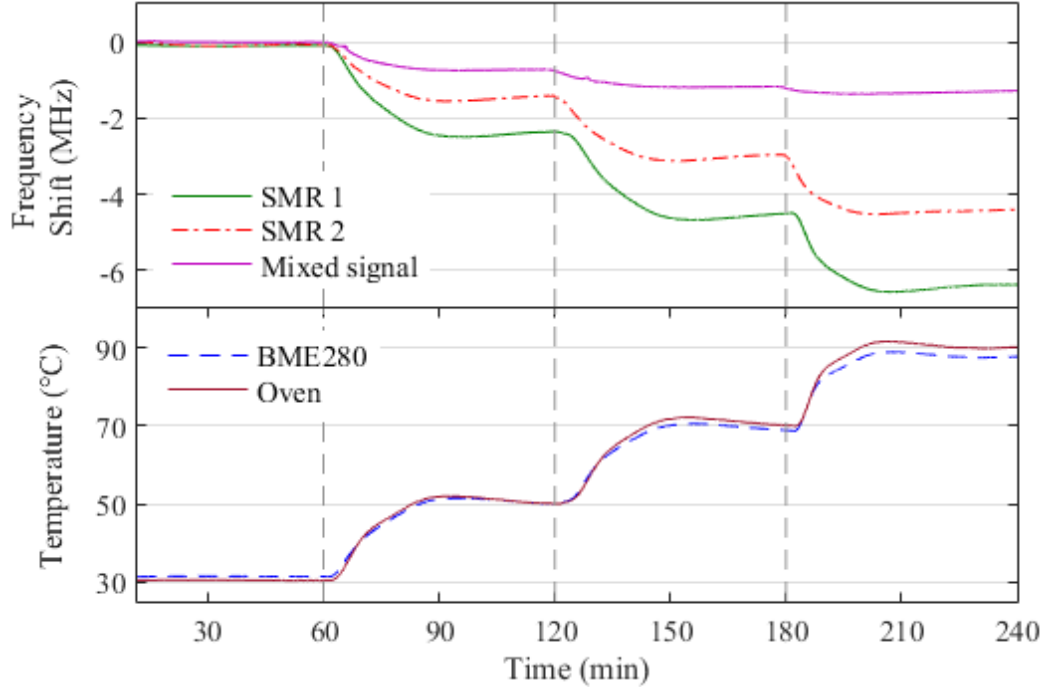
Figure 4.8 Oscillator temperature stability and temperature compensation technique.

TCF_{osc} of -110.8 ppm/°C and -76.4 ppm/°C were measured for two devices. It was found that identical devices from the same batch have different TCFs due to fabrication tolerances. Particularly, devices located close to each other within the wafer had similar TCFs. A comparison of extracted TCFs is shown in Figure 4.7b.

The measured TCF_{osc} of the integrated system was rather high to be used in sensing applications unless a temperature compensation method was used. Although the TCF of the SMR itself can be improved through the addition of SiO_2 layers (section 3.1.4), other methods can be applied for the integrated system. Zhang *et al*. [7] proposed a supply voltage tuning technique in which the oscillator voltage is adjusted to compensate for temperature effects. Vilander [8] proposed the use of an integrated heating element, to compensate for temperature and improve device oscillator accuracy. In this work, a dual configuration method will be used for the suppression of ambient effects in which one device is used as the reference and another one as the sensing element [9].

Temperature characterisation of the complete sensing system (working in dual configuration) was performed. The result is shown in Figure 4.8 labelled as "Mixed signal". This is the typical single differential output obtained from the readout circuitry. The TCF_{osc} of the sensing system is considerably smaller at -24 ppm/°C. However, this is still a high value for sensing applications, were the frequency shift caused by the physical parameter being measured can be smaller than the temperature effects. The measured TCF_{osc} corresponds to the difference between the individual TCF_{osc} of the SMR devices used. When using SMRs with similar TCFs, temperate effects are practically eliminated with $TCF_{osc} < -2$ ppm/°C. Therefore, this method relies on both reference and sensing devices to have very similar TCFs, which should be considered prior performing experimental measurements.

To avoid damaging the electronic components, the sensor system was tested up to a temperature of 90°C. The SMR device together with the readout circuitry were able to work reliably up to this temperature. While the SMR device was tested at 150°C and found to resonate, the electronic components were not exposed to high temperatures beyond their specified maximum limits (industry standard 125°C).

4.4.2   HUMIDITY EFFECTS

To characterise the humidity dependence of the SMR devices, they were exposed to conditions in the range of 15 to 60 %RH. For these experiments, the response of a single ended SMR device was tested (using an Agilent frequency generator as a stable reference signal), as described previously for the temperature characterisation. To isolate the effects of humidity variance, the SMR sensor was tested in a constant temperature environment. Humidity levels and temperature inside the oven were monitored with the BME280 sensor. The time response is shown in Figure 4.9. A linear fit was applied to the data to remove the offset due to temperature drift caused by the injection of humidity vapour.

When exposed to a humid environment, water molecules are absorbed on the surface of the ZnO film [10, 11] causing an increase in the density of the layer. This in turn results in a decrease of the resonant frequency of the SMR. Sealed packages can be used to isolate the SMR and avoid this effect (e.g. for other applications such

as accelerometers, filters). However, for gas sensing, the sensor needs to be exposed to the sample.
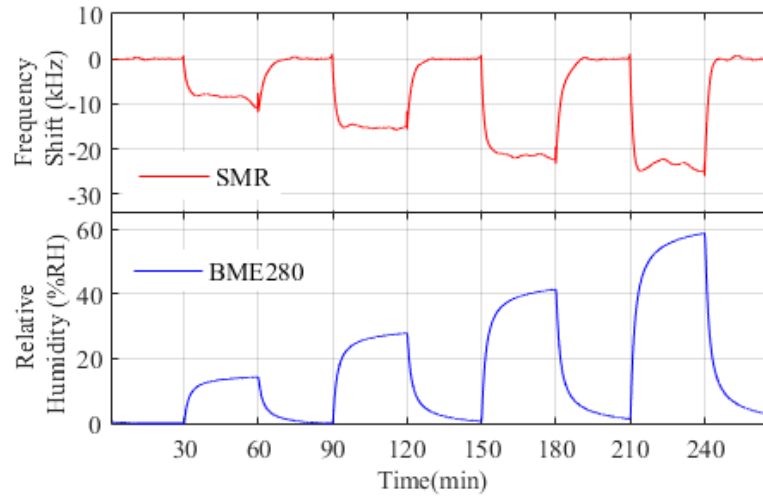
Figure 4.9 SMR dependence of humidity (15%RH to 60%RH).

It is usually reported that the principal cause of the change in frequency of ZnO based FBARs is due to water molecules being absorbed in the ZnO layer [12, 13]. The change in frequency is likely to be a combination of the mass loading caused by the water molecules being absorbed into the ZnO film and the change in density of the sample air (at a constant temperature, humid air is less dense as water molecules, with a lower molar mass, replace the dry air molecules [14, 15]). This additional cause is not usually reported in the literature, and thus needs to be investigated further. A humidity dependence of approximately 580 Hz/%RH was found for the experiment in Figure 4.9, which is comparable to a value of ~289 Hz/%RH for a 701 MHz device reported by Ashley *et al.* [16].

4.5 CONCLUSIONS

The solidly mounted resonators were fabricated at the designed frequencies of 870 MHz and 1.5 GHz. Fabrication was performed using standard microfabrication technologies in a 3-mask photolithography process, with piezoelectric ZnO and Al and Au/Cr electrodes. Two batches of devices were fabricated with a total of 12 wafers processed. Individual dies were obtained with a small footprint of 1.5 mm $\times$ 1.5 mm.

The devices were characterised using a network analyser to obtain the scattering parameters. A large variance (up to +24 %) was found in the layer thicknesses of the first batch (compared to the design parameters), which in turn caused a large variance of the resonant frequency of the devices. Fabrication tolerance was improved for the second batch of devices, with thickness variance of ~ 15%. SMR devices from the second batch (resonance at 900 MHz) exhibited a typical quality factor of 170 and electromechanical coupling coefficient of 2.6%.

The devices were characterised to ambient effects, both with and without interface circuitry. Temperature was varied between 30 and 90 °C and humidity was varied between 15 to 60 % RH. A network analyser was used to monitor the series and parallel frequencies of the device. TCF values were measured as -55 ppm/°C and -49 ppm/°C for series and parallel resonance, respectively. When used in a single ended output, with associated electronics, the SMRs were found to be very susceptible to changes in temperature and humidity. The TCF and humidity dependence were measured as -110 ppm/°C and ~580 Hz/%RH, respectively. Using a differential configuration demonstrated that the effects of temperature and humidity variance were significantly reduced. Temperature and humidity effects can be further reduced, by using signal processing techniques (environmental parameters can be measured using dedicated sensors).

In the next chapter, these sensors are used for applications of particle sensing. A particle sensing unit is developed using the dual configuration technique, which reduces the effect of the temperature and humidity variation when the devices are used outside of a controlled environment. These devices were used in the development of a prototype air quality monitor and they formed the basis for the development of a CMOS compatible device.

4.6 REFERENCES

[1]   Osbond, P., Beck, C. M., Brierley, C. J., Cox, M. R., Marsh, S. P. and Shorrocks, N. M. (1999). "The influence of ZnO and electrode thickness on the performance of thin film bulk acoustic wave resonators", *1999 IEEE Ultrasonics Symposium. Proceedings. International Symposium (Cat. No.99CH37027)*. pp. 911-914 vol.2.

[2]   García-Gancedo, L., Pedrós, J., Zhu, Z., Flewitt, A. J., Milne, W. I., Luo, J. K. and Ford, C. J. B. (2012). "Room-temperature remote-plasma sputtering of c-axis oriented zinc oxide thin films", *Journal of Applied Physics*. **112**(1): 014907.

[3]   García-Gancedo, L., Ashley, G. M., Zhao, X. B., Pedrós, J., Flewitt, A. J. and Milne, W. I. (2011). "Deposition and characterisation of ultralow-stress ZnO thin films for application in FBAR-based gravimetric biosensors ", *Int. J. Nanomanufacturing*. **7**(3/4): 371-382.

[4]   Johnston, M. L. (2012). "Thin-film Bulk Acoustic Resonators on Integrated Circuits for Physical Sensing Applications", PhD. Columbia University,

[5]   Campanella, H. (2010). "Acoustic wave and electromechanical resonators: concept to key applications". Norwood, MA: Artech House.

[6]   Zhang, X., Xu, W., Abbaspour-Tamijani, A. and Chae, J. (2009). "Thermal analysis and characterization of a high Q film bulk acoustic resonator (FBAR) as biosensors in liquids", *2009 IEEE 22nd International Conference on Micro Electro Mechanical Systems*. pp. 939-942.

[7]   Zhang, X., Xu, W. and Chae, J. (2015). "A Temperature Compensation Concept for a Micromachined Film Bulk Acoustic Resonator Oscillator", *IEEE Sensors Journal*. **15**(9): 5272-5277.

[8]   Vilander, A., *Acoustic wave resonator with integrated temperature control for oscillator purposes*. 2007, United States Patent.

[9]   Benes, E., Groschl, M., Seifert, F. and Pohl, A. (1997). "Comparison between BAW and SAW sensor principles", *Proceedings of International Frequency Control Symposium*. pp. 5-20.

[10]   Li, Y., Valle, F. D., Simonnet, M., Yamada, I. and Delaunay, J.-J. (2009). "Competitive surface effects of oxygen and water on UV photoresponse of ZnO nanowires", *Applied Physics Letters*. **94**(2): 023110.

[11]   Zhang, Y., Yu, K., Jiang, D., Zhu, Z., Geng, H. and Luo, L. (2005). "Zinc oxide nanorod and nanowire for humidity sensor", *Applied Surface Science*. **242**(1–2): 212-217.

[12]   Qiu, X., Oiler, J., Zhu, J., Wang, Z., Tang, R., Yu, C. and Yua, H. (2010). "Film Bulk Acoustic-Wave Resonator Based Relative Humidity Sensor Using ZnO Films", *Electrochemical and Solid-State Letters*. **13**(5): J65-J67.

[13]   Ashley, G. M., Kirby, P. B., Butler, T. P., Whatmore, R. and Luo, J. K. (2010). "Chemically sensitized thin-film bulk acoustic wave resonators as humidity sensors", *Journal of The Electrochemical Society*. **157**(12): J419-J424.

[14]   Picard, A., Davis, R. S., Gläser, M. and Fujii, K. (2008). "Revised formula for the density of moist air (CIPM-2007)", *Metrologia*. **45**(2): 149.

[15]   (2009). "Pilot's Handbook of Aeronautical Knowledge".

[16]   Ashley, G., Luo, J., Kirby, P., Butler, T. and Cullen, D., *Thin Film Bulk Acoustic Wave Resonators for Continuous Monitoring in the Physical, Chemical and Biological Realms.* , in *Materials Research Society Symposium*. 2010.

CHAPTER 5

PARTICLE SENSING WITH SOLIDLY MOUNTED RESONATORS

5.1 INTRODUCTION

The design, modelling, fabrication and characterisation of solidly mounted resonators for air quality monitoring was reported in Chapters 3 and 4. This chapter investigates the use of these devices for particle sensing in air. Finite element analyses (COMSOL Multiphysics) were performed using a three-dimensional model to evaluate the suitability of these devices for the detection of micro-sized particles (<10 µm).

Preliminary characterisation was performed with the SMR devices (resonant frequency ~900 MHz); fine particles of known size and composition (PTFE 1 µm and talcum powder 7 µm) were deposited on the active area of devices, connected to a network analyser.

The development of a portable particle sensing unit based on the SMR devices is described. The sensing unit is tested in a dual mode configuration. Experimental characterisation of the particle sensor unit is reported, with experiments performed in a particle sensing chamber at the University of Warwick, UK and inside an environmental chamber at VITO, Belgium.

Development of a virtual impactor (to separate the PM2.5 from larger particles) is presented. The impactor was designed to be integrated as part of a hybrid particle microsensor system using an ASIC chip.

5.2 PARTICLE - SURFACE INTERACTION

For particle sensing applications, it is important to understand the effect of discrete masses on the surface of SMR resonators compared to homogenous masses. The frequency response of acoustic resonators is dependent on the strength of the interaction between the particle and the sensor surface (the top electrode).

Sauerbrey's equation (2.6) describes the effect of mass loading on the resonant frequency of a QCM device. However, this relationship only applies to a homogenous thin rigid film firmly attached to the surface of the resonator. Dybwad developed a one-dimensional mechanical model of a solid particle in contact with a quartz resonator [1]. The model demonstrated that a particle attached to the surface forms a coupled oscillator system resonating at a new frequency. A strong particle binding to the surface will cause a decrease in the resonant frequency of the system leading to Sauerbrey's equation, this is termed *inertial loading*. A weak particle-surface coupling is called *elastic loading*. In this situation, the resonant frequency of the system increases, proportional to the stiffness of the binding.

Dybwad's findings were supported by Johannsmann who expanded the one dimensional model and developed mathematical equations to explain the phenomena [2, 3]. As the coupling strength of the particle-surface interaction is directly related to the particle size, a negative frequency shift can be observed when the particles are small enough and rigidly attached to the surface. On the other hand, positive frequency shifts are predicted for larger particles due to an increase of the effective stiffness of the composite resonator. The same behaviour was observed in other experimental

studies with a solid particle in contact with a thickness shear mode (TSM) sensor in air and colloidal objects on the surface of a QCM in liquid phase media [4].

The following section investigates the mass loading of small particles on a SMR through FEM. There are a limited number of experimental studies in the literature on the contact mechanics of the particle surface interactions with acoustic resonators. Furthermore, these studies are usually performed with commercial QCM resonators, with no comprehensive reports or analysis with SMR devices. Johannsmann calculated a cut-off particle size of 60 µm, between particles categorised as large or small; large particles exhibited elastic loading while small particles were noted to bind strongly to the surface of the resonators. As the particles used in this work were in the range of 1-10 µm, it was assumed the particles would interact with a strong binding to the surface of the device.

5.3   FINITE ELEMENT MODELLING ON PARTICLE SENSING

The frequency response of the SMRs was simulated pre- and post-deposition of fine particles using FEM. The 3D model was introduced in section 3.2.2, and further details can be found in Appendix B.

The fine particles (<10 µm) were modelled as cubic geometries instead of spheres, to ensure the good binding to the surface of the electrode was represented in the model. This follows the assumption that particles with small diameter are strongly bound to the surface of the device. A decrease in the resonant frequency of the device is expected when particles are loaded. Figure 5.1 shows the meshed model with PM2.5 loaded onto the sensing area of the SMR device. The series resonant frequency of the unloaded resonator was evaluated at 875.12 MHz. The resonant frequency was again evaluated after the deposition of a number of particles (incrementally deposited from 2 to 10) and the frequency shifts computed.
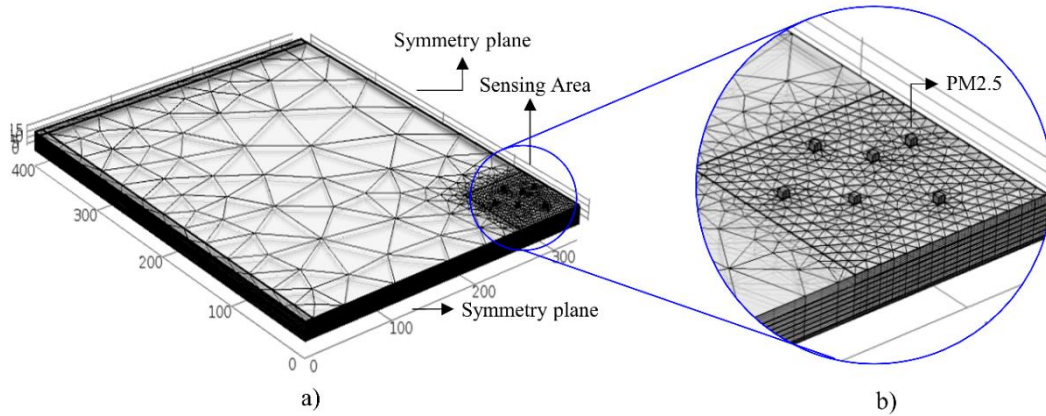
Figure 5.1 (a) Geometry of the developed finite element model (quarter structure) and (b) the fine particles deposited on the sensing area.

The developed model suffered from two limitations: (1) the capabilities of the workstation limited the total number of simulated particles and (2) the particles could only be deposited on the simulated quadrant of the complete geometry. A maximum of 10 particles were added onto the surface of the resonator model as the simulations became extremely time consuming after this point (>96 hours). It would be preferable to simulate the entire geometry of the SMR (requiring a dedicated high-performance workstation), as when only a quadrant was simulated, in effect, the particles were only placed on one corner of the sensing area. Although these limitations are clear, the model was suitable to perform a comprehensive analysis of the capabilities of the SMR devices, including an investigation into the effect of varying the location of the particles on the surface of the SMR and the sensitivity to particles (PM2.5 and PM10) depending on the resonant frequency (870 MHz and 1.5 GHz).

The variation of the frequency response of the devices to different particle locations was analysed. Three different arrangements of particles were simulated with up to ten particles deposited randomly in the central area of the quadrant as shown in Figure 5.2a. It was observed that the different particles arrangements on the top surface produced different frequency shifts with variations within ±5%. Figure 5.2b and c show the computed frequency shifts for PM2.5 and PM10, respectively for the 870 MHz device. Higher variation was observed when PM2.5 particles were deposited compared to the PM10 as shown in Figure 5.2d and e.

Campanella *et al.* similarly reported a large variation in frequency shifts caused by the placement of a mass at the centre, lateral and diagonal locations on a FBAR. Their experimental work demonstrated sensitivity dependence of the resonator to the position of the localised mass [5].
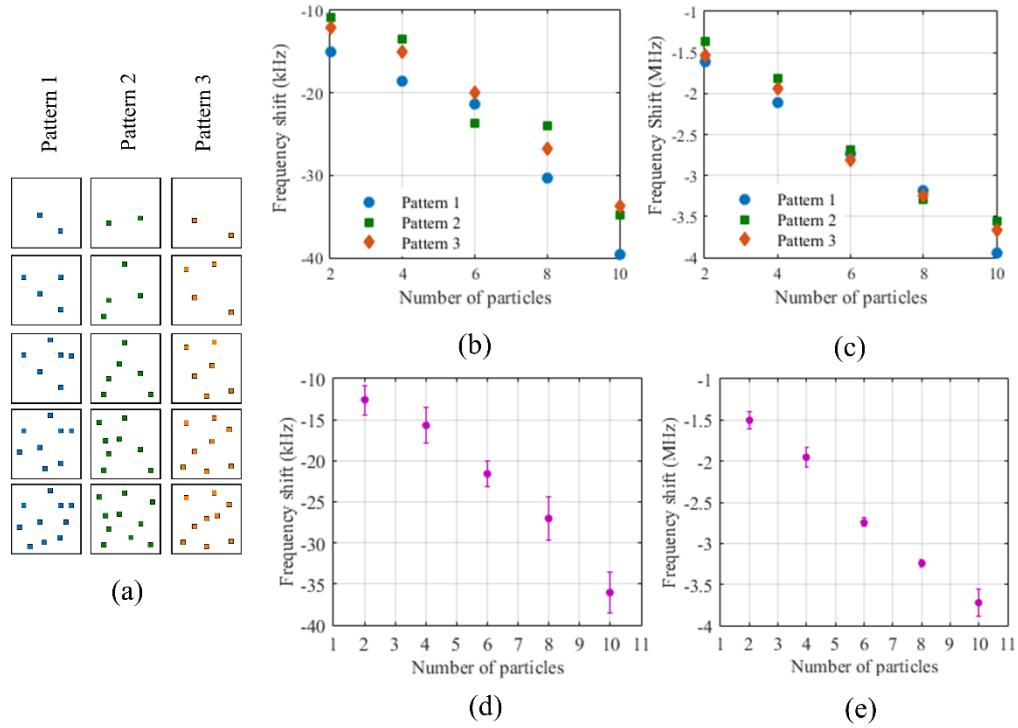
Figure 5.2 Dependence of the sensitivity of the SMRs to three patterns of deposited particles: (a) Particle arrangements; (b) and (c) frequency shifts for PM2.5 and PM10, respectively; (d) and (e) variance between arrangements.

The computed frequency shifts from the three patterns were averaged and these values were used to estimate the sensitivity of the SMRs. Figure 5.3 summarises the estimated sensitivity of the modelled devices when detecting PM2.5 and PM10.

The mass sensitivity of the 870 MHz SMR with Al electrodes was found to be slightly higher than the devices with Au/Cr electrodes when detecting both PM2.5 and PM10 (+24% and +14%, respectively). Similarly, the 1.5 GHz SMR with Al electrodes produced a 22% higher response for PM2.5 and +20% for PM10 compared to the one with Au/Cr electrodes. The greater sensitivity of the SMRs with Al top electrode could be attributed to the lower mass of the electrode compared to that of the Au/Cr electrode, as suggested by Gabl [6].
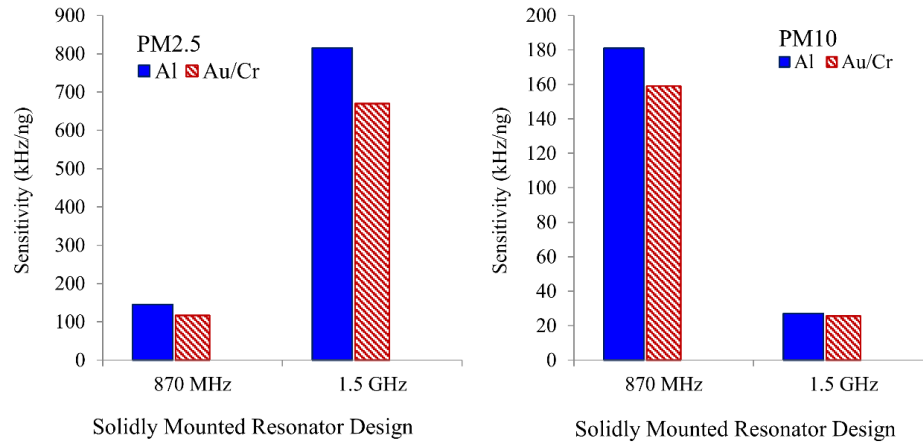
Figure 5.3 Estimated sensitivity of the designed SMRs to the deposition of fine particles obtained from the simulation results.

Sauerbrey's equation (2.6) states the frequency shift of an acoustic resonator for a given mass is directly proportional to the resonant frequency of the device. This relationship can be observed for the detection of PM2.5. However, for the detection of PM10 the inverse phenomenon was observed.

These results suggest that the magnitude of the frequency shift is related to the fraction of the particle detected on the surface of the device, as proposed in previous works [7, 8]. The 870 MHz device with a wavelength of ~7.3 µm would detect a bigger fraction of the PM10 particle compared to the 1.5 GHz device with a wavelength of ~4.22 µm. Hence, a higher frequency shift is observed with the 870 MHz device when detecting the larger particles. SMR devices with tailored resonant frequencies may be used for the monitoring of airborne particles with different size distribution. In the next section, experiments are performed to verify these observations from the simulations.

5.4 CHARACTERISATION OF SMRs TO THE DEPOSITION OF PARTICLES

Initial characterisation was performed with the first batch of SMR devices to the deposition of micro-sized particles (1 µm and 7 µm). The batch included devices designed to operate at 870 MHz and 1.5 GHz but the fabricated devices were found to resonate at 970 MHz and 1.7 GHz, respectively. The 970 MHz SMRs (Al electrodes) were selected from this batch for initial characterisation. From the analysis of the FEM results above, the 1.5 GHz SMRs offered far greater sensitivity to PM2.5, compared to the 870 MHz SMRs, but very limited sensitivity to PM10. In order to test the device

to 1 µm and 7 µm diameter particles, the 970 MHz devices were preferred to obtain reliable and reproducible results.

A photograph of the experimental setup is shown in Figure 5.4. A micrometre wire (25 µm thick) attached to a three-axes linear stage was used to manually deposit particles of known size and composition (PTFE 1 µm and talcum powder 7 µm) on top of the active area of the device. Throughout the experiment, the device was kept inside a temperature controlled chamber, to remove the effect of environmental temperature variance. A digital microscope (AnMo Electronics, Taiwan) was used to magnify the apparatus. The micrometre wire with particles on the tip is placed directly above the sensing area and lowered down onto the device, where particles attached to the wire are deposited on the surface of the sensor.
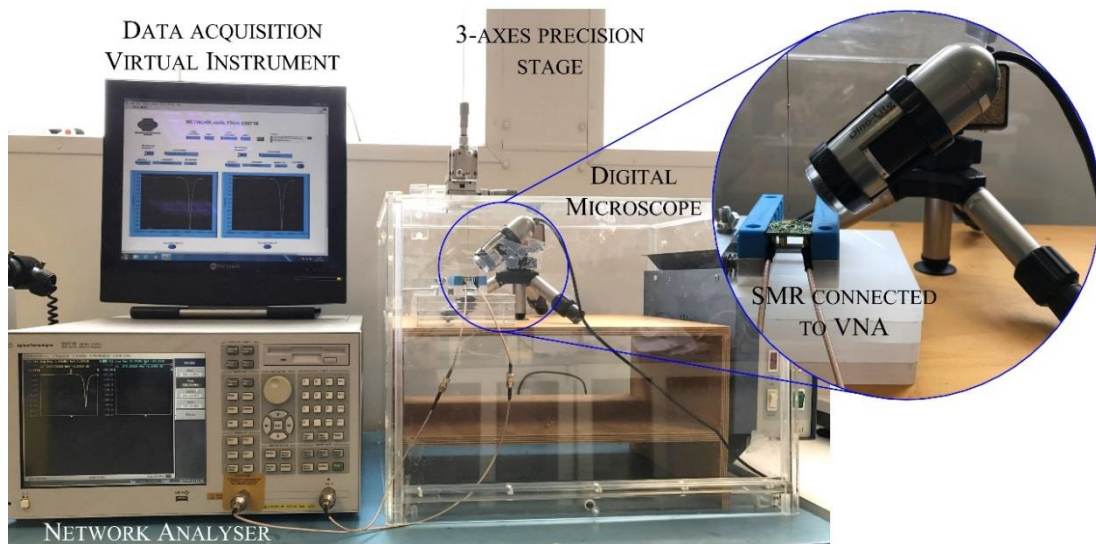
Figure 5.4 Experimental setup for SMR characterisation for particle deposition.

The frequency response of the SMR device was monitored with the Vector Network Analyser (VNA) E5071B (Agilent Technologies). A LabVIEW virtual instrument was developed to control the VNA, which allowed continuous monitoring and logging of the series and parallel resonant frequencies of the device.

The number of particles deposited onto the surface of the SMR devices was observed using an optical microscope (100x magnification), which is not shown in the photograph of the experimental setup. A digital camera connected to the lens of the microscope was used to photograph the sensing area of the SMR devices. Figure 5.5

shows these photographs, taken before deposition, after deposition of a low number of particles and after deposition of a large number of particles.
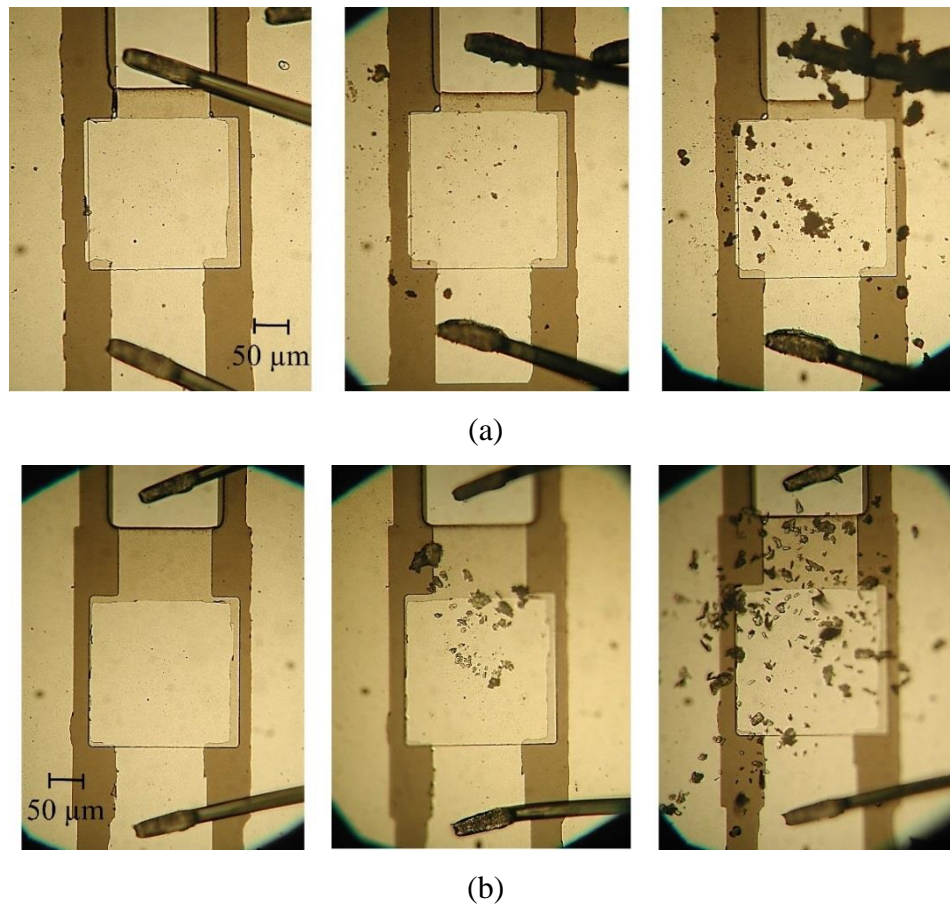
Figure 5.5 Photographs of the SMR surface before and after the deposition of (a) PTFE 1 µm particles and (b) talcum powder (7 µm).

Four depositions of 1 µm particles were made onto the surface of a single SMR. After each deposition, the frequency shift from the baseline value was recorded and a photograph of the surface was taken under the microscope. Image processing was used to approximate the total mass on the surface of the sensing area of the sensors. This total mass together with the recorded frequency shifts were used to calculate the sensitivity of the device. Figure 5.6 shows the calculated mass load onto the surface of the SMR after each deposition and the corresponding frequency shift. A linear relationship was noted between the frequency shift and total mass of the particles. The device demonstrated a sensitivity of ~90 kHz/ng and a minimum detectable mass of 0.72 ng (lower masses were not tested).
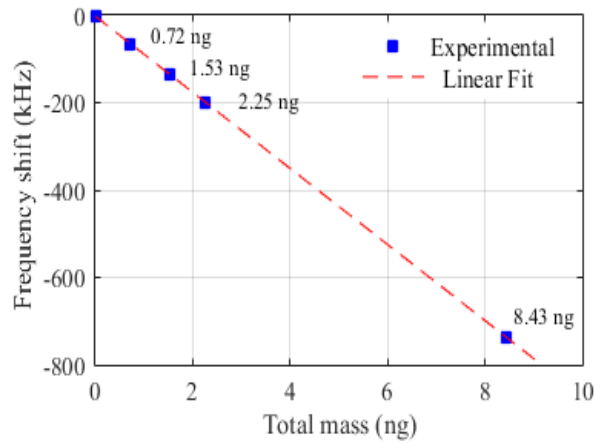
Figure 5.6 Relationship between total mass of the particles (PTFE 1 µm) on the surface of the SMR and measured frequency shifts.

The experiment was repeated with particles of 7 µm diameter, using a clean SMR surface. In a similar manner, particles were deposited four times onto the surface of the device. Experiments were repeated three times. One representative result is shown in Figure 5.7. No experiments demonstrated a clear relationship between the loaded mass and the frequency shift. Positive and negative frequency shifts occurred during the experiments with no evident pattern.
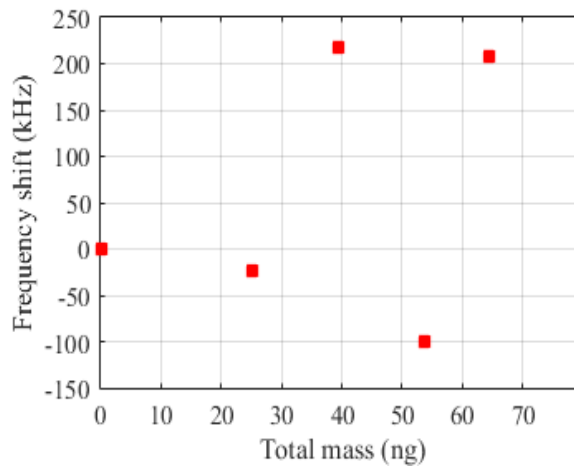
Figure 5.7 Total mass of 7 µm talcum particles loaded onto the surface of the SMR with corresponding frequency shifts.

As discussed in section 5.2, a decrease in resonant frequency would be expected for an increase of mass loading on the sensor. When a positive frequency shift is measured, for example in Figure 5.7, this demonstrates a weak interaction has occurred between the particles and the surface which increases the stiffness of the

resonator. In this manner, the shift in resonant frequency is proportional to the stiffness of the contact and is independent of the mass of the particles [2].

Particles of different sizes and shapes experience different interactions with the sensor surface (contact area). The SEM images in Figure 5.8 show the irregular shapes of typical PTFE particles (<1 µm) and talcum powder (mean size of 12 µm) [9, 10]. The angular shape of the talcum powder mean that the particles have more corners. These sharp edges increase the possibility that the particles will make discrete points of contact with the surface. This is particularly visible in Figure 5.8b where talcum powder particles are angular and flaky, making poor contact to the surface. Conversely, the PTFE particles in Figure 5.8a are more rounded but not spherical. The irregularity of the talcum particles can explain the different results obtained during the experiments shown above, where both positive and negative shifts were obtained due to unpredictable shape of the particles deposited on the surface.

(a) (b)
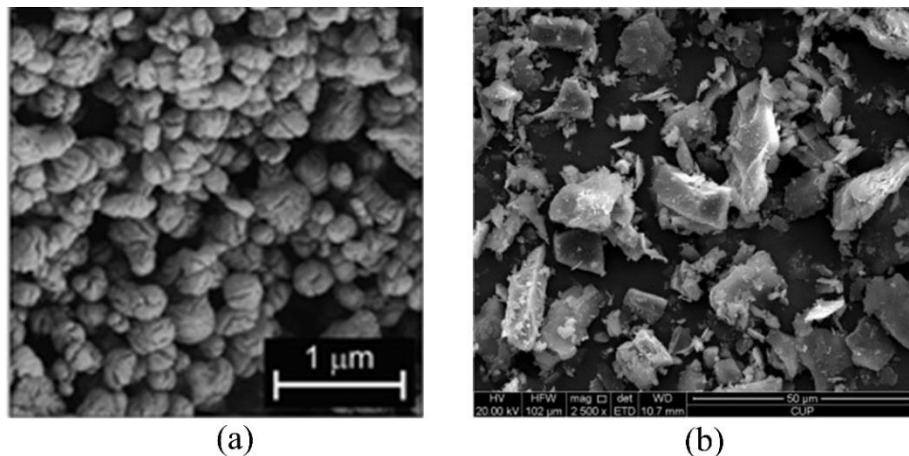
Figure 5.8 SEM photographs of typical (a) PTFE micro-sized particles and (b) talcum powder (50 µm scalebar). Photographs from [9, 10].

The experiments in this section demonstrated the 970 MHz was suitable for PM2.5 particle sensing. Excellent results were found with the 1 µm particles, although inconclusive data was obtained for the larger particles (7 µm). For this work, in terms of air quality monitoring, small particles <2.5 µm are of particular interest due to their associated health risks. The larger diameter particles do not pose significant danger when inhaled compared to the smaller particles, thus PM2.5 is the focus of this work.

Following the characterisation of the SMR, a particle sensor unit was constructed based on the 970 MHz SMR device. The development of this sensing unit is discussed in the next section.

5.5 DISCRETE PARTICLE SENSING UNIT

A particle sensing unit was developed to operate in dual mode configuration with two 970 MHz SMR devices. In this section, the development of the electronic interface circuity and readout system is described. The completed sensing unit represents the basis towards a portable, real-time and low-power particle sensor based on solidly mounted resonators.

5.5.1 OVERALL DESCRIPTION OF THE SYSTEM

The block diagram in Figure 5.9 shows an overview of the developed particle sensor. The system operates in dual mode configuration for the suppression of common environmental effects, with one SMR working as a reference channel and the second as a sensing channel.
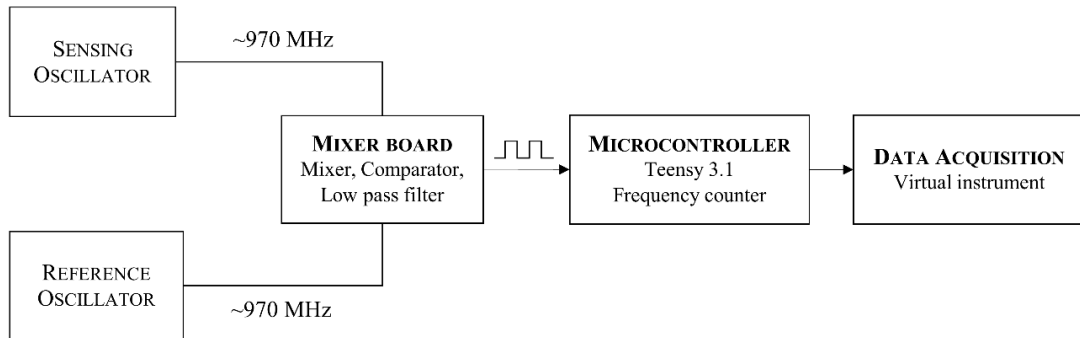
Figure 5.9 Overall outline of the discrete particle sensor based on SMRs.

The 970 MHz SMR devices were driven by Colpitts type oscillators. The output signals of the oscillators are sent to an interface mixer board comprising of an RF mixer, a low pass filter and a comparator, as shown by the block diagram in Figure 5.9. The high frequency signals of the oscillators are mixed in a heterodyne process and the mixer output is filtered (10 MHz low pass filter) to obtain a differential frequency output. A comparator is used to turn the sinusoidal signal into a low

frequency square wave (<10 MHz) which can be measured using a microcontroller at high resolution (1 Hz).

The output frequency data are logged to a PC via USB serial communication using National Instruments LabVIEW virtual instrumentation. An exploded view of the particle sensing unit is shown in Figure 5.10. Each component of the diagram is discussed in detail in the following subsections.
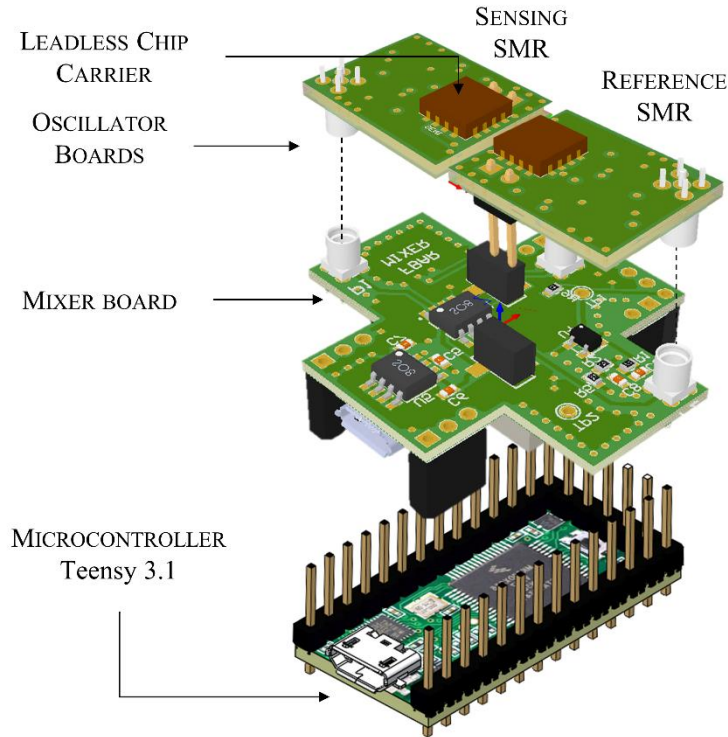
Figure 5.10 Overall structure of the developed particle sensing unit showing the three main parts forming the particle sensor.

5.5.2 READOUT CIRCUITRY

VNAs can provide useful information on the electrical performance of SMRs (as presented in Chapter 4). However, due to their high cost and physically large size, they are only suitable for performing device characterisation and in-lab measurements, such as those described in section 5.4. To develop a portable, low-cost and low-power system for use in real-time air quality monitoring applications, an electronic readout circuit is necessary. This section describes the development of a discrete system comprising of Colpitts oscillators (to drive the SMRs) and mixer circuitry.

5.5.2.1   DISCRETE COLPITTS OSCILLATOR

To drive the SMR devices, a Colpitts type oscillator was designed by Mr Sanju Thomas, research assitant at the University of Warwick (UK). For the oscillator design, an equivalent MBVD model was used. The circuit was designed in parallel with the fabrication of the SMR devices. To obtain the equivalent MBVD model, the COMSOL modelling data presented in section 3.3.3 was employed, together with performance characteristics measured from an available FBAR device (740 MHz),

The designed Colpitts oscillator circuit is depicted in Figure 5.11a. The SMR device operates in a one port configuration with one terminal grounded. A low noise silicon transistor BFR92P (Infineon Technologies) provides the gain stage in the oscillator loop. An oscillator based on a RF transistor was selected due to its desirable performance (significantly reduced parasitic capacitances) and lower cost compared to an op-amp based solution. Further details on the Colpitts oscillator design are reported by Thomas *et al.* [11]. The measured output spectrum of the SMR-Colpitts oscillator used in the particle sensing unit is shown in Figure 5.11b. The oscillator demonstrated satisfactory performance, although poor frequency stability was observed. Furthermore, operating the Colpitts circuit at higher frequencies (>600 MHz) can lead to reduced performance, due to the build-up of parasitic impedance, which can cause the oscillator to become damped.

The SMRs were wire-bonded onto a 16 pin leadless chip carrier (LCC) package (0.25 inch square, LCC01627 Spectrum Semiconductors, USA) to be interfaced to the oscillator boards. The reference SMR was covered with a small and thin cap fabricated using a Perfactory® III Mini SXGA+ (EnvisionTech, Germany) rapid prototyping machine via microstereolithography (MSL). This cap prevented particles from falling onto the surface of the reference device while still being exposed to the same ambient conditions.

(a)   (b)
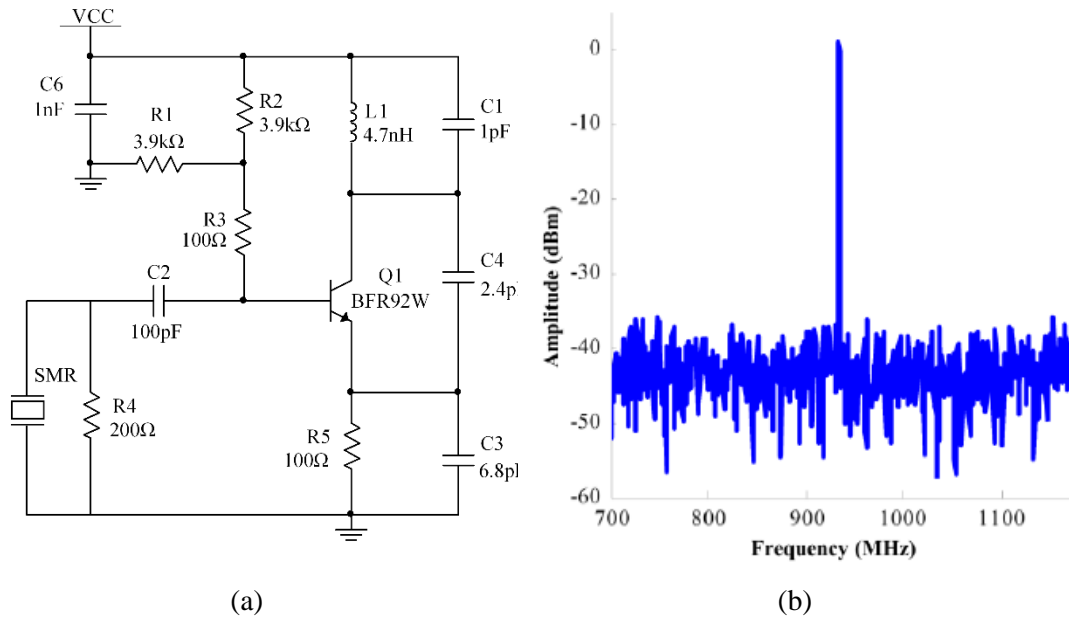
Figure 5.11 (a) Schematic diagram of the Colpitts Oscillator circuit to drive the SMR devices and (b) Output spectrum of the SMR-Colpitts oscillator [11].

5.5.2.2 MIXING CIRCUIT

A separate interface board was designed to mix the SMR signals, based on a basic circuit schematic provided by Mr Sanju Thomas, University of Warwick (UK). The implementation of the circuit is shown in Figure 5.12. The mixer board consisted of a double balanced RF signal mixer HMC207AS8 (Hittite Microwave Corporation), a RF low pass filter SCLF-10 (Mini-circuits®) and a comparator ADCMP600 (Analog Devices).
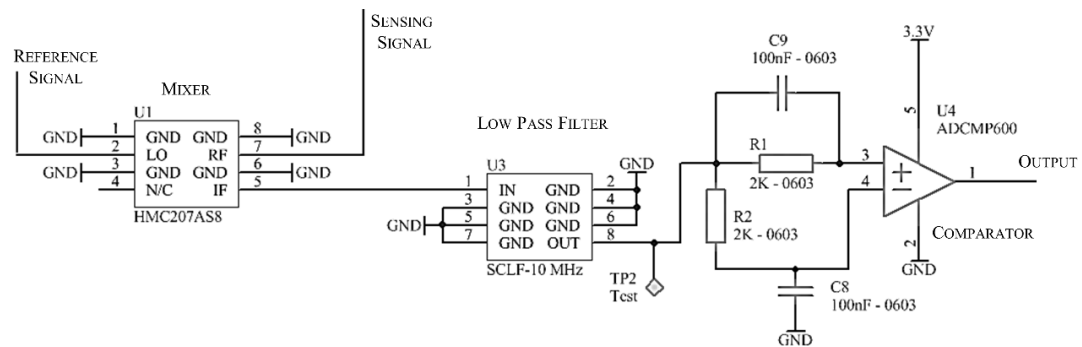
Figure 5.12 Basic mixer circuitry schematic design.

The reference and sensing oscillator frequencies are mixed using a heterodyne down-conversion technique. The low pass filter (cut-off frequency of 10 MHz) was

used to output only the differential frequency. In this way, the mixer circuit helps reduce both the effects of common mode variations and the output frequency signal range (to the kHz range). The comparator converts this differential output into a square signal with a voltage level of 3.3 V (the maximum tolerated voltage for the microcontroller input pin).

The low current consumption of the circuitry (300 mA) allowed the boards to be powered from a single 5 V USB port. A micro USB connection is included in the mixer board, so the oscillator circuitry can be tested independently, without a microcontroller. In the assembled sensor unit, the mixer board is powered from the 5 V rail on the microcontroller, which is powered from a USB connection to a PC.

A dual linear voltage regulator MIC5212 (Micrel®) was used to generate 2.5 V for the SMR-Colpitts oscillators and 3.3 V for the comparator. The shape of the board was designed to be integrated with the selected microcontroller (Teensy 3.1, PJRC) and to accommodate two SMR oscillator boards.

The mixer board was designed as a four-layer PCB with separate ground and power planes. RF cross-talk was reduced and impedance mismatching minimised through careful layout design. The characteristic impedance of the PCB tracks was set to 50 Ω. The length of the RF tracks was kept as short as possible to minimise current flow and loop area with multiple vias connected to ground in close proximity to the signal tracks. MMCX RF connectors (50 Ω impedance) were used to connect to the oscillator board signals ensuring several ground connections were made.

The majority of the components were placed on the top layer of the PCB with only the low pass filter placed on the bottom layer. Vias carrying the RF signals were avoided where possible. The mixer and oscillator boards were designed using Altium Designer (15.0) and manufactured by Eurocircuits (Belgium).

5.5.3 DATA ACQUISITION

Professional acquisition systems, such as National Instruments data acquisition (DAQ) cards, can be used to record the sensor response in a laboratory setting. These costly systems offer high resolution measurements (16-bit) and convenient companion

software. During the first stages in the development of the particle sensor, a DAQ board PCI-6602 (National Instruments) was used to acquire data output of the unit for initial testing. However, portable air quality monitoring systems need to be low power, low-cost and physically small. Microcontrollers offer an affordable solution for these requirements and are ideal for recording sensor data and transmitting it to a central database.

For the development of the particle sensing unit, a low-cost microcontroller Teensy 3.1 was selected to count the frequency of the output square wave signal [12]. The compact size of this microcontroller (17.8 mm $\times$ 35.6 mm) enabled it be integrated within the acoustic sensor system as shown in Figure 5.13. The Teensy board offers a simple access to a powerful microprocessor, without unnecessary and bulky components or interfaces (e.g. additional USB ports, power connectors or switches). The Teensy 3.1 microcontroller has excellent data acquisition properties, with a built-in high quality (16 bit) analogue to digital converter and a 72 MHz Coretx-M4 processor. A dedicated pin is available to measure a high frequency input (~65 MHz).
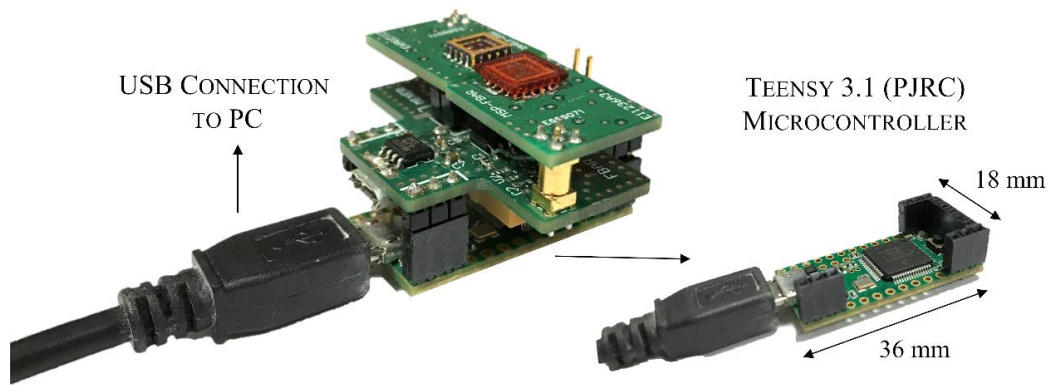
Figure 5.13 Low-cost microcontroller was integrated within the particle sensor for data acquisition and interfaced to the PC via USB serial communication.

A software library was used to perform the frequency counting on the Teensy microcontroller. In brief, the dedicated frequency input pin is connected to a timer in the microprocessor. A short period of data is captured (of precisely 100 ms) and analysed using the software library. The frequency of the signal is calculated, in real-time on the microcontroller, by counting the number of cycles found in this captured

data. The dedicated interrupt time on the microcontroller enables frequency measurement to within ± 1 Hz (with an input signal measured in the MHz range).

To visualise the sensor response (i.e. a change in output frequency), the microcontroller was linked to a computer via a USB serial connection. The frequency data transmitted from the microcontroller was recorded and plotted in real time with a virtual instrument developed using National Instruments LabVIEW software. A screen print of the front panel user interface is shown in Figure 5.14. The software was designed to enable real-time visualisation and storage of the response data from multiple particle sensors simultaneously.
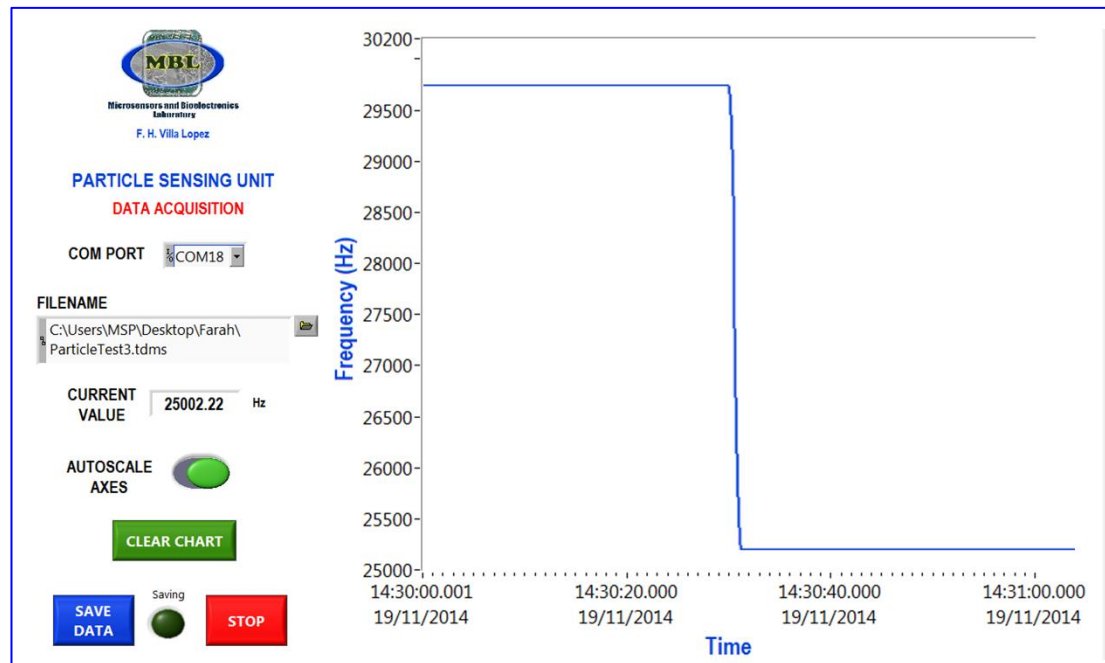
Figure 5.14 Screen shot of developed LabVIEW front panel showing frequency response data of one particle sensor unit acquired using the microcontroller.

5.5.4 EXPERIMENTAL SETUP

The assembled particle sensing unit (shown in Figure 5.15) was enclosed in an acrylic housing to protect the electronic circuitry. Overall dimensions of the enclosed unit are 49 mm × 44 mm × 34 mm. However, the sensing unit itself is smaller with overall dimensions of 41 mm × 36 mm × 25 mm. An alternative case, fabricated using 3D printing technology can be fabricated to minimise the footprint of the enclosed sensing unit and allow easy access to the USB port.

(a)   (b)
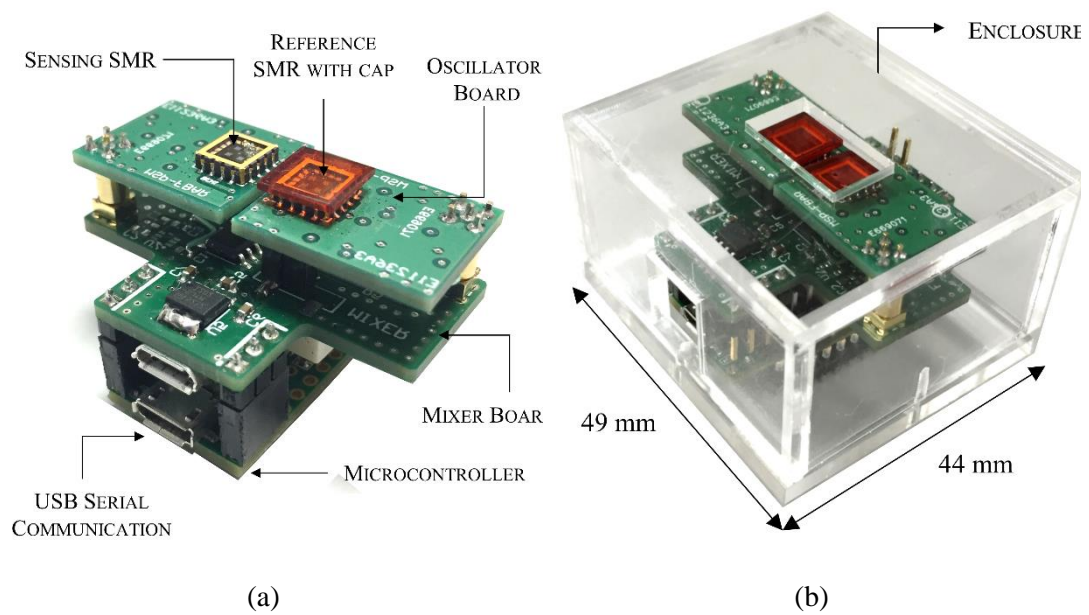
Figure 5.15 Photograph of (a) the discrete particle sensing unit and (b) enclosed unit.

Preliminary testing of the sensing unit was performed at the Microsensors and Bioelectronics Laboratory within a particle testing chamber (experimental setup shown in Figure 5.16). The test particles are deposited onto a conveyer belt driven by a DC motor with adjustable speed and direction. A Venturi tube is located above the belt system. Particles are drawn into the chamber by the Venturi tube connected to the compressed air supply. Residual particles are collected in a tray located underneath the belt system. For the safe disposal of the particles, the air exhaust of the chamber connects to a vacuum pump that empties the remaining particles.

The sensing unit was placed inside the chamber (5.625 L) together with reference particle monitors, namely the DC1700 air quality monitor (Dylos Corporation, USA) and the DN7C3CA006 Dust sensor (Sharp Corporation, Japan). These are affordable instruments based on optical principles (<$200). The Dylos instrument has a serial output which allows data to be logged on a computer (using provided data logging software). It takes one measurement per minute and can classify PM2.5 and PM10 particles.
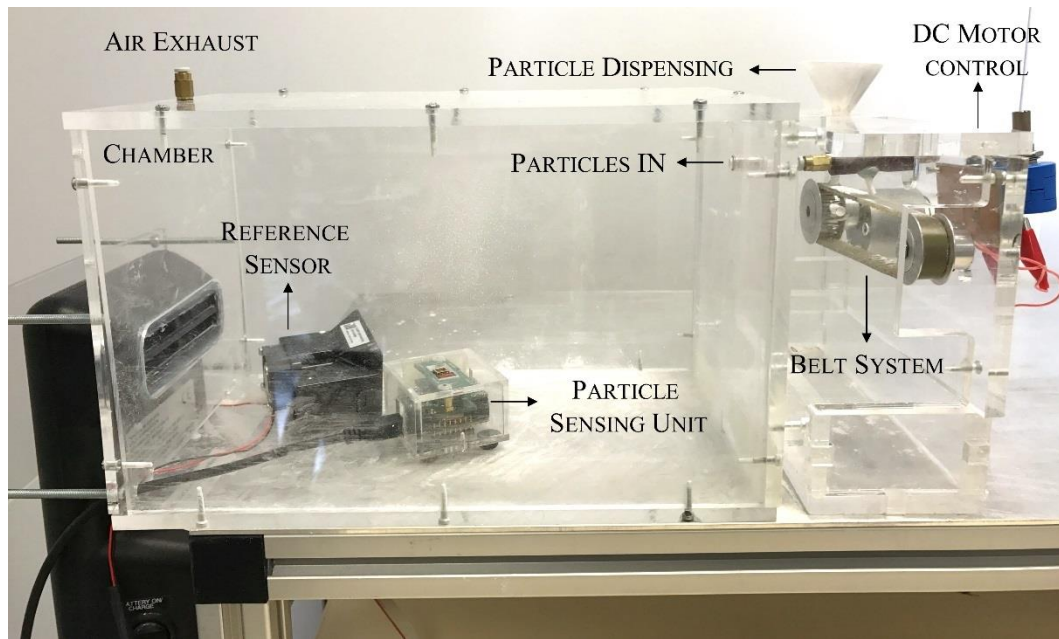
Figure 5.16 Photograph of the experimental setup used for particle testing.

The Sharp dust sensor was interfaced to an electronic circuit and microcontroller (Teensy 3.2) for data acquisition. A dedicated LabVIEW virtual instrument was developed for the real-time monitoring and data logging of the three signals measured from the sensing unit and reference instruments (Figure 5.17). Data was logged at 1 Hz for the Dylos and at 10 Hz for the Sharp and SMR sensor.
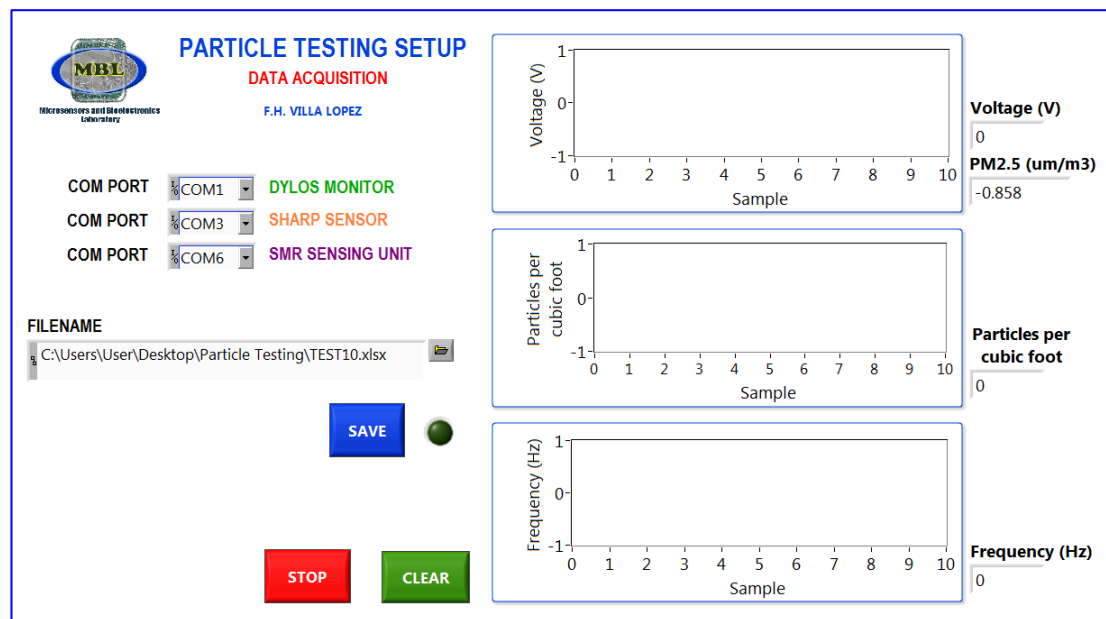
Figure 5.17 Data acquisition software and instrumentation used within the testing setup.

A stabilisation period of 45 minutes was allowed prior to the injection of any test particles. PTFE 1 µm particles were then injected into the chamber for 10 seconds using the Venturi system. Response data from the devices were logged for a further period of 65 minutes to allow the outputs to stabilise, as shown in Figure 5.18. The raw data recorded by the Dylos monitor is given in units of particles/ft^3; for useful comparison, the data was converted into units of µg/m^3.
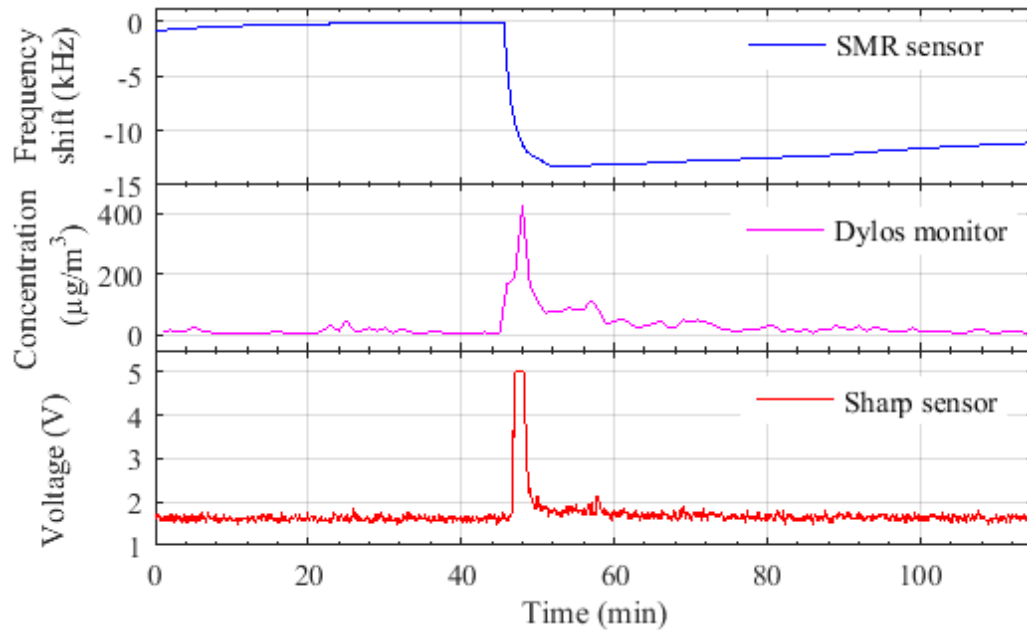
Figure 5.18 Time response of SMR based particle sensor unit to PTFE 1 µm particles compared to commercial optical devices (Sharp corporation and Dylos monitor).

A fast response was produced from the reference sensors following the injection of the test particles. The response from the SMR sensor was slower compared to the commercial optical sensors. The commercial devices both use an active sampling technique (fans draw air into the instruments) as opposed to the passive method (gravitational sedimentation) used in the SMR.

The SMR sensor had a response time t_{10} (time to reach 10% of the final value) of 43 seconds and t_{90} (time to reach 90% of the final value) of 207 seconds. By comparison the Sharp sensor had a t_{10} of 100 seconds and t_{90} of 116 seconds, assuming a maximum output of 5 V. The output from the Sharp sensor was saturated by the particle density in the chamber. The slow logging frequency (1 sample/minute) of the

Dylos sensor prevented the response time calculation. The peak value is recorded on the third data point after the injection.

Momentarily after the injection of the test particles, the air in the chamber has a very high density of particles. As the particles settle on the base of the chamber, the density of particles in the air decreases. The SMR sensor does not recover to its baseline resonant frequency as particles accumulate on the surface during the experiment (no method is employed to remove the particles). A frequency shift of ~13 kHz was measured for a particle concentration of 422 µg/m^3 (recorded by the Dylos). The temperature inside the chamber increased during the experiment, which caused the SMR sensor output to drift by ~2 kHz over the 115 minute experiment.

A photograph of the surface of the sensing SMR is shown in Figure 5.19, taken using an optical microscope after the experiment. Several large clumps of particles are visible, as well as hundreds of individual particles. Due to their size and mass the large clumps become deposited quickly causing the initial response of the SMR sensor. The individual particles take a longer period of time to deposit. The final recorded frequency shift reflects the total mass of particles on the sensor surface.
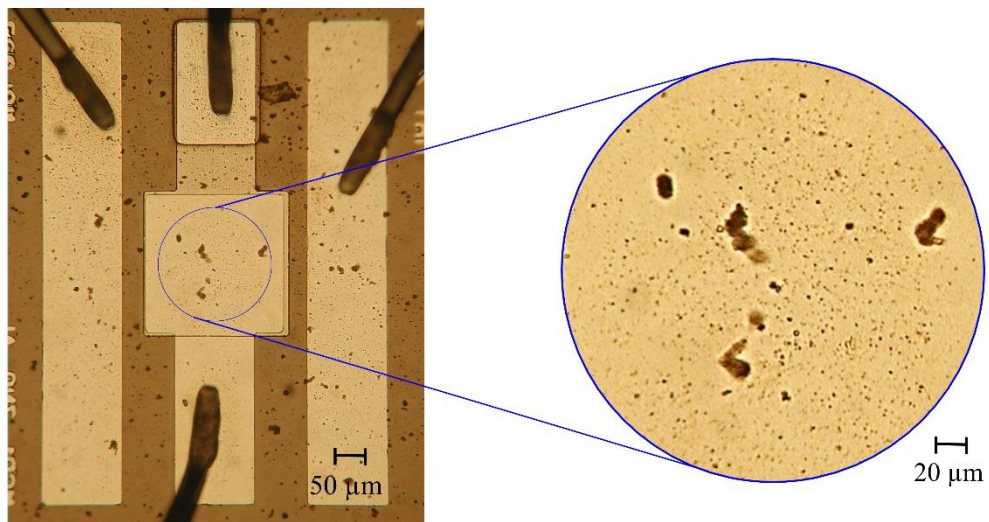
Figure 5.19 Particles deposited on the sensing area of the SMR, view at 20× magnification.

The commercial devices sample air from inside the chamber. Both devices produced a large response immediately following the injection of the particles. As the particles settle, the amount suspended in the air decreases, which causes a reduction in

the values recorded by the commercial devices. Towards the end of the experiment, the output values from the commercial instruments return close to their baseline values. The devices do not recover completely to their initial readings, as a low number of particles remain in the air.

The developed particle sensor unit relies on gravitational sedimentation of particles to deposit on the sensor surface. Large particles (>30 µm) will settle in a few seconds in the chamber shown above (with the particle injection point at only 15 cm above the particle sensor). Smaller sized particles (<10 µm) can stay in the air for longer periods of time (several minutes) and UFPs are unlikely to deposit due to their insignificant gravitational forces. Although the gravitational collection method used with this sensor is not optimal, it provides a good approach for characterisation purposes with valuable information obtained from the characterisation of this first prototype.

To calculate the sensitivity of the sensor unit, the device was exposed to different concentrations of 1 µm PTFE particles. Figure 5.20 shows the frequency shift of the SMR after each injection together with the corresponding particle concentrations measured by the Dylos monitor. A linear fit was applied to the data and the sensitivity was calculated as 27.5 Hz per µg/m^3. The SMR produced a linear response to the concentrations over the tested particle concentration range. A good R^2 value of 0.9686 (R is coefficient of correlation) was obtained.
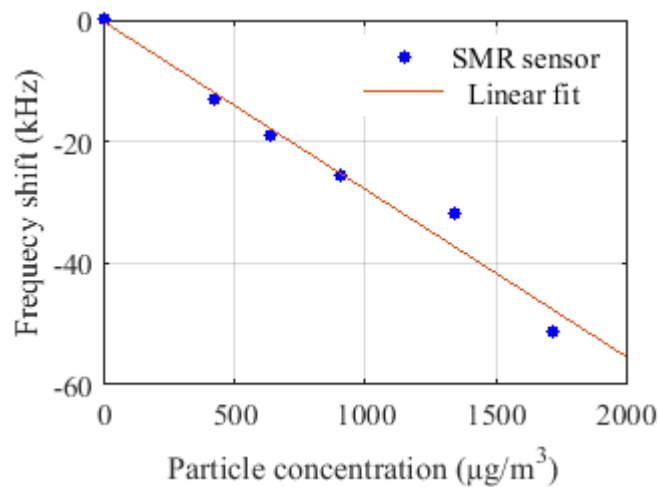
Figure 5.20 Frequency shift of the SMR sensor unit following the exposure to particle concentrations in the range of 400 to 1720 µg/m^3.

Further characterisation of the developed particle sensor was performed at VITO NV, Belgium as part of the European Commission 7th Framework Programme, Project entitled "Multi-sensor Platform for Smart Building Management". VITO is a leading research organisation with expertise in air quality monitoring and particulate matter measurements. Several sensing units were constructed and tested before being sent to the facilities at VITO were the particle testing was performed[3] inside an environmental chamber with aerosol particles of known size and composition. A block diagram of the experimental setup at VITO is depicted in Figure 5.21.
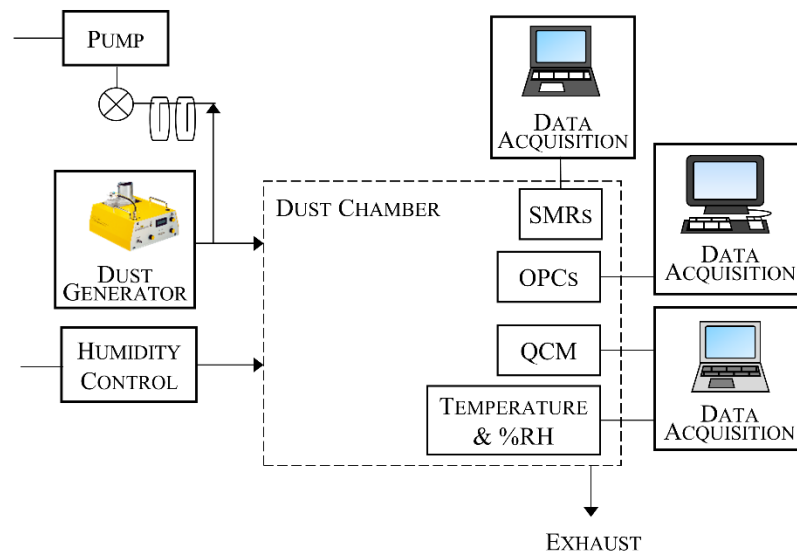
Figure 5.21 Schematic of the experimental setup performed in the environmental chamber.

A large test chamber with internal volume of 720 L (shown in Figure 5.22a) was used to test the SMR based particle sensors. A commercial quartz crystal microbalance (Vitrolcell® Systems, Germany) was placed adjacent to the SMR research sensors together with two commercial optical based particle counters: the Dylos optical sensor, used in preliminary laboratory testing, and a second instrument (Grimm Technologies Inc., USA). The experimental setup is shown in Figure 5.22b. Real-time PM concentration readings from all the instruments were logged to dedicated computers. The environmental conditions inside the chamber (temperature and humidity) were monitored, with typical values of 24 °C and 22 %RH, respectively and variations within 1°C and 1 %RH.

---

[3] Experiments were conducted by Mr Sanju Thomas from the University of Warwick (UK); and Dr Jan Theunis and Dr Jan Peters from VITO (Belgium).

(a)   (b)
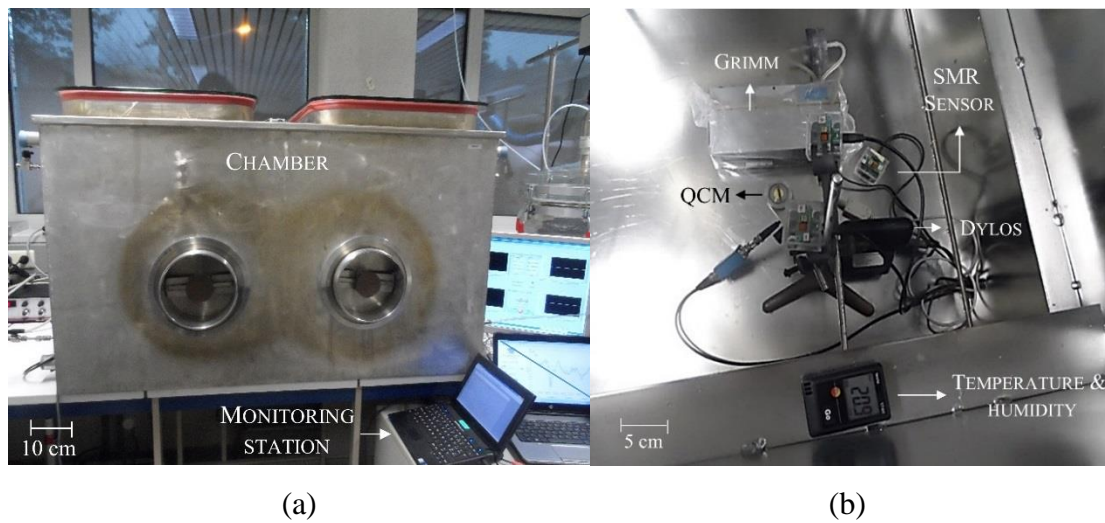
Figure 5.22 (a) Measurement chamber and logging equipment; (b) SMR based units and commercial instruments inside the chamber, located together in one corner. Temperature and humidity is monitored in the chamber.

A dust generator (TOPAS®) was used to generate the test particles, which were then injected into the test chamber using a suction pump. Arizona test dust (Powder Technology Inc., USA) was the target aerosol used in the experiments (nominal particle diameter of 0-3 µm). The median particle size distribution (d_{50}) of these particles was 0.927 µm. Only 10% of the particles tested were found to be below 0.712 µm (d_{10}); the remaining 90 % (d_{90}) of the particles were found to be below a diameter of 1.526 µm.

The free-settling velocity of Arizona dust particles was estimated from the Stokes' law, assuming spherical particles at ~180 µm/s for particles of 1.5 µm in size and ~80 µm/s for finer particles (1 µm diameter) [13]. In this experimental setup, it is therefore very unlikely that particles below 1 µm in size were detected given the large size of the chamber. Only the bigger particles were fall onto the resonator.

A number of experiments were performed, with particles injected into the chamber for a range of times (varying from 2 s up to 10 min). The commercial optical devices provided measurements of the particle concentration in the testing chamber in units of µg/m³. The reference Grimm monitor measured concentrations as low as 20 µg/m³ and as high as 30,000 µg/m³ (naturally, the highest concentrations were obtained with the longer injection periods).

For acoustic devices, the magnitude of the frequency shift is related to the number of particles which settle on the sensors of the surface (a greater number of particles is expected on the surface of the device when a greater amount is injected). A frequency shift is only shown when the particles have settled on the surface of the device, thus a slower response is likely from devices which do not use an active sampling method.

During the experiments, no facilities were available to photograph or view the particles deposited onto the surface of the acoustic devices. The mass of the particles on the sensor surface could not be determined. Therefore, the sensitivity of the SMR devices was estimated in terms of frequency shift per $\mu g/m^3$ with particle mass concentration inferred from the optical reference instruments.

To ensure the ambient temperature inside the environmental chamber remained constant, the chamber was sealed using a rubber gasket. Sealing the chamber was also important to prevent the deposition of any foreign matter onto the sensors and to avoid air movement effects disrupting the particle deposition process. The cap used to cover the reference SMR device is semipermeable and thus sufficient time (of at least 2 hours) was left for stabilisation of the system to ensure that both the reference and sensing devices were exposed to the same environmental conditions. The differential mode operation of the SMR sensor helped to eliminate any gradual changes in temperature or humidity.

The injection of the test particles into the environmental chamber caused a change in the oscillating frequency of the SMR based sensor, when the system was exposed to a predefined amount of dust concentration. The additional mass on the surface of the sensor (i.e. the nanoparticles) decreased the resonant frequency of the SMR device. A typical response of the sensor is shown in Figure 5.23. For a particle concentration of ~60 mg/m^3 recorded by the Grimm 1.107 monitor (Grimm technologies), a frequency shift of ~315 kHz was observed for the SMR based sensor exposed to Arizona dust.

The SMR sensor system demonstrated a response to the Arizona dust after a period of ~2 min after the dust was injected into the chamber. As the deposition method was based on the sedimentation of the particles, a delay (in the range of minutes) was

expected until the first particles deposit on the device. The commercial QCM device, which works on the same principle as the SMR demonstrates a similar delay before a response is produced for the injection of the dust particles. The mass of the particles on the sensor surfaces of both the SMR and QCM based devices caused a decrease in their respective resonant frequencies. An advantage of the SMR system, operating at high frequency, is greater mass sensitivity compared to the commercial QCM sensor (which operates at a lower frequency of 5 MHz). The mass sensitivity demonstrated by the SMR sensor is orders of magnitude higher than the QCM device (kHz range compared to low Hz range, respectively), as shown in Figure 5.23.
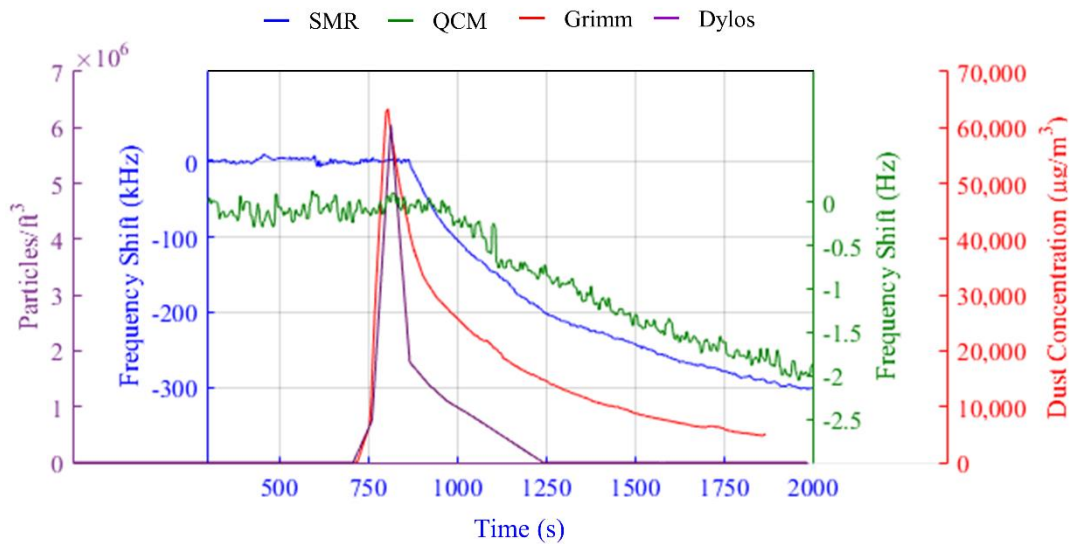
Figure 5.23 Response of the particle sensors to an injection of Arizona dust particles. Frequency response of the SMR and QCM compared to the reference commercial OPC.

To calculate the sensitivity of the SMR particle sensor, the frequency response of the device was measured to various levels of dust concentrations. A linear relationship was found, as shown in Figure 5.24, between the SMR frequency shift and particle concentration. An R^2 value of 0.9812 was calculated demonstrating the linear fit is a good approximation of the SMR output. Considering the set of experiments shown, a sensitivity of 4.6 Hz per µg/m^3 was calculated. The limit of detection was noted as ~ 20 µg/m^3 for the SMR based particle sensor. As the layers of particles start to build up on the sensor surface, it is expected that the sensor will saturate. However, no saturation was observed up to a particle concentration of 60,000 µg/m^3 in this work.
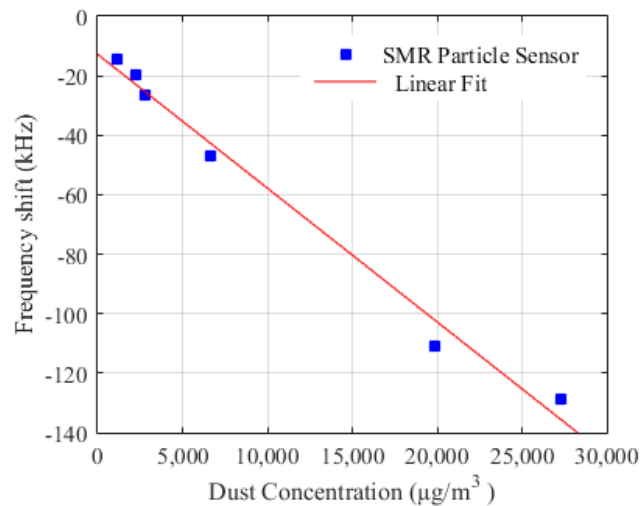
Figure 5.24 Linear response of SMR sensor to dust concentration in the range of 20 to 25,000 µg/m³.

The particle sensing unit relied upon gravitational sedimentation for the particles to deposit on the surface of the SMR sensors. The experimental results demonstrated that this passive sampling method did not provide an effective means of determining the particle concentration inside a chamber. A far greater sensitivity was achieved in the experiment performed in the small chamber (27.5 Hz per µg/m³), shown in Figure 5.20, compared to the sensitivity calculated from the Figure 5.24 (4.6 Hz per µg/m³, performed in the large chamber at VITO).

A possible cause of the lower sensitivity is uneven particle distribution in the larger chamber. The commercial optical sensors use fans to sample air from across the chamber. The SMR sensor can only sample the concentration of particles that are immediately above the unit (which deposit onto the sensor surface). Therefore, the SMR sensor was vulnerable to uneven particle distribution, as only a tiny area of the large chamber is sampled and the sensors were located in one corner. In the small chamber the SMR unit was placed in the centre of the chamber, at a suitable distance from the particle inlet so that the volume above the sensing surface would contain a uniform distribution of particles.

In real field conditions, the sensing unit would not be selective to the target PM2.5. Particles of any size (i.e. of greater diameter) could become deposited on the surface of the device and produce a false response. The sensing unit had a slow

response time (order of several minutes) due to the slow settling velocity of the micro-sized particles. Thus, the system is not suitable for real-time monitoring. The following section presents the design of a virtual impactor to overcome the sampling issues found with this first prototype unit.

5.6 VIRTUAL IMPACTOR FOR PORTABLE PARTICLE SENSOR SYSTEM

To address the limitations of the first unit, a second particle sensing system was developed, incorporating a custom virtual impactor for particle sampling and separation. The system was further miniaturised by the use of an ASIC chip, which replaced the discrete oscillator boards and mixer circuitry from the previous design. The ASIC interfaced two SMR devices and performed the necessary signal processing to produce a signal suitable for acquisition with a microcontroller.

5.6.1 OVERALL OUTLINE

The particle sensing system was comprised of two main parts, a hybrid electronic system for signal processing and a virtual impactor for selective particle sampling. A block diagram for the operation of the system is shown in Figure 5.25. The top part of the diagram shows how air is drawn through the system using a low-power miniature fan and then desired particles are separated using a virtual impactor. The lower part of the diagram shows the electronic operation of the system (discussed in section 5.6.2).

The hybrid electronic system consisted of three components: an ASIC chip, a reference SMR device (not exposed to the particles) and a sensing SMR device (to detect PM2.5). The ASIC chip reduced the discrete components required in the system, thereby reducing the power consumption of the setup and the overall size of the interface PCB. The ASIC and SMRs were wire-bonded to the interface PCB, which provided a test bench for the integrated system to characterise the devices and the substrate for the virtual impactor to be integrated. Control circuitry for the sampling mini fan was also included in the PCB design. A drawing of the complete implementation of the system is shown in Figure 5.26.
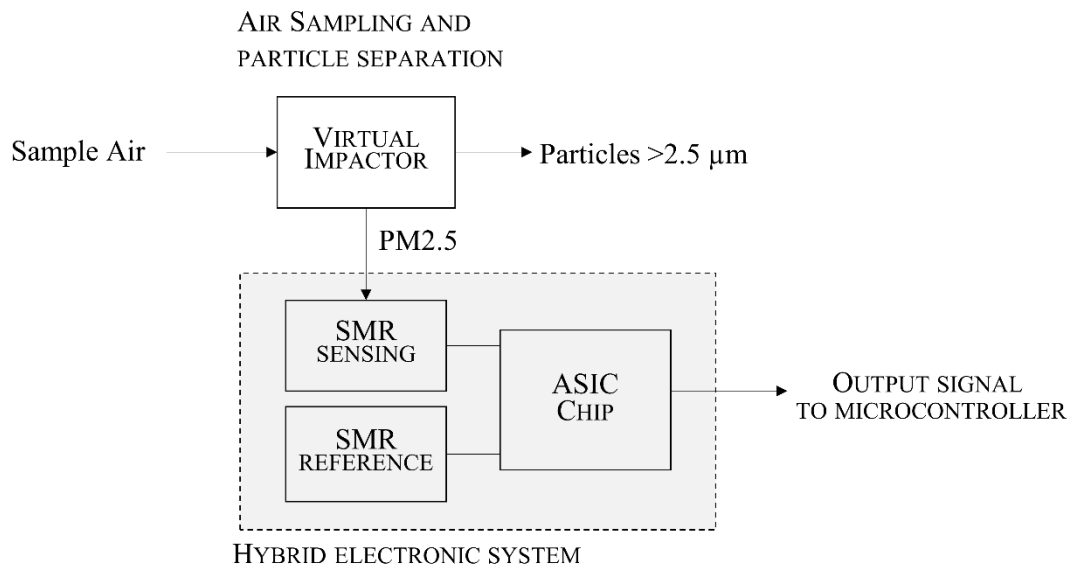
Figure 5.25 Block diagram to show operation of particle sensing system.
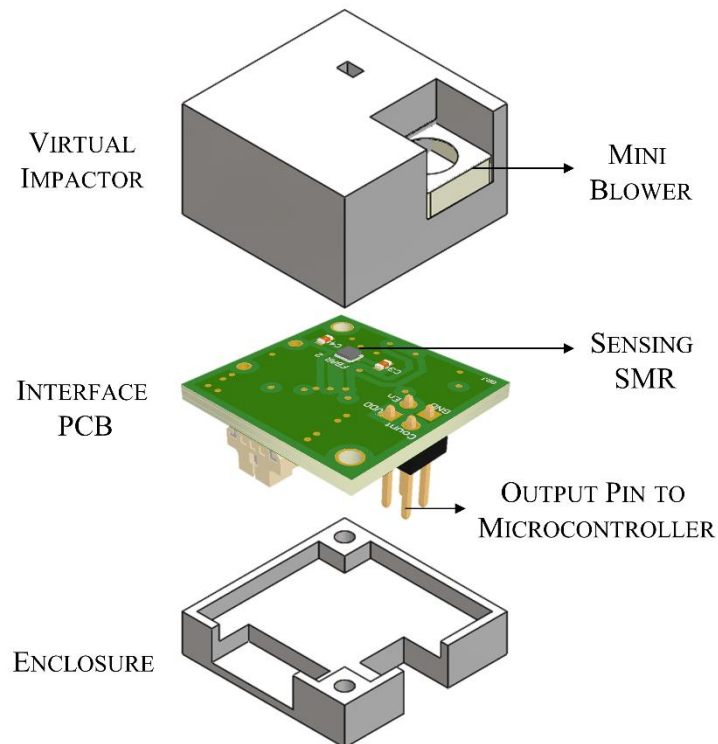
Figure 5.26 Exploded drawing of particle sensing system with overall dimensions of 22 mm × 22 mm.

The virtual impactor was designed for a cut-off particle diameter of 2.5 µm. A miniature blower was used to continuously draw samples of air through the virtual impactor. A blower was selected to miniaturise the system and to reduce the power consumption compared to an alternative pump. Thus, a compact, lightweight but robust system could be obtained. The impactor separated the particles according to their aerodynamic diameter, with the PM2.5 directed towards the surface of the sensing SMR device and larger diameter particles ejected back to the ambient air.

5.6.2   HYBRID ELECTRONIC SYSTEM

The ASIC was developed to replace the majority of the discrete circuitry needed in the previous system, to enable the particle sensing unit to be compact and portable. The chip was designed and simulated using Cadence spectreRF (2013) by Mr Sanju Thomas, University of Warwick (UK). It was fabricated at AMS (Austria) using a 0.35 µm CMOS process.

A block diagram of the internal circuitry of the chip is shown in Figure 5.27. A low-power Pierce oscillator configuration was selected for use in the ASIC. This oscillator design replaced the Colpitts oscillator used in the discrete oscillator circuitry, to give the advantages of self-biasing, current-reuse and low power consumption [14]. A Gilbert Cell active mixer was used in the ASIC to provide high conversion gain and efficient frequency translation. The signals from the oscillator circuitry are converted from single to doubled-ended form, suitable for the Gilbert cell mixer.

A balun (balanced-to-unbalanced) converter translates the doubled-ended output signal from the Gilbert mixer to a single-ended signal, for further signal processing. A low-pass filter is used to remove harmonics at high frequencies above the fundamental mixer output. Finally, the signal is passed through a comparator, to produce a form suitable for reading with a microcontroller.
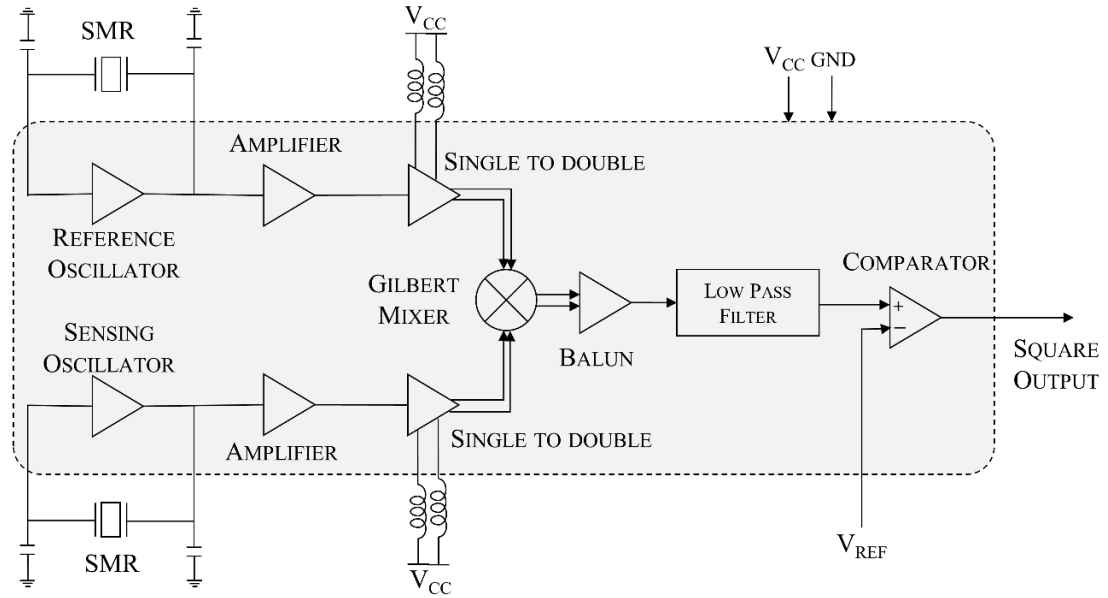
Figure 5.27 Block diagram of ASIC showing internal operation. Circuitry in the ASIC is highlighted.

The interface PCB (designed by Mr Rhys Jones, PhD student at University of Warwick) was developed to test the SMR sensors with the ASIC chip to exposure of PM2.5. This interface PCB was integrated with the designed virtual impactor and provided a square wave output from the ASIC ready to be acquired by the microcontroller. A photograph of the ASIC and SMR devices wire-bonded onto the PCB is shown in Figure 5.28. The ASIC chip measures an area of 1.65×1.55 mm^2, including input and output pads.

(a)   (b)
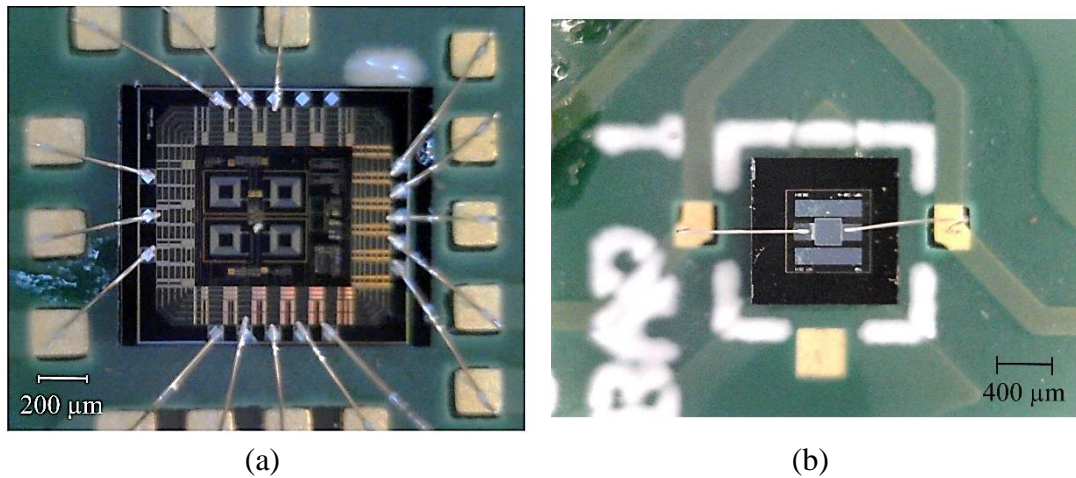
Figure 5.28 Photograph of (a) the ASIC chip and (b) the SMR wire-bonded to the interface PCB.

5.6.3   VIRTUAL IMPACTOR DESIGN

An air sampling system comprising of a virtual impactor and a miniature blower was incorporated into the sensing unit for the separation and collection of airborne particles according to their aerodynamic size. The use of a virtual impactor allows particles of the desired size to be directed towards the surface of the sensor. The blower draws samples of air through the impactor, where the particle separation takes place. A diagram of a virtual impactor depicting the air flow distribution and design dimensions is shown in Figure 5.29.
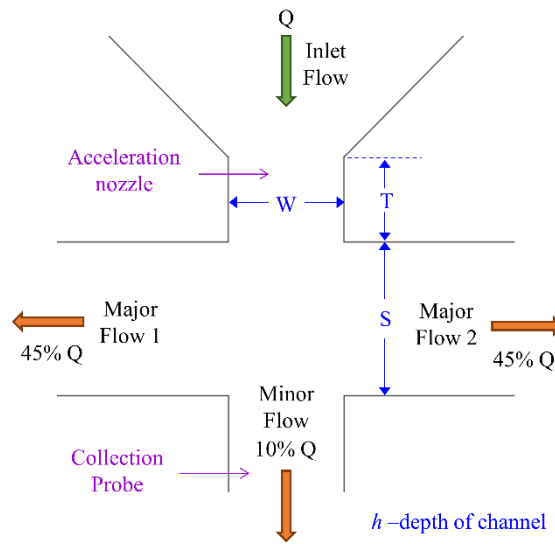
Figure 5.29 Diagram of rectangular nozzle virtual impactor.

The sample air, with total flow rate Q, is drawn through the acceleration nozzle of the virtual impactor of width W and length T. This sample air containing large and small particles flows in three separate trajectories. A minor portion of the total flow (~10%) continues straight towards the collection probe carrying the larger particles (with aerodynamic diameter greater than the design cut-off size) due to their large inertia. The smaller particles (with low inertia and particle size below the design cut-off diameter) follow the two major flow channels (of width S), normal to the acceleration nozzle and away from the collection probe with a total of ~90% of the inlet flow.

The Stokes' number, St_{50}, defined as the ratio of the particle stopping distance to the half width of the impactor nozzle [15] and the Reynolds number, Re, are the two main parameters in the design of the virtual impactor, both of them dimensionless. For a rectangular nozzle impactor, these two parameters are given as [16]:

$$St_{50} = \frac{\rho_p Q C d^2{}_{50}}{9\mu h W^2} \tag{5.1}$$

$$Re = \frac{2\rho Q}{\mu h} \tag{5.2}$$

where ρ_p and d_{50} are the particle density and cut-off diameter (aerodynamic diameter of a particle with collection efficiency of 50 %), respectively. Q is the total flow rate at the acceleration nozzle, ρ and μ are the air density and dynamic viscosity, W and h are the width of the acceleration nozzle and height of the channel, respectively. C is the Cunningham slip correction factor given as:

$$C = 1 + \frac{2}{Pd_{50}}(6.32 + 2.01 \cdot e^{-0.1095 Pd_{50}}) \tag{5.3}$$

where P is the absolute pressure in cmHg. The collection efficiency, η, of a virtual impactor measures the ratio between the number of particles collected from the minor channel, N_m, to the total number of particles entering the inlet flow, N_{in}. It can be expressed as:

$$\eta = \frac{N_{in} - N_m}{N_{in}} \times 100 \tag{5.4}$$

A laminar flow is required to minimize particle losses through the impactor channels. Sharp curves of collection efficiency are obtained with laminar flows (Reynold's number between 500 and 3000) [16, 17]. Following these criteria, the width of the acceleration nozzle and height of the rectangular channel were obtained for a Stokes' number of 0.23 [17].

The width of the major channels (also known as the jet to plane distance) was set to a minimum of 1.5 times the width of the acceleration nozzle. The ratio between

these two dimensions can strongly affect the collection efficiency of the impactor with a minimum recommended ratio of 1.5 for rectangular nozzles [16]. Finally, the length of the minor channel was chosen to achieve the desired flow rate distribution, with a total length of 150 mm.

A rectangular nozzle virtual impactor was designed for a cut-off particle diameter of 2.5 µm and particle density of 1000 kg/m^3. The impactor will direct particles with aerodynamic diameter below 2.5 µm towards the surface of the SMR device for the detection of PM2.5. A total flow rate of 1.17 l/min is provided by a mini blower (Sunon, Taiwan) with a low power consumption of 280 mW and compact size (9 mm×9 mm×3 mm). Final design parameters of the impactor are summarised in Table 5.1.

Table 5.1 Design parameters for the virtual impactor for integration with the portable particle sensor.

PARAMETER	FINAL DESIGN
Flow rate (Q)	1.17 l/min
Cut off diameter (d_{50})	2.5 µm
Particle density (d_p)	1000 kg/m^3
Stokes number (St_{50})	0.23
Air density (ρ)	1.225 kg/m^3
Air viscosity (μ)	1.98 ×10^{-5} Pa·s
Width of acceleration nozzle (W)	1.5 mm
Length of acceleration nozzle (T)	2.25 mm
Height of channel (h)	1.5 mm
Jet to plane distance (S)	2.25 mm
Reynolds number (Re)	1600
Footprint (mm^2)	4.84

The designed virtual impactor was simulated by means of computational fluid dynamics (CFD) using the flow simulation toolbox and particle trace study in SOLIDWORKS 2015. A drawing of the final impactor design (to be integrated with the sensing unit) is shown in Figure 5.30.
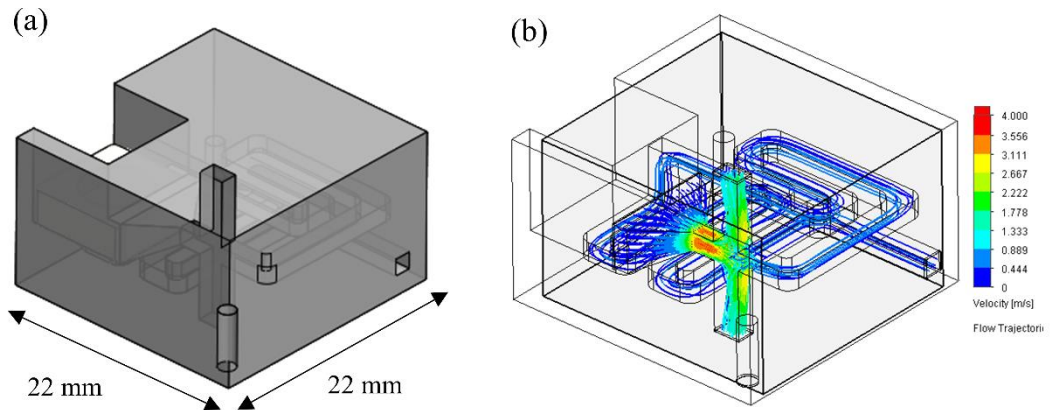
Figure 5.30 (a) Solidworks drawing for simulation of the virtual impactor the SMR based and (b) flow simulation of the structure.

The air flow distribution through the impactor and the separation of particles was analysed. Particles with a range of sizes (0.1 µm to 15 µm) were simulated at the inlet flow. Particles were defined considering their aerodynamic diameter (spherical particles with nominal density of 1000 kg/m^3). Computed particle trajectories were analysed and functionality of the impactor design was tested. The simulations results are presented in Figure 5.31.

The flow distribution ratio (minor and major channels) met the design criteria of 10% and 90%, respectively. The number of particles at the outlets of the minor and major flow was computed and the collection efficiency was calculated as shown in Figure 5.32. The majority of particles with aerodynamic diameter above 10 µm follow the minor channel flow, while most of the particles below the cut-off diameter are collected at the outlet of the major channels. The data were fitted using a sigmoidal function, from which a cut-off diameter of 2.5 µm was observed.

Flow distribution (velocity)	10 µm particle	7 µm particle
5 µm particle	PM2.5	0.5 µm particle
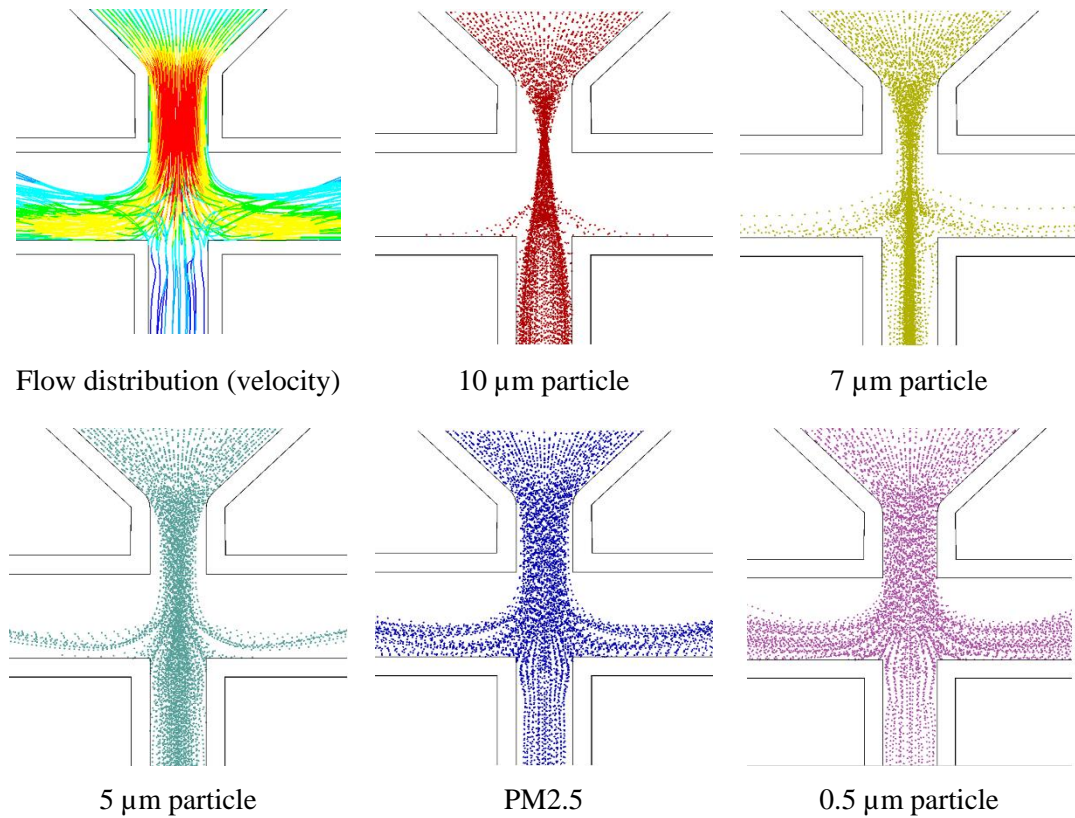
Figure 5.31 Virtual Impactor simulation results: distribution and particle trajectories.
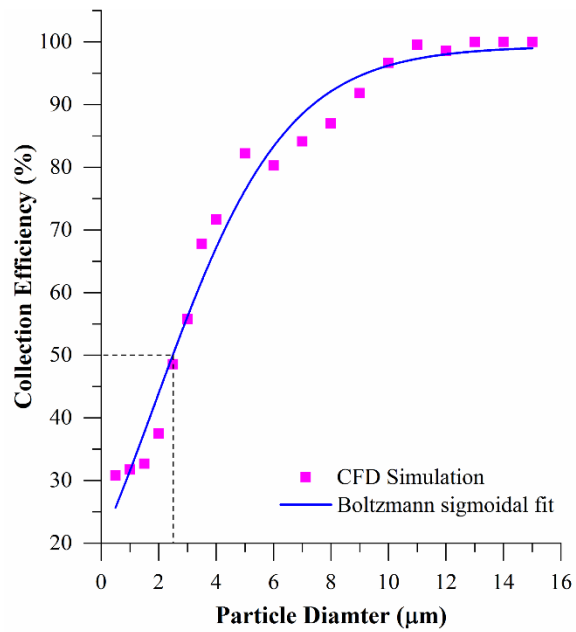
Figure 5.32 Simulated collection efficiency of the designed virtual impactor.

Design of the virtual impactor was optimised to avoid particle clogging in the channels. The channels were designed to have smooth corners and minimum 90° bends. After prolonged used in a high-density particle environment it is likely that high volume of particles will accumulate on the walls of the channels and clog the impactor. This is especially likely if great quantities of large diameter particles (>30 µm) are present in the environment. If the device is to be used in such environments it would be beneficial to used cascaded virtual impactors. In this way, larger diameter particles could be separated during a first stage impactor (with wider channels which are unlikely to clog).

5.6.3.1 MANUFACTURE OF THE VIRTUAL IMPACTOR

The virtual impactor was manufactured using a 3D printer (Formlabs Form 2), which offered flexible designs and rapid prototyping. 3D printing the part allowed the virtual impactor design to be optimised and iterative improvements were made during its design cycle. The total cost of the materials used in the 3D printing method is too expensive for bulk manufacturing although it was affordable (€1.5) compared to the alternative subtractive manufacturing using other materials such as aluminium or polyacetal.

The Formlabs resin used to print the virtual impactor was chosen for its excellent resolution and perfectly smooth finish. The 'clear' resin was used for prototyping, to produce near optically transparent parts. This enabled the internal features of the impactor to be inspected. Therefore, the channels inside the impactor could be checked for particle clogging or manufacturing defects after each experiment. The material has excellent tensile strength (65 MPa) and reasonable elongation at failure (6.2 %, after curing). The manufactured parts are not brittle and offer a durable but smooth finish. The part was able to withstand thorough laboratory testing without the need to be housed in a protective case. Furthermore, the resin is compatible with the excellent 25 µm resolution possible with the Formlabs Form 2 printer so accurate designs could be obtained. A photograph of the 3D printed impactor and its integration with the hybrid electronics and SMRs are shown in Figure 5.33.
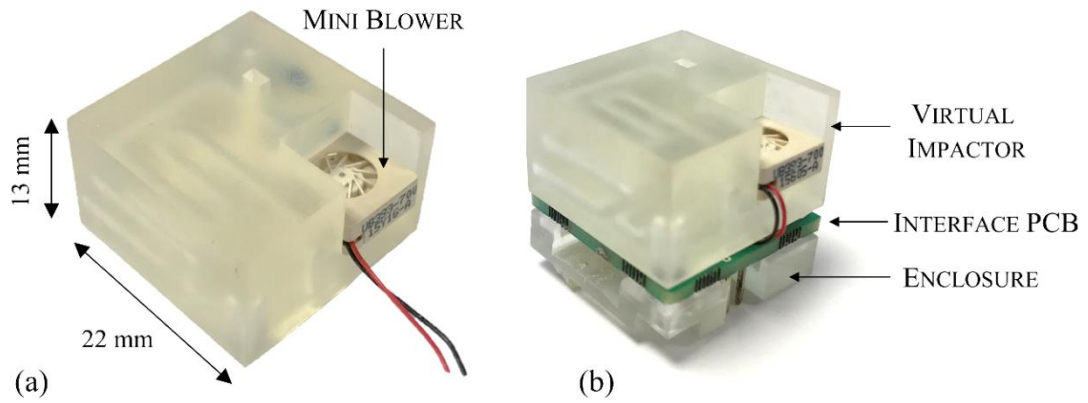
Figure 5.33 Photograph of the (a) 3D-printed virtual impactor with miniature blower, and (b) Virtual impactor integrated with the hybrid electronics.

5.6.3.2 CHARACTERISATION OF THE VIRTUAL IMPACTOR

Characterisation of the virtual impactor was performed inside the particle testing chamber described in section 5.5.4. Glass particles with diameters ranging between 0.5 and 10 µm (Sigma Aldrich) were continuously injected into the chamber for a period of 5 minutes. The integrated mini blower was operated for a total time of 10 minutes to draw a continuous sample of air into the virtual impactor. Polished silicon dies (3×5 mm) were placed at the outlets of the minor and major channels of the virtual impactor to collect the particles. Photographs of the particles collected at each of the channels are shown in Figure 5.34.
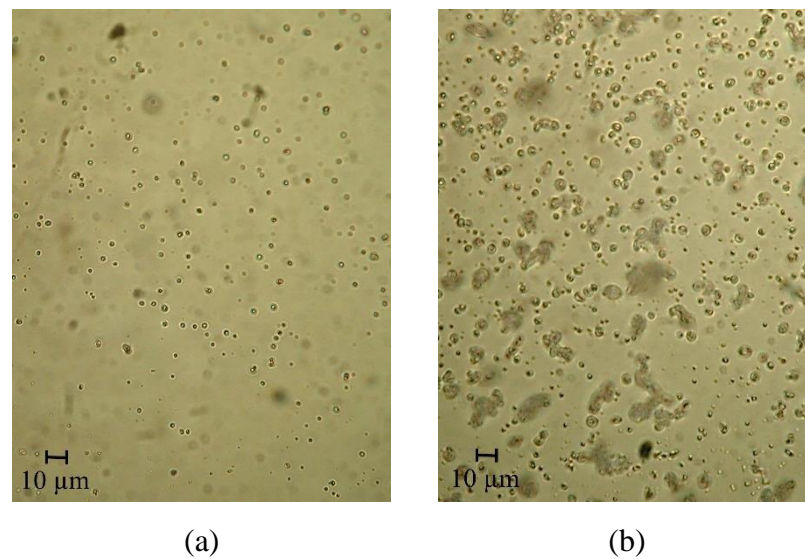
Figure 5.34 Photograph of particles collected at the outlets of the (a) major channel and (b) minor channel of the virtual impactor.

Particles collected from the major flow were counted and measured using image processing. The size distribution is shown in Figure 5.35, where the particles are categorised by diameter (<2.5, 2.5 to 5, 5 to 10 and >10 µm). For the experiment shown in Figure 5.34, 45.6 % of the particles had a diameter of less than 2.5 µm. This compares favourably with the simulated results shown in Figure 5.32 (virtual impactor designed with 50% cut-off at 2.5 µm particle size). The virtual impactor successfully removed the majority of particles with large diameters (only 12.5 % of the collected particulate matter was categorised as >10 µm diameter).
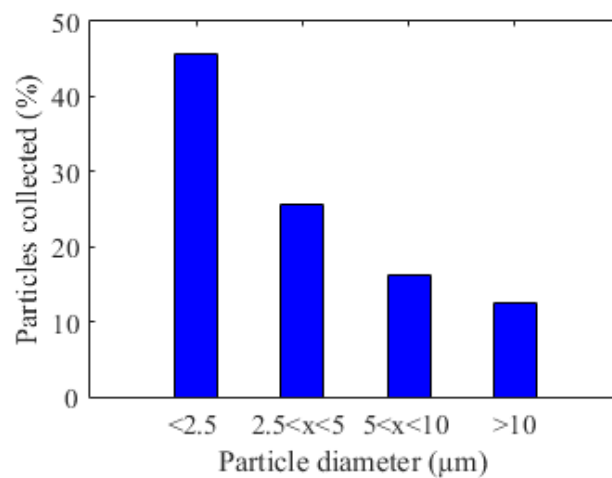
Figure 5.35 Size distribution of particles collected from the major channel.

The functionality of the virtual impactor has been verified through a series of experiments, including large and small particles (range 0.5 to 10 µm). The impactor is ready for integration with the ASIC. The final design, discussed above, meets the agreed criteria in terms of physical size, fixing locations and air flow speed. The latest available revision of the ASIC interface PCB was characterised using a frequency spectrum analyser, but demonstrated poor performance for the application of particle sensing. Therefore, it was not possible to test the virtual impactor with the entire sensing system.

5.7 CONCLUSIONS

The concept of particle detection using SMR devices was initially simulated using FEM. A 3D COMSOL model was developed to test the frequency shifts produced by particles becoming deposited on the surface of the resonators. The effect on the frequency shift of the arrangement of particles on the sensor surface was tested. Three different patterns were trialled. A 5% variation in frequency shifts was recorded between the particle arrangement experiments.

The design of resonators at 870 MHz and 1.5 GHz was detailed in Chapter 3. In this chapter, simulations were performed to characterise the mass sensitivity of the devices to PM2.5 and PM10. Sauerbrey's equation states the mass sensitivity of a resonator is proportional to the resonant frequency. The results from simulations of PM2.5 deposited on the SMRs, followed the relationship from this equation. A higher sensitivity was found for the 1.5 GHz device compared to the 870 MHz resonator (800 kHz/ng and 120 kHz/ng, respectively). However, the opposite effect was observed for the detection of PM10. These findings can be explained if the magnitude of the frequency shift is related to the fraction of the particle detected on the surface of the device (considering the wavelength of the resonator), rather than the size of the particle itself.

To verify the theoretical modelling, experiments were performed with 1 µm and 7 µm particles with the fabricated SMRs. A thin wire was used to deposit the particles onto the surface of the SMR. The frequency shift was measured using a network analyser and the total mass deposited on the sensor was estimated from photographs taken after the deposition. For the 1 µm particles, a range of masses was tried from 0.72 ng to 8.43 ng. The SMR was successfully able to detect the lowest mass, which produced a negative frequency shift of 66 kHz. A linear relationship was found between the total mass loading and the frequency shift with a sensitivity of 90 kHz/ng was calculated.

The same methodology was used to deposit 7 µm particles onto the surface of a second 970 MHz SMR. The total masses tested ranged from 25 ng to 65 ng. For these experiments, there was no clear relationship between the mass loading and the

frequency shift. Positive and negative frequency shifts were observed with no correlation with mass loading. These results suggest a weak particle-surface interaction occurs, which increases the stiffness of the resonator and thus causes an increase in the resonant frequency. This was attributed to the angular shape of the talcum powder particles. Further investigation is required to confirm the source of this frequency behaviour.

A discrete particle sensing unit based on the 970 MHz SMR devices was developed, which comprises of Colpitts oscillators and mixer circuitry. The sensing unit operates in dual mode configuration to reduce common environmental effects. Colpitts type oscillators were used to drive the SMRs and a separate interface board used to mix the sensing and reference oscillator signals.

The output frequency from the sensor unit is counted (resolution 1 Hz) using a low-cost, compact microcontroller (Teensy 3.1, PJRC). The discrete SMR based particle sensor is a portable, compact (41 mm $\times$ 36 mm $\times$ 25 mm) and low-power (300 mA) unit. It is powered from a single 5V USB port to a PC which also enables serial communication with the microcontroller. Measurement data is visualised and logged in real time with a virtual instrument developed in LabVIEW software.

Initial testing of the sensing unit was performed within a small chamber (5.625 L) where the sensing unit was placed in the centre together with two reference optical-based instruments. PTFE 1 µm particles were injected with concentrations ranging between 420 and 1720 µg/m^3. The frequency shifts caused by the deposition of the particles onto the SMR were recorded through a dedicated LabVIEW virtual instrument. A linear fit was applied to the frequency shift data and a sensitivity of 27.5 Hz per µg/m^3 was calculated.

Further characterisation was performed in a larger chamber (720 L) at VITO. Three reference sensors (two optical based, one QCM) were placed in the chamber, with the SMR sensor unit. Arizona dust particles (nominal diameters of 0-3 µm) were injected into the chamber for periods of between 2 s and 10 minutes. Particle concentrations in the range of 1,100 to 27,000 µg/m^3 were created (measured using a reference optical sensor). The limit of detection of the SMR sensor was ~20 µg/m^3. A sensitivity of 4.6 Hz per µg/m^3 was found.

The SMR sensor unit demonstrated a lower sensitivity to particle concentrations in the larger chamber. The unit did not use an active sampling method to collect particles on the sensor surface, but only sampled the particles that were deposited through gravitational sedimentation. In the larger chamber, it is assumed the lower sensitivities were caused by an uneven distribution of particles, as the sensor systems were located in one corner of the volume. This problem was not apparent in the smaller chamber, as the unit was placed in the centre of the chamber, at a suitable distance from the particle inlet.

During the testing phase, the sensing surface of the SMR devices had to be cleaned in-between experiments. Sensor life-time is a main consideration for air quality monitoring, where low maintenance is desired. Although a saturation point of the device was not found, up to a maximum concentration tested of 60,000 $\mu g/m^3$, it is expected that as the particles accumulate over time, the sensor will become saturated (long-term assessment of the unit was not performed). Thus, a method of self-cleaning the sensor surface is necessary, for the implementation of the SMR device in a particle monitor.

The experiments inside the environmental chamber revealed an active sampling system was required to produce real-time measurements. A new system was proposed to actively sample the air and separate the particulate matter of interest (PM2.5). A mini blower draws samples of air (1.17 L/min) through a virtual impactor which has a cut-off particle diameter of 2.5 µm (i.e. a collection efficiency of 50 %). Particles <2.5 µm are directed towards the sensor surface (major channel). Large particles are exhausted through the minor channel. The physical size of the system was reduced through the use of an ASIC that replaced the discrete circuitry.

The virtual impactor was rapid prototyped using the Formlabs Form 2 printer, based on the results from simulations performed in Solidworks. The overall dimensions of the final impactor were 22 mm×22 mm×13 mm. Characterisation of the impactor was performed using the small chamber (5625 cm^3). Glass particles (diameter 0.5 -10 µm) were injected for a period of 5 minutes. Particles at the outlets of the impactor were collected and image processing used to determine their size and quantity. The performance of the manufactured virtual impactor was similar to the

predicted theoretical results; 45.6 % of the particles collected in the major channel were <2.5 µm diameter. The test results proved the virtual impactor is ready for inclusion in a portable air quality monitor. However, characterisation of the complete system (hybrid system and impactor) was not possible due to the poor performance of the electronic circuitry (ASIC internal mixer saturated from oscillator signal).

The next chapter continues the characterisation of the SMR devices to another application of air quality monitoring, i.e. the detection of volatile organic compounds. To this aim, the SMRs are polymer coated to target specific VOCs of interest to air quality control.

5.8 REFERENCES

[1]   Dybwad, G. L. (1985). "A sensitive new method for the determination of adhesive bonding between a particle and a substrate", *Journal of Applied Physics*. **58**(7): 2789-2790.

[2]   Johannsmann, D. (2015). "The quartz crystal microbalance in soft matter research : fundamentals and modeling". Springer.

[3]   Johannsmann, D., Reviakine, I. and Richter, R. P. (2009). "Dissipation in films of adsorbed nanospheres studied by quartz crystal microbalance (QCM)", *Analytical Chemistry*. **81**(19): 8167-8176.

[4]   Pomorska, A., Shchukin, D., Hammond, R., Cooper, M. A., Grundmeier, G. and Johannsmann, D. (2010). "Positive frequency shifts observed upon adsorbing micron-sized solid objects to a quartz crystal microbalance from the liquid phase", *Analytical Chemistry*. **82**(6): 2237-2242.

[5]   Campanella, H., Uranga, A., Romano-Rodríguez, A., Montserrat, J., Abadal, G., Barniol, N. and Esteve, J. (2008). "Localized-mass detection based on thin-film bulk acoustic wave resonators (FBAR): area and mass location aspects", *Sensors and Actuators A: Physical*. **142**(1): 322-328.

[6]   Gabl, R., Green, E., Schreiter, M., Feucht, H. D., Zeininger, H., Primig, R., Pitzer, D., Eckstein, G. and Wersing, W. (2003). "Novel integrated FBAR

sensors: a universal technology platform for bio- and gas-detection", *Proceedings of IEEE Sensors 2003*. pp. 1184-1188.

[7]   Thomas, S., Racz, Z., Cole, M. and Gardner, J. W. (2013). "Dual high-frequency surface acoustic wave resonator for ultrafine particle sensing", *IEEE Sensors Conference 2013*. pp. 1-4.

[8]   Nirschl, M., Schreiter, M. and Vörös, J. (2011). "Comparison of FBAR and QCM-D sensitivity dependence on adlayer thickness and viscosity", *Sensors and Actuators A: Physical*. **165**(2): 415-421.

[9]   Wong, J. C. H., Tervoort, E., Busato, S., Gonzenbach, U. T., Studart, A. R., Ermanni, P. and Gauckler, L. J. (2010). "Designing macroporous polymers from particle-stabilized foams", *Journal of Materials Chemistry*. **20**(27): 5628-5640.

[10]   Song, J., Wei, Y., Sun, G. and Chen, J. (2017). "Experimental and CFD study of particle deposition on the outer surface of vortex finder of a cyclone separator", *Chemical Engineering Journal*. **309**(Supplement C): 249-262.

[11]   Thomas, S., Villa-López, F. H., Theunis, J., Peters, J., Cole, M. and Gardner, J. W. (2016). "Particle sensor system using solidly mounted resonators", *IEEE Sensors Journal*. **16**(8): 2282-2289.

[12]   Stoffregen, P. Teensy USB Development Board. Updated: September 2016, Accessed: December 2017; Available from: https://www.pjrc.com/teensy/.

[13]   She, K., Trim, L. and Pope, D. (2005). "Fall velocities of natural sediment particles: a simple mathematical presentation of the fall velocity law", *Journal of Hydraulic Research*. **43**(2): 189-195.

[14]   Paidimarri, A., Nadeau, P. M., Mercier, P. P. and Chandrakasan, A. P. (2013). "A 2.4 GHz multi-channel FBAR-based transmitter with an integrated pulse-shaping power amplifier", *IEEE Journal of Solid-State Circuits*. **48**(4): 1042-1054.

[15]   Fuchs, N. A. (1964). "The mechanics of aerosols". New York: Pergamon Press.

[16]   Marple, V. A. and Willeke, K. (1976). "Impactor design", *Atmospheric Environment*. **10**: 891-896.

[17]   Sioutas, C., Koutrakis, P. and Burton, R. M. (1994). "Development of a low cutpoint slit virtual impactor for sampling ambient fine particles", *Journal of Aerosol Science*. **25**(7): 1321-1330.

CHAPTER 6

VOC DETECTION WITH SOLIDLY MOUNTED RESONATORS

6.1 INTRODUCTION

Experiments reported in Chapter 5 demonstrated the fabricated SMR devices were able to detect fine particles (PM2.5). This chapter reports on the use of the SMR devices for another application of air quality monitoring, i.e. the detection of volatile organic compounds. Acoustic wave devices can be used as chemical sensors by applying selective coatings to their sensing areas (e.g. monolayer coating, carbon nanotubes or polymer films).

Appropriate selection of the polymer films is important to ensure good sensitivity and selectivity to the target vapours, such as toluene and acetone. An investigation into

polymer-vapour interactions was performed using linear solvation energy relationships. The strength of this interaction is described by the partition coefficients.

Following the selection of the polymers, finite element analysis was performed using a 2D model. This model investigated the changes in resonant frequency of the SMR devices caused by the absorption of the vapour in the polymer film. The effect of the polymer thickness on the sensitivity was studied.

A drop-coating system was developed to apply thin polymer films to the sensors. Different thickness coatings were trialled to investigate the relation between the polymer thickness and sensor response. Experiments were performed with PDMS and PEG polymer coated SMR devices, to toluene and acetone vapours, results were analysed and presented in this chapter.

Readout circuitry was developed for the characterisation of these devices. The SMR devices were driven with a Pierce oscillator. The PCBs developed previously (Chapter 5) were redesigned to be used with the VOC experimental setup. A test station was developed to expose the SMR devices to low ppm concentrations of VOC vapours (in dry and humid conditions). The test station used mass flow controllers and cylinders of VOCs to generate precise mixtures of VOC concentrations. A sensor chamber was designed and fabricated for the test station to house four differential pairs of the SMR devices.

6.2 POLYMER COATINGS

The use of acoustic devices for chemical vapour sensing is accomplished by applying selective coatings onto the surface of the device, which absorb the vapour molecules from the gas phase. A diagram of the SMR is shown in Figure 6.1, including the polymer coating and vapour molecules. The schematic shows a representation of the process of the gas molecules absorbing into the coating.
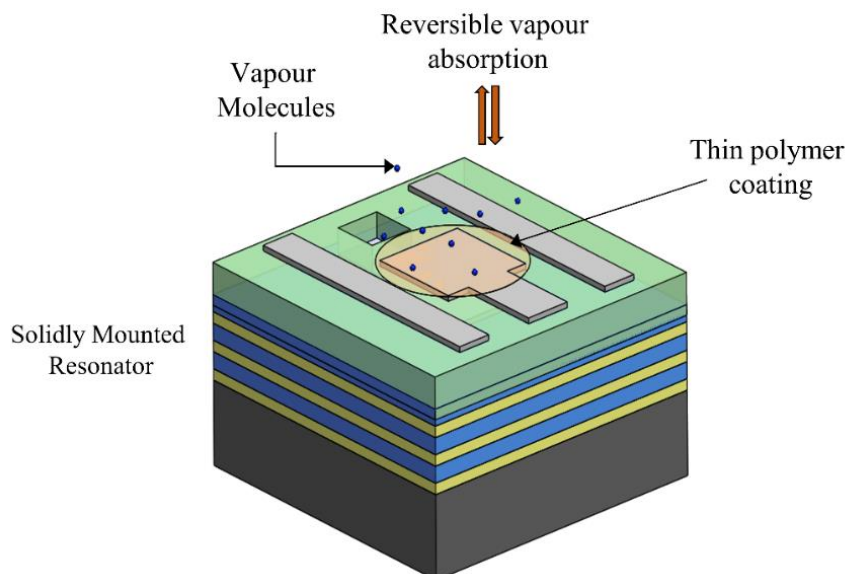
Figure 6.1 Schematic of polymer coated SMR for VOC detection.

The absorption of vapour molecules into the polymer layer causes a change in mass which in turn results in a frequency shift of the resonator. The absorption of the vapour molecules into the polymer coating is a reversible process: when the polymer coated device is exposed to a clean sample of gas, the vapour molecules desorb, allowing the sensor to recover its baseline [1]. This is a desirable characteristic for their use in air quality monitoring applications as the device can be capable of continuous and real time monitoring [2].

For the detection of organic vapours, soft and rubbery polymers are commonly used to improve sensor sensitivity and response times [3]. The high permeability, low density and low crystallinity of these polymers allows fast vapour absorption and diffusion.

Polymers with increasing polar properties are often glassy in nature (with low permeability), so they are not preferred as selective coatings. However, the sensitivity of the polymer films is not determined from their properties alone but from the interaction between the vapour and the polymer. Therefore, appropriate selection of the polymer coating is necessary to ensure good sensitivity and selectivity to the target vapour.

The strength of the interaction between the polymer and vapour molecules can be described by the vapour-polymer partition coefficient, K_p, shown in equation (6.1), which relates the concentration of vapour molecules absorbed in the polymer film, C_p, to the concentration of the sampled vapour in the gas phase, C_v [4].

$$K_p = \frac{C_p}{C_v} \tag{6.1}$$

The partition coefficient is therefore only a function of the polymer and vapour properties. The larger the partition coefficient values, the stronger the vapour sorption and thus the higher the frequency shift, Δf, of the resonator due to vapour sorption [5].

$$\Delta f \propto K_p C_v \tag{6.2}$$

Linear Solvation Energy Relationships (LSER) can be used to describe the vapour-polymer interaction and estimate the partition coefficient values. For the sorption of a vapour into the polymer a solvation equation is expressed by the LSER as [5]:

$$log\, K_p = c + rR_2 + s\pi_2{}^H + a\alpha_2{}^H + b\beta_2{}^H + l\, log\, L^{16} \tag{6.3}$$

where the solvation parameters of the vapour R_2, $\pi_2{}^H$, $\alpha_2{}^H$, $\beta_2{}^H$ and $log\, L^{16}$, that characterise the solubility properties of the vapour, are related to the coefficients c, r, s, a, b and l of the polymer. These parameters are defined in Table 6.1.

Table 6.1 Solute and polymer parameters in the solvation equation (6.3).

SOLUTE VAPOUR PARAMETERS		POLYMER SOLUBILITY PARAMETERS	
R_2	Excess molar refraction	c	Constant resulting from regression.
$\pi_2{}^H$	Dipolarity	r	Polarisability
$\alpha_2{}^H$	Hydrogen-bond acidity	s	Dipolarity
$\beta_2{}^H$	Hydrogen-bond basicity	a	Hydrogen-bond basicity
$log\, L^{16}$	L^{16} is the gas-liquid partition coefficient for n-hexadecane.	b	Hydrogen-bond acidity
		l	Solvation cavity effects and dispersion

Solute vapour parameters of the VOCs of interest in this work are listed in Table 6.2. LSER solvation parameters for a wide range of polymers were collected from published articles (experimental data obtained from gas-liquid chromatography) [4, 6-9] and the partition coefficients were computed for each polymer-vapour pair as defined by equation (6.3).

Table 6.2 Solvation parameters at 298 K of target solutes [10].

SOLUTE	R_2	$\pi_2{}^H$	$\alpha_2{}^H$	$\beta_2{}^H$	$log\ L^{16}$
Acetone	0.179	0.7	0.04	0.49	1.696
Acetaldehyde	0.208	0.67	0.0	0.45	1.230
Ammonia	0.139	0.35	0.14	0.62	0.68
Benzene	0.61	0.52	0	0.14	2.786
Ethanol	0.246	0.42	0.37	0.48	1.485
Formaldehyde	0.22	0.70	0.0	0.33	0.73
Toluene	0.601	0.52	0.0	0.14	3.325
n-octane	0.0	0.0	0.0	0.0	3.68

Figure 6.2 shows the computed partition coefficients for selected polymer-vapour pairs. The complete dataset of partition coefficients can be found in Appendix D for a wide range of polymer-vapour pairs.
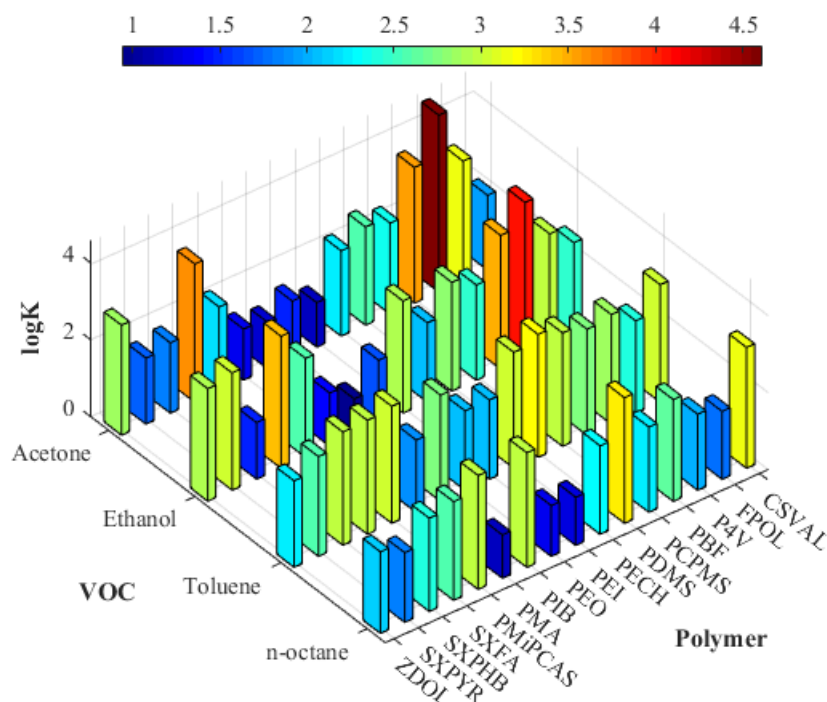
Figure 6.2 Polymer-vapour partition coefficients of selected pairs.

Partition coefficients values, K_p, of selected vapour-polymer pairs are summarised in Table 6.3. Solvation parameters for PEUT were not available to calculate the partition coefficients of the vapour-pairs. However, high partition coefficients, K_p, of 850 and 1610 have been reported for PEUT to n-octane and toluene, respectively [11].

Table 6.3 Partition coefficients of selected analytes and vapours.

VOC	PDMS	PECH	PEG	PEUT	PIB	SXFA
Acetone	67.8	166.9	30.5	-	16.3	3948
Acetaldehyde	24.5	50.5	13.4	-	5.2	1078
Ammonia	10.4	11	4.4	-	1.16	1968
Benzene	410.1	371.8	62.9	-	164.1	377
Ethanol	82.7	117.2	46.5	-	8.85	2734
Formaldehyde	9.2	17.9	8.3	-	1.64	149.8
Toluene	1164.5	1039.5	117.4	1610	583.2	930
n-octane	1867	201.5	21	850	963	371.2

Polymer coatings for target vapours in this work (toluene and acetone) were selected not only based on the partition coefficient values but also on their availability (only commercially available polymers were used), price, polymer solubility in common solvents and cross-sensitivity between the vapours of interest. Based on these criteria the selected polymer coatings in this work are shown in Table 6.4.

Table 6.4 Polymer coatings chosen for the detection of VOCs and their densities.

POLYMER	ACRONYM	DENSITY	SUPPLIER
Poly(dimethyl-siloxane)	PDMS	0.965 g/cm^3	Sigma Aldrich Ltd., UK
Polyethylene glycol	PEG	1.13 g/cm^3	Sigma Aldrich Ltd., UK

In the following section, the absorption of toluene into different polymer coatings (PDMS, SXFA, PIB and PMA) is investigated and its effects on the resonant frequency are analysed using a FEM model developed in COMSOL. A model of the PEG coated SMR device was not developed as the material parameters of this polymer were not disclosed.

6.3 FINITE ELEMENT MODELLING ON VOC ABSORPTION

The change in the resonant frequency of a SMR due to the absorption of vapour molecules into a polymer coating was simulated in COMSOL. A thin layer was added on top of the 2D SMR model (described in Chapter 3) to simulate the polymer film. The absorption of the analyte in the polymer film was represented as an increase in the density of the polymer given by

$$\rho_{VOC/polymer} = K_p \cdot M \cdot c \tag{6.4}$$

where K_p is the partition coefficient of the polymer-vapour pair given in Table 6.3, M is the vapour molar mass and c is the VOC concentration in air given by $c = (c_0 P)/(RT)$. This equation converts the volumetric VOC concentration c_0 (in units of parts per million) to the amount of VOC (in units of moles/m^3) using the ideal gas law, considering the pressure P, temperature T and the universal gas constant R. The simulation parameters were defined as ambient temperature (25°C) and atmospheric pressure (101 kPa).

The simulations performed in this section focus on four polymer coatings for comparison (PDMS, SXFA, PIB and PMA). The first simulations performed investigated the effect of the thickness of the polymer film on the magnitude of the frequency shift of the SMR device. For these simulations, the polymer thickness was varied from 50 nm to 500 nm while the target analyte remained fixed (toluene vapour). The simulations were repeated for toluene vapour concentrations from 5 to 100 ppm (maximum safe exposure limit concentration). The results for the PDMS coating are summarised in Figure 6.3a.

The sensitivity of the SMR sensor (with polymer film) is determined by considering the gradient of the frequency shift versus analyte concentration relationship. The sensitivity for the four polymer coatings was calculated for each of the polymer thicknesses, as shown in Figure 6.3b (toluene vapour).

(a)   (b)
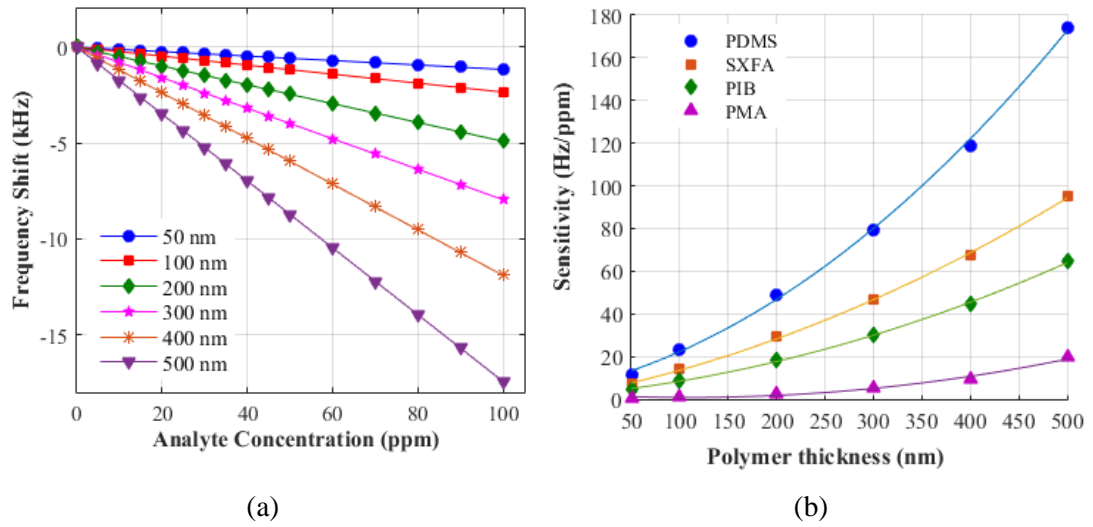
Figure 6.3 (a) Frequency shift of PDMS coated SMR to toluene, (b) Relationship between sensitivity and polymer thickness for four polymer coatings to the exposure of toluene.

A linear relationship between frequency shift and VOC concentration was observed, irrespective of polymer thickness. The sensitivity of the device exponentially increased with the polymer thickness. The frequency shift of the sensor is directly proportional to the partition coefficient. The PDMS polymer has the highest partition coefficient (1164.5, shown in Table 6.3) to toluene and offers the highest sensitivity to the toluene vapour. The PMA has the lowest partition coefficient to toluene (76.2), and thus is less sensitive to the tested vapour.

Thicker coatings offer higher sensitivities, but at the expense of higher electrical insertion losses and slower response times. The gain of the oscillator circuitry must exceed the insertion loss of the device for oscillations to occur. However, these simulations were not used to predict the increase in insertion loss of the device, caused by a thicker polymer coating (coatings over 500 nm were considered beyond the maximum viable thickness). Furthermore, thinner coatings are often preferred due to the trade-off between sensitivity and response time, although it was not possible to consider the response time in the simulations.

A comparison between the sensitivity of a 900 MHz and a 1.4 GHz SMR device was also performed. Figure 6.4 shows the simulated frequency shifts of PDMS coated SMR devices (100 nm) due to the exposure to toluene. The device working at a higher frequency exhibited greater sensitivity at -48.7 Hz/ppm compared

to -23.45 Hz/ppm of the 900 MHz device. This behaviour was expected, as per equation (2.7). Simulations were not used to predict if the devices would be able to continue resonating at high loading with the finite gain available from a real circuit.

There is a trade-off between the sensitivity and film thickness in high frequency SMR devices. For a given thickness of the coating, the attenuation due to the polymer film is greater at higher frequencies. High sensitivities are not necessarily obtainable at high frequencies because thinner coatings are needed to prevent the attenuation of the device [3].
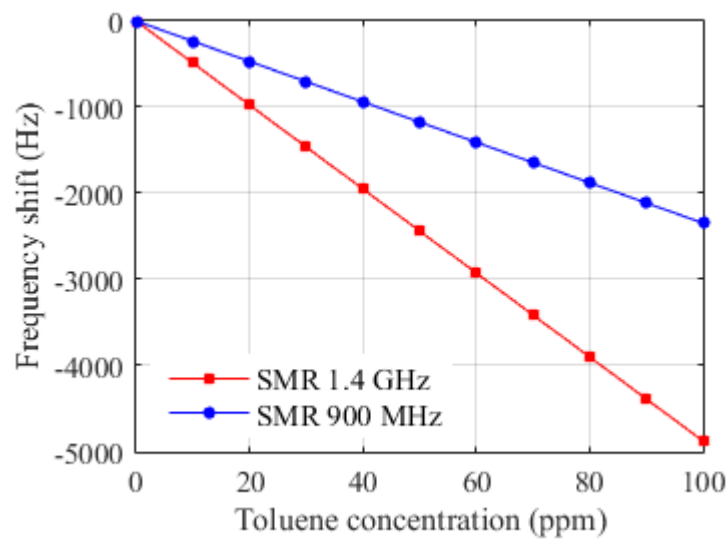
Figure 6.4 Simulated PDMS coated SMR devices.

Deposition of uniform and thin coatings is challenging. The polymer must be deposited in a very localized area (200×200 μm^2) to avoid damaging other components. A deposition apparatus capable of creating nm-thick coatings was not readily available. The next section details the development of two alternative techniques that were used to deposit coatings as thin as 70 nm.

6.4 DEPOSITION OF THIN POLYMER FILMS

6.4.1 POLYMER COATING APPARATUS

In this work, two main coating methods were employed to apply the polymer films on the surface of the resonator, namely spray coating and drop coating. Initially

a spray coating system was implemented. Later, a drop coating system was developed which allowed efficient use of polymers (for example, if only a limited quantity was available) and accurate positioning of the polymer coating over the sensing area.

A schematic of the developed spray coating system in shown in Figure 6.5a. The system consisted of a single action airbrush (Iwata HP-SAR) which used compressed air, as a carrier gas, to continuously spray the polymer solution onto a rotating disk (10 cm diameter) driven by a DC motor. An opening in the disk (1 cm diameter) allowed the polymer solution to pass through to reach the SMR located beneath the plate. The SMR was covered with a 3D printed mechanical mask (shown in Figure 6.5b) to expose only the active area of the resonator. The SMR was placed (in the mask) at a distance of ~10 cm beneath the airbrush nozzle.
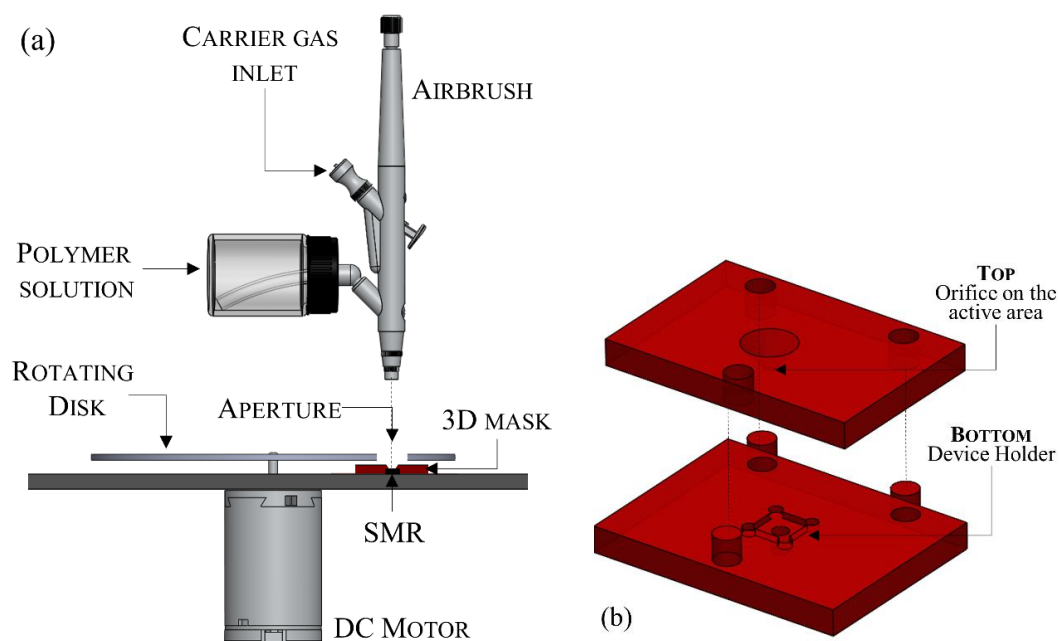
Figure 6.5 (a) Drawing of the spray coating system for deposition of thin coatings; (b) drawing of the 3D printed mechanical mask.

During initial trials, the frequency response of the SMR was monitored during the polymer coating procedure (using the spectrum analyser, with the SMR on an interface board). This procedure required a special mechanical mask that was difficult to position over the interface PCB. Once the deposition parameters were established (distance between sensor and nozzle, speed of the disk, spraying time) the devices were firstly coated using the mask shown Figure 6.5b and then bonded to the circuitry.

A LabVIEW control interface was developed to control the air dispersion (i.e. spraying time), using a solenoid actuator. The interface also allowed the user to adjust the speed and direction of the disc by using a microcontroller (Teensy 3.1, PJRC) and additional circuitry. In this way, small amounts of polymer droplets could be delivered to the targeted area for a set period. The automatic, precise and rapid dispersion method allowed thin and uniform layers to be created. Typically, a spraying time of 30 s produced coatings with thicknesses of ~150 nm. A photograph of the assembled spray coating system is shown in Figure 6.6a.

(a)   (b)   (c)
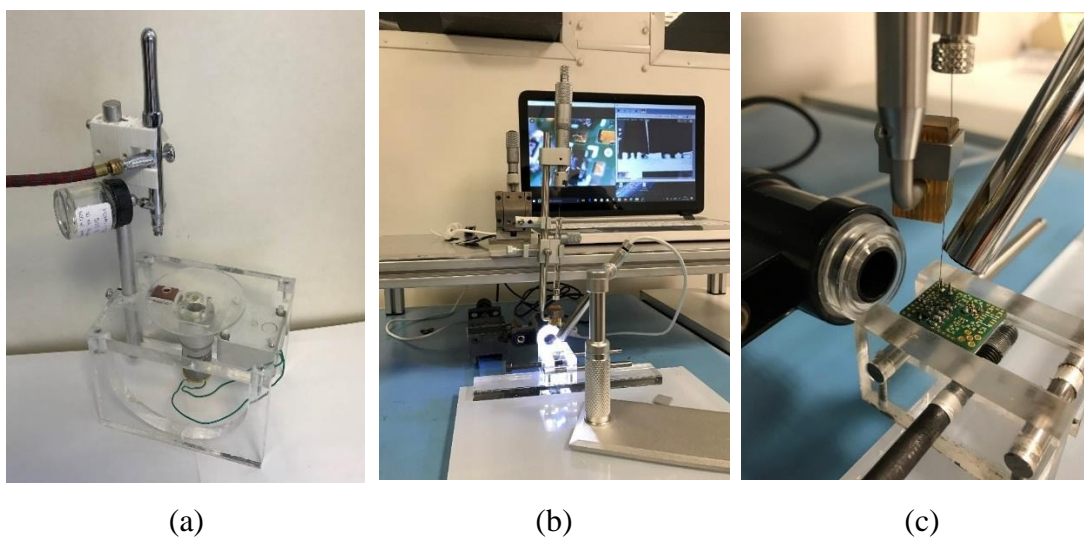
Figure 6.6 Polymer coating deposition methods used (a) spray coating, (b) drop coating system, (c) enlarged view of the device undergoing coating procedure.

Even though thin and uniform layers could be achieved with the spray coating system, accurate positioning of the device was difficult due to the small sensing area of the SMR. Furthermore, wasted polymer solution (i.e. solution not sprayed onto the surface of the device) could not be reused. A drop coating system (Figure 6.6b) based on deposition using a manual micro syringe injector (World Precision Instruments Ltd.) was developed. The system offered the advantages of accurate and localized deposition of the polymer solution, with the device interfaced to the circuitry, achievement of uniform films and the efficient use of the polymer solution. Thus, the system was suitable for monitoring the resonant frequency while applying the polymer solutions.

A micro syringe (10 µL volume) with a small needle internal diameter of 100 µm (gauge 33) was placed in the precision microinjector holder. The micro syringe was capable of delivering low volumes (~1.6 nanolitres) of the polymer solution. Two digital microscopes (AnMo Electronics, Taiwan/Andostar, China) were used to provide a magnified view of the apparatus and help with the 3D positioning of the needle exactly over the centre of the SMR device (Figure 6.6c). Typical images observed from these microscopes are shown in Figure 6.7 below.

Figure 6.7 Screenshot of monitoring microscopes during SMR drop coating procedure: photographs shows side view (left) and top view (right) of the device with the deposition needle above the sensing area.

Similar polymer thicknesses could be achieved with both deposition techniques. However, due to the ease of use (accurate positioning of the sensor) and achievement of slightly more uniform layers, the drop-coating method was preferred. Figure 6.8 shows photographs of coated SMRs (PDMS layer), using these two different coating methods. The drop coating method allow for the device to be mounted on an interface board (wire bonds shown in photograph) and therefore its resonant frequency and attenuation can be monitored during the coating process.
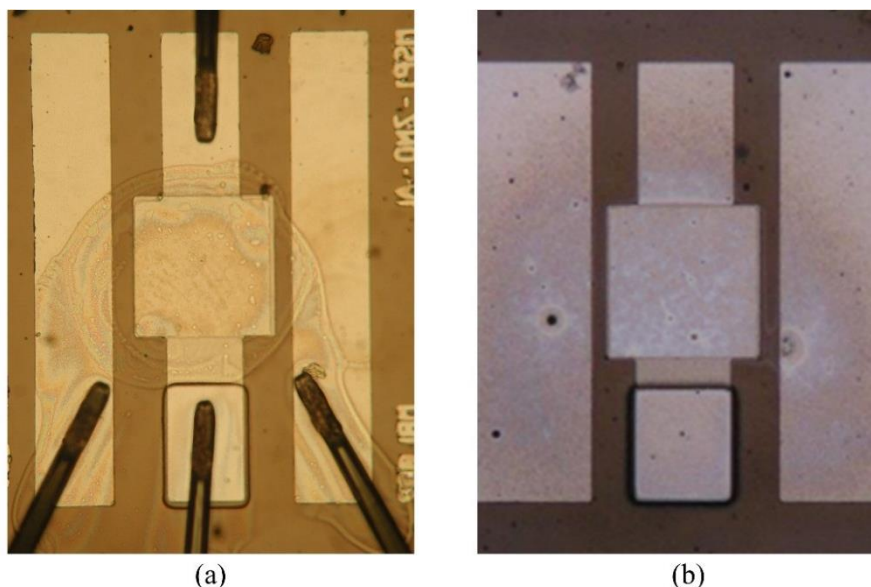
Figure 6.8 Photographs of polymer coated SMR devices using (a) drop coating and (b) spray coating method**.**

6.4.2   PREPARATION OF POLYMER SOLUTIONS

The preparation of the PDMS solution started by mixing uncured PDMS with the curing agent in a 10:1 ratio by weight (Sylgard 184 Elastomer kit). This mixture (1.5g of PDMS and 0.15 g of curing agent) was then diluted in an organic solvent (hexane) in an initial 10:1 solution (15 g of hexane). This base solution was further diluted with the same solvent to obtain a solution at 3.5% weight by weight (w/w) of the original polymer loading. In the case of PEG, the flakes were dissolved in ethanol at 5% w/w solution. The polymer mixtures were solvated at room temperature on a magnetic stirring plate for a minimum of 24 hours. Table 6.5 summarises the recipes used for the preparation of the polymer solutions in this work.

Table 6.5 Polymer and solvent mixing ratios.

POLYMER	SOLVENT	RATIO
PDMS, 600 µL	Hexane, 30 mL	3.5% w/w
PEG, 1.25 g	Ethanol, 30 mL	5% w/w

In initial trials, a PDMS/toluene solution was also prepared. However, the solvent in the hexane based solution was found to evaporate faster (during the polymer

coating procedure) and thus was preferred over toluene. Furthermore, the use of hexane prevented any remaining toluene solvent from interfering during the detection of the target vapour (in this case also toluene). The mixing ratios given in Table 6.5 were found to produce suitable solutions for deposition onto the devices. The viscosity of the solution was controlled, thus allowing the solution to be ejected from the spraying system or needle (without clogging) but with a sufficient quantity of polymer so a layer could be deposited.

After the deposition of the polymer coatings, the devices were baked a minimum of 12 hours at the temperature of 100 °C, to evaporate any remaining solvent. After baking, devices were left to stabilise at room temperature for a period of at least 10 hours. The next section details the procedure followed in this work to measure the thickness of the applied polymer films.

6.4.3 THICKNESS MEASUREMENT OF POLYMER FILMS

For the experimental results shown in this work (section 6.7), the polymer coatings were applied using the drop coating method, previously described. The sensitivity of the 900 MHz SMRs was approximated from equation (2.7) as $S_m = 548$ Hz·cm^2/ng and the thickness of the deposited polymer film, d_{film}, was estimated from the Sauerbrey equation (2.6) by:

$$d_{film} = \frac{\Delta f}{\rho S_m} \tag{6.5}$$

where Δf is the change in resonant frequency due to deposition of the polymer film and ρ is the density of the polymer given in Table 6.4.

The SMR oscillation frequency was monitored during the coating process (details of the driving circuitry are presented in section 6.5). A spectrum analyser (Tektronix MDO3012) was interfaced to a LabVIEW virtual instrument for the real-time acquisition of the data. In this way, the frequency shift caused by the addition of the polymer film was monitored. Using equation (6.5), expected frequency shifts were calculated for the target thicknesses of 100 nm and 150 nm for the selected polymers (PDMS and PEG), as summarised in Table 6.6. According to the target thickness, a

small amount of polymer solution was dropped onto the sensing area to achieve a frequency shift close to the estimated values.

As the drop of polymer solution contacted the SMR surface, the oscillator signal attenuated completely (with no trackable resonant frequency) due to the damping caused by the liquid solution in the propagating longitudinal waves. Once the solvent evaporated (<5 seconds), the resonator recovered and the resonant signal could be again tracked to determine the thickness of the polymer film.

Table 6.6 Estimated and measured thickness of the applied polymer coatings.

POLYMER	TARGET THICKNESS (nm)	ESTIMATED FREQUENCY SHIFT (MHz)	MEASURED THICKNESS (nm)	MEASURED FREQUENCY SHIFT (MHz)
PDMS	100	5.28	70 ±5	4.2
	150	7.93	110 ±5	6.9
PEG	150	9.28	120 ±5	8.5

The deposited polymer films were measured using an optical profiler (ContourGT-K, Bruker). Initially a stylus profiler (XP-100, AMBiOS technology) was used to measure the film thickness. This method did not produce satisfactory results, as the polymer film was disturbed when the profiler stylus made contact with the surface, as a result of the softness of the coatings (typical Young's modulus values <10 MPa). The optical profiler non-contact method was preferred, as the polymer coating was not damaged during the measurement, thus allowing accurate profiling. Figure 6.9a shows an example profile of the SMR device shown previously in Figure 6.8a. The polymer coating can be seen as the highest layer in the centre of the device.
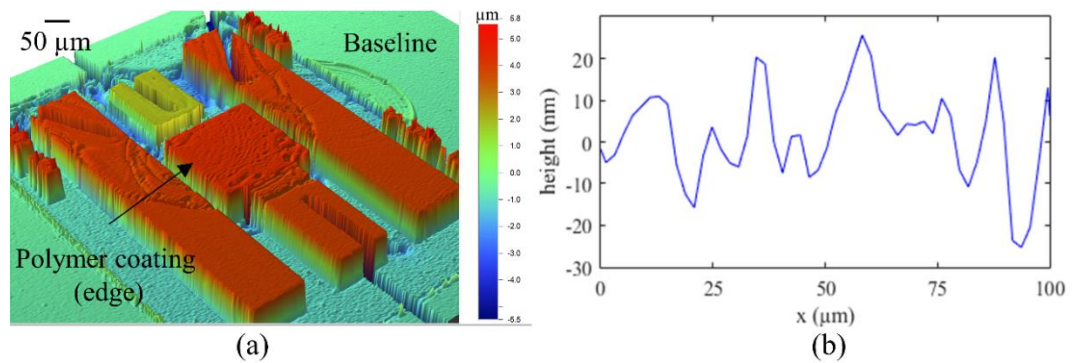
Figure 6.9 (a) 3D scanning profile of PDMS coated SMR device and (b) cross section height curve of the polymer surface .

A 3D scanning profile was performed before and after the polymer coating. The height of the sensing area relative to the baseline surface was measured each time. The thickness of the polymer coating was calculated as the difference in height between each measurement. The baseline was chosen as a reference area of the device which would not be covered with any polymer. For the devices shown, the thickness of the polymer was calculated as 180 nm ±5%.

For the polymer solution to be deposited on the surface of the device, a drop is formed on the tip of the nozzle which is then deposited when it contacts the surface. Although localized coatings can be easily achieved with this method, accurate reproducibility of the applied film thickness is not possible due to the variable volumes of solution needed for the droplet to form.

Application of the polymer films on the SMR surface caused a decrease on the quality factor of the device and the consequent attenuation of the sensor response signal. However, this deterioration in quality factor (measured after temperature treatment of the films) was small for the polymer films deposited (oscillator signal was attenuated <2 dB). For a polymer thickness of ~300 nm, the SMR device became extremely attenuated, making it impossible to track the oscillator signal.

In the next section, development of the interface circuitry is presented. The interface circuitry comprises of an oscillator driving circuit and mixer circuitry. The oscillator circuit was used to track the SMR response during the polymer deposition procedure presented in this section.

6.5   INTERFACE CIRCUITRY

In Chapter 5, a Colpitts oscillator circuit was described (section 5.5.2.1) and used for the development of a particle sensing unit based on the SMRs. Adequate performance was observed when the SMRs were tested with the interface circuitry. However, in this section the development of a Pierce oscillator is described, which offers improved performance at high frequencies (>600 MHz) in terms of frequency stability and gain (to match the resonator losses).

For the design of the SMR-Pierce oscillator, the lumped elements of an equivalent MBVD model (described in section 3.2.3) were extracted for the 900 MHz SMR device with aluminium electrodes. The electrical characterisation data (S-parameters) of the fabricated devices were used to obtain this equivalent model, shown in Figure 6.10.
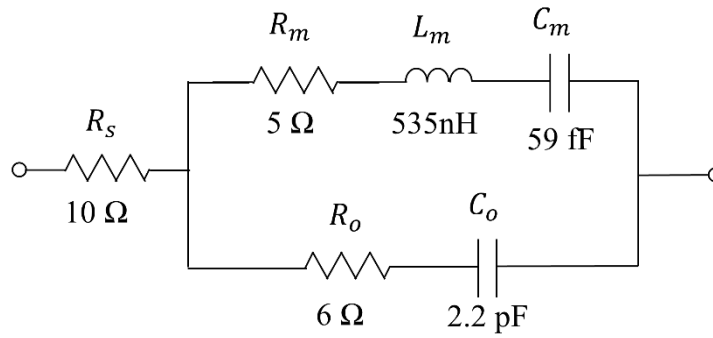
Figure 6.10 Equivalent MBVD model of the SMRs resonating at 900 MHz.

The MBVD model is formed by the motional arm (R_m, L_m and C_m) representing the electro-acoustic interaction of the resonator. R_o and C_o form the static arm, representing the acoustic losses (related to the piezoelectric layer) and the electrical plate capacitance, respectively. The series resonance of the circuit is determined by the inductance and capacitance of the motional arm; whereas the parallel resonance is set by the motional inductance and the static parallel capacitance. The resistor, R_s, models the electrical Ohmic losses due to the electrodes.

A transistor-based Pierce oscillator (discussed in Chapter 2) was designed in this work as shown in Figure 6.11. The SMR symbol represents the equivalent MBVD model as shown above. A low noise silicon RF transistor (BFR92, Infineon technologies) provides the gain in the oscillator loop with bias provided by resistors R1 and R2. The feedback network is formed by capacitors C1, C2 and the SMR device, which determines the oscillator frequency.
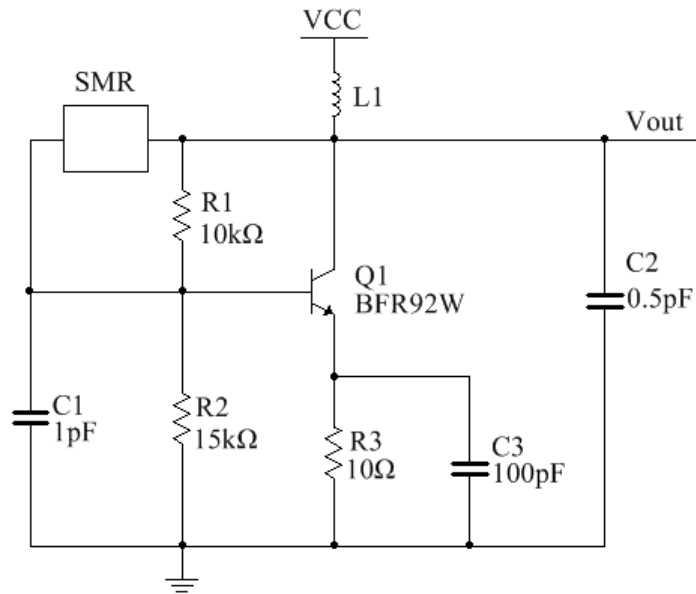
Figure 6.11 Schematic diagram of Pierce oscillator circuit.

For sustained oscillations to occur, the Barkhausen criterion must be met. Figure 6.11b shows the simulated loop gain and phase shift of the oscillator. As seen from this plot, at a frequency close to 900 MHz, the loop gain is greater than one, while the phase shift equals zero, satisfying both criteria. The output spectrum of the oscillator is shown in Figure 6.11c, showing a fundamental resonant frequency at 900.6 MHz and the harmonic signals (e.g. the first and second harmonics at 1.801 GHz and 2.702 GHz).
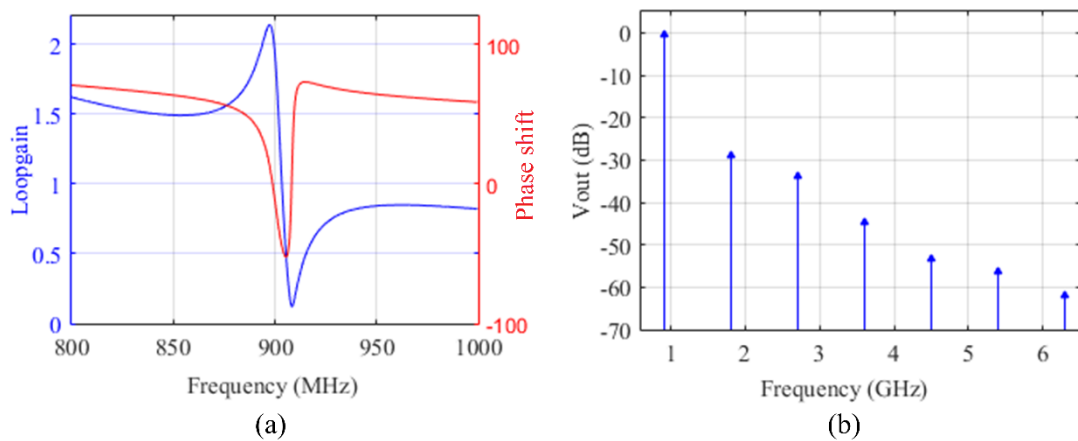
Figure 6.12 (a) Simulated loop gain and phase shift and (b) output spectrum of the Pierce oscillator circuit.

The Pierce oscillator circuit was implemented in a 4-layer PCB (overall size of 20×16 mm). The SMR was directly wire bonded onto the populated board to avoid parasitics (as opposed to using a package). RF capable components were used in the design, to ensure the circuit functioned at the resonant frequency of the SMR. Two connectors were needed on the board (power supply and signal output). Both of these connectors were located on the top of the PCB, to allow the SMR board to be stacked on top of a mixer PCB in a differential configuration.

To perform the VOC measurements, two SMRs are used in a dual configuration (similar to that described for particle sensing in Chapter 5), where one bare device serves as a reference channel and the polymer-coated SMR as the sensing channel. The dual setup reduces the effects of temperature and humidity variation. Therefore, in addition to the oscillator boards, a mixer board was designed (modified layout compared to previous circuit) to suit the VOC experimental setup, where the sensors must be contained within a small chamber.

The output signals of the oscillator board were visualised with an RF spectrum analyser (Tektronix MDO3012) and oscilloscope (Tektronix DPO5204B). The output spectrum is shown in Figure 6.13a (0.5 to 3 GHz spectrum shows harmonics of the fundamental resonant frequency). Figure 6.13b shows the fundamental resonant frequency (901 MHz). A time series plot of the output signal is shown in Figure 6.13c (amplitude 2.8 V).
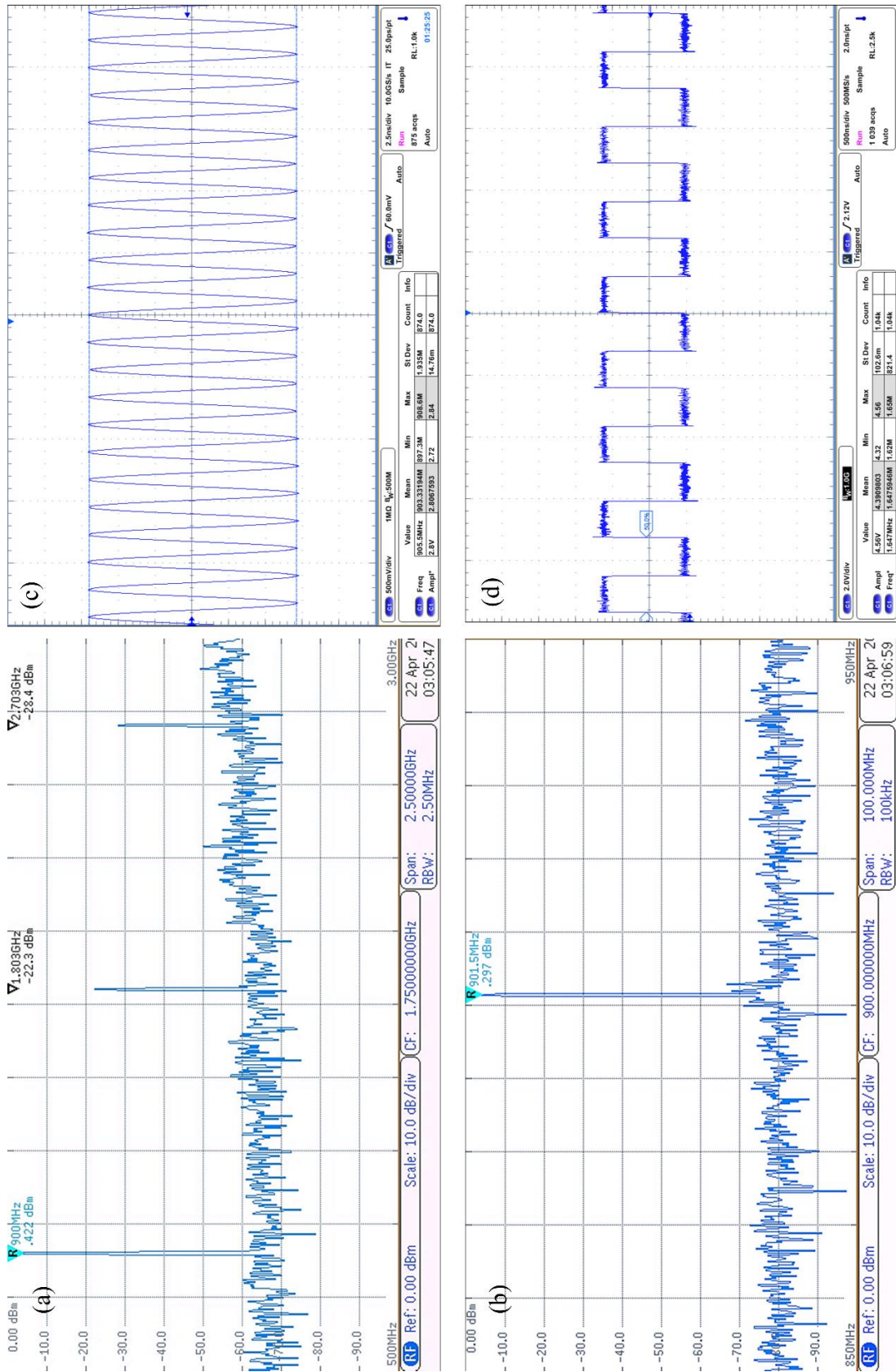
Figure 6.13 Measured output signals of the interface circuitry: (a) Broad output spectrum of SMR-Pierce oscillator, (b) Output spectrum of fundamental frequency, (c) Time series sinusoidal signal and (d) Final comparator output to measure the SMR sensor response.

The mixer circuit processes the two signals from the SMR devices and outputs a sinusoidal differential signal. The mixer output is transformed into a square wave signal (shown in Figure 6.13d) via a comparator, which can then be acquired using a microcontroller. The system has a low power consumption (total 210 mW, each SMR board 90 mW and 30 mW for the mixer board) when powered at 3.3 V. Photographs of the completed PCBs for the Pierce oscillator and mixer circuitry are shown in Figure 6.14. The circuit diagrams for the implementation of these boards are presented in Appendix E. Two of the oscillator boards (reference and signal) are plugged onto the mixer board in a stacked configuration.
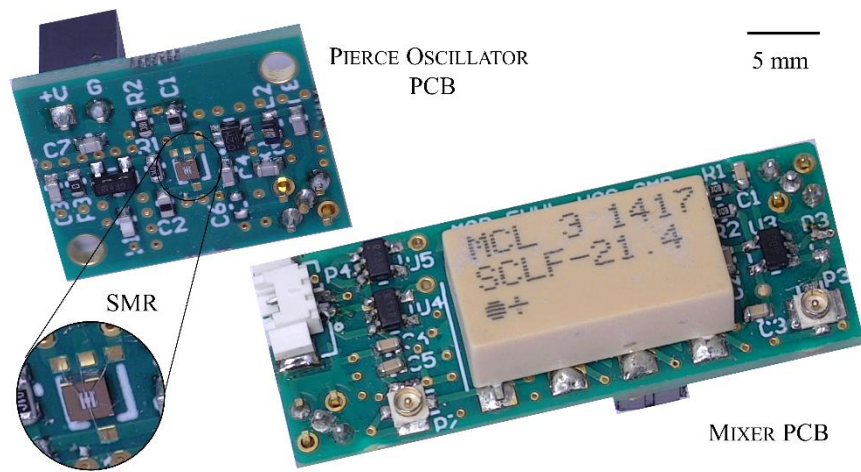
Figure 6.14 Pierce oscillator and mixer PCBs designed for the VOC experimental setup.

6.5.1   DATA ACQUISITION

The differential output signal of the sensor system (square wave at frequencies <20 MHz) was acquired using a microcontroller (Teensy 3.2, PJRC). Microcontroller software was developed to measure the frequency of the square wave (maximum frequency 75 MHz), with the output printed via a serial connection. The frequency measurements were performed at 10 Hz resolution. Details on the data acquisition have been previously presented in section 5.5.3. The output signal of the interface circuitry was connected to the microcontroller input pin using a micro coaxial RF cable.

A LabVIEW virtual interface was created to acquire the signal from the microcontroller and save the data to a measurement file. The measurement data was saved to a National Instruments *.TDMS (technical data management streaming) file

format, which allows high speed streaming, necessary to store the large amounts of data generated during the VOC experiments.

To characterise the SMR sensors to low ppm concentrations of VOCs, a test rig is needed. The next section describes the development of a test rig and the development of a sensor chamber, which is used to expose the SMRs to vapours. The chamber was designed around the dimensions of the interface PCBs, to allow a total of 4 pairs of sensors to be tested simultaneously.

6.6 AUTOMATED VOC TEST STATION

An automated VOC test station was developed to characterise the SMR devices to the exposure of target analyte vapours (toluene and acetone). The VOC station is capable of delivering a wide range of VOC mixtures at controlled concentrations and atmospheric conditions (i.e. temperature, humidity and flow rate) to replicate environmental conditions.

The test station developed in this work is a major redesign of an existing Flow Injection Analysis (FIA) station [12]. The station developed in this work comprises of state-of-the-art equipment and features three substantial improvements: (1) the system can deliver concentrations in the low parts per billion (ppb) levels, (2) devices can be tested to the exposure of vapour mixtures in different ratios (up to two VOCs can be delivered into a chamber simultaneously) and (3) a zero-air generator is used for air supply (instead of synthetic air from gas cylinders), with the advantages of constant air purity and uninterrupted supply. The system reduces health risks as handling of pure analytes in liquid form is no longer necessary (VOC mixtures in air are stored in pressurised cylinders).

6.6.1 OVERALL STRUCTURE

The VOC test station was designed to be fully computer controlled (hardware and data acquisition automatically controlled). This allowed the user to perform tests over long periods of time with repeatability and minimal user interaction. A block diagram of the developed VOC test system is shown in Figure 6.15. The test station consists of

three main parts: the hardware, the valve control circuitry and the control software. Details on these components are presented in the following sections.
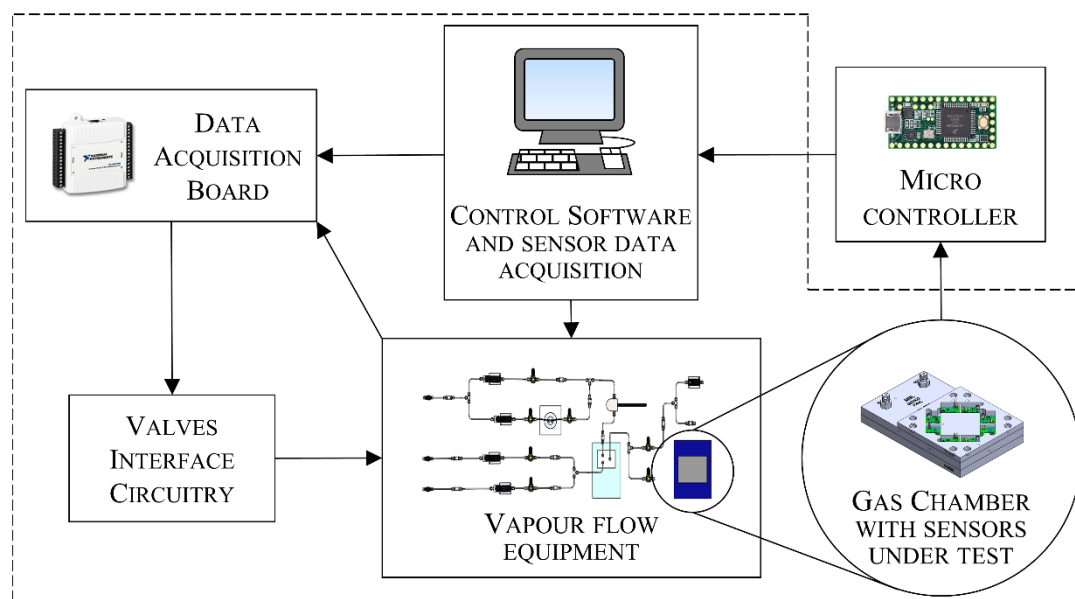
Figure 6.15 General overview of the VOC test station.

6.6.2   HARDWARE

The hardware comprises all physical elements and mechanical parts used to build the VOC station such as mass flow controllers (MFCs), valves, pipe work, mixing chamber, heating units, etc. A schematic layout of this part of the system is shown in Figure 6.16.

Test vapours are supplied from pressurised gas cylinders (BOC Ltd.) with premixed concentrations (ppm levels) of desired compounds diluted in synthetic air. Pressure from these cylinders is controlled by double stage regulators. When further diluted with air supplied by the zero-air generator (Parker Balston®), the system can deliver concentrations in the low parts per billion (ppb) levels. These elements are situated in a storage room adjacent to the gas testing room, where the VOC test station is located, and connected to the lines via stainless steel tubing across the ceiling. The cylinders are kept in cylinder cabinets which are connected to a ventilation system. If any part of the test station was to fail, the cylinders can be turned off remotely without entering the gas testing room.
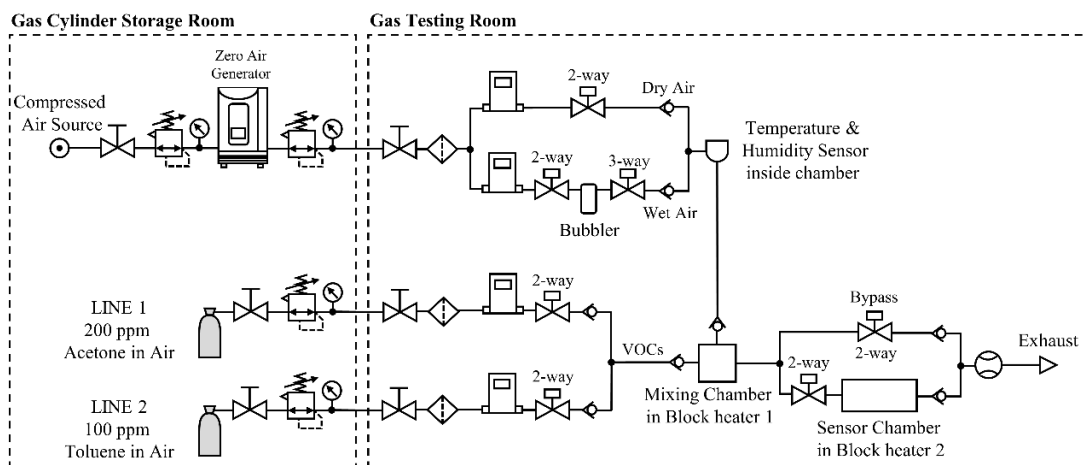
Figure 6.16 Schematic of the hardware used in the VOC test station.

The system consists of two VOC lines, each one controlled by a separate MFC (Alicat Scientific, USA). In this way, the system can deliver vapour mixtures in specific ratios as required. A third MFC is used to control the air bubbled (using a sinter) through a Dreschel bottle containing water ('the bubbler'), to introduce humidity in the system. A dedicated commercial sensor (Rotronic AG, UK) is used to verify the temperature and humidity conditions. An additional MFC controls the dry air line which is used to further dilute the vapour concentration.

A mixing chamber, located within a heating unit (IKA Ltd., Germany), is used to combine all four lines and ensure that no condensation forms when the gases are mixed [12]. The outlet from the mixing chamber is delivered to the inlet of the sensor chamber.

Solenoid valves (Bürkert Ltd., Germany) are used to electrically open/close the lines as needed to create the required gas mixtures. Stainless steel tubing (1/8" OD, 0.028 in wall) and compression fittings (Swagelok, USA) were used to connect the components throughout the system. A 3D rendered view of the assembled VOC test station is shown in Figure 6.17. Details on the hardware components used are given in Appendix F.
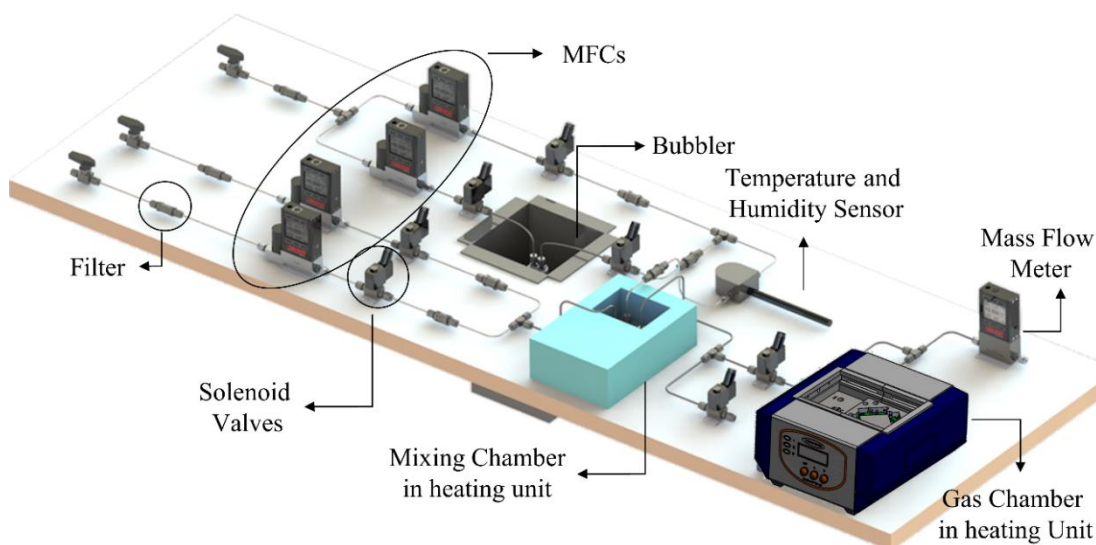
Figure 6.17 Assembly of the VOC test station.

The sensor chamber was designed to fit within the second heating unit with dimensions of 15 cm × 9.5 cm. The chamber is heated to keep the sensors at a constant temperature and maintain a positive temperature gradient through the system (to prevent condensation). A low flow rate is preferred to ensure the flow through the system is laminar. The vapour enters the chamber through a single inlet and is evenly distributed to the eight sensors. The vapour mixture leaves the chamber via a single outlet, which is connected to the exhaust. A mass flow meter (Alicat Scientific, USA) is used to monitor any leakage in the system.

The sensor chamber is formed from three separate plates that stack together (as shown in Figure 6.18), similar to previously designed chambers [12, 13]. The bottom plate features a heat exchanger for the sample analyte to reach the temperature of the sensors. The middle plate provides the dead space volume (3.5 mL) in which the devices are exposed to the vapour, which is injected through eight aperture holes (1 mm diameter), located immediately below the devices. An exhaust hole is located at the centre of the dead space through which the sample vapour is evacuated. The top plate was designed to accommodate up to eight oscillator boards (described in section 6.5). To prevent leakage, the boards were glued in place. A total of 4 differential sensors could be tested at a time.

Raised lips around the channels were implemented in the bottom plate to minimise leaks when the chamber was assembled. These lips slot in the matching grooves created in the underside of the middle plate (not visible in figure). Additionally, O-rings seals were included at the bottom and top plates. The three plates are held together by 20 screws.
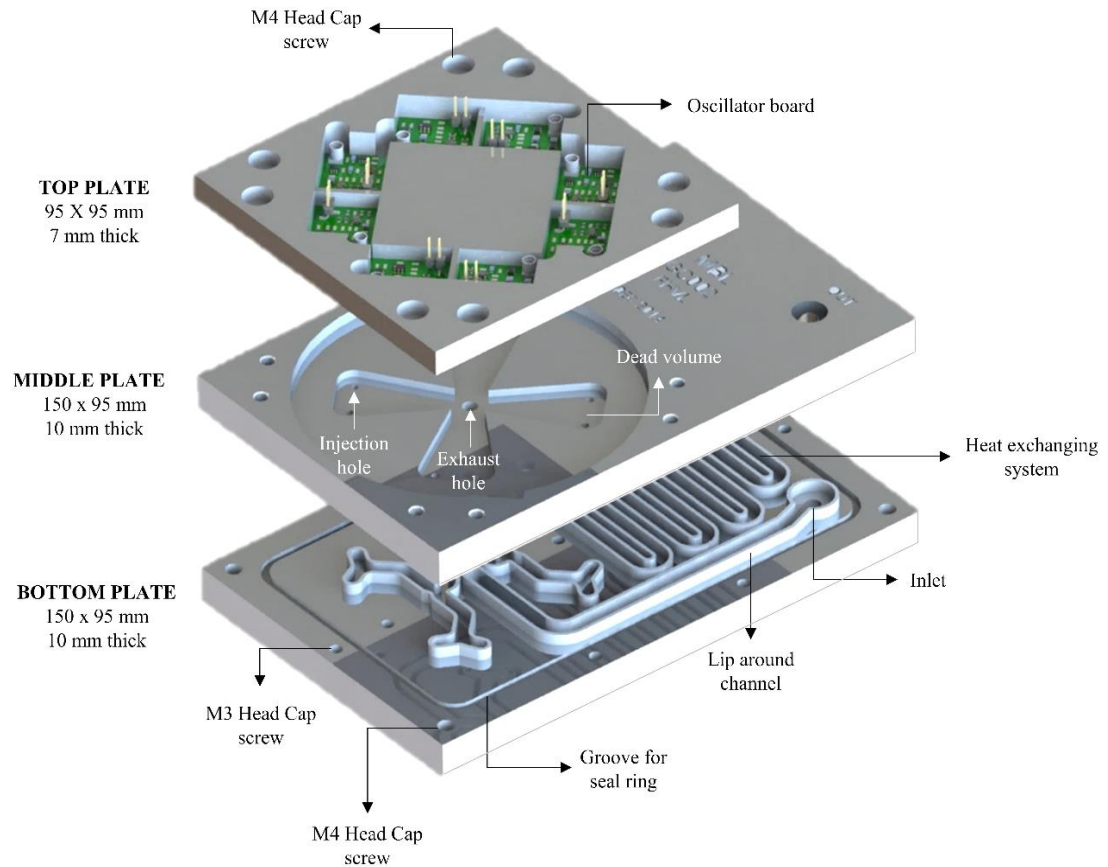
Figure 6.18 Sensor chamber for SMRs.

6.6.3 VALVE CONTROL CIRCUITRY

A National Instruments data acquisition board (NI USB-6009) was used to generate the digital signals that activate the solenoid valves and to acquire analogue signals from the temperature and humidity sensor (Rotronic AG, UK).

An interface circuit between the control software and the hardware was required to drive the solenoid valves. The DAQ board does not provide sufficient current to operate the valves directly. This interface circuit is shown in Figure 6.19a for a single valve. An optocoupler is used to electrically isolate the DAQ board from

the solenoids to avoid damage to the electronics or valves from contact bouncing. Each digital signal generated from the DAQ drives the corresponding switching MOSFET driving the valve with a 12 V power supply.

A photograph of the printed circuit board fabricated in-house is shown in Figure 6.19b implemented for a total of 7 valves used in the system.

(a)   (b)
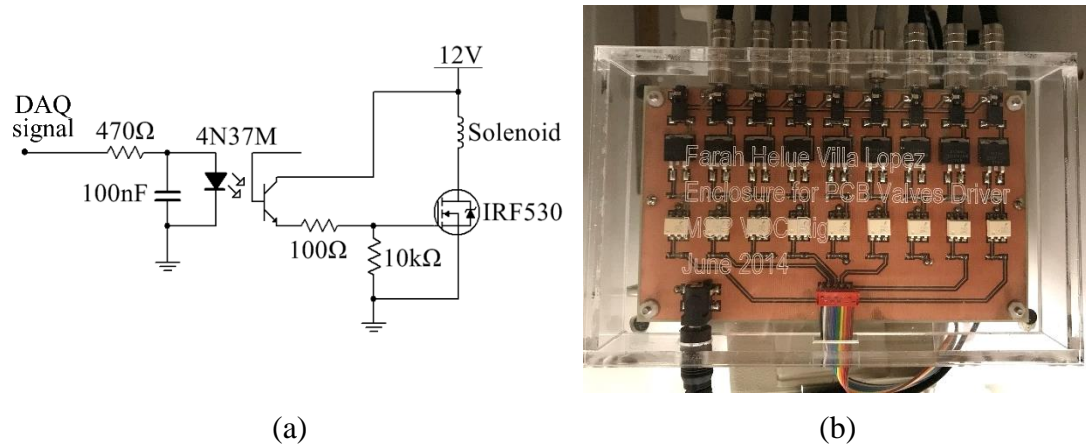
Figure 6.19 Solenoid valve interface electronics.

The MFCs are connected to a Multi-Drop box (Alicat BB9-USB) that carries both power and communication signals to all the MFCs and the mass flow meter simultaneously. The box is connected to the desktop computer via a USB port. No additional interface circuitry was required for the mass flow controllers. The manufacturer provides instrument drivers (compatible with the control software, LabVIEW^{TM}) that allow writing and reading the flow set point for each of the instruments.

6.6.4   CONTROL SOFTWARE

Operation of the VOC station is completely automated. A virtual instrument, developed in LabVIEW^{TM} 2015, allows the control of the rig using a desktop computer. This virtual instrument comprises a block diagram (the graphical programming code) and the front panel (the user interface).

The front panel (Figure 6.20) is the main virtual interface the user interacts with to control the hardware of the VOC station. This front panel is user-friendly,

providing a graphical representation of the rig that allow the user to monitor the process at all times and ensure the system is working as desired.

The MFCs and the mass flow meter in this representation show an indicator which displays the real-time flow rate values, read from the hardware. Temperature and humidity data are displayed as numerical indicators and shown in plots for easy reference. These data together with the flow rates read from the mass flow instruments can be saved to a file, if required.

Automatic and manual operation can be selected. When using the automatic mode, tests can be performed over long periods of time. A file containing the input test data (required VOC concentration and exposure times) is uploaded to the program. The system converts the user input data to mass flow rates (VOC and air lines). The system steps through each row of data. It generates the desired concentrations for a specified time and controls the position of the solenoid valves as required. In manual mode, the flow rates of the MFCs and the position of the valves are controlled solely by the user. This mode is normally used to test the system for leaks or to quickly observe the response of the sensors. The block diagram and further details on the virtual instrument, including operating instructions, are presented in Appendix G.
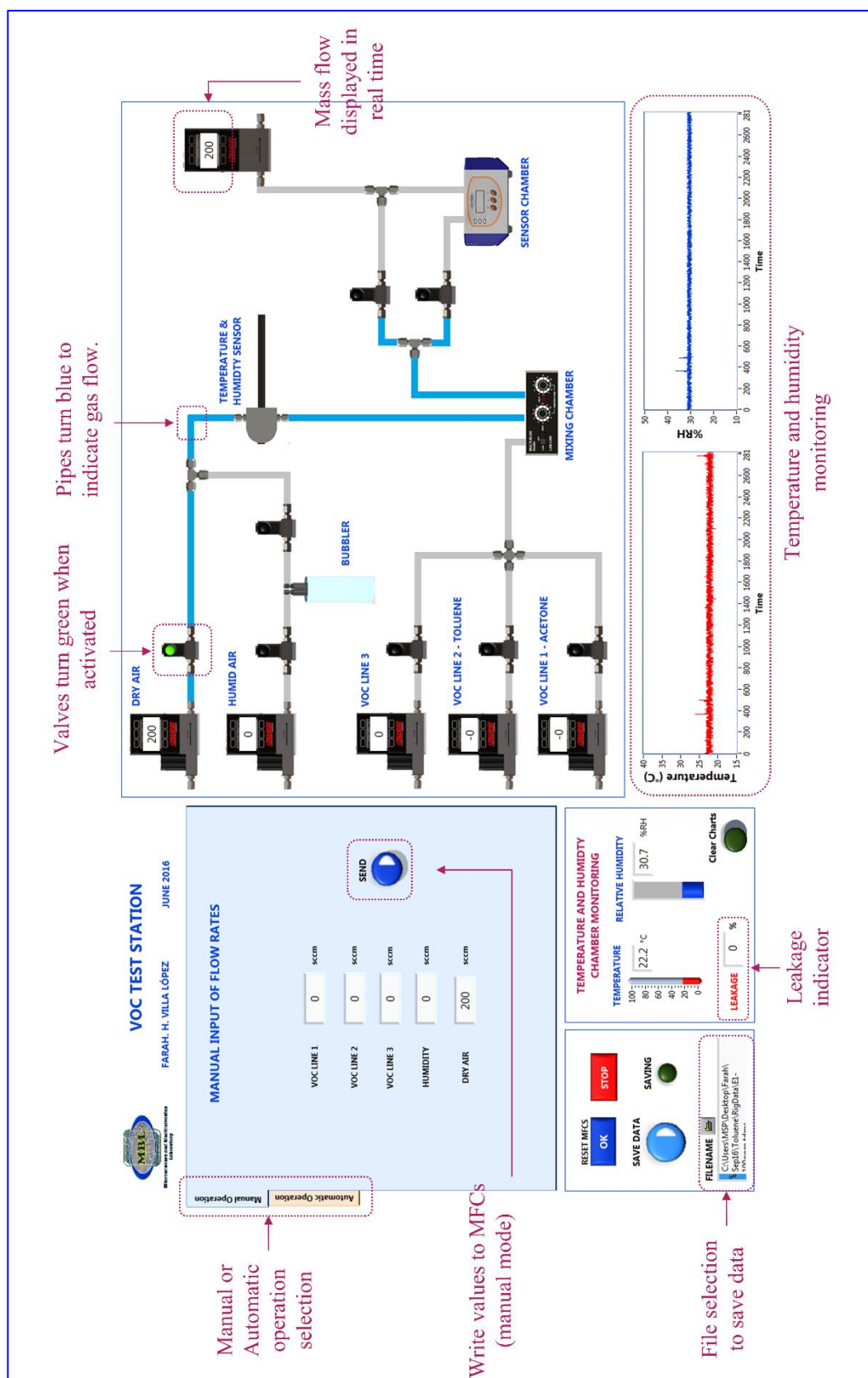
Figure 6.20 Front panel to control the VOC test station. To create a user-friendly interface the panel depicts an overview of the system.

6.7 EXPERIMENTAL SETUP AND RESULTS

The VOC test station was constructed, according to the layout designs shown previously. A photograph of the completed system is shown in Figure 6.21. The computer controlling the testing station (not visible in the photograph) is located above the VOC test chamber.
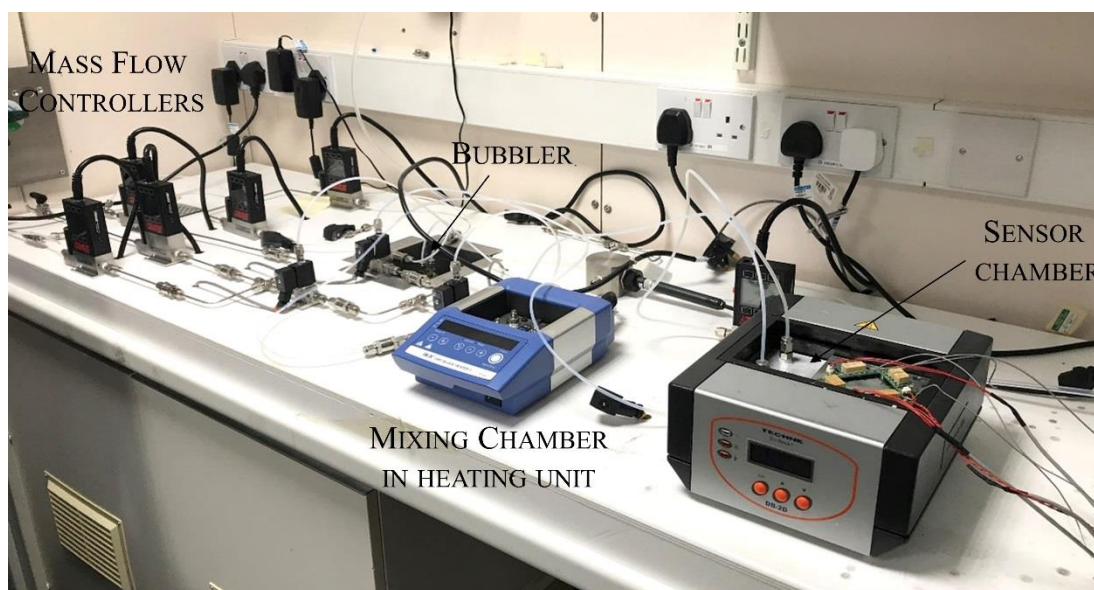
Figure 6.21 Photograph of the automated VOC test station showing the MFCs and temperature controlled chamber.

Two channels on the VOC test station are dedicated to specific VOCs (toluene and acetone). A separate line is used for each compound to avoid cross-contamination. The lines can be cleared using zero air, to allow other VOCs to be tested. The test station allows the VOCs to be diluted in zero air (a mixture of dry and humid as required). The following maximum concentrations were possible for each of the VOCs (i.e. the cylinder concentration, with no dilution): toluene 100 ppm and acetone 200 ppm. Each MFC allows a maximum flow rate of 500 SCCM, and permits flow rates as low as 2.5 SCCM, i.e. this defines the minimum possible concentrations that can be generated with the test station, according to the maximum concentration of the cylinder. The minimum possible VOC concentrations are 0.5 and 1.0 ppm for toluene and acetone, respectively.

The VOC sensor chamber is shown in Figure 6.22, showing four pairs of SMR sensors, each consisting of a sensing and reference oscillator board. The chamber is positioned inside a Dri-block heater to maintain a constant temperature. The mixer boards are visible in the photograph. These boards are powered with a 3.3 V supply and each of them provide one differential sensor output to the microcontroller.
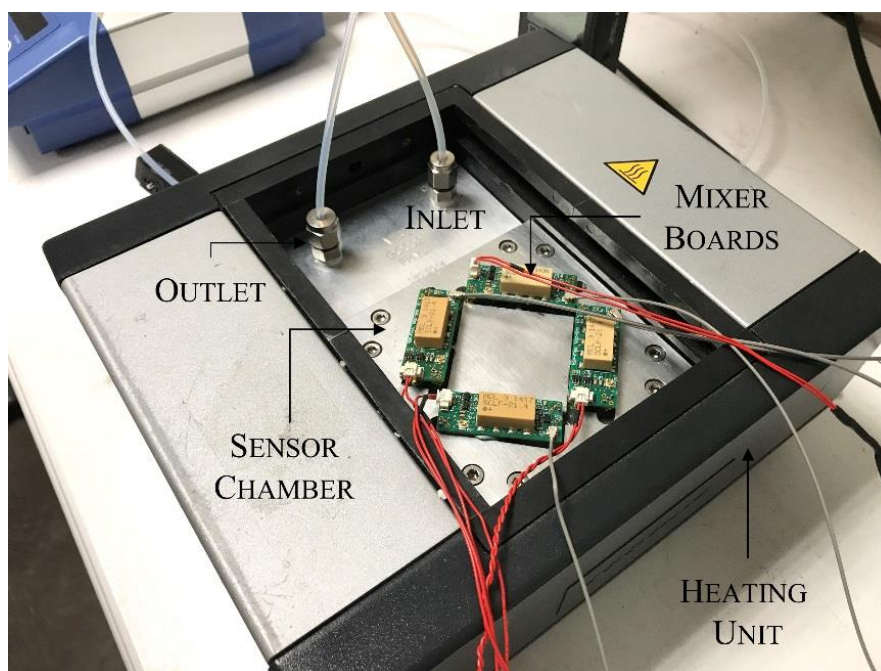
Figure 6.22 Photograph of the testing chamber containing four pairs of sensors. System includes 8 SMR boards connected to four mixer boards.

As discussed in Chapter 1, benzene is the only VOC with a regulated exposure limit in the EU, and thus it is of great interest for air quality monitoring. However, these strict regulations (maximum exposure limit set at 1 ppm) and the stringent health and safety requirements for the University of Warwick entailed the VOC was too hazardous for testing to be performed in the laboratory.

Toluene and acetone are also of high interest to air quality monitoring as they are the two vapours most commonly found in the background air as discussed in section 1.2.2. The safe exposure limits for these vapours are set at 50 ppm and 500 ppm for the long-term exposure (8-hr reference period) and 100 ppm and 1500 ppm for short-term exposure (15-minute reference period), respectively. These exposure limits are orders of magnitude higher than for benzene, and thus experiments could be realised in a controlled environment.

For the experiments presented in the following sections, the SMR sensors were exposed to toluene and acetone at maximum concentrations of 100 ppm and 200 ppm, respectively.

6.7.1 TOLUENE DETECTION

The polymer coated SMR sensors (PDMS and PEG) were left to stabilise (in zero air) for a period of at least 24 hours prior to the start of the experiments. The sensors were exposed to pulses of toluene concentrations in the range of 5 ppm to 100 ppm. Typically sensors are exposed to a high concentration of VOC and then stepped down to low concentrations, before returning to high concentrations). The absorption of toluene in the polymer coating produced a change in mass, which caused a negative change in resonant frequency of the sensing device. In between the toluene pulses, the chamber was flushed with the baseline gas (zero air) for a period of 10 minutes. The baseline period allowed the vapour molecules to desorb from the polymer coating on the SMR sensor.

A constant flow rate of 200 SCCM was used throughout the VOC pulses and stabilisation periods (flow rate maintained regardless of gas concentration). The chamber was kept at a constant temperature of 35 °C, using the Dri-block heater, discussed previously. An example transient response from a 180 nm PDMS coated SMR sensor is shown in Figure 6.23a, where the device was exposed to toluene in the range of 100 to 25 ppm. Figure 6.23b shows a second transient response from these devices, where the SMR sensors were exposed to lower concentrations of toluene in the range of 25 to 5 ppm.
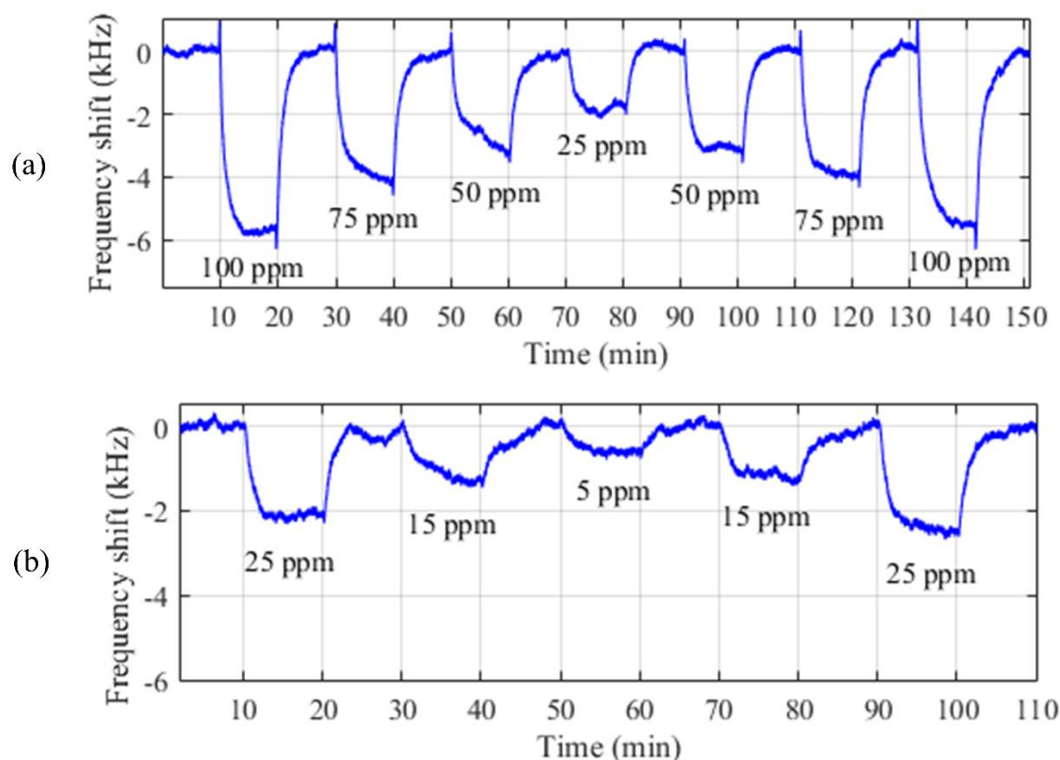
Figure 6.23 Transient response of PDMS coated SMR sensor (180 nm coating) at 35 °C. Toluene concentrations varied from (a) 25 ppm to 100 ppm and (b) 5 ppm to 25 ppm with constant flow rate of 200 sccm.

A typical experiment had a duration of 150 mins. Over the course of an experiment, the differential sensor output typically drifted ~5 kHz. The dual configuration used prevented larger drifts due to thermal variations. However, drift, caused by the instability of the oscillator circuits was apparent on the output from the dual configuration. Each resonator in a pair exhibited a different level of instability, thus the drift cannot be eliminated entirely through use of a dual sensor system.

The drift present in the raw sensor data was removed using signal processing, after the experiment data was captured. In the processed data, spikes are visible when the VOC concentration is changed. These effects were due to the flow rate changing inside the chamber, while switching from zero air to VOC mixture and vice versa. The MFCs and valve configuration in the test station allowed very fast switching between a VOC and zero air (<2 s), although a spike in flow rate was still apparent (~10 % flow variation during the short switching period). This change in flow caused a corresponding change in pressure, which is not normally experienced in the application of air quality monitoring.

The thickness of the coating on the sensing SMR device has an effect on the response of the sensor (e.g. sensitivity, response time, etc.), when exposed to a VOC. To investigate this effect, two different PDMS coating thicknesses were trialled (70 nm and 180 nm). Figure 6.24 shows the measured frequency shifts for toluene concentrations in the range of 5 ppm to 100 ppm.

Linear fits were applied to the data (shown in the same figure), with R^2 values of 0.9939 and 0.9961 for the 70 nm and 180 nm PDMS coated sensors, respectively. Thus, these fits demonstrate the strong linearity of the SMR response. The sensitivities of these devices were measured as approximately -25 Hz/ppm and -60 Hz/ppm, respectively. Both devices demonstrate favourable sensitivities compared to values previously reported (7.29 Hz/ppm) [14].
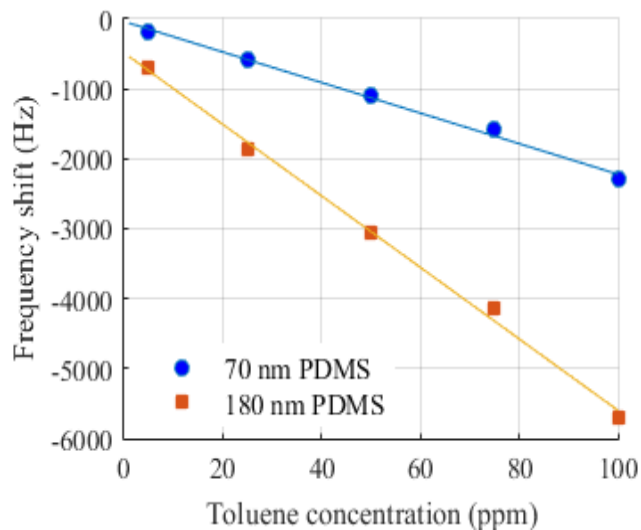
Figure 6.24 Frequency shift of PDMS coated SMR sensors to the exposure of toluene (5 to 100 ppm). Linear fit shows sensitivities of devices.

The sensitivities obtained from these experiments were similar to those obtained from the finite element simulations. From the simulation data, sensitivities of -17.5 Hz/ppm and -45 Hz/ppm were calculated for a 70 nm and 180 nm PDMS coatings, respectively. The simulated values are lower than those found from experimental data (errors of 7.5 Hz/ppm and 15 Hz/ppm, for the 70 nm and 180 nm coatings, respectively). The simulations assume a uniform coating over the sensing area of the SMR, thus variations in the surface of the deposited polymer coatings

caused a higher sensitivity, through stronger interactions with the vapour molecules (higher specific surface area).

Two short (240 s) periods of the sensor time series response are shown in Figure 6.25. These periods show the response and recovery of two SMR sensors coated with PDMS (two thicknesses of 70 nm and 180nm) to 100 ppm of toluene vapour. The frequency response data was normalised (from 0 to 1) to account for the difference in sensitivities between the thicknesses of the coatings. For the 70nm PDMS coated device the response and recovery times (time to reach 67% of the final frequency shift) were measured as 68 s and 50 s, respectively. For the 180 nm coating, a response time of 87 s and a recovery time of 93 s were measured.
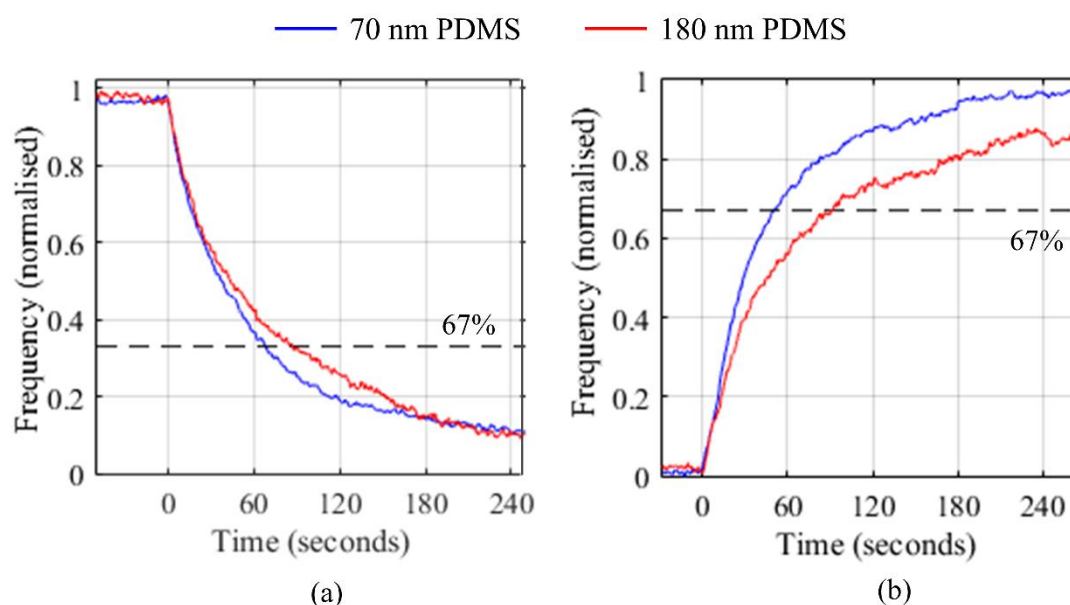
Figure 6.25 Time series sensor response and recovery times, when exposed to toluene vapour at 100 ppm for PDMS coated SMRs (70 nm and 180 nm).

The sensor response data shown in Figure 6.24 and Figure 6.25 demonstrate the variation in sensor response caused by the thickness of the polymer coating. A trade-off between sensitivity and response time is visible, where a thicker coating enables higher sensitivity, but at the expense of response time. For the example PDMS coating shown, the thicker coating (180 nm compared to 70 nm) caused the following parameters to increase: sensitivity (by a factor of 2.4), the response time (average +28 %) and the recovery time (average +86 %).

In addition to a PDMS coated SMR, it is proposed that a PEG coated SMR sensor is needed, for the detection of acetone, in an air quality monitoring system. The PEG coating was chosen for its good sensitivity to acetone, and for low sensitivity to toluene (partition coefficients ratio of 3.8). Experiments were performed using a PEG coated SMR sensor (differential configuration, as previously discussed) with toluene vapour to investigate the cross-sensitivity of the device.

A time series response of a PEG coated SMR (120 nm film) is presented in Figure 6.26 for the detection of toluene concentrations between 25 ppm and 100 ppm. The sensitivity observed by the PEG coated SMR device (6 Hz/ppm) is approximately 4 times lower than the PDMS coated SMR (120 nm PEG coating compared to 70 nm PDMS). This response confirms the low sensitivity to toluene, shown previously by the partition coefficients calculated in Table 6.3. The partition coefficient for the PDMS-toluene pair is ~10 times higher than that for PEG-toluene pair.
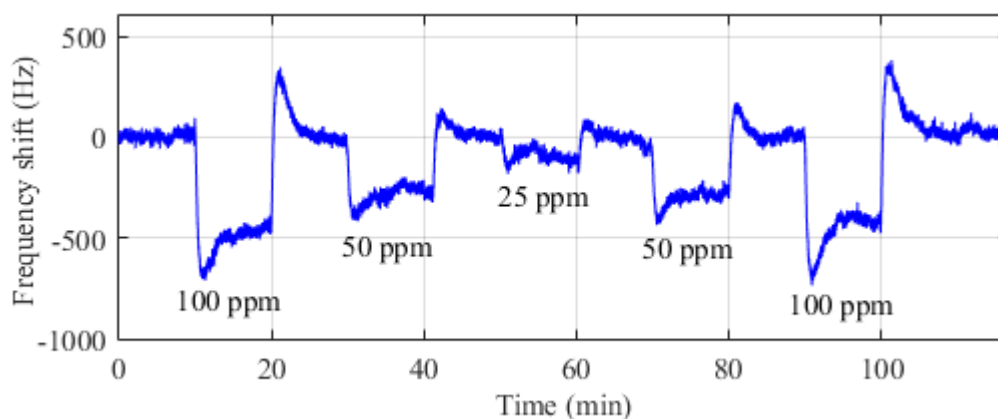
Figure 6.26 Transient response of PEG coated SMR (120 nm thick) at 35°C. Toluene concentration varied from 25 ppm to 100 ppm.

In both cases, the SMR sensors demonstrated good repeatability. Comparable results were obtained for three repetitions of the experiments. The sensors also exhibited good reversibility (the absorption/desorption of the vapour molecules) when going from low to high concentrations of toluene and vice versa. The frequency shifts observed for each of the concentrations are summarised in Figure 6.27 for the PDMS and PEG coating with similar thickness.
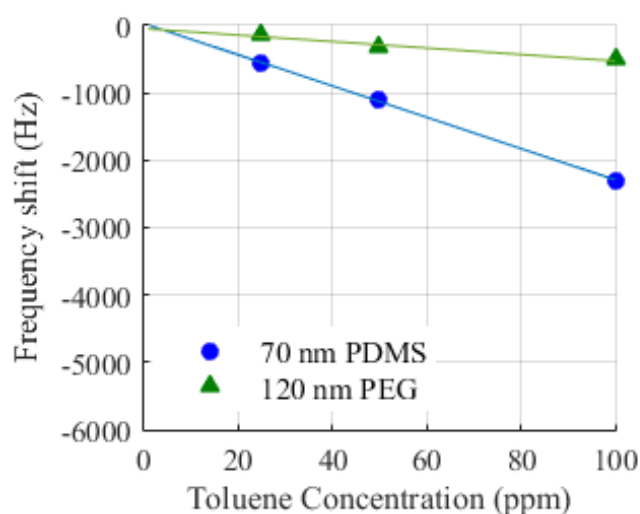
Figure 6.27 Comparison of SMR frequency shifts for the PDMS and PEG coated devices (exposure to between 25 and 100 ppm toluene).

The PDMS coated SMR system was capable of detecting toluene concentrations as low as 5 ppm, which is well below the maximum safe exposure limit (50 ppm short term exposure). The sensitivity of the 180 nm coated device (60 Hz/ppm) and low noise level of the sensing system (25 Hz) demonstrate the potential for a limit of detection in the low ppm range (for example, 1 ppm). The VOC test station, in its current form, was not able to generate toluene vapours of <5 ppm concentrations (i.e. 1 ppm could not be generated without a cylinder containing a lower concentration toluene mixture).

6.7.2 ACETONE DETECTION

A SMR sensor coated with a PEG layer (120 nm thick) was previously trialled to ppm-level toluene concentrations. The coating was selected as it offered lower sensitivity to toluene compared to alternative polymers and reasonable sensitivity to acetone. To investigate the sensitivity of the PEG sensor to acetone, the system was tested to vapour concentrations in the range of 50 ppm to 200 ppm, as shown in Figure 6.28.

The sensor was capable of detecting 50 ppm of acetone vapour (10 times lower than the maximum safe exposure limit, 500 ppm). The sensitivity of the device was ~3.5 Hz/ppm. Thinner sensor coatings need to be tested to improve the performance of the device. Wang and Chen reported sensitivities between 300-700 Hz/ppm based

on a 2.5 GHz SMR, with PMMA coatings between 20-80 nm thickness [15] with concentrations tested between 0.1 and 1%.
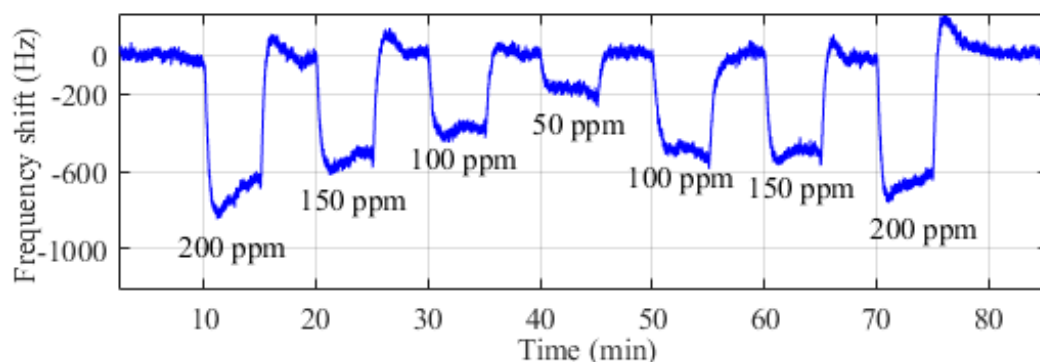
Figure 6.28 Time series response of PEG coated SMR sensor (120 nm film) at 35°C to the exposure of acetone vapour (50 ppm to 200 ppm)

The sensor system exhibited a low level of drift throughout the experiment, for example, the second 100 ppm response (~480 Hz) was greater than the first 100 ppm response (~360 Hz). A comparison of the PEG coated SMR sensor response to low ppm concentrations of acetone and toluene is shown in Figure 6.29 and the sensitivities for the PDMS and PEG coated sensors are summarised in Table 6.7.
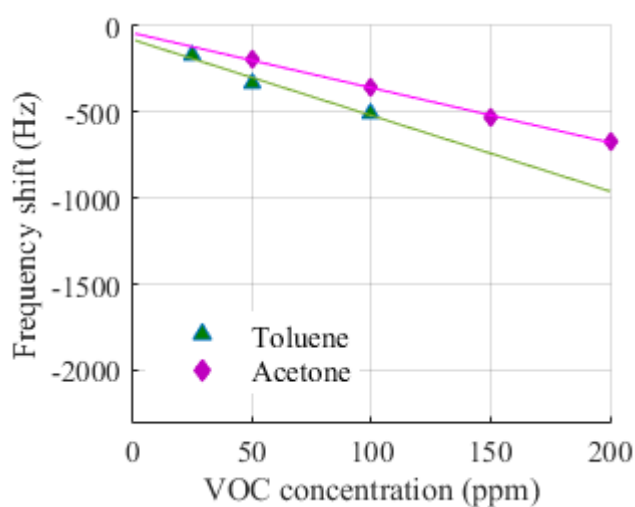
Figure 6.29 Comparison of SMR frequency shifts for the PEG coated device exposed to acetone and toluene vapours.

As expected, from the partition coefficients shown in Table 6.3, the sensitivity of the PEG coated SMR is higher when detecting a toluene vapour, compared to acetone. However, it is a factor of 10 lower, compared to the sensitivity of a PDMS coated SMR.

Table 6.7 Sensitivity of polymer coated SMR devices (900 MHz) for the detection of toluene and acetone (in Hz/ppm).

	TOLUENE	**ACETONE**
PDMS 70 nm	-25	-
PDMS 180 nm	-60	-
PEG 120 nm	-6	-3.5

6.7.3 HUMIDITY EFFECT

The experiments were mainly performed in a dry environment (~0 % RH). It is likely most air quality monitors will be used in environments with varying RH between 20 and 80 % (e.g. indoor or outdoor locations). Variations in RH have been reported to affect the resonant frequency of polymer-coated acoustic sensors, as the water vapour becomes absorbed in the polymer coatings [16]. A differential measurement can help reduce the baseline variation, although if a significant amount of water vapour becomes absorbed, the sensitivity of the device can be affected.

The test station allowed humid zero air to be mixed with the VOC vapour and dry zero air to create a humid mixture. However, to keep a constant level of humid air the maximum concentration of the VOC was limited (i.e. as the VOC was diluted with the humid air, it was not possible to test the cylinder concentration of the VOC with any level of RH). An initial experiment was performed in humid conditions at 40 % RH, similar to that found in a domestic environment. The time series response is shown in Figure 6.30, using the PDMS coated sensor (180 nm). Further experiments were desired, but to generate a wider range of concentrations, cylinders with higher concentrations of the VOCs are required.
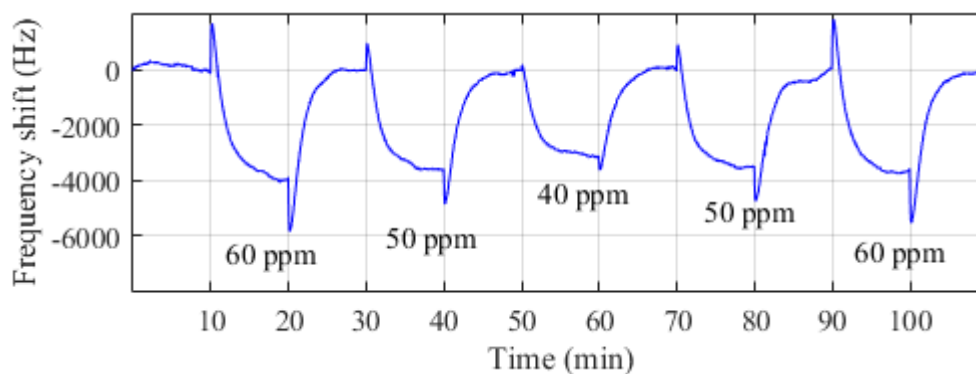
Figure 6.30 Transient response of PDMS coated SMR sensor at 35°C and 40% RH to the exposure of toluene concentrations (40 ppm to 60 ppm).

The increase in RH considerably shifted the baseline frequency of the SMR sensors (~20 kHz) but had a minimal effect on the sensor performance, in terms of response time and recovery. Relative to the experiments performed in dry conditions, the recovery time increased by only 2 s (average 95 s) but the response time increased by 23 s (average 110 s). However, the sensitivity of the sensor was slightly increased to -70 Hz/ppm (compared to -60 Hz/ppm).

Further work involves testing in humid conditions. The level of humidity generated by the test station was not stable, as measured by the commercial RH/temperature sensor. This caused the SMR sensor response to be unstable. Sudden spikes in RH concentration were visible, caused by water droplets forming in the pipes used to connect the mixing chamber to the sensor chamber. The formation of water droplets could be prevented by heating the pipes to the same temperature as the mixing chamber. Further work involves improving the test station to ensure a continuous positive temperature gradient is created from the humidity bottle to the sensor chamber.

The effects of humidity in the sensor response (and in the polymer coating) is not greatly reported in the literature. Zellers and Han [16] concluded the properties of the polymer coating (i.e. polarity) and the VOC under test have the strongest effect. Polar coatings are more prone to water absorption. However, there is not a consistent link between a polymer polarity and effects of humidity in the sensor response. Thus, the effect needs to be investigated for each specific polymer-vapour combination.

6.8 CONCLUSIONS

A SMR based sensor system was developed, capable of detecting low ppm concentrations of toluene (5ppm) and acetone (50 ppm). It is proposed an air quality monitor based on these devices can be developed, based on the detection limits of the devices (compared to the safe exposure limits for toluene and acetone of 50 ppm and 500 ppm, respectively). However, further testing is still required to evaluate the performance of the devices in typical environmental conditions of temperature and humidity (including variable conditions).

The SMR devices (resonating at 900 MHz) were employed along with a thin polymer film (<200 nm) to detect the toluene and acetone vapours. To select the polymer coatings, an analysis of the partition coefficients (for specific polymer-vapor pairs) was performed using linear solvation energy relationships. PDMS and PEG were the selected polymers, due to their high partition coefficients and low cross-sensitivities for the target vapours.

To realise the coated SMR devices, a drop coating system was developed. Thin polymer films were deposited on the sensing area of the SMRs using this system. The system allowed small volumes of polymer solutions to be deposited in a localized area of the SMR device (70 nm coatings possible). The sensor system worked in a dual configuration with a polymer-coated SMR device as the sensing device and an uncoated SMR as the reference channel. Interface circuitry consisted of a Pierce oscillator board to drive the resonators and mixing circuitry to output a low frequency square output signal (<20 MHz) acquired by a microcontroller at 10 Hz sampling rate. Typical power consumption of the sensing system was ~210 mW.

Testing of vapours at specific low ppm concentration levels was made possible through development of a benchtop gas test station. The automated VOC station was designed to expose the sensors to step changes in vapours with long experiments possible (minimal user interaction needed). A gas exposure chamber with very low dead space volume (3.5 mL) was designed to accommodate up to eight oscillator boards (4 differential sensors).

The SMR sensors were mainly tested in dry conditions to the exposure of toluene (in the range of 5 ppm to 100 ppm) and acetone (in the range of 50 ppm to 200 ppm). A trade-off between coating thickness, sensitivity and response time was found (thicker coatings offer high sensitives, but slow response times). A 180 nm PDMS coated SMR device exhibited a linear response for the detection of toluene vapour, with a high sensitivity of -60 Hz/ppm in dry conditions. Response and recovery times were calculated as 87s and 93s, respectively. Good repeatability and vapour absorption/desorption was observed throughout the experiments. Thinner coatings (70 nm PDMS) exhibited a lower sensitivity (-25 Hz/ppm) but faster response and recovery times (68s and 50s, respectively). These experimental results confirmed the validity of the finite element simulations (sensitivities of -45 Hz/ppm and -17.5 Hz/ppm were calculated for PDMS coatings of 70 nm and 180 nm, respectively).

PEG coated SMRs were used to detect acetone vapours (50 to 200 ppm). The devices demonstrated a sufficiently low detection limit (50 ppm) to be used for air quality monitoring, although the sensitivity (-3.5 Hz/ppm) was lower than that previously reported in the literature (300 Hz/ppm).

The test station was not able to produce stable levels of humidity for the long durations of the experiments. Initial experiments were trialled at 40 % RH, with toluene vapour (40-60 ppm) and the PDMS coated SMRs. The higher level of humidity caused the sensitivity of the sensor to increase slightly (-70 Hz/ppm, 180 nm coated device), but the response time increased by 23 s (average 110 s). Further experiments are required to investigate the effect of increased humidity levels. Each polymer coating and vapour pair is effected in a different manner, and thus must be characterised individually.

In general, the experimental results presented in this chapter show a thermal drift (~5 kHz) over the long experiment period (150 min). Although the use of a differential configuration helped on reducing the effects of temperature variations, temperature compensation methods are required in the implementation of such a system in an air quality monitor.

The SMR sensors could detect concentration levels below the safe exposure limits of toluene and acetone, but their performance can be improved in terms of sensitivity, selectivity, response time and circuitry performance (e.g. thermal drift, noise level). In the experiments presented in this chapter, the SMR sensors were exposed to a single VOC at a time. Polymer-coated SMRs are not selective to a specific organic compound but exhibit different sensitivities according to the polymer-vapour partition coefficient.

In a real environment, which could contain multiple VOCs, a single SMR sensor cannot identify the range of compounds present. An array of SMR sensors coated with a range of polymer films can be used for improved selectivity in order to classify the different compounds via pattern recognition using techniques such a Principal Component Analysis (PCA).

In the next chapter, a novel SMR device is proposed to be included in a low-cost air quality monitor to enhance the sensitivity and selectivity, among other improvements, of the SMR sensors.

6.9 REFERENCES

[1]   McGill, R. A. (1996). "Choosing polymer coatings for gas and liquid chemical microsensors", *ANTEC 1996 Plastics -Racing into the Future, Society of Plastics Engineers*. pp. 2080-2084.

[2]   Grate, J. W., Abraham, M. H. and McGill, R. A. (1996). "Sorbent polymers for chemical sensors", *ANTEC 1996 Plastics -Racing into the Future, Society of Plastics Engineers*. pp. 2075-2079.

[3]   Grate, J. W., Martin, S. J. and White, R. M. (1993). "Acoustic wave microsensors. Part II", *Analytical Chemistry*. **65**(22): 987A-996A.

[4]   McGill, R. A., Mlsna, T. E., Chung, R., Nguyen, V. K. and Stepnowski, J. (2000). "The design of functionalized silicone polymers for chemical sensor detection of nitroaromatic compounds", *Sensors and Actuators B: Chemical*. **65**(1–3): 5-9.

[5]   McGill, R. A., M.H.Abraham and Grate, J. W. (1994). "Choosing polymer coatings for chemical sensors", *CHEMTEC*. **24**(9): 27-37.

[6]   Santiuste, J. M. a. and García-Domínguez, J. A. (2000). "Study of retention interactions of solute and stationary phase in the light of the solvation model theory", *Analytica Chimica Acta*. **405**(1–2): 335-346.

[7]   Matatagui, D., Martí, J., Fernández, M. J., Fontecha, J. L., Gutiérrez, J., Gràcia, I., Cané, C. and Horrillo, M. C. (2011). "Chemical warfare agents simulants detection with an optimized SAW sensor array", *Sensors and Actuators B: Chemical*. **154**(2): 199-205.

[8]   Demathieu, C., Chehimi, M. M. and Lipskier, J.-F. (2000). "Inverse gas chromatographic characterization of functionalized polysiloxanes. Relevance to sensors technology", *Sensors and Actuators B: Chemical*. **62**(1): 1-7.

[9]   Hierlemann, A., Zellers, E. T. and Ricco, A. J. (2001). "Use of linear solvation energy relationships for modeling responses from polymer-coated acoustic-wave vapor sensors", *Analytical Chemistry*. **73**(14): 3458-3466.

[10]   Abraham, M. H., Andonian-Haftvan, J., Whiting, G. S., Leo, A. and Taft, R. S. (1994). "Hydrogen bonding. Part 34. The factors that influence the solubility of gases and vapours in water at 298 K, and a new method for its determination", *Journal of the Chemical Society, Perkin Transactions 2*,(8): 1777-1791.

[11]   Kurzawski, P., Hagleitner, C. and Hierlemann, A. (2006). "Detection and discrimination dapabilities of a multitransducer single-chip gas sensor system", *Analytical Chemistry*. **78**(19): 6910-6920.

[12]   Covington, J. A. (2001). "CMOS and SOI CMOS FET-based Gas Sensors", PhD Thesis. *School of Engineering,* University of Warwick, Coventry, UK.

[13]   Ingleby, P. (1999). "Modelling and characterisation of conducting polymer chemoresistors", PhD Thesis. *School of Engineering,* University of Warwick, Coventry, UK.

[14]   Johnston, M. L., Edrees, H., Kymissis, I. and Shepard, K. L. (2012). "Integrated VOC vapor sensing on FBAR-CMOS array", *2012 IEEE 25th International Conference on Micro Electro Mechanical Systems (MEMS)*. pp. 846-849.

[15]   Wang, J. and Chen, D. (2013). "Investigation of polymer-coated film bulk acoustic wave resonator for acetone vapor detection", *2013 IEEE International Conference on Green Computing and Communications and IEEE Internet of Things and IEEE Cyber, Physical and Social Computing*. pp. 1680-1684.

[16]   Zellers, E. T. and Han, M. (1996). "Effects of Temperature and Humidity on the Performance of Polymer-Coated Surface Acoustic Wave Vapor Sensor Arrays", *Analytical Chemistry*. **68**(14): 2409-2418.

CHAPTER 7

DESIGN OF CMOS BASED SOLIDLY MOUNTED RESONATOR

7.1   INTRODUCTION

Chapters 5 and 6 demonstrated the use of solidly mounted resonators for two air quality monitoring applications (particulate matter and VOC detection). The developed sensing systems consisted of ZnO based SMR devices fabricated on a silicon substrate and interfaced to discrete circuitry in a dual configuration. Results obtained with these prototypes demonstrated the suitability of SMR devices in air quality monitoring, but three major aspects need to be considered for their implementation:

(1) To develop a low cost, lightweight and low-power personal air quality monitor, the SMR devices must be capable of being manufactured in mass production at a low cost, have a small footprint and improved performance, and the circuitry be optimised to minimise power consumption. To address this point, the current

state-of-the-art in monolithic integration of BAW devices with the CMOS circuitry was reviewed in Chapter 2. Current implementations of SMR-IC integration suffer from an increased number of required lithography steps, lower manufacturing yield and performance.

(2) A real-time particle sensor based on SMRs requires an active method of cleaning the sensing surface after a period of time (currently not possible with the proposed approach). In this way, a sensor with a long-life span can be produced.

(3) A method of increasing the sensitivity and selectivity of the SMR based VOC sensor is needed to obtain a highly sensitive sensor with fast response times, capable of detecting common organic compounds (within the safe exposure limits) found in the ambient air.

To address the afore-mentioned limitations, the development of a novel CMOS based SMR device is presented in this chapter. The SMR sensor advances upon the current generation of acoustic devices, through the fabrication of the acoustic mirror within a standard CMOS process. It is proposed that the complete electronic resonator circuitry can be monolithically integrated into the same CMOS process; thus, a complete sensor system can be manufactured with a significant reduction in the required post-processing stages.

The sensor design consists of an integrated heater, an acoustic mirror (formed from CMOS layers) and the resonator structure (piezoelectric layer and electrodes). The integrated microheater is used to enhance the sensitivity of the SMR sensor through the use of a thermal modulation technique (temperature variations of the sensing area to target specific analytes).

The CMOS based SMR design concept, including mapping the heat distribution of the integrated heater, was evaluated by means of finite element modelling. The device was fabricated and characterised. Experimental results for the detection of fine particles are presented.

7.2   STRUCTURE OF NOVEL CMOS BASED SMR

As discussed in Chapter 2, three of the main problems encountered in the integration of SMR devices with the CMOS circuitry can be summarised as follows:

(1)   The total number of photolithography steps, required to fabricate the integrated system, is increased (processing steps for the IC add to the processing steps required for the SMR device).

(2)   The manufacturing yield of the combined process is lower compared to the yield obtained from the individual processes. This is especially the case when combining SMR devices with a small footprint (<1 mm^2) with larger ICs, which can also significantly increase the manufacturing costs.

(3)   The distance between the interconnections of the IC and the SMR device is increased due to the total thickness of the deposited layers above the CMOS substrate (between 4 µm and up to 10 µm, that form the acoustic mirror layers, the electrode and piezoelectric).

The CMOS based SMR device proposed in this work comprises of three parts: (1) a single crystal silicon (SCS) microheater, (2) a CMOS based acoustic mirror and (3) the resonator structure. The overall structure of the novel SMR device is shown in Figure 7.1. Possible integration of the device with CMOS interface circuitry is depicted in the same figure. However, this work only focused on the development of the CMOS based SMR device for its future integration with the IC.

In the proposed device, both the SCS microheater element and the acoustic mirror of the SMR are fabricated during the same standard CMOS process (together with the IC). Only the resonator structure (electrodes and piezoelectric layer) are deposited and patterned in a post-CMOS process. The proposed device advances the current state-of-the-art through the fabrication of the acoustic mirror stack (high and low acoustic impedance layers) during a standard CMOS fabrication process. The high acoustic impedance and low acoustic impedance layers are formed by the metal and oxide layers of the selected CMOS process (deposited during the metallization process), respectively.
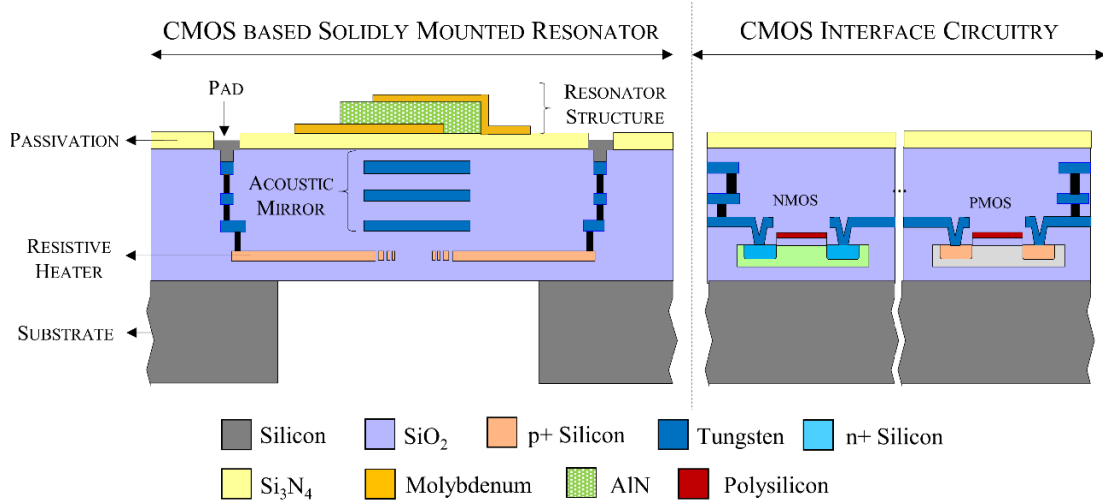
Figure 7.1 Structure of the CMOS based solidly mounted resonator device (CMOS acoustic mirror) with integrated SCS heater for temperature modulation. Integration with CMOS circuitry is shown. Figure is not to scale.

As opposed to current approaches of SMR fabrication and SMR-IC monolithic integration (shown in Figure 7.2) [1-3], only the resonator structure (electrodes and piezoelectric layer) need to be deposited in the post-CMOS process.
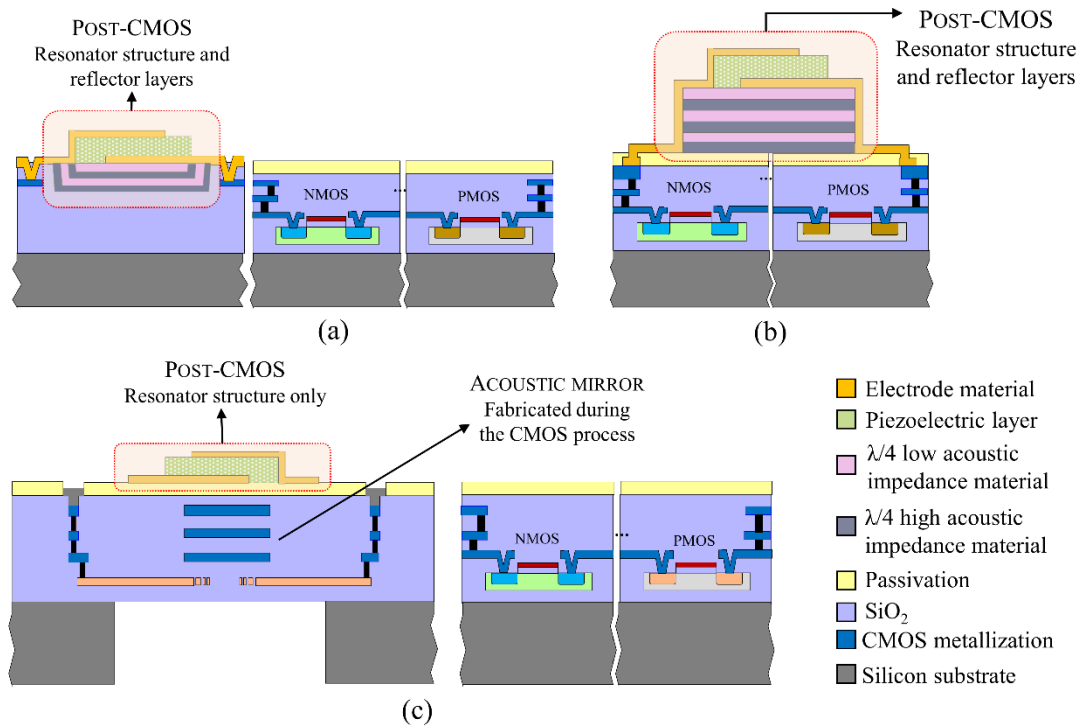
Figure 7.2 (a) and (b) Current state of art in SMR-CMOS integration compared to (c) the proposed novel SMR device with integrated circuitry.

Volume manufacturing of SMR devices (e.g. for mobile communications applications) is performed at conventional CMOS manufacturing facilities [4], making use of existing IC equipment. Non-standard CMOS processes are used to form the acoustic mirror (layers of $\lambda/4$ thickness). This is only possible for volume manufacturing as the process must be tailored to a specific run, i.e. specifications of the layers for acoustic mirror must be given, in terms of material and thickness (CMOS-compatible materials only).

For the proposed device, the acoustic mirror is fabricated within a standard CMOS process (with defined metallization and layer thicknesses). Using these process-defined layers gives place to asymmetric acoustic mirror structures. Compared to the configuration in Figure 7.2a and b, the integration proposed in this work has the advantages of reduced post-fabrication steps. Only the electrodes and piezoelectric layer need to be deposited above the CMOS wafer. The acoustic mirror layers are formed by the metal layers and oxide layers of the CMOS process. This not only reduces the post-CMOS manufacturing time and costs, but also offers improved manufacturing tolerances from batch to batch.

In the proposed design, the acoustic mirror uses all three metal layers available in the selected CMOS process (XI10 1.0 µm SOI CMOS process) and thus the IC must be implemented next to the resonator. CMOS processes with at least five metal layers would allow the acoustic mirror to be integrated in the layers immediately above the circuitry and inside the substrate. This will further reduce the overall size of the integrated system as a stacked structure can be obtained.

Design and finite element simulations of the proposed structure are presented in the following sections. Initially the acoustic mirror was simulated alone to evaluate the suitable operating frequencies of an SMR fabricated using the selected XI10 1.0 µm SOI CMOS process. The heater was thoroughly simulated to envisage the heat distribution across the device, considering the addition of the acoustic mirror layers on top. Finally, the complete device was simulated, including the resonator structure to be fabricated during post-processing to validate the operation of this novel sensor.

7.3   DESIGN AND MODELLING OF CMOS BASED ACOUSTIC MIRROR

For the implementation of the proposed structure, a silicon on insulator (SOI) wafer was selected. By using this substrate, the area underneath the integrated heater is passivated, reducing thermal losses and simplifying the fabrication process [5]. In particular, the standard XI10 1.0 µm SOI CMOS process (XFAB, Germany) was used. This process allows the use of up to three metal layers with a choice of aluminium or tungsten metallization.

As discussed in Chapter 3, the acoustic mirror in SMR structures is formed by alternating layers of low and high acoustic impedance materials, commonly with a $\lambda/4$ thickness. The total number of layers required to obtain a good reflectivity depends on the low to high acoustic impedance ratio of the materials chosen (usually at least four layers are required with a minimum of 6 usually used). In this work, thicknesses and materials of the layers used to form the acoustic mirror are entirely defined by the selected CMOS process. For the standard XI10 SOI CMOS process selected, the available layers and their thicknesses are summarised in Table 7.1.

Table 7.1 Typical thicknesses of the standard XFAB XI10 SOI CMOS process for tungsten and aluminium metallization.

LAYER	TUNGSTEN (nm)	ALUMINIUM (nm)
Passivation (Si_3N_4)	550	550
Oxide 3	200	200
Metal 3 (M3)	500	940
Oxide 2	900	650
Metal 2 (M2)	300	650
Oxide 1	650	650
Metal 1 (M1)	300	720
SiO_2	2000	2000
Polysilicon	300	300
Active Silicon	250	250

Using the standard thicknesses and layers shown above, an asymmetric acoustic mirror structure will be obtained (all layers have different thicknesses). Asymmetric acoustic mirrors can exhibit reduced transmissivity at specific

frequencies. The operating frequencies of a resonator built upon these CMOS based acoustic mirror are determined by the transmissivity of the mirror. To obtain high quality factors, the resonator must operate at frequencies where the mirror exhibits maximum reflectivity. Thus, careful design of the complete structure is required.

The transmissivity of an acoustic mirror formed by the various combinations of these layers was evaluated, for both aluminium and tungsten metallization, using the one-dimensional Mason model. The simulated transmissivities are shown in Figure 7.3. The acoustic impedance ratio of Al and SiO_2 is very low at a value of only 1.3 (refer to section 3.3.2). Therefore, a very poor performance of the reflector stack was obtained for the aluminium metallization with a maximum transmissivity of only -10 dB (as seen from Figure 7.3a). On the other hand, W and SiO_2 layers offer a large ratio of high to low acoustic impedance (at a value of ~8). The simulated mirror transmissivity with W layers is shown in Figure 7.3b. The transmittance of such structure is at least three times better than that with Al metallization. Thus, the SOI 1.0 µm CMOS process with W metallization was chosen to implement the proposed CMOS based acoustic mirror.
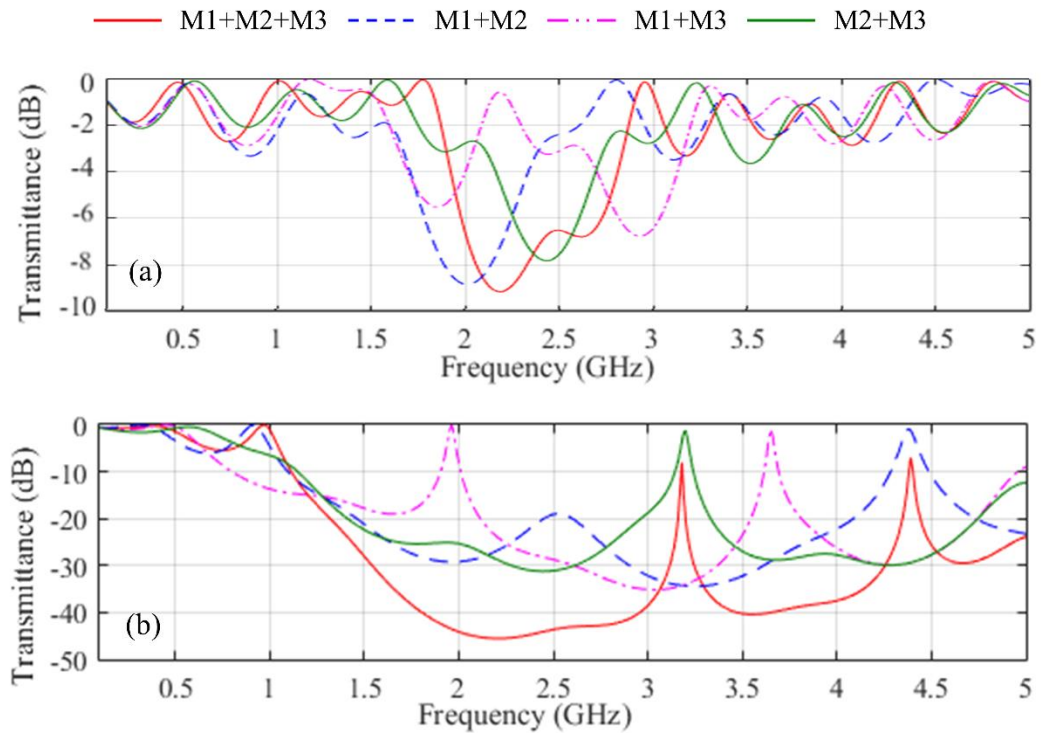

Figure 7.3 Simulated transmissivity of CMOS acoustic mirror formed by (a) aluminium and (b) tungsten metallization of the XI10 process layers.

The wave reflection is maximised when all three W metal layers (and oxide layers) are used to form the acoustic mirror. The resulting asymmetric acoustic mirror structure exhibits excellent performance with high reflectivity and a wide bandwidth of transmittance. A transmittance of almost -50 dB is obtained at frequencies between 2 to 3 GHz, but also good reflectivity is obtained at frequencies between 3.5 and 4 GHz. A SMR device with resonant frequencies between 2 and 3 GHz (a range commonly used for mobile applications) can be obtained using the selected CMOS process. Suitable thicknesses of the electrodes and selected piezoelectric material (to be deposited in a post-fabrication process) need to be selected according to these requirements.

Following the analysis of the CMOS based acoustic mirror, a 2D finite element model (COMSOL Multiphysics v4.2) was used to analyse the frequency response of the entire CMOS based SMR device (including the layers of the resonator structure). For the development of a complete CMOS based resonator, capable of being fabricated entirely in a CMOS foundry, careful selection of the piezoelectric material is needed, as well as for the electrodes material as only CMOS compatible materials are suitable.

In terms of piezoelectric material, AlN is preferred over ZnO or PZT. The latter two pose severe contamination problems inside CMOS fabrication facilities, as they can degrade the carrier lifetime of the semiconductor devices [6]. This characteristic together with the low TCF (-25 ppm/°C), low density (3260 kg/m^3) and high thermal conductivity (~150 W/m·K) of AlN, make this piezoelectric material a good candidate for the implementation of this CMOS based SMR device.

Even though AlN was preferred over ZnO for this implementation, simulations were performed with both AlN and ZnO using molybdenum as the chosen material for the electrodes. Mo offers a good compromise between density, acoustic impedance and resistivity. In this work, the piezoelectric layer will be deposited in a post-CMOS process (outside CMOS facilities). Figure 7.4 shows a schematic of the simulated structure, with the thicknesses of the layers as summarised in Table 7.1. Simulations were performed with a range of thicknesses between 500 nm and 2 µm for the piezoelectric layer. Both the bottom and top electrodes were set to a thickness of 200

nm. Material properties used within the simulations are those previously summarised in section 3.3.1.
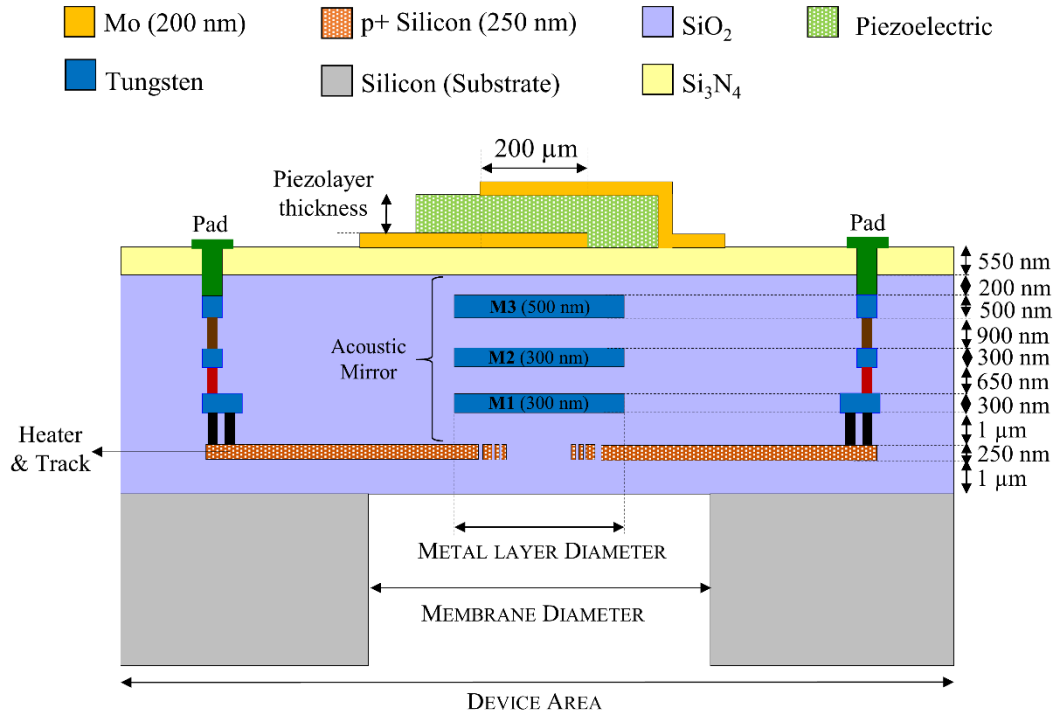
Figure 7.4 Schematic cross section view of the complete structure of the CMOS based SMR device, showing layer thicknesses and important dimensions. Figure not to scale.

For the SMR to resonate at frequencies between 2 and 3 GHz (as determined by the transmissivity of the CMOS based acoustic mirror), piezoelectric layer thicknesses between 600 nm and 1.2 µm are required for ZnO, and between 700 nm and 1.6 µm for AlN. The impedance curves obtained from the simulations are shown in Figure 7.5 with both devices showing a similar response.

A resonant frequency of 2.1 GHz was selected for the design of the acoustic mirror. Based on simulation results, thicknesses of 1.1 µm and 800 nm were chosen for AlN and ZnO respectively. These material thicknesses were chosen as thicker layers could cause undue stress on the film, while thinner layer would risk worsening the piezoelectric properties of the material.
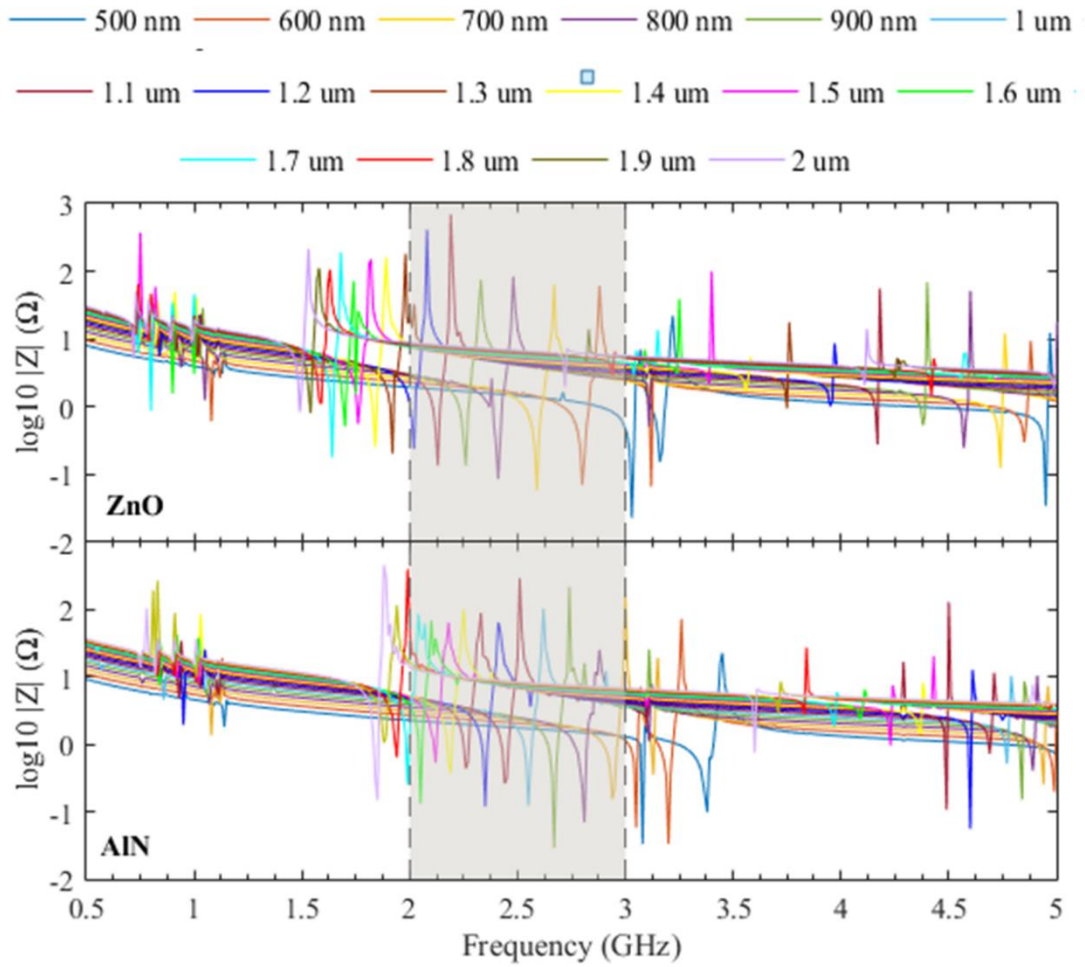
Figure 7.5 Simulated frequency response of the CMOS based SMR device for piezoelectric thicknesses ranging from 500 nm to 2 µm for both ZnO and AlN layers.

7.4   DESIGN AND MODELLING OF INTEGRATED MICROHEATER

The integration of a heating element in the substrate of a resonator structure (SAW and BAW devices) has been proposed by Vilander for temperature compensation purposes (i.e. temperature control of the resonator for improved frequency accuracy) [7]. In this work, the CMOS based SMR device also includes an integrated microheater. However, the microheater is proposed to serve two main purposes within an air quality sensor system: (1) sensitivity enhancement through the use of a temperature modulation technique (in the case of VOC detection) and (2) cleaning of the sensor surface to detach accumulated particles (in the case of particle sensing).

The development of a fully CMOS based SMR device requires the integrated heater to be CMOS compatible. Traditional materials used in the design of resistive heater structures are either not CMOS compatible (i.e. platinum), suffer from high chemical reaction at grain boundaries (polysilicon) or suffer from electro-migration at high temperatures >400 °C (e.g. Al, Cu) [8-10]. Iwaki *et al.* proposed SOI based micro heaters employing doped single crystal silicon to overcome these limitations (they are CMOS compatible and can operate at high temperatures up to 600°C with low power consumption, <100 mW) [11].

An alternative option to implement the heater within the CMOS based SMR is the use of tungsten heaters. Tungsten is not prone to electro-migration problems and has a good electrical resistivity, which allows its use as both a heater element and interconnections in a CMOS based device. They can operate at high temperatures (600°C) at very low power consumption (12 mW) and have good stability and mechanical strength [12]. In this work, however, a W heater was not implemented because all three tungsten layers available within the 1.0 µm SOI CMOS process are dedicated to form the acoustic mirror structure. In a CMOS processes featuring more than 6 tungsten layers, a metal heater can be embedded underneath the acoustic mirror.

Therefore, doped single crystal silicon (SCS) was selected to form the integrated microheater in this work. It is a CMOS compatible material which, as opposed to polysilicon, does not have any grain boundaries. This allows for better thermal stability (<1% drift) [5] and thus it can be operated reliably at high temperatures. In particular, the *p+* region of the SOI CMOS process was used as the resistive heater material because of its high dopant concentration (10^{20}/cm^3) and consequent low resistivity (1.17×10^{-5} Ω·m), which allow the heater to operate at low voltage levels, compared to the alternative *n+* region. Relevant material properties of semiconductors in this CMOS process are summarised in Table 7.2.

Table 7.2 Material properties of semiconductors in the CMOS process [5].

PROPERTY	*n+*	*p+*	Polysilicon
Sheet resistance [Ω]	40	65	30
Temperature coefficient of resistance α_1 [1/K]	1.35×10^{-3}	1.51×10^{-3}	0.85×10^{-3}
Temperature coefficient of resistance α_2 [1/K^2]	0.29×10^{-6}	0	0.35×10^{-6}

The power, P, of a resistive heater, including the tracks, is described by Joule's law as:

$$P = I^2 R_H + I^2 R_T \tag{7.1}$$

where I is the electric current, R_H is the resistance of the heater and R_T is the resistance of the tracks. As electric current passes through the resistive structure, heat is generated. The power generated by the heater can be dissipated by conduction through the membrane, by convection (proportional to the heated area) and by radiation to the surrounding environment. The heat generated in the heater area raises the temperature of the membrane while the majority of the heat generated on the resistive tracks is dissipated to the substrate.

The resistivity of silicon heaters is considerably higher compared to that of metal heaters (e.g. the resistivity of $p+$ silicon is 1.17×10^{-5} $\Omega{\cdot}$m compared to that of tungsten at 5.46×10^{-8} $\Omega{\cdot}$m). For silicon heaters, wide tracks are preferred to reduce the resistance and thus reduce the power consumption. However, using wide tracks will also cause more heat to be dissipated to the substrate. To avoid this problem, two design procedures have been previously proposed: the use of sector shape silicon tracks and the use of tungsten tracks connected to the silicon heater [11].

The microheater structure in this work is based on a previous design by Iwaki on resistive SOI-CMOS microheaters for gas sensing [5], using sector shape silicon tracks. The use of metal tracks was not possible within the current CMOS based SMR structure, as all metal layers are used to form the acoustic mirror. The resistive heater ($p+$ silicon, 150 µm diameter) is embedded in a thin membrane of SiO_2 (2 µm thickness and 600 µm diameter) and located underneath the acoustic mirror structure. The first metal layer of the acoustic mirror also acts as a heat spreading plate to improve temperature distribution on the sensing area. A cross and top section of view of the heater structure is depicted in Figure 7.6.
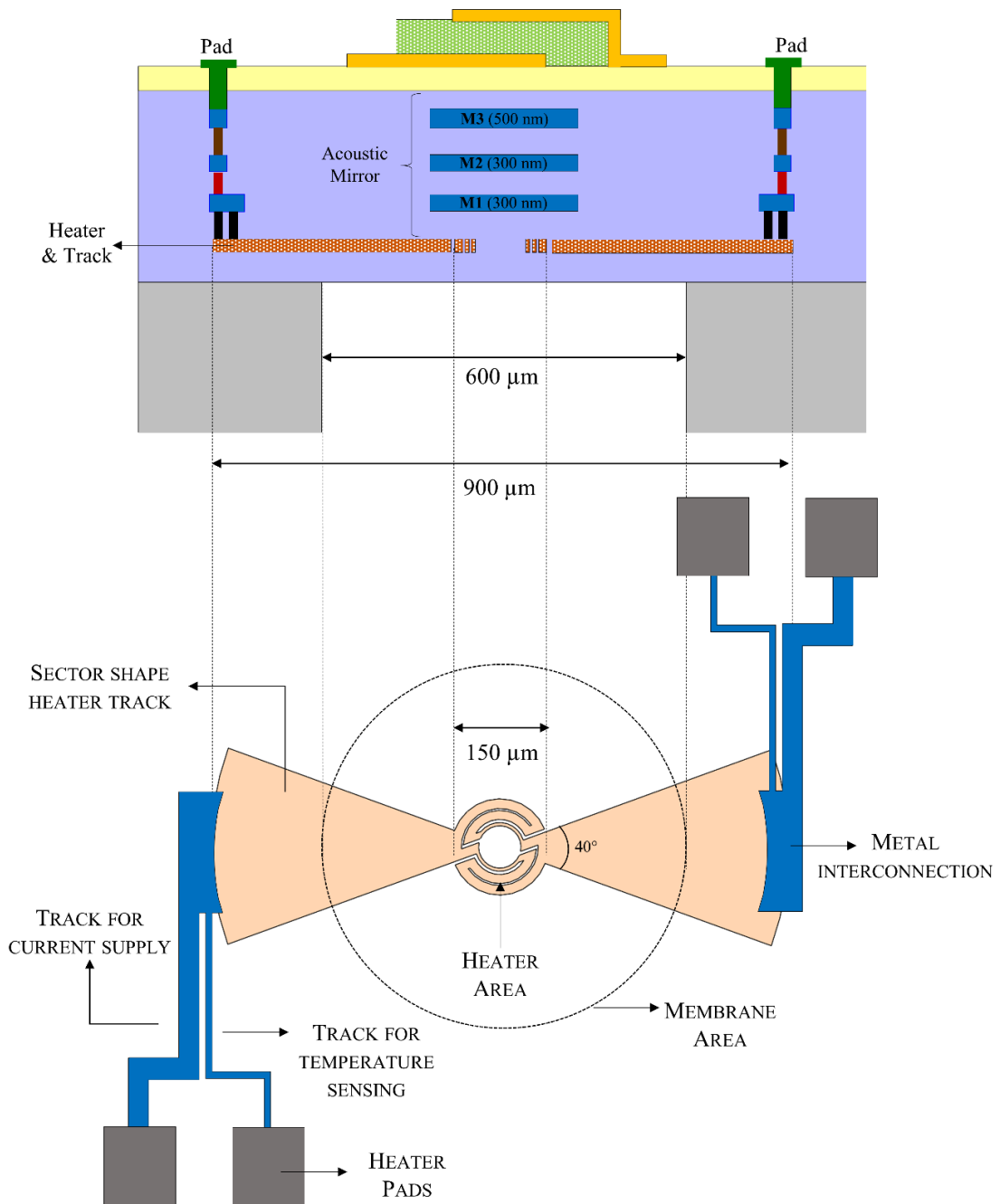
Figure 7.6 Structure of the resistive heater integrated within the CMOS based SMR
structure with sector shape silicon tracks ($\angle 40°$).

A small heater area of 0.018 mm^2 and a membrane to heater ratio of 4 is used
to reduce convection heat losses. The heater element consists of two resistors
connected in parallel, each formed by three concentric half rings connected in series.
A circular structure of the heater and the membrane is used to avoid possible fracture
due to stress. The tracks are made of the same heater material ($p+$ silicon) with a sector

shape at a 40° angle. Using such sector shape tracks allows the generation of more heat in the inner area of the track, efficiently raising the temperature of the heater area. The tracks have metal connections (tungsten interconnections) in the area outside the membrane.

In order to obtain an accurate reading of the temperature of the heater, a four-probe temperature measurement method is used. This is implemented by using a dual metal track configuration (with two wide tracks for current drive and two narrower tracks for voltage measurement), as shown in the figure above. Using this four-probe configuration, accurate measurements of the heater resistance can be performed [13]. The measured resistance of the heater can then be related to heater temperature using the temperature dependant expression of the material resistivity:

$$\rho(T) = \rho_0[1 + \alpha_1(T - T_0) + \alpha_2(T - T_0)^2] \tag{7.2}$$

where $\rho(T)$ is the temperature-dependant electrical resistivity, ρ_0 is the resistivity at the temperature T_0, T_0 is a fixed temperature (commonly room temperature), and α_1 and α_2 are the temperature coefficients of resistance, given in Table 7.2.

7.4.1 3D ELECTRO-THERMAL SIMULATIONS OF THE MICROHEATER

Three dimensional (3D) electro-thermal FEM simulations of the microheater were performed using the Joule heating multiphysics interface in COMSOL v5.2. This interface couples the *electric currents* and *heat transfer* interfaces to solve for the combined effects of resistive heating and heat loss mechanisms in solids. In this way, the heat distribution across the CMOS based SMR was evaluated and the power consumption together with the thermal power losses in the heater were computed.

The mathematical model for heat transfer in solids used in COMSOL solves for the heat equation (7.3)

$$Q = \rho C_p \frac{\partial T}{\partial t} - \nabla \cdot (k \nabla T) \tag{7.3}$$

where Q is the heat source (generated from the resistive heating), ρ is the electrical resistivity, C_p is the heat capacity, k is the thermal conductivity and T is the temperature.

The electrical power supplied to the microheater can be dissipated through the heat loss mechanisms of conduction (to the membrane), convection (to surrounding air) and radiation. In a steady-state operation (temperature does not change with time), the electrical power consumption equals the thermal losses, which can be expressed as:

$$\sigma(\nabla V)^2 = P_{\text{cond}} + P_{\text{conv}} + P_{\text{rad}} \tag{7.4}$$

where σ is the electrical conductivity, V is the electric potential applied to the heater and P_{cond}, P_{conv} and P_{rad} are the power losses (per unit volume) by conduction, convection and radiation, respectively. The electric conductivity (reciprocal to the resistivity) is given as temperature-dependant, following equation (7.2):

$$\sigma(T) = \frac{1}{\rho_0[1 + \alpha_1(T - T_0) + \alpha_2(T - T_0)^2]} \tag{7.5}$$

The heat loss mechanisms were computed by COMSOL through the following equations:

$$P_{\text{cond}} = -\nabla \cdot (k\nabla T) \tag{7.6}$$

$$P_{\text{conv}} = hA(T_0 - \text{T}) \tag{7.7}$$

$$P_{\text{rad}} = \varepsilon\sigma_B(T^4 - T_0^4) \tag{7.8}$$

where k is the material thermal conductivity, h is the heat transfer coefficient (10 W/m^{2}K), T_0 is the ambient temperature, ε is the emissivity constant (set at 0.8 for the SiO$_2$ membrane) and σ_B is the Stefan-Boltzmann constant (5.67 $\times 10^{-8}$ W/m^{2}K^4). Only natural convection is assumed in the model and ambient temperature (298 K) is assumed at the outer edges of the membrane and substrate. Material properties used within the simulations are summarised in Table 7.3.

Table 7.3 Properties of materials used within the simulations.

MATERIAL	DENSITY [Kg/m^3]	RESISTIVITY [$\Omega \cdot$m]	THERMAL CONDUCTIVITY [W/m·K]	HEAT CAPACITY [J/kg·K]	TEMPERATURE COEFFICIENT OF RESISTANCE	
					α_1 [1/K]	α_2 [1/K^2]
Si	2330	1×10^{-5}	168	678	-	-
$p+$ Si	2330	1.62×10^{-5}	168	678	1.51×10^{-3}	0
W	19350	1.2×10^{-7}	177	134	2.05×10^{-3}	3×10^{-7}
SiO$_2$	2200	-	1.4	730	-	-
Si$_3$N$_4$	3100	-	20	700	-	-

Figure 7.7a shows the developed 3D model of the microheater embedded within the silicon dioxide layers. A custom mesh with triangular elements was used to reduce the number of mesh elements generated in the model. This is possible by using a *swept mesh* function as the model comprises of very thin layers ($< 5\mu$m). The resulting mesh is shown in Figure 7.7b for the heater area.
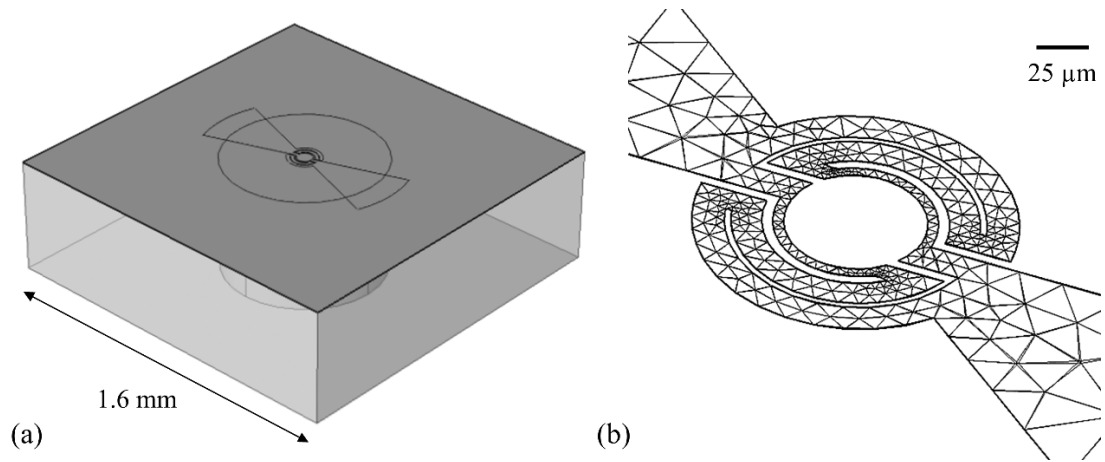
Figure 7.7 (a) 3D finite element model of the integrated heater and (b) magnified view of the meshed heater area.

First, an analysis of the embedded heater structure was performed, without the acoustic mirror layers deposited (shown in Figure 7.8). Later simulations were performed (presented in section 7.4.2) which included all the layers used within the complete CMOS based SMR to observe the effects on the heater performance due to the additional layers.

THICKNESS OF LAYERS	
Silicon Substrate	500 μm
Heater (p+ Silicon)	250 nm
SiO$_2$ (BOX)	1 μm
SiO$_2$	2.8 μm
Passivation (Si$_3$N$_4$)	550 nm

DIMENSIONS	
Heater Radius	75 μm
Membrane Radius	300 μm
Track length	375 μm

(a)   (b)
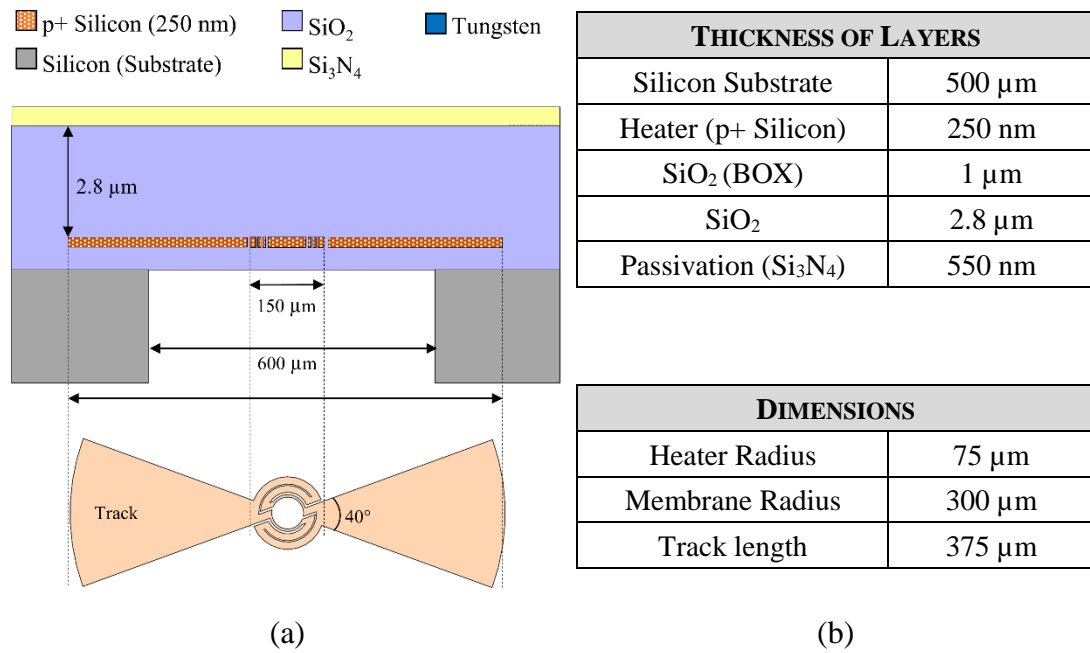
Figure 7.8 (a) Structure of microheater embedded in the silicon dioxide layers and (b) summary of thicknesses and dimensions for simulation.

The simulated temperature distribution over the membrane is shown in Figure 7.9 for a maximum temperature of 555 °C. A near uniform temperature distribution is observed over the centre area. This temperature uniformity would improve the sensitivity and selectivity of the SMR based sensor. The outer rings forming the heater are wider than the inner rings to improve the temperature uniformity, as more heat is lost in the outer region through conduction to the membrane [11].

Figure 7.9 Temperature distribution of the micro heater (a) 3D view of the entire model and (b) Top view of heater and membrane.

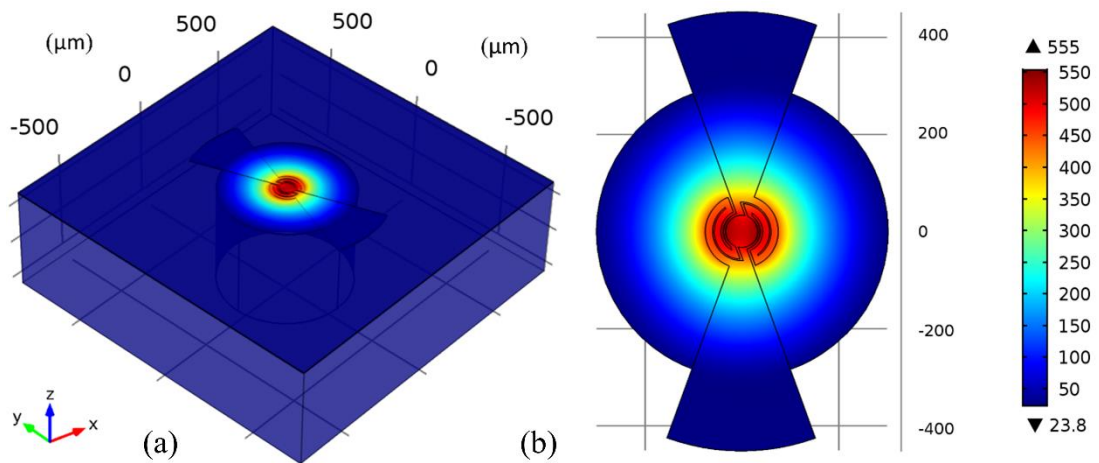The temperature profiles along the x and y axes of the heater are shown in Figure 7.10a over the membrane area. A more uniform temperature distribution is observed along the y axis compared to that of the x-axis. The inclusion of a heat spreading plate in the centre area of the heater can improve this temperature distribution [11]. However, this area was reserved for the future implementation of a temperature diode. Furthermore, the first metal layer of the CMOS acoustic mirror will also act as a heat spreading plate, to improve temperature uniformity. Figure 7.10b shows the thermal loss contribution of each of the dissipation mechanisms. As expected, heat dissipation by conduction to the membrane is the dominant loss mechanism, at ~83% of the total power. Heater resistance of ~1000 Ω is estimated at room temperature.
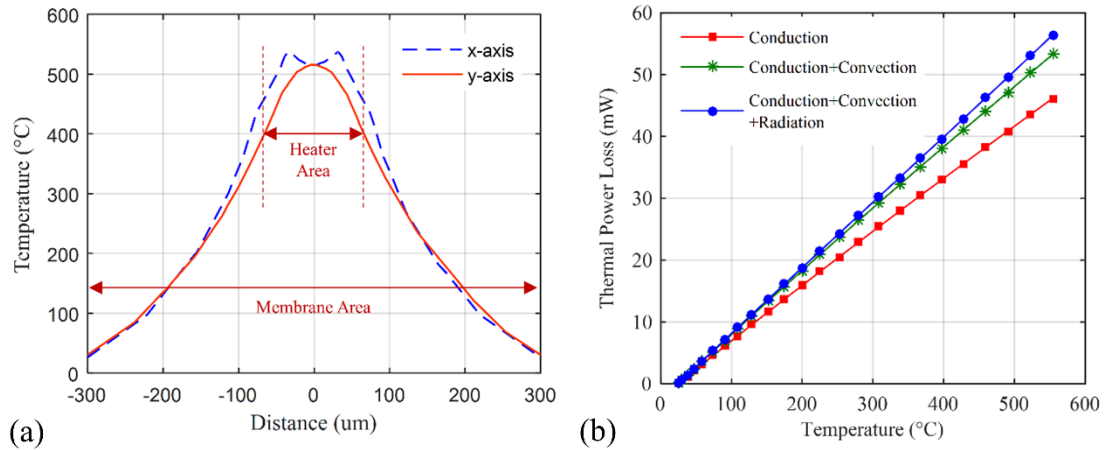
Figure 7.10. (a) Temperature Profile in x-axis and y-axis of the heater along the membrane. (b) heat dissipation contributions on the heater.

The next section presents the thermal simulations of the microheater including the CMOS based acoustic mirror. The results are compared to those obtained with the configuration presented in this section (temperature distribution over the membrane area).

7.4.2 CMOS ACOUSTIC MIRROR WITH EMBEDDED MICROHEATER

In the CMOS based acoustic mirror design, the CMOS metal layers that form the acoustic mirror are to be patterned to avoid cross talk and parasitic capacitances between devices on the same wafer (especially beneficial in the case of sensor arrays

being used). These metal layers were designed to have a circular shape to reduce mechanical stress due to sharp corners. An appropriate radius of these metal layers was investigated through 3D electro-thermal simulations.

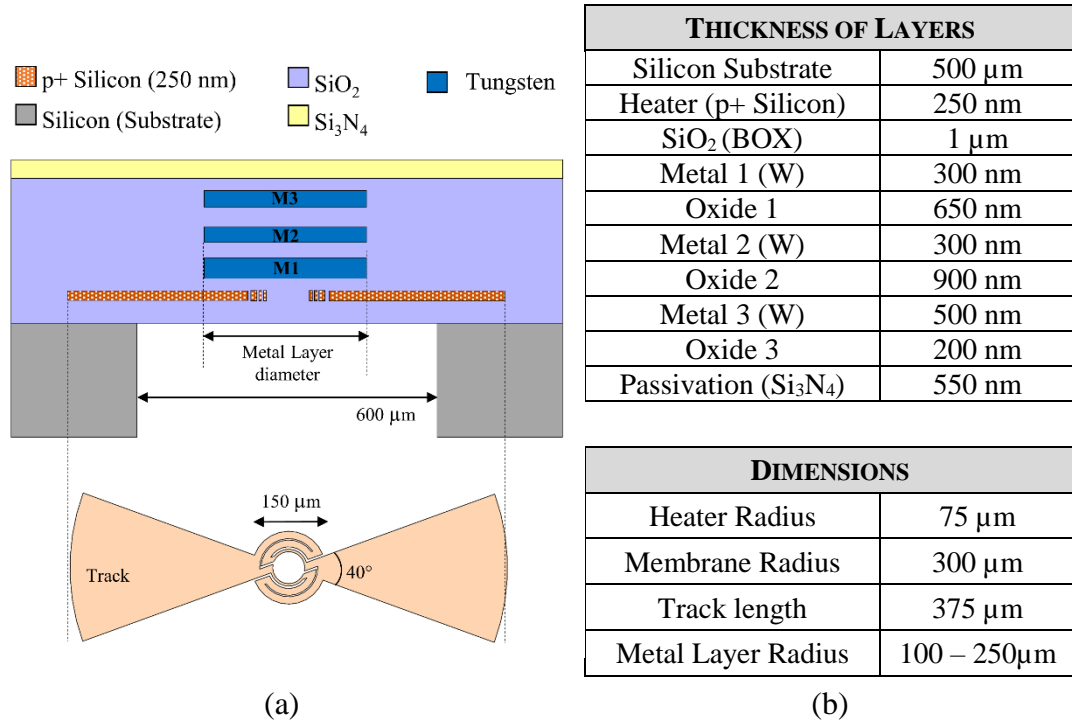| THICKNESS OF LAYERS	
Silicon Substrate	500 µm
Heater (p+ Silicon)	250 nm
SiO$_2$ (BOX)	1 µm
Metal 1 (W)	300 nm
Oxide 1	650 nm
Metal 2 (W)	300 nm
Oxide 2	900 nm
Metal 3 (W)	500 nm
Oxide 3	200 nm
Passivation (Si$_3$N$_4$)	550 nm

DIMENSIONS	
Heater Radius	75 µm
Membrane Radius	300 µm
Track length	375 µm
Metal Layer Radius	100 – 250µm

(a)   (b)

Figure 7.11. Schematic of the heater with acoustic mirror used for the simulations. The Radius of the metal layers that form the acoustic mirror is varied from 100 µm to 250 µm.

The temperature distribution over the acoustic mirror structure (schematic and summary of the layers are given in Figure 7.11) was analysed through the simulations. The radius of the metal layers was varied from 100 to 250 µm. The results of these simulations are shown in Figure 7.12. All four variations exhibit a circular temperature profile. However, the heat is not localized over the central heater area. As the radius of the metal layers is increased, the maximum temperature decreases over the acoustic mirror. The maximum temperature over the reflector layers (for a fixed 12 V supply) is 387 °C for the configuration with metal layers of 100 µm radius. This maximum temperature is 30% lower than the maximum temperature over the membrane (for the same voltage supply). For a metal layer radius of 250 µm, the maximum temperature is already ~65% lower and the temperature is not localized.
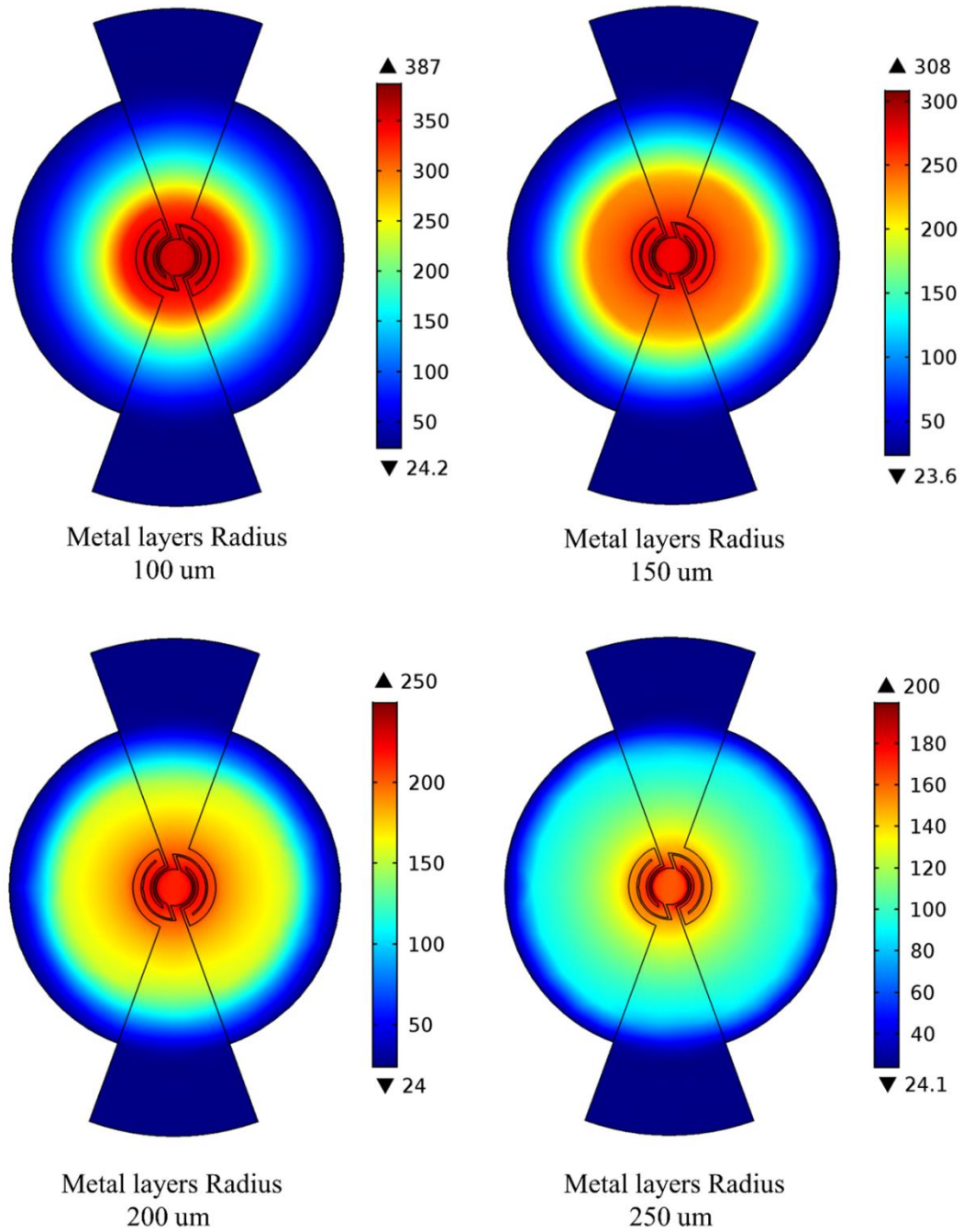
Figure 7.12. Temperature distribution of the heater and acoustic mirror as a function of the diameter of the W metal layers that form the acoustic mirror.

The power consumption and plot of temperature against applied voltage are presented in Figure 7.13 for all these four configurations together with the data previously obtained only over the membrane structure. Power consumption of the CMOS SMR structure and embedded heater (metal layers radius 250 µm) is the highest at 75 mW at 150 °C. Higher power consumption values (>120 mW) will be required to reach temperature values above 300 °C to heat the sensing area of the SMR device.

The configuration with metal layer radius of 100 µm exhibits the lowest power consumption. However, an acoustic mirror of this size (100 µm radius) is not large enough to form a resonator active area of 200 µm (for particle sensing). Therefore, an acoustic mirror layer with radius of 150 µm was selected for the CMOS based SMR device (heater to metal layer ratio of 2), as it presents the best compromise between power consumption, temperature profile distribution and size for the acoustic resonator. For the sensing applications in this work, a maximum temperature of 200 °C is required, which can be obtained with the selected configuration (radius of 150 µm) at a power consumption of only 40 mW.
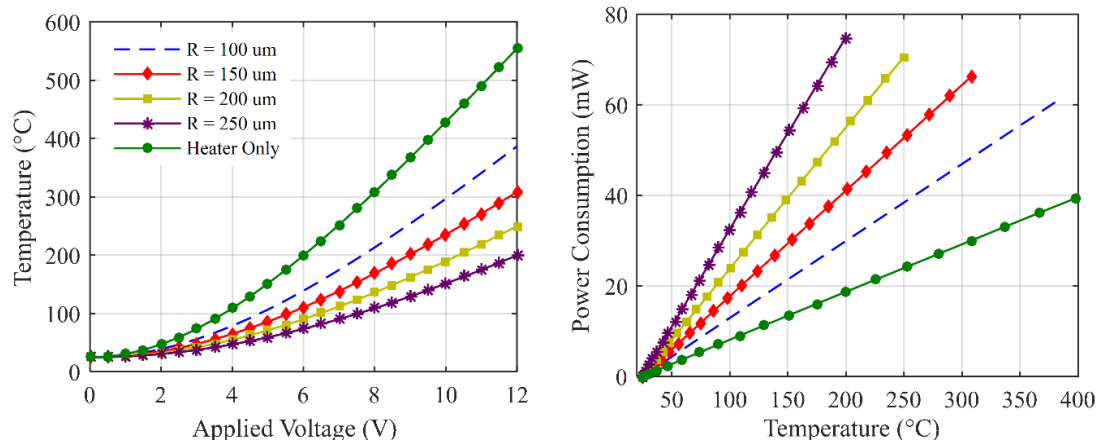

Figure 7.13. (a) Temperature vs applied voltage and (b) power consumption of the heater and acoustic mirror with different radius for the metal layers.

7.4.3   TRANSIENT RESPONSE

The transient response of the CMOS acoustic mirror with embedded micro heater was simulated using the same FEM model in COMSOL. A square voltage signal (12 Vdc) at a frequency of 10 Hz was applied. Figure 7.14 shows the transient response of the CMOS acoustic mirror with heater for metal layer radius of 150 µm, compared to that of the heater (with no additional mirror layers). The time constant of the microheater (i.e. the time required to reach 63% of the final temperature value) was determined from simulation results to be 4.3 ms for the heater structure with membrane only (maximum temperature of 555 °C). The thermal time constant for the heater embedded within the CMOS based acoustic mirror was found to be 1.6 ms for a temperature final value of 400 °C. The fast response time of the micro heater can allow its operation in pulsed mode to further decrease the average power consumption [12].
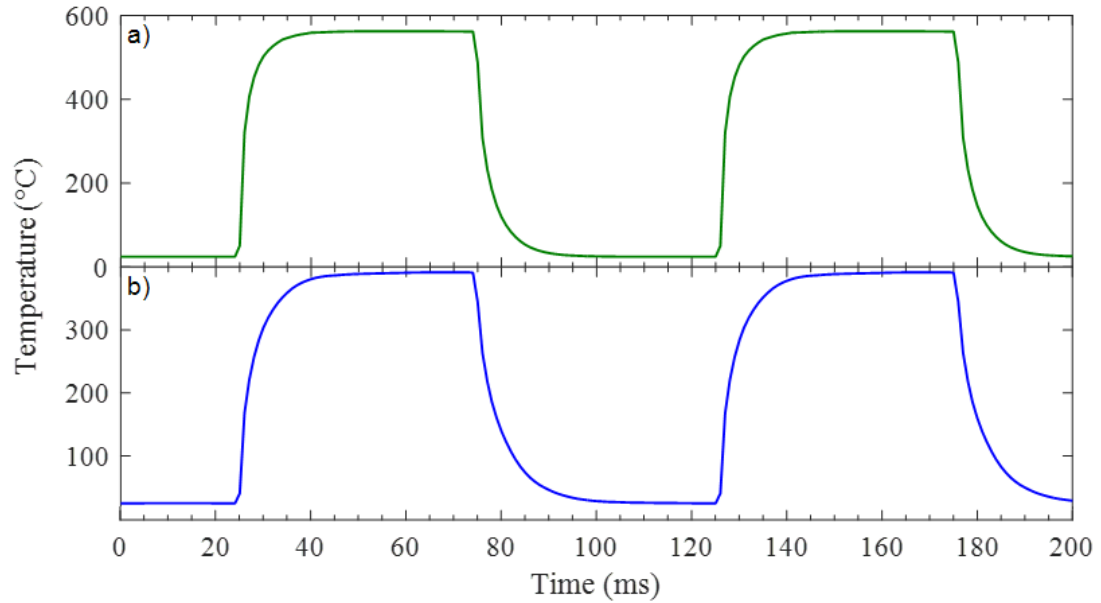
Figure 7.14. Transient response for the microheater with acoustic mirror (square voltage signal of 12 V at a frequency of 10 Hz): (a) Heater Only (b) Metal layer radius = 100 µm.

In the next sections, the fabrication of the designed CMOS based SMR device is presented. Fabrication is completed in two separate stages: 1) fabrication of the CMOS based acoustic mirror and embedded heater (fabricated in the standard XI10 1.0 µm SOI CMOS process); and (2) post-fabrication steps required to form the resonator structure (deposition of the electrodes and piezoelectric material).

7.5   FABRICATION OF CMOS BASED ACOUSTIC MIRROR AND HEATER

The CMOS based acoustic mirror was fabricated through the XI10 1.0 µm SOI-CMOS process at XFAB, Germany as part of a multi project wafer (MPW) run. Both bulk and SOI wafers were requested, where the microheater design was only included in the SOI wafers.

Fabricated devices were returned from the foundry in May 2017. However, only the bulk wafers with CMOS acoustic mirror were received. The SOI wafers containing the acoustic mirror and microheater are due in late September 2017 (after the completion of this thesis). Post-processing of the received CMOS devices was performed and characterisation of the resulting SMR devices was performed as a proof-of-concept of both CMOS acoustic mirror design and fabrication.

7.5.1 CMOS LAYOUT DESIGN

Layout design of the CMOS acoustic mirror and integrated heater was performed using the layout editor L-Edit v16.2 (Tanner Tools). The final layout is shown in Figure 7.15. The tracks for temperature sensing and current supply are connected to pads of 150×150 µm. Two additional pads are included in the chip for possible connection to the bottom and top electrodes of the SMR during post-fabrication.

The membrane (600 µm) is outlined. This is the area of the SOI wafer to be back etched to release the membrane. This cavity is created on the silicon substrate only for thermal purposes (i.e. to reduce dissipation by isolating the heater from the substrate and it is not intended for acoustic isolation of the resonator). Devices with and without cavities were fabricated to analyse the performance of the CMOS acoustic mirror on top of the bulk substrate. To prevent mechanical failure, the metal tracks are connected to the silicon heater tracks outside the membrane area (where the temperature is close to ambient temperature).
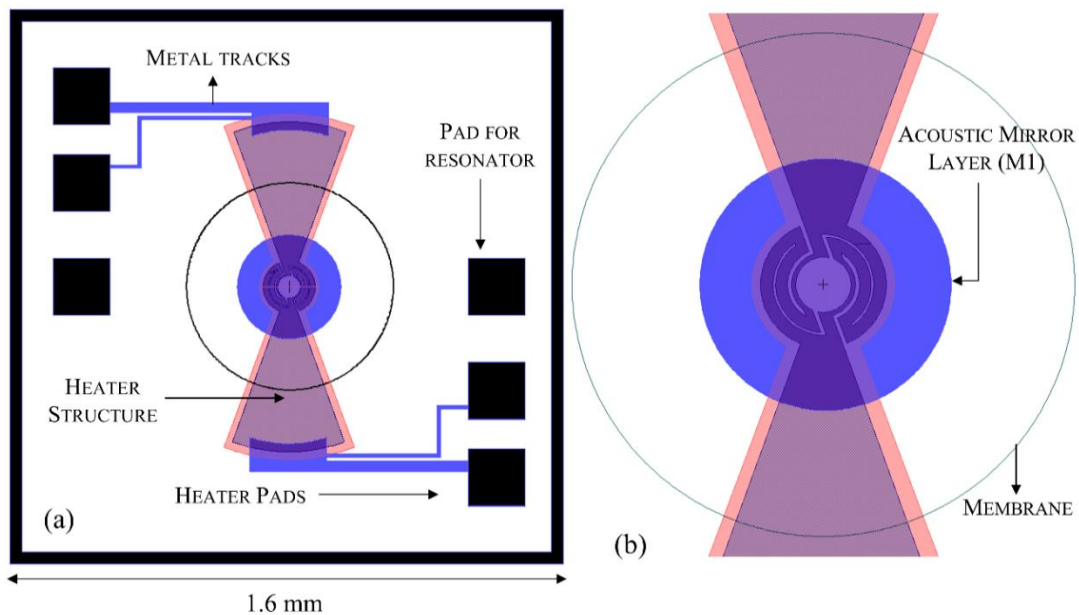

Figure 7.15 Layout of the CMOS based SMR chip drawn in Tanner tools: (a) The entire layout and (b) magnified view of the heater area. (Metal 2 and Metal 3 layers are not shown).

7.5.2 FABRICATION PROCESS STEPS

The processing steps for fabrication of the CMOS acoustic mirror and integrated heater follow the fabrication process of the standard XI10 XFAB process. Thus, these two elements (acoustic mirror and heater) and the electronics can be fabricated simultaneously on the same substrate. These process steps are briefly summarised below and depicted in Figure 7.16. The fabrication of the driving electronics is shown to depict the simultaneous fabrication of all these elements. However, the IC was not realised in this work. The steps outlined below, describe the planned SOI CMOS process, whereas in this work only bulk devices were received.

The process starts with a 6-inch silicon-on-insulator wafer (1000 µm BOX, 250 nm active silicon). The active silicon layer is etched to isolate the MOSFETs. This same trench etching process is used to pattern the resistive heater. Next, the p-well is created by ion implantation in order to form the NMOS structure.

Ion implantation to dope the drain and source of the MOSFETs (*p+* and *n+* regions) is performed. In this same step, the resistive heater is doped (*p+*). The next step is the metallization process, where the metal and oxide layers of the process are deposited. Here the interconnections in the circuitry and to the integrated heater are formed and the layers of the acoustic mirror are patterned (circular shape). The final step, after the metallization process, is the deposition of a passivation layer (550 nm of Si_3N_4) to protect the devices for further processing (dicing and handling).

After fabrication of the acoustic mirror and heater in the standard CMOS process, the cavity to release the heater membrane is created by a deep reactive ion etching (DRIE) process in a post-fabrication step, performed at the same foundry (this step is not shown in the schematic).

CMOS ACOUSTIC MIRROR AND HEATER   **CMOS INTERFACE CIRCUITRY**

a) 6-inch SOI wafer

b) Patterning of the resistive heater and MOSFET isolation

c) Ion implantation to form the p-well.

d) Formation of resistive heater, source and drain: ion implantation.

e) Formation of gates of NMOS and PMOS: deposition and patterning of gate oxide and polysilicon

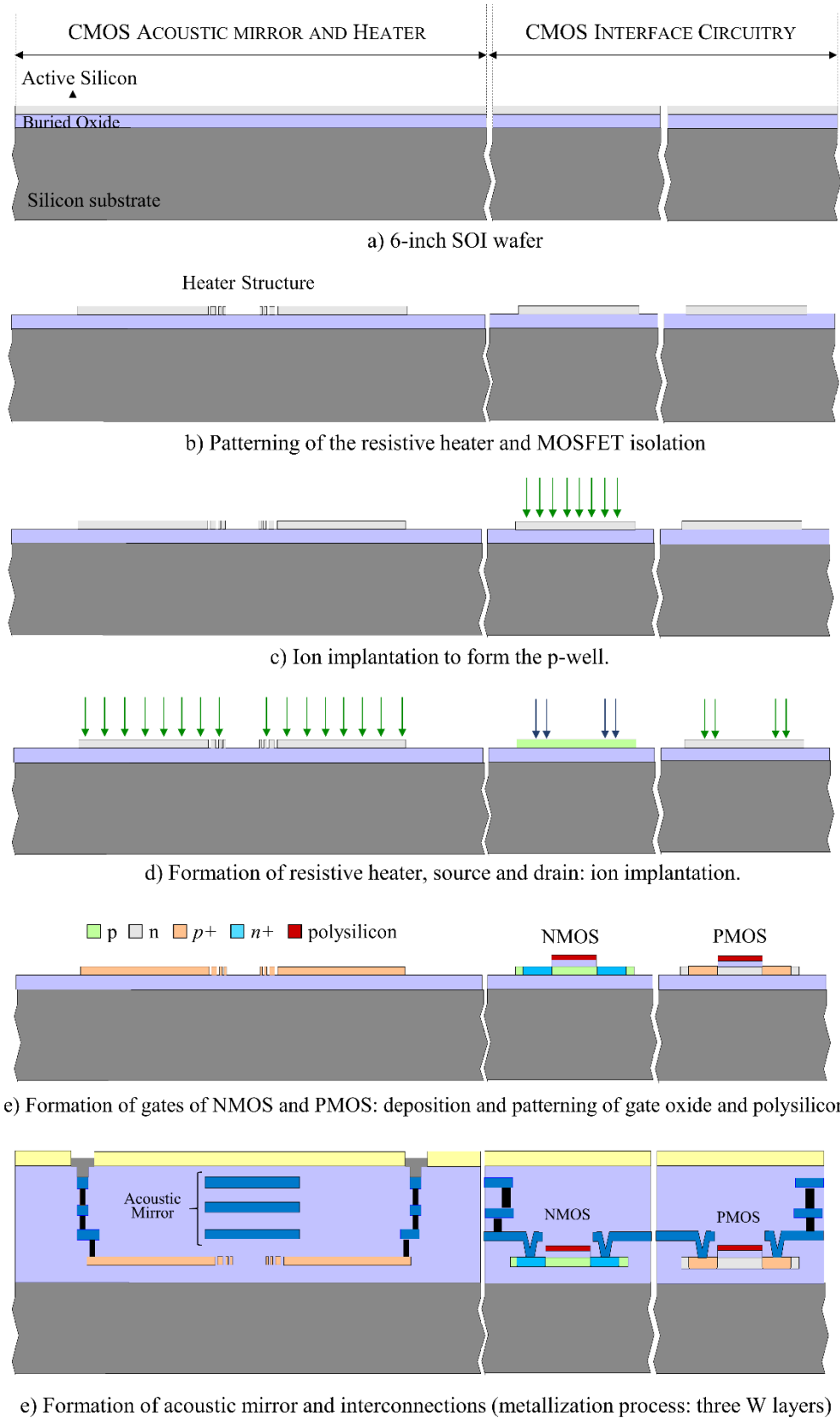e) Formation of acoustic mirror and interconnections (metallization process: three W layers)

Figure 7.16 Fabrication steps of the SOI-CMOS process to form the acoustic mirror and integrated heater.

7.5.3 FABRICATED CMOS DEVICES

A photograph of a fabricated 6-inch MPW wafer is shown in Figure 7.17. The wafer contains a total of 121 different designs, of which only one is the CMOS based SMR device designed in this work. The wafer was diced in individual devices with an overall chip size of 1.6 mm × 1.6 mm at DISCO HI-TEC (Germany).
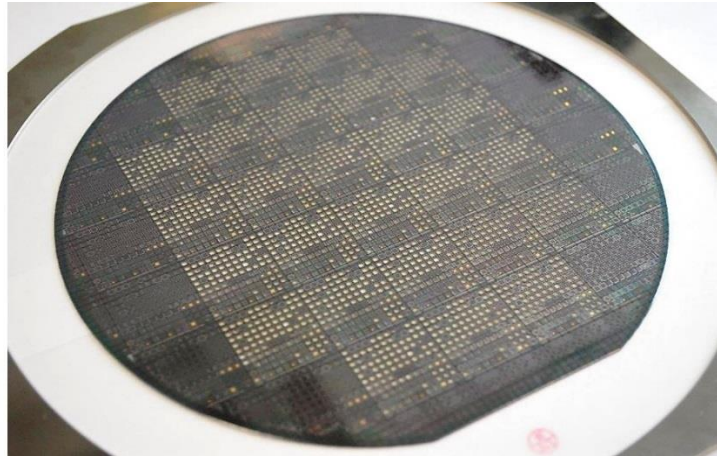

Figure 7.17 Fabricated 6-inch bulk CMOS wafer.

A total of 115 dies for the CMOS based SMRs were obtained from three fabricated MPW wafers. Devices with and without membrane were obtained. Figure 7.18 shows an optical photograph of the fabricated devices.
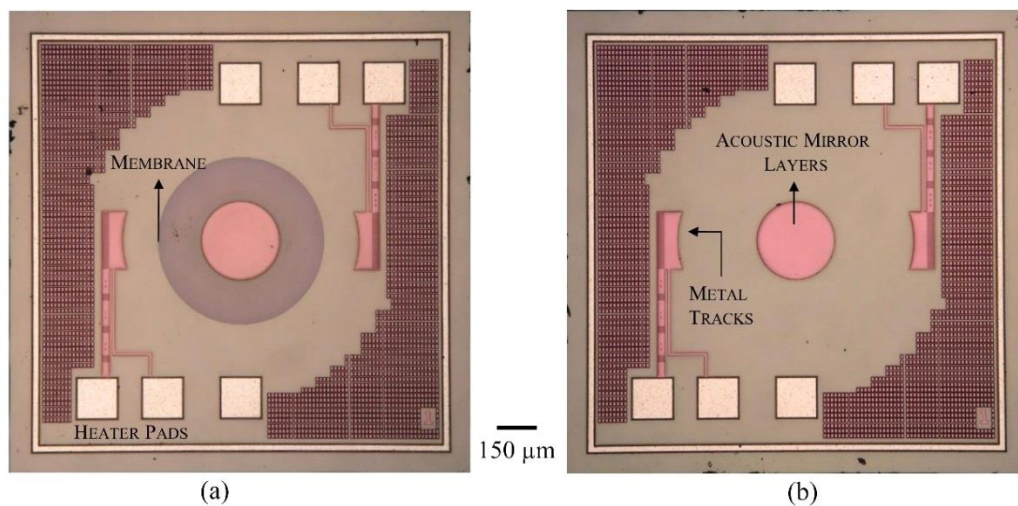

Figure 7.18 Top view of fabricated devices in the XFAB process (a) device with membrane and (b) device without membrane.

Only processed bulk wafers were returned from the foundry, which means that the integrated heater was not fabricated in the current batch. Due to a failure in the fabrication process (foundry related), the SOI process had to be repeated and thus, only the acoustic mirror structure is included in the current chips. The actual structure of the fabricated devices is depicted in Figure 7.19.
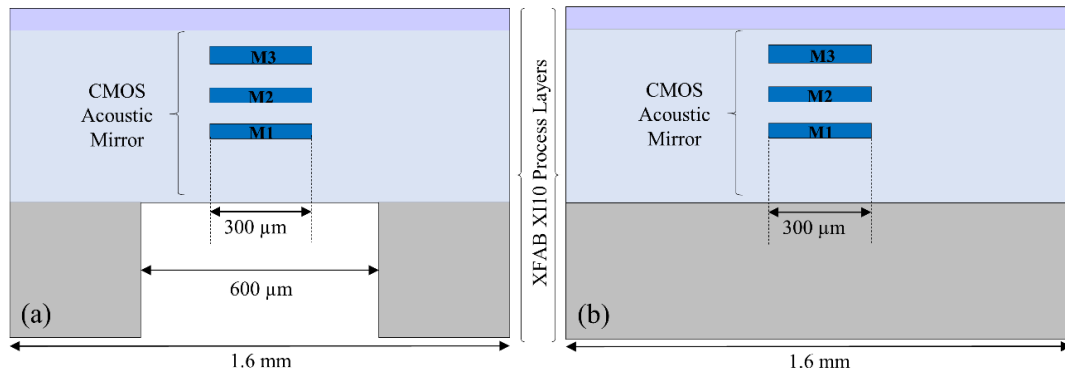

Figure 7.19 Schematic cross-section of fabricated CMOS based SMR devices in the bulk process: device (a) with and (b) without membrane (bulk device).

7.6   POST-PROCESSING[4]

Fabrication of the acoustic mirror was performed using a standard CMOS process. To complete the CMOS based SMR device, post-processing steps are required to form the resonator structure on top of this CMOS substrate. The number of post-processing steps required here is significantly reduced compared to the current state-of-the-art processes for integrated SMRs. Only the piezoelectric layer, bottom and top electrodes need to be deposited and patterned. A summary of the layer thicknesses required for the resonator is given in Table 7.4, based on the simulations performed in section 7.3.

Table 7.4 Material thicknesses for bottom, top and piezoelectric layer to be deposited during post-processing.

	MATERIAL	**THICKNESS**
BOTTOM ELECTRODE	Ti/Mo Cr/Ir	15nm/200 nm 15 nm/110 nm
PIEZOELECTRIC LAYER	AlN	1.1 µm
TOP ELECTRODE	Mo	150 nm

---

[4] The work presented in this section was performed in collaboration with the group lead by Prof Enrique Iborra, from the Technical University of Madrid.

Post-processing of the CMOS substrate was performed at two different locations: (1) for ZnO based SMR devices, post-fabrication took place at the Centre for Advanced Photonics and Electronics (CAPE), University of Cambridge, UK and (2) for AlN based SMR devices, post-processing was performed at the ETSI of Telecommunications, Technical University of Madrid, Spain. Here, only the post-fabrication of AlN based devices is presented. These devices were preferred over the ZnO based devices (detailed in Appendix H), due to their CMOS compatibility and superior performance.

To form the resonator structure, a capacitive coupling method was used. A large-area bottom electrode is capacitively coupled to a metallic layer surrounding the top electrode. In this way, the bottom electrode can be accessed through the capacitive coupling. The surrounding area of the top electrode is large enough that the effects of the parasitic capacitance are practically negligible.

As no opening vias are required through the piezoelectric layer, the post-fabrication process is further simplified. No etching/patterning of the piezoelectric layer is needed, which usually involves wet etching processes that can easily damage other layers of the structure if the process is not carefully controlled). Design of the required photomasks to implement this structure and a detailed description of the fabrication process are presented in the next sections.

7.6.1   POST-CMOS LAYOUT DESIGN

A total of two photomasks are required to pattern the bottom and top electrodes. The masks were designed using the layout editor L-Edit v16.2 (Tanner Tools, EDA). A sample mask design is shown in Figure 7.20. The active area of the resonator was designed to have a circular shape to fit above the acoustic mirror area (also of circular shape, $\emptyset = 300\,\mu m$). Masks were designed with top electrode active area ranging from 100 to 250 µm in diameter.

The photomasks were manufactured on a 4×4 inch glass/chrome mask plate (0.060" thick) at 256k dpi resolution (JD Photo Tools, UK) and a minimum critical dimension of 5 µm. The specifications of the masks (polarity and view side) are summarised in Table 7.5.
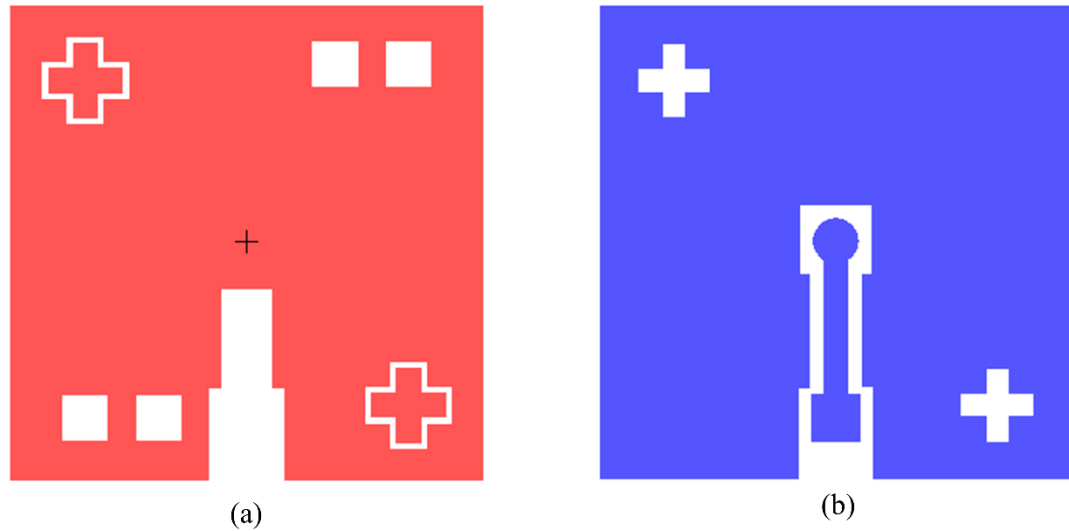
(a)   (b)

Figure 7.20 Designed photomasks for patterning (a) bottom and (b) top electrodes of the resonator structure using capacitive coupling.

Table 7.5 Mask specifications for post-processing of CMOS acoustic mirror substrate.

MASK	POLARITY	VIEW SIDE	TYPE OF RESIST	DESCRIPTION
Mask 1 (BOT)	Clearfield	Right read Chrome down	Positive	Patterning of bottom electrode.
Mask 2 (TOP)	Clearfield	Right read Chrome down	Positive	Patterning of top electrode.

7.6.2 POST-FABRICATION PROCESS

Post-fabrication of the CMOS acoustic mirror consisted of a 2-mask photolithography process as outlined below and depicted in Figure 7.21.

1. DEPOSITION AND PATTERNING OF BOTTOM ELECTRODE. The bottom electrode materials were deposited directly on top of the CMOS substrate containing the acoustic mirror. Two electrode materials were used: Ti/Mo electrodes and Cr/Ir electrodes, where Ti and Cr were used as adhesion layers. All electrode materials were deposited by sputtering.

Patterning of the bottom electrode was performed by a contact photolithographic process using a wet etching process (in the case of Ti/Mo electrodes) or a lift-off process (for the case of Cr/Ir electrodes).

2. DEPOSITION OF PIEZOELECTRIC LAYER. AlN films were deposited on a custom-made ultra-high vacuum sputtering system (MAREA). The samples were placed into a transfer chamber, evacuated to 5 mTorr. Prior to the sputtering process, the Al target and the substrate are cleaned with a pure Ar plasma for a total time of 5 min and 3 min for the target and substrate, respectively. The films were sputtered at 400°C from an Al target (150 mm diameter, 99.999% purity) using an Ar/N_2 mixture. A pre-sputtering stage is performed for 5 minutes, time after which the RF bias was set to a dc voltage of -55 for the deposition of the AlN film.
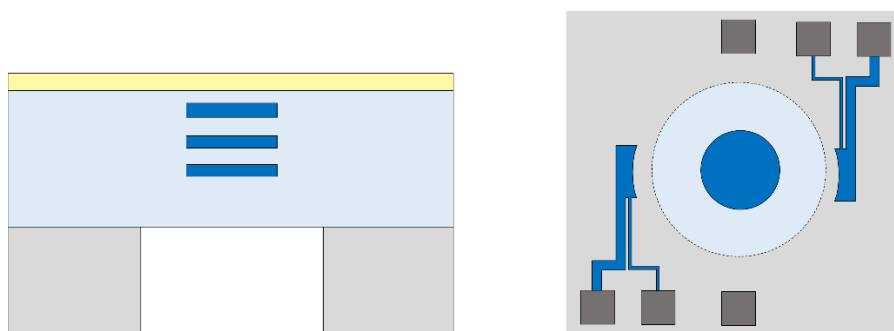
3. DEPOSITION AND PATTERNING OF TOP ELECTRODE. The Mo top electrode was deposited by sputtering and was patterned in a similar way as the bottom electrode (using contact photolithography and a wet etching process).

The photolithographic process was performed using a MJB4 mask aligner (SÜSS MicroTec, Germany). A thin photoresist S1818 (~1.5 µm thick) was used. The deposition parameters of all materials used during post-processing are summarised in Table 7.6.

Table 7.6 Sputtering and etching parameters of materials used during post-processing of the CMOS substrate.

| PARAMETER	AlN	Ti	Mo
DEPOSITION METHOD	Sputtering (MAREA)	Sputtering (Leybold Z550)	Sputtering (Leybold Z550)
TARGET (PURITY)	Al (99.999%)	Ti (99.999%)	Mo (99.999%)
BASE PRESSURE [mTorr]	1.6	4	1.5
TARGET POWER [W]	1200	150	400
AR FLOW RATE [sccm]	44.5	30	18
N_2 FLOW RATE [sccm]	60	0	0
SUBSTRATE BIAS [V]	-55	-	-
DEPOSITION RATE [nm/min]	~65	~30	~110
ETCHING METHOD	-	Wet	Wet
ETCHANT	-	BHF 4:1	Al etchant at RT
ETCHING RATE [nm/min]	-	~120	~480

*Ir layers were deposited in a sputtering system (MRC) from a Ir magnetron target (∅=75mm). The Cr adhesion film is deposited during the same vacuum cycle. Power is supplied by a DC source (150 W), operating at 50 kHz (duty cycle of 72%). Deposition rate was ~20 nm/min.
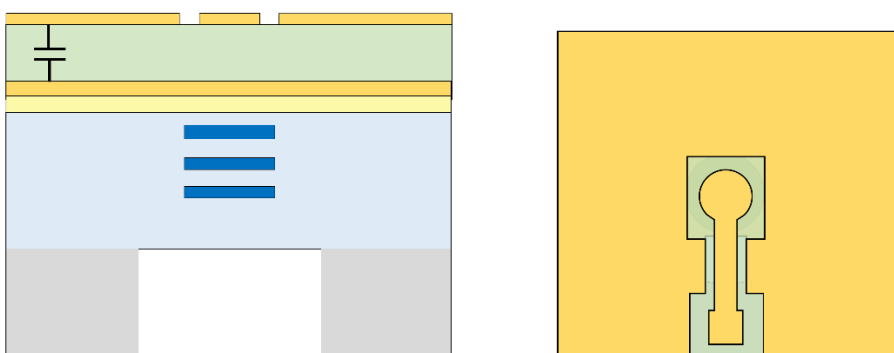
(a) CMOS Acoustic Mirror ready for post-processing
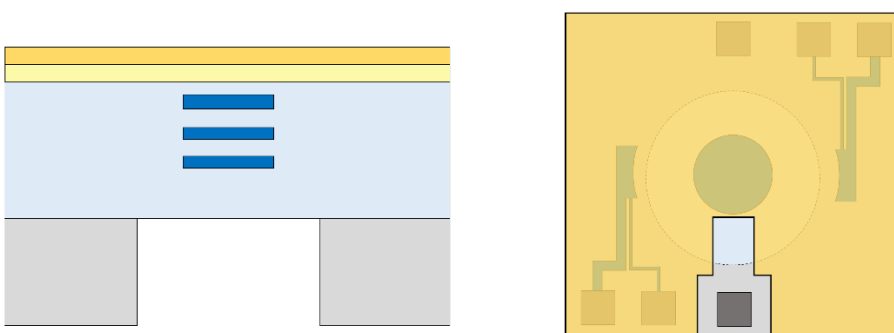
(b) Deposition and patterning of bottom electrode (Ti/Mo or Cr/Ir).
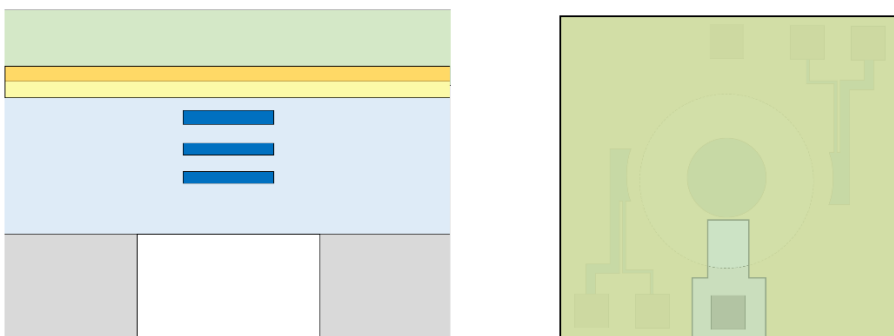
(c) Deposition of piezoelectric layer (AlN)

(d) Deposition and patterning of top electrode

Figure 7.21 Cross and top section representation of the post-processing steps. Device with membrane is depicted but devices without membrane were also processed.

Both devices with bulk substrate (no etching of the silicon substrate) and devices with membrane were successfully processed. Only a small number of devices (with membrane) were broken during an initial ultrasonic cleaning process. A photograph of a fabricated CMOS based SMR device is shown in Figure 7.22. As discussed before, the device comprises of the CMOS fabricated acoustic mirror ($\emptyset$=300 µm) made of W/Oxide layers of the CMOS process. Although the integrated silicon heater was not fabricated in this run, performance of this SMR device can be characterised, as a proof of concept for the CMOS-fabricated acoustic mirror. Results from this characterisation are discussed in the following section.

In the presented design, the acoustic mirror layers were patterned for a circular area of 300 µm in diameter. As discussed in section 7.4.2, the dimensions of the acoustic mirror layers were chosen taking into account the thermal distribution of the integrated heater. The electrical extensions of the top electrode, however, were located in the area outside the acoustic mirror. This compromise degraded the performance of the device compared to SMRs without integrated heaters, which have larger acoustic mirrors.
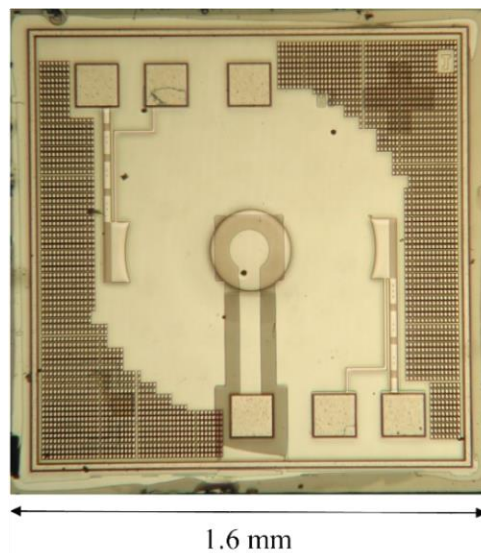

1.6 mm

Figure 7.22 Photograph of completed CMOS based SMR device. Acoustic isolation provided by the CMOS fabricate acoustic mirror. Device with bulk substrate.

7.7 CHARACTERISATION OF CMOS BASED SMR

After completion of the post-processing steps for a first batch of CMOS based SMR devices (with thicknesses as summarised previously in Table 7.4), the devices were electrically characterised with a network analyser using GSG RF probes, in a one-port configuration. Figure 7.23 shows the measured resonances for a set of completed CMOS based SMR devices. Devices with the same deposition parameters and materials exhibited very similar responses.
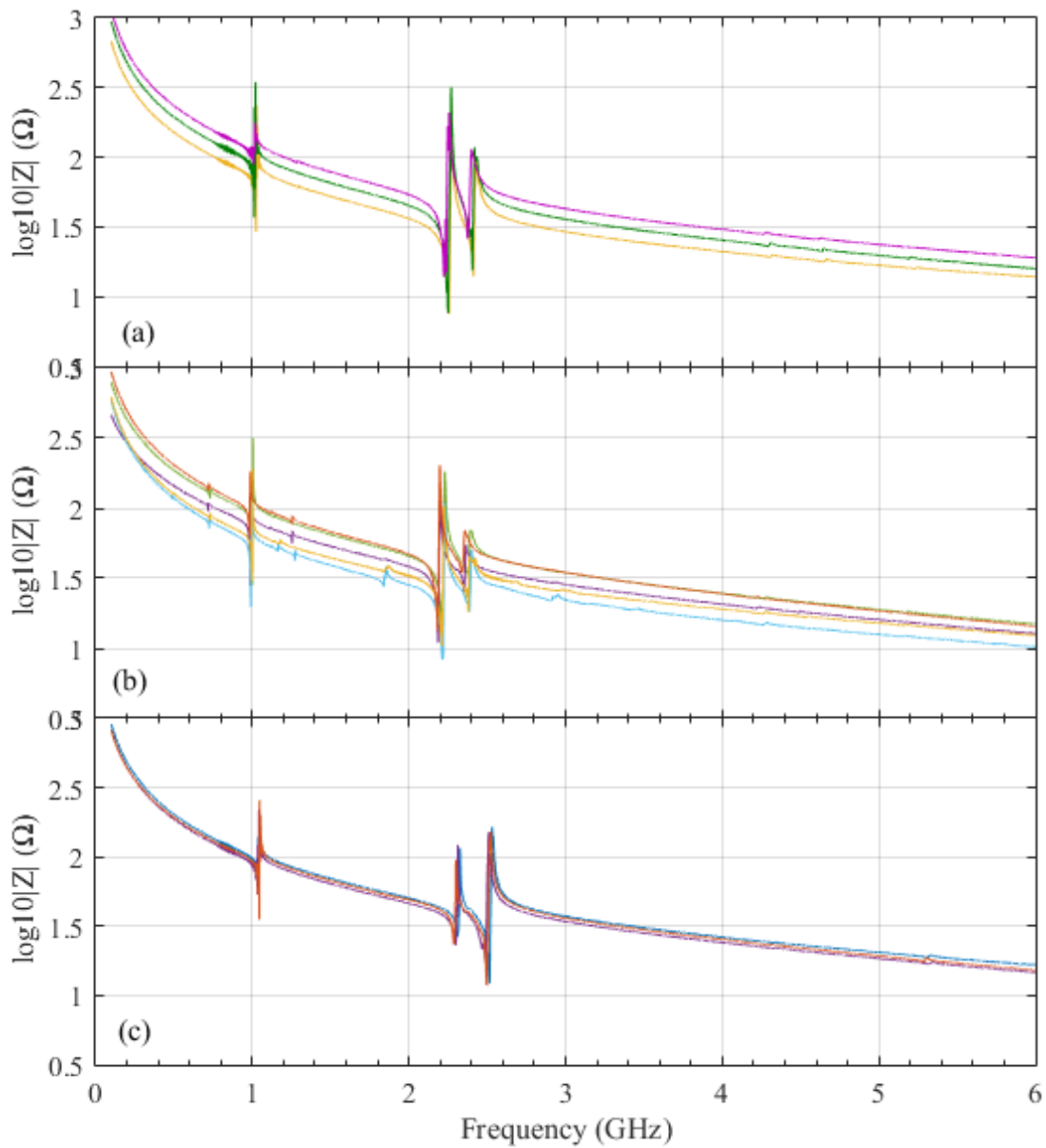

Figure 7.23 Experimental frequency response of CMOS based SMR devices. (a) Bulk substrate (no membrane), (b) devices with membrane. Both (a) and (b) have Ti/Mo electrodes. (c) Bulk substrate with Cr/Ir electrodes. AlN thickness for all devices is 1.1 µm.

Three very distinctive resonance peaks can be observed for all the devices. The Mason's model was used to find a fit to the measured frequency spectrum and identify the source of these resonance modes. The first peak (not an actual resonance) occurs at a frequency of ~1 GHz, where the transmissivity of the acoustic mirror structure is minimum (shown previously in Figure 7.3b). The second peak, at a frequency of ~2.2 GHz is the fundamental resonance of the AlN layer. In addition to this fundamental resonance, a $\lambda/2$ resonance is observed, attributed to the thick SiO_2 layer (Oxide 2) forming the acoustic mirror structure (third peak at 2.4 GHz), as shown in Figure 7.24.
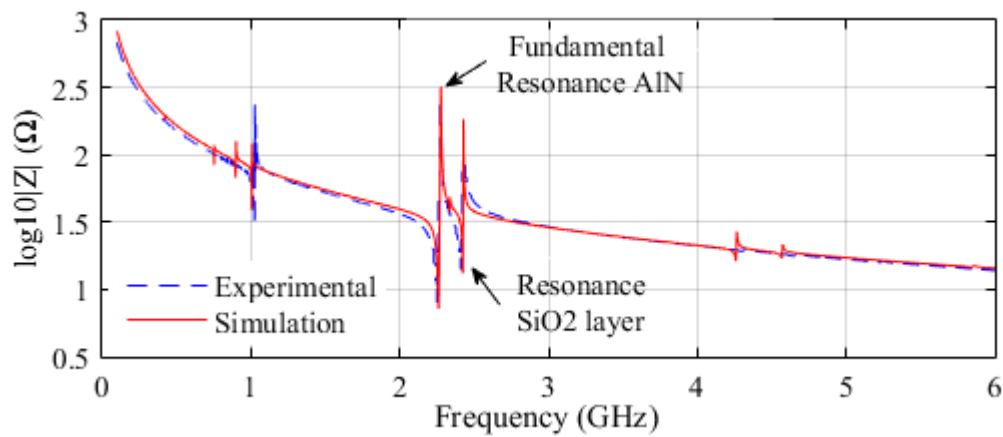

Figure 7.24 Measured frequency response of CMOS based SMR compared to the simulated fit model.

These experimental measurements and analytical model suggested that the expected thicknesses of the reflector layers (formed within the CMOS process) differ to the typical values used in the initial simulations. To investigate this phenomenon a cross-sectional SEM micrograph of the fabricated acoustic mirror was taken (shown in Figure 7.25). The metal and oxide layers of the CMOS process (tungsten metallization using all three layers of the process) can be observed. This is the CMOS substrate where the acoustic resonator structure (electrodes and piezoelectric layer) was deposited.

Thicknesses of the layers were estimated from the SEM photographs using an image processing software. Measured thicknesses of the metal layers lay within the tolerance values given by the process specifications. The thickness of all three metal layers were within ±5% of the typical values. However, thicknesses of the oxide layers fell into the maximum tolerance values, at +25%.
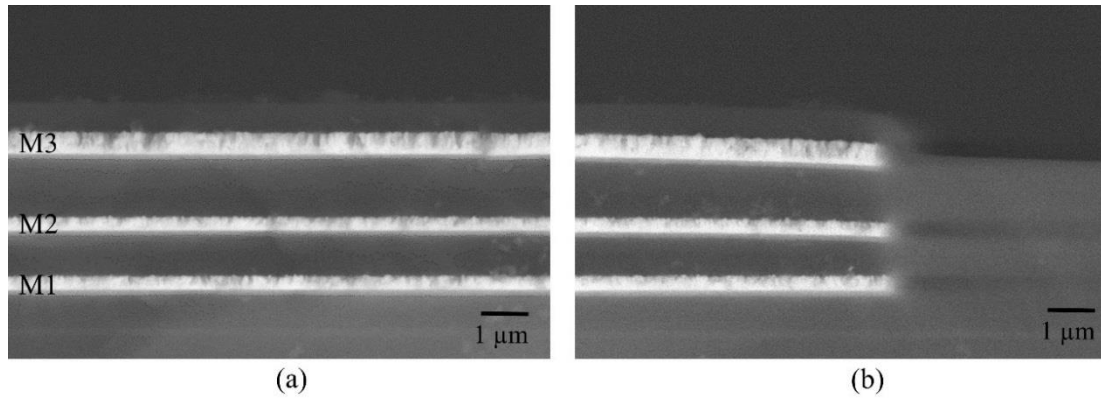
Figure 7.25 Cross-sectional SEM photographs of the fabricated CMOS acoustic mirror: (a) middle section and (b) edge region of the mirror structure.

Further 1D simulations were performed to simulate the transmittance of an acoustic mirror formed by layers of such thicknesses. The resulting transmittance plot is shown in Figure 7.26 below and compared to the original simulation data presented in Figure 7.3b. (using typical thicknesses of the CMOS process as given in the process specifications). A +25% variation in the oxide layers of the process had a significant effect on the transmittance of the acoustic mirror. Excellent transmittance of the fabricated reflector structure is obtained at frequencies between 1.8 GHz and 2 GHz and the best reflectivity is found at 3 GHz (at -43 dB). The bandwidth of transmittance in this structure, however, is considerably narrower (200 MHz) compared to the original simulation (1 GHz).
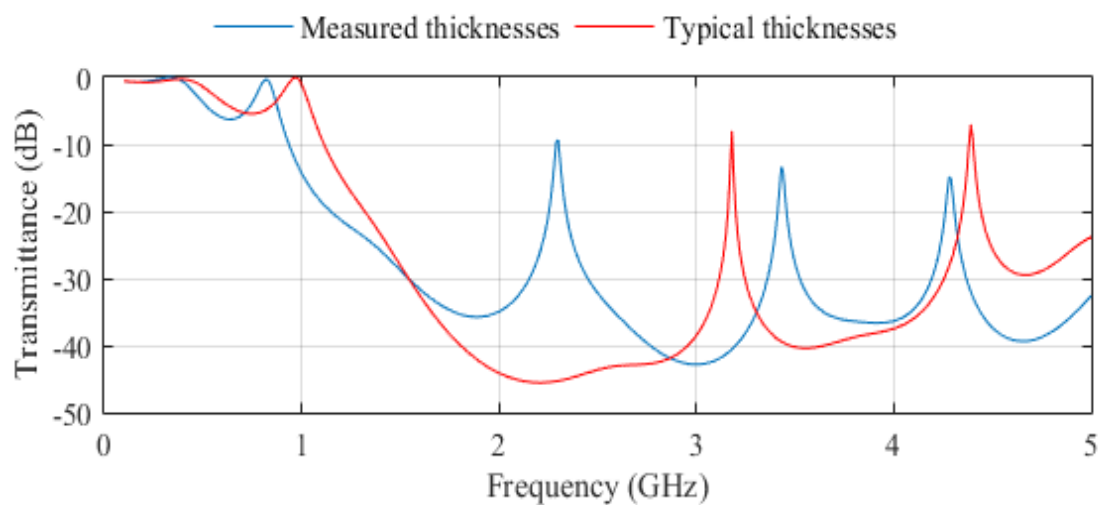

Figure 7.26 Simulated transmittance (1D model) of the acoustic mirror formed by the CMOS layers. Measured thicknesses of the fabricated devices and typical thicknesses of the process were used in the simulation.

Taking into account the above findings, a second batch of devices was processed (post-CMOS fabrication), to deposit a thicker AlN film (1.8 µm). The thicker layer was proposed to obtain a CMOS based SMR device resonating at ~1.9 GHz (mirror transmittance of -37 dB, and frequency value chosen to avoid interference with the 2.4 GHz resonance frequency of the thick SiO_2 layer). The typical characterisation data for these devices (from a total of 5 data sets) is shown in Figure 7.27. The frequency response of all five devices shown in the plot was very similar, with series and parallel resonant frequencies measured at ~1.889 GHz and ~1.92 GHz, respectively.
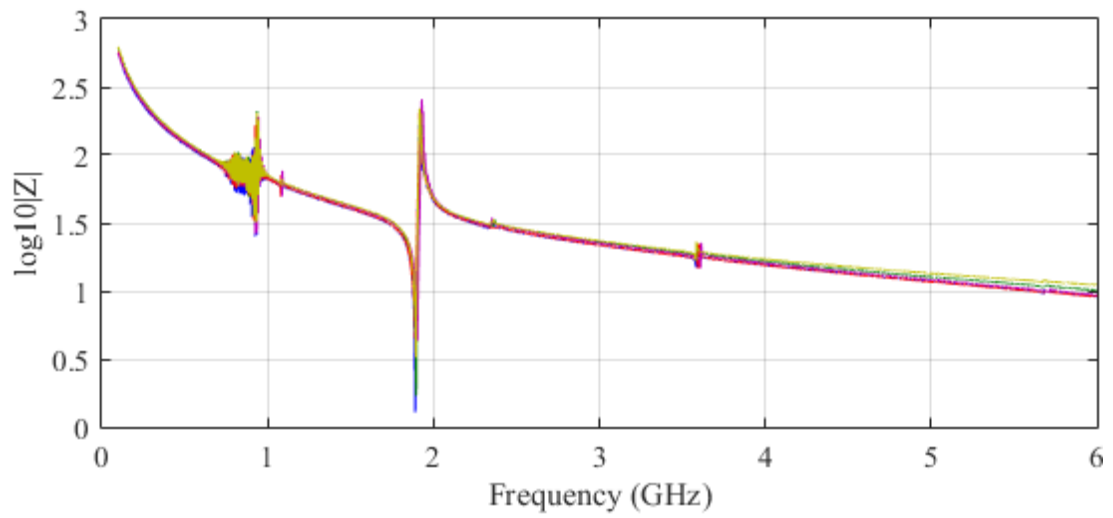
Figure 7.27 Impedance plot of CMOS based SMR devices (Mo electrodes and 1.8 µm AlN piezoelectric layer). Devices do not have a membrane.

The active resonator area of the fabricated devices shown in the figure above was ~ 52,000 µm². Quality factors in excess of 1500 were measured but typical values of ~500 were obtained from these devices, with an effective coupling factor value, k_{eff}^2, of ~3.8 %. Figure 7.28 shows the measured quality factors at the series and parallel frequencies, as well as the effective coupling factor for five different samples. The material coupling factor was obtained at k^2=4.2 %.

Figure 7.28 Measured quality factors and electromechanical coupling coefficients of the SMR devices.

The high Q factor values obtained from the fabricated devices indicate that the CMOS fabricated acoustic mirror is capable of efficiently confining the acoustic energy within the resonator structure, with very low energy dissipation into the silicon substrate. For the standard CMOS process used in this work (XFAB 1.0 µm process) SMR based devic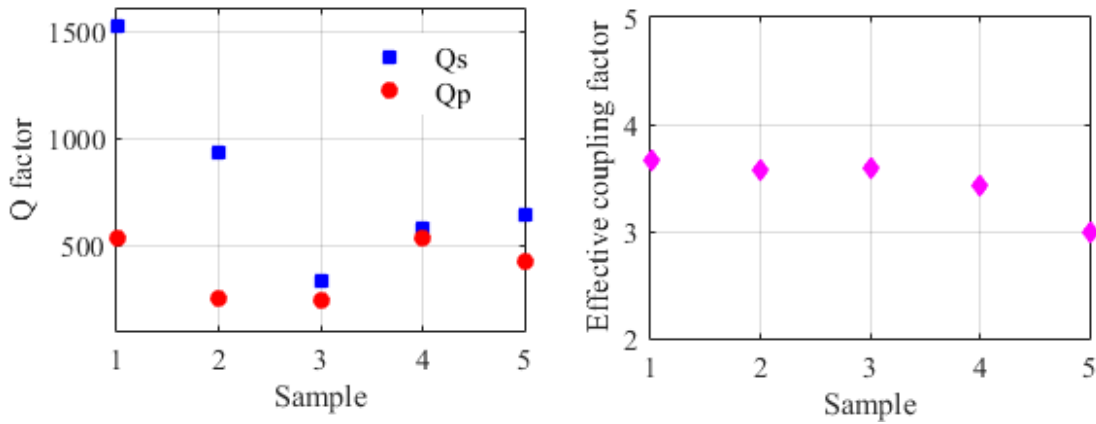es operating at a frequency between 1.9 GHz and 2.3 GHz were obtained. Experimental results for particle sensing applications using these fabricated devices are presented in the next section.

7.8   PARTICLE DETECTION

Characterisation of the CMOS based SMR devices was performed for the detection of fine particles (PTFE, 1 µm). The experiments shown in this section should be considered as an initial proof of concept to verify the use of the SMRs as particle sensors.

In these experiments, the resonant frequency of the SMR device was tracked using the network analyser (E5071B, Agilent Technologies). Particles were manually deposited onto the surface of the resonator using a micrometre wire guided by a three-axes linear stage. A detailed description of the experimental setup has previously been presented in section 5.4. The devices were placed in a temperature controlled unit to reduce the effects on temperature variations on the response of the device during the experiments. The development of a sensing unit employing these sensors would require a temperature compensation method to eliminate any temperature effects.

Figure 7.29 shows a typical time response as measured using the network analyser during the deposition of the PTFE particles. The amount of particles (total mass) deposited on the sensing area cannot be accurately controlled using the described method but a range of masses were achieved (i.e. 1 ng to 8.5 ng) and the frequency shifts for each deposition were recorded. Depositions below 1 ng were not possible using this method so the limit of detection of these devices could not be tested.
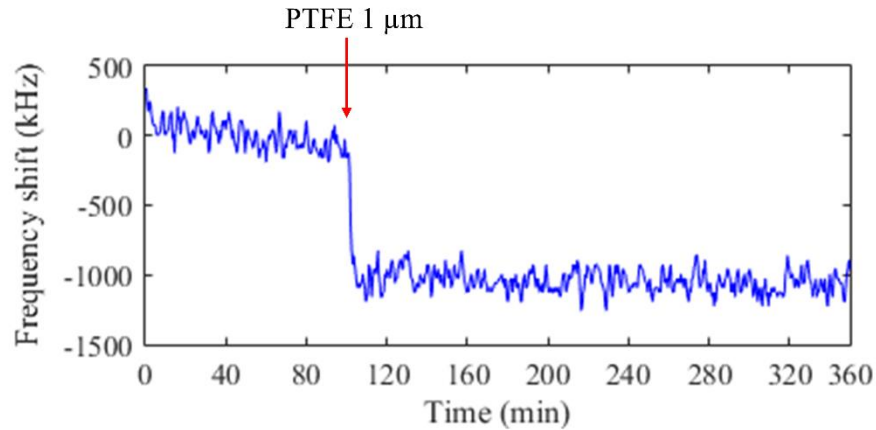
Figure 7.29 Plot of frequency response of the SMR device when loaded with PTFE 1 µm particles (8.5 ng)**.**

The SMR device was loaded with five different masses of particles. The measured frequency shifts are shown in Figure 7.30. The total mass was estimated from optical micrographs taken before and after each particle deposition. An example of one of these photographs is shown in Figure 7.31. A fit was applied to the data, to demonstrate the linear relationship between the mass loading and frequency shift. The sensitivity of the device was calculated from the linear fit as 117 kHz/ng. The sensitivity recorded with the novel CMOS based SMR is slightly greater than the 90 kHz/ng sensitivity previously recorded for the 900 MHz SMR (section 5.4).
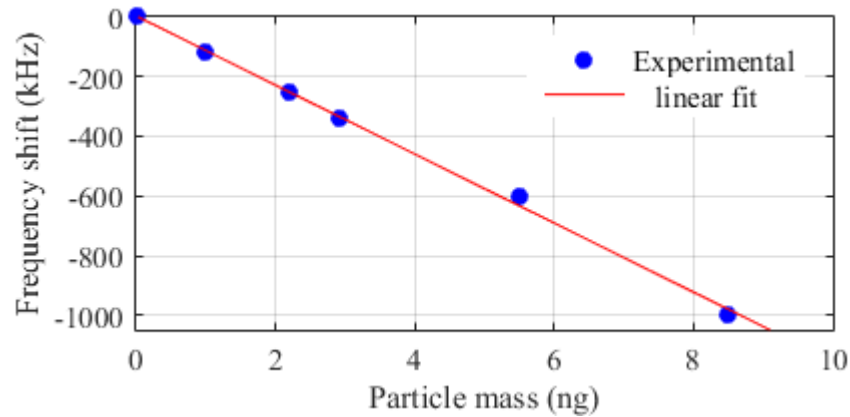
Figure 7.30 Measured frequency shifts for the 2.1 GHz CMOS based SMR device to mass loading between 1 ng and 8.5 ng.
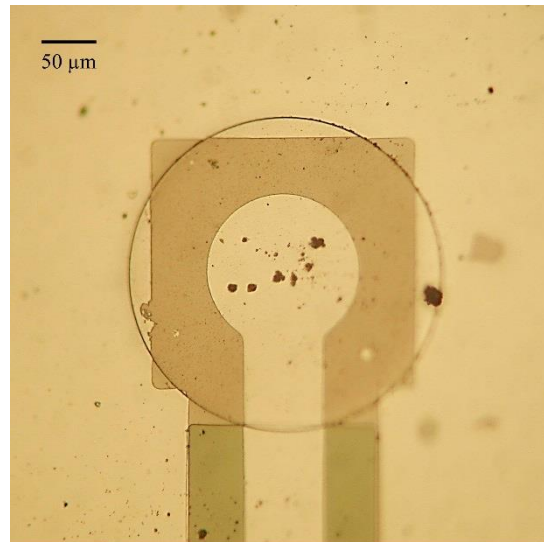
Figure 7.31 Photograph of particles deposited on the sensing area of the SMR device.

The experimental results presented above demonstrate this CMOS based SMR device is capable of particle detection in a laboratory setting. The device is suitable for use for air quality monitoring applications. However, to realise a complete portable, low-power system the developed device must be coupled to a compact interface board with driving circuitry. The final target is to fabricate these devices together with the CMOS interface circuitry.

7.9 CONCLUSIONS

In this chapter, a novel SMR device was developed for air quality monitoring applications. The device was designed to address previous limitations found in the characterisation of the SMR devices, presented in Chapter 5 and Chapter 6. Three main advantages were proposed: ability to be fabricated in large volumes at low-cost, contain a self-cleaning sensing area (through use of a microheater) and demonstrate high sensitivity VOC detection (optimal performance obtained through temperature modulation).

The novel device comprises of three distinct parts: a CMOS integrated microheater, a CMOS fabricated acoustic mirror, and a post-CMOS resonator structure. The majority of the device (i.e. the acoustic mirror and microheater) can be fabricated within a standard XFAB 1.0 µm SOI-CMOS process. The design of the CMOS based device was finalised in Spring 2016. Delays beyond the control of this project, caused the tape-out of the designs to be postponed until Winter 2016. Furthermore, due to a failure at the foundry, during the SOI fabrication run, only bulk processed devices were fabricated during this work (i.e. the microheater was not included in these devices). However, the concept of the CMOS based acoustic mirror was proven in this chapter.

A standard XFAB 1.0 µm SOI-CMOS process was chosen for the fabrication of the CMOS based SMR. Prior to fabrication, simulations were performed to select the process metallization (aluminium or tungsten) and the number of metal layers used (maximum of three). The tungsten metallization was chosen due to the high impedance ratio with the oxide layers (ratio of ~8), which allowed good reflectivity of the mirror structure (maximum transmittance of -48 dB). This optimal performance was obtained between 2 and 3 GHz.

The operating frequencies of a resonator built upon this CMOS based acoustic mirror are determined by the transmissivity bandwidth of the mirror. To obtain high quality factors, the resonator must operate at the suitable frequencies determined by the maximum reflectivity of the mirror (i.e. between 2 and 3 GHz). Simulations of the SMR device were performed to determine the thickness of the piezoelectric layer. A

thickness of 1.1 µm was chosen for AlN, which resonated at a suitable frequency (2.1 GHz).

An integrated microheater was designed employing single crystal silicon as the resistive material (*p+* silicon) to allow good thermal stability. The heater is CMOS compatible, and can be fabricated within the selected CMOS process in this work. The microheater has a small area of 0.018 mm^2 (circular shape with 150 µm diameter), a membrane to heater ratio of 4 and uses sector shape silicon tracks (angle of 40°). Using this structure allowed the reduction of convection heat losses and generation of the heat in the inner area of the track. A four-probe temperature measurement method is used with metal tracks connected to the silicon tracks outside the membrane.

Three-dimensional electrothermal simulations of the integrated heater with the CMOS acoustic mirror were performed to optimise the dimension of metal layers forming the acoustic mirror. A design trade-off is encountered between the power consumption of the heater, temperature profile distribution and dimensions of the acoustic mirror. The radius of the metal layers was selected at 150 µm, which offered the best compromise between the three parameters. For a maximum temperature of 200 °C, the chosen heater dimensions offer low power consumption (40 mW). A heating time constant of < 2 ms is predicted.

Fabrication of the designed device was performed in two separate processes: (1) the CMOS based acoustic mirror was fabricated at XFAB (Germany) in a MPW run and (2) the resonator structure was fabricated in a post-CMOS process. Devices of 1.6 mm × 1.6mm were obtained from the CMOS bulk wafers, with devices with and without membrane. Fabrication of the acoustic mirror through a standard CMOS process significantly reduced the number of post-processing steps required (thus reducing fabrication time and cost).

Post-processing steps involved the deposition and patterning of the top and bottom electrodes (Mo) and deposition of the piezoelectric layer (AlN). The devices employ a capacitive coupling method to access the bottom electrode. A first batch of processed CMOS based SMR devices, found to resonate at ~2.2 GHz, revealed that the thicknesses of the reflector layers differed from the typical values of the CMOS process specifications. Measurements from SEM photographs of these layers

confirmed a variation of the thicknesses within ±5% for the metal layers and +25% for the oxide layers. A new batch of devices was fabricated considering these variations.

Fabricated devices (sensing area of ~52,000 µm²) exhibited high quality factors of ~500 and k_{eff}^2 of ~3.8%, which demonstrated the CMOS acoustic mirror was capable of efficiently trapping the acoustic energy of the resonator. The operating frequencies of these devices were measured at ~1.9 GHz. Further work is required on the optimisation of these devices, e.g. the deposition of higher quality piezoelectric films.

Characterisation of the devices (performed with a network analyser) demonstrated they were able to detect 1 µm PTFE particles deposited on the sensing area. A sensitivity of 117 kHz/ng was found for total particle mass tested between 1 ng and 8.5 ng. Further work involves developing a prototype PCB, so the sensor can be interfaced with a microcontroller. To take advantage of the possible CMOS integration of this SMR, the prototype circuit could then be developed into a complete ASIC. The characterisation of the SMR is a significant step towards developing a complete acoustic sensor system on a single chip.

7.10 REFERENCES

[1]   Elbrecht, L., Aigner, R., Lin, C. I. and Timme, H. J. (2004). "Integration of bulk acoustic wave filters: concepts and trends", *2004 IEEE MTT-S International Microwave Symposium Digest*. pp. 395-398.

[2]   Tukkiniemi, K., Rantala, A., Nirschl, M., Pitzer, D., Huber, T. and Schreiter, M. (2009). "Fully integrated FBAR sensor matrix for mass detection", *Procedia Chemistry*. **1**(1): 1051-1054.

[3]   Johnston, M., Shepard, K. and Kymissis, I., *Monolithic FBAR-cmos structure such as for mass sensing*. 2012: United States Patent.

[4]   Aigner, R. (2004). "Volume manufacturing of BAW-filters in CMOS fab", *2nd International Symposium on Acoustic Wave Devices for Future Mobile Communication Systems*. pp. 129-134.

[5]   Iwaki, T. (2007). "Ultra-low power single crystal silicon SOI-CMOS micro-hotplate with novel temperature-modulation principle for chemical sensing", PhD Thesis. *School of Engineering,* University of Warwick,

[6]   Aigner, R. (2003). "High performance RF-filters suitable for above IC integration: film bulk-acoustic- resonators (FBAR) on silicon", *Proceedings of the IEEE 2003 Custom Integrated Circuits Conference, 2003.* pp. 141-146.

[7]   Vilander, A., *Acoustic wave resonator with integrated temperature control for oscillator purposes*. 2007, United States Patent.

[8]   Bhattacharyya, P. (2014). "Technological journey towards reliable microheater development for MEMS gas sensors: a review", *IEEE Transactions on Device and Materials Reliability*. **14**(2): 589-599.

[9]   Simon, I., Bârsan, N., Bauer, M. and Weimar, U. (2001). "Micromachined metal oxide gas sensors: opportunities to improve sensor performance", *Sensors and Actuators B: Chemical*. **73**(1): 1-26.

[10]   Udrea, F., Gardner, J. W., Setiadi, D., Covington, J. A., Dogaru, T., Lu, C. C. and Milne, W. I. (2001). "Design and simulations of SOI CMOS micro-hotplate gas sensors", *Sensors and Actuators B: Chemical*. **78**(1): 180-190.

[11]   Iwaki, T., Covington, J. A., Udrea, F., Ali, S. Z., Guha, P. K. and Gardner, J. W. (2005). "Design and simulation of resistive SOI CMOS micro-heaters for high temperature gas sensors", *Journal of Physics*. **15**: 27-32.

[12]   Ali, S. Z., Guha, P. K., Lee, C. C. C., Udrea, F., Milne, W. I., Iwaki, T., Covington, J., Gardner, J. W., Maeng, S. and Park, J. (2006). "High temperature SOI CMOS tungsten micro-heaters", *2006 5th IEEE Conference on Sensors*. pp. 847-850.

[13]   Gardner, J. W., Guha, P. K., Udrea, F. and Covington, J. A. (2010). "CMOS interfacing for integrated gas sensors: A review", *IEEE Sensors Journal*. **10**(12): 1833-1848.

CHAPTER 8

CONCLUSIONS AND FURTHER WORK

8.1 PREFACE

The main objective of this work was to develop a low-cost, miniature device, capable of high volume production and monolithic integration, that could be used as part of a portable air quality monitor. Solidly mounted resonators, based on acoustic wave technology, were investigated to meet this aim. The project was divided into two main parts: modelling, development and testing of SMR devices for the detection of particulate matter and volatile organic compounds, and the development of a novel CMOS based SMR device with integrated heater to enhance sensor sensitivity and selectivity, improve sensor life-time and allow monolithic integration and high-volume production.

An analytical model and finite element models (COMSOL Multiphysics) of solidly mounted resonators were developed to aid the design of the devices. These models were used to simulate the frequency response, the temperature dependency and

the sensitivity of the devices for the detection of volatile organic compounds and fine particles.

The designed devices were successfully fabricated and characterised. A sensing system employing these devices was developed. The sensing system worked in a dual mode configuration. The devices were tested in a laboratory environment to the deposition of fine particles (<1 µm) and to the exposure of volatile organic compounds (toluene and acetone). The experimental results were found to be similar to those produced from the simulations, and demonstrated the high sensitivity of the SMR sensors and their suitability as the main sensing element in a portable air quality monitoring system.

In addition, a novel CMOS based SMR with integrated heater was designed. The device advanced upon the current generation of SMR devices through the inclusion of a CMOS fabricated acoustic mirror and a SOI-CMOS resistive microheater. The resonator structure was successfully fabricated in a post-CMOS process, to complete the SMR device. The novel device exhibited good electrical performance and it was found to be able to detect fine particles. Further work involves characterisation of the microheater, which was proposed to enhance the sensitivity and selectivity of the VOC sensor system, and the monolithic integration of the device.

8.2 AIR QUALITY MONITORING

Human exposure to hazardous air pollutants has been associated with a wide range of health problems and linked to an increasing rate of mortality around the world. In 2016, it was estimated that around 40,000 deaths per year were caused by the exposure to outdoor air pollutants across the UK, with a consequent £20 billion cost to individuals and health services [1]. Particulate matter and volatile organic compounds contribute to over 20% of the total pollutants present in air and have been strongly related to several respiratory and cardiovascular diseases.

There is a growing awareness of the dangers to health caused by VOCs and PM, and their monitoring is becoming increasingly important. Commercial instruments for the detection of these pollutants are bulky, expensive and complex. A detailed review on the available technologies was provided in Chapter 1. As the

population becomes aware of the effects of air pollution, there has been an increased demand for low-cost, low-power and portable (or wearable) air quality monitors, which are capable of monitoring concentration levels of these pollutants, below their safe exposure limits.

The main aim of this work was to develop a low-cost, miniature device, capable of high volume production and monolithic integration, to be used as part of a portable air quality monitor, with VOCs and PM as the main target pollutants.

From the available technologies (reviewed in Chapter 1 and Chapter 2), solidly mounted resonators were chosen for use in this work. Compared to commercially available particle sensors (optical based) and VOC sensors (PIDs, MOX), they offered advantages of high sensitivity, small footprint, long life-time, good power handling capability and the possibility of CMOS integration (which allows for improved performance, miniaturisation and low power consumption).

8.3 DESIGN AND MODELLING OF SOLIDLY MOUNTED RESONATORS

The first step towards the development of a low-cost, monolithically integrated sensor involved the design and development of SMR devices suitable for particle detection and VOC detection (gravimetric sensing). On the design of a SMR device, materials properties and thicknesses of the layers are critical as they directly impact the operating frequency and performance of the device.

In this work, ZnO based devices were designed with an acoustic mirror formed by three pairs of alternating layers of Mo/SiO_2. ZnO was selected due to its high piezoelectric coupling coefficient (8.5 %) and low film stress (when deposited at room temperature). Mo/SiO_2 layers were selected for their good adhesion and large high to low impedance ratio (~5). Al and Au/Cr were used as the material for the electrodes. Al offered low density and good conductivity, while Au/Cr offered a high acoustic impedance.

To aid the design procedure, a 1D analytical model, as well as 2D and 3D finite element models, were developed. These models were used for the analysis of the transmissivity of the acoustic mirror, the frequency response of the devices and their

temperature coefficient of frequency. Based on these models, SMR devices were designed to resonate at the frequencies of 870 MHz and 1.5 GHz, for which the required thicknesses of the materials were extracted. The 1D Mason model aided the design of the acoustic mirror. Based on the simulations, a total of 3 pairs of alternating layers of Mo and SiO_2 were chosen for the acoustic mirror structure with a simulated mirror transmissivity of -40 dB at the designed centre frequency of 870 MHz, which corresponds to 99.99 % reflection. The temperature dependency of these devices was estimated from the 2D FEM simulations at about -35 ppm/°C (temperature-dependant material properties were introduced in the model to simulate these temperature effects).

A study on the SMR sensor response (sensitivity to the absorption of vapours and the detection of fine particles) was also performed using the FEM models. The 2D model was used to simulate the VOC detection capability of the SMR, which required the addition of a thin polymer film. For a 70 nm PDMS polymer coating, a sensitivity of -17.5 Hz/ppm was estimated (870 MHz device). From the simulation results, it was observed that thicker coatings produced larger frequency shifts for a given vapour concentration and thus, higher sensitivities were calculated for thicker polymer films. These results were compared to the simulations performed for a higher frequency device (resonant frequency of 1.4 GHz). The sensitivity of the 1.4 GHz device was noted to be twice as high as that of the 870 MHz SMR.

The sensitivity of the SMR devices with different polymer coatings was also studied through the FEM simulations. Polymer coatings with higher partition coefficients to specific vapours were expected to exhibit higher sensitivities. The simulations confirmed this behaviour. SMR devices with a PDMS coating were estimated to have a higher sensitivity, compared to three other polymers trialled (PMA, PIB and SXFA) for the detection of toluene vapours.

Simulations of particle detection were performed used the developed 3D FEM model. This model consisted of only a quarter of the complete SMR structure, to reduce computation times (compared to the complete model). Particles were simulated on the sensing area of the SMR model, with cubic geometries to ensure good binding to the surface. Although the developed model has some limitations (maximum number

of particle simulated, only one quadrant of the sensing area simulated), the simulation results provided valuable information on the effect of the particles located on the sensing area of the SMR devices. Particles were placed in three different arrangements on top of the SMR device, variations in the location of the particles produced frequency shifts with variation within ±5%. The sensitivity of the 870 MHz devices (Al electrodes) to the detection of PM2.5 particles was estimated at ~120 kHz/ng.

8.4 FABRICATION AND CHARACTERISATION OF SMRS

The SMR devices were fabricated using standard microfabrication techniques at CAPE, University of Cambridge, UK. Although a 6-mask fabrication process was originally proposed (Appendix C), the process was optimised to a 3-mask photolithography process. The required photomasks were designed (Tanner Tools, EDA) and manufactured in 5" glass/chrome plates.

The thicknesses of the layers from the fabricated devices were estimated from SEM images (reflector layers) or measured with a stylus profiler (ZnO layer). Compared to the design parameters, variations (in the range of ± 20%) of the thicknesses of the material layers were observed, which caused the discrepancy between modelled and measured resonant frequencies. Two batches of SMR devices were fabricated, with the second batch featuring improved performance and thicknesses closer to the designed values.

Fabricated SMR devices from the second batch resonated at 900 MHz (variation of 3.5% to the designed value). The performance metrics of these devices were measured at Q_s=170 and k_{eff}^2=2.6 %. The devices had a small footprint of 1.5 mm $\times$ 1.5 mm. These devices (MBL003) were mainly used throughout the experimental work.

The SMRs were characterised to ambient variations before being tested for particle detection and sensing of organic compounds. For this characterisation, the devices were exposed to controlled temperatures (30° - 90°C) and humidity levels (15-60 %RH). The response of the SMRs was recorded together with a reference temperature and humidity sensor (BME280). TCFs were measured as -55 ppm/°C

and -49 ppm/°C for the series and parallel frequencies, respectively and the humidity dependence was measured as 580 Hz/%RH. A higher TCF was measured, compared to that estimated from the simulation results (-35 ppm/°C), which can be attributed to the properties of the deposited materials. To reduce the effects of ambient variations of the sensors, a dual differential mode configuration (with electronic circuity) was proposed and tested to the same temperature and humidity conditions. It was observed that ambient effects can be significantly reduced, when using a differential configuration (TCF <2 ppm/°C), provided that the TCF of the SMR devices are comparable.

8.5 SMRS FOR PARTICLE SENSING

The SMR devices were characterised for the detection of fine particles (<10 µm). Initial characterisation demonstrated the devices were able to detect particles <1 µm with a high sensitivity of 90 kHz/ng (minimum trialled mass of 720 pg of PTFE particles). The obtained sensitivity was larger by two orders of magnitude, compared to reported values in the literature using alternative SAW devices, with typical sensitivities <0.9 kHz/ng. [2-4] and other devices such as thin film piezoelectric on silicon resonators, with reported sensitivities of 4.2 kHz/ng [5].

After proving the devices were capable of detecting fine particles, a particle sensing unit was developed. The compact sensor system (41 mm × 36 mm × 25 mm) consisted of Colpitts oscillators to drive the SMR devices and additional interface circuitry to output a low frequency differential signal (<10 MHz) for acquisition with a low-power microcontroller. This sensing unit was tested inside a particle chamber along with other reference commercial devices (mainly optical based).

The SMR based particle sensing unit demonstrated a linear response to the deposition of fine particles with a calculated sensitivity of 4.6 Hz per µg/m^3 and a limit of detection of ~20 µg/m^3. The performance of the unit met the requirements to detect the maximum exposure value of 25 µg/m^3 for PM2.5. However, discrepancies in the sensitivity were found when testing was performed inside a small (5.625 L) and large (720 L) environmental chamber (sensitivity recorded from the small chamber was 6

times higher). This was attributed to the passive sampling method (gravitational sedimentation) employed by the sensor system.

The discrepancy in the sensitivity and the slow response times observed from the sensing unit (120 s) demonstrated the need of an active sampling method to produce real-time measurements and obtain reproducible results. A virtual impactor was designed to address this problem. The impactor actively draws a sample of air and separates the particles according to their aerodynamic diameter. Particles <2.5 µm are directed towards the sensor surface. The impactor was designed to be integrated with a new hybrid system (SMR interfaced to an ASIC chip). Characterisation results of the impactor demonstrated it was effective to separate the particles and direct them towards the sensor surface. However complete testing of the entire system (hybrid system and impactor) was not possible due to the non-optimal performance of the ASIC chip (and interface board).

It is expected that the particles accumulating of the sensor surface will cause the SMR device to saturate, although for a maximum particle concertation tested of 60,000 µg/m^3, saturation was not observed. An active method of self-cleaning the sensor surface is required to extend the sensor life-time in an air quality monitor.

8.6 SMRs FOR VOC SENSING

For the detection of volatile organic compounds, the SMR devices were coated with thin polymer films (PEG and PDMS). An investigation of the partition coefficients for the polymer-vapour pairs was performed for the target vapours using linear solvation energy relationships. PDMS was chosen due to its high affinity to toluene, while PEG was chosen for its low-cross-sensitivity to toluene and moderate sensitivity to acetone.

To deposit the polymers onto the surface of the SMR devices, a custom drop-coating system was developed. The system allowed small volumes of the polymer solution to be deposited onto the device, thus thin coatings could be created (<100 nm possible). A similar differential system to that discussed previously for the particle sensing, was used to measure the frequency of the SMR sensor. A gas chamber was constructed to house four differential sensor units, and expose the devices to the VOCs.

The chamber was located within a fully automated test station, developed to expose the differential sensor pairs to low ppm vapour concentrations.

The SMR sensors successfully detected toluene and acetone vapours in concentrations below their safe exposure limits (5 ppm of toluene and 50 ppm of acetone). A trade-off between polymer film thickness and sensor response time was observed, with thinner coatings exhibiting faster response times but lower sensitivity. A 180 nm PDMS coated SMR demonstrated a linear response and a high sensitivity of -60 Hz/ppm for toluene detection (in the range of 5 ppm to 100 ppm).

Although capable of detecting the low ppm concentrations of acetone required for air quality monitoring applications (50ppm), the sensitivity of the PEG coated sensor (-3.5 Hz/ppm) was low, compared to previous reported studies [6, 7]. The sensitivity of these devices need for be further investigated using alternative polymer coatings (PMMA, SXFA). An array of different polymer coated SMRs is also desirable, to identify the individual vapours within a toluene-acetone mixture. Further testing is required to evaluate the performance of the devices with variable environmental (temperature and humidity) conditions, where previously experiments were realised in dry conditions at a constant temperature of 35°C.

It was observed that the differential sensor setup still exhibited drift (~5 kHz), even after a long period of stabilisation. Thus, further analysis of the stability of the sensor circuits is required, before the system can be integrated within an air quality monitor. Further improvements in terms of sensitivity, selectivity, response time and circuitry performance (e.g. drift, noise level) are needed, but the results obtained from these experiments were promising, demonstrating the suitability of these devices for their application in air quality monitoring.

8.7 CMOS BASED SMR

Based on the results obtained from the characterisation of the SMR devices to particle sensing and VOC detection, a novel SMR device was designed to address the limitations encountered with these devices. The novel device comprised of three main parts: an integrated SOI-CMOS resistive microheater, a CMOS based acoustic mirror and a post-CMOS resonator structure. The integrated microheater was designed as the

self-cleaning mechanism of the SMR device (for particle sensing) and to enhance the sensitivity and selectivity of the sensor to VOCs, through the use of a temperature modulation technique. It is proposed, the rates at which individual VOCs are absorbed into the polymer coatings vary depending on the temperature of the layer. Therefore, the sensitivity of the SMR could be tuned towards a certain VOC if the optimal operational temperature was found. This could be extended to modulating between several temperatures, allowing optimal sensor detection performance to several VOCs.

The microheater and the acoustic mirror of the SMR device were both designed to be fabricated within a standard XI10 XFAB 1.0 µm SOI-CMOS process. Only the resonator structure (piezoelectric layer and electrodes) need to be deposited in the post-CMOS fabrication steps. The fabrication of the acoustic mirror within the CMOS process itself, advanced the current generation of SMR devices. This has the potential to enable the SMR device to be monolithically integrated and fabricated in large volumes, at low-cost with reduced post-processing steps.

The concept of the CMOS fabricated acoustic mirror was proven in this work with devices fabricated in a bulk CMOS process (XFAB, Germany) and post-fabrication performed at the Technical University of Madrid, Spain. The fabrication of the devices within the designed SOI-CMOS process is still currently being performed (a failure at the foundry during the SOI run delayed the fabrication). Thus, characterisation of the microheater was not possible.

The CMOS based acoustic mirror was designed from the metal layers and oxide layers of the CMOS process. The thicknesses of these layers are process-defined. From a choice of aluminium and tungsten metallization, tungsten was used as it offered a larger high to low acoustic impedance ratio (~8), which allowed a maximum reflectivity (-48 dB transmittance) of the acoustic mirror at frequencies between 2 and 3 GHz.

Only CMOS compatible materials were used in the post-fabrication of the CMOS substrate (AlN for the piezoelectric layer and Mo for the electrode). Completed CMOS based SMR devices (1.6 mm × 1.6 mm) resonated at ~1.9 GHz and exhibited good performance with quality factor values of ~500 and k_{eff}^2 of ~3.8%. The high Q

values obtained proved the CMOS acoustic mirror was capable of efficiently confining the acoustic energy of the resonator.

The integrated microheater was designed using a *p+* silicon region to allow good thermal stability. It was designed with a circular shape ($\phi = 150$ µm) and sector shape silicon tracks (40° angle) connected to metal tracks outside the membrane in a four-probe configuration for temperature sensing and current supply [8]. Based on simulation results, a trade-off between power consumption of the heater, temperature profile distribution and dimension of the metal layers forming the acoustic mirror was observed. Metal layers of 150 µm in diameter were found to offer the best compromise between these parameters. 3D electro-thermal simulations predicted a low power consumption of 40 mW and a heating time constant <2 ms (temperature of 200 °C).

The suitability of these devices for particle sensing was demonstrated with initial characterisation performed with PTFE particles (<1 µm), using a network analyser to track the resonant frequency of the devices. A linear response was observed for particle masses in the range of 1 ng to 8.5 ng, with a calculated sensitivity of 117 kHz/ng.

This experimental proof-of-concept work demonstrated the potential of the designed SMR devices to be integrated as the main sensing element in a portable, low-cost air quality monitor. Furthermore, it is believed that these devices offer the potential to impact not only the sensing field but also many consumer electronics applications (mobile phones, wearable devices) which extensively use RF filters based on BAW devices operating at frequencies around 2-3 GHz. Further work is needed involving optimisation of device performance, characterisation of the microheater and integration with CMOS circuitry. Details on this further work are presented in section 8.9.

8.8 ACHIEVEMENTS

The aims of this project were previously presented in Chapter 1. Here, the main achievements of this work are summarised.

- The one-dimensional Mason analytical model for an SMR device was implemented in a Matlab script to aid the design of the resonators. This model was used in the design of the acoustic mirror (simulations of the transmissivity) and to predict the frequency response of the devices.

- Finite element models of the SMRs devices were developed. The models were used to study temperature dependency, to predict sensitivity to the exposure of VOCs and to study frequency response to the deposition of fine particles.

- SMR devices were designed to operate at two different frequencies (870 MHz and 1.5 GHz) and for operation in a longitudinal mode, suitable for the air quality monitoring applications in this work. Designed devices were fabricated and characterised.

- The SMR devices were characterised to observe the effect of ambient variations (temperature and humidity). A temperature dependency of -55 ppm/°C was measured for the devices and humidity dependence was recorded at 580 Hz/%RH.

- Fabricated devices were characterised for the detection of fine particles (<2.5 µm). A particle sensing unit was developed (working in a dual mode configuration). The sensing unit was characterised in environmental chambers, and demonstrated the ability of the SMRs to detect PM2.5 concentrations with a sensitivity of 4.6 Hz per $µg/m^3$ and limit of detection of ~20 $µg/m^3$, which is below the safe exposure limit established at 25 $µg/m^3$.

- For particle detection, a virtual impactor was designed, fabricated and tested for the separation of particles with aerodynamic diameter of 2.5 µm. The impactor was designed to fit within the same footprint as a hybrid ASIC-SMR interface board. Air was sampled using a low-power miniature blower.

- For VOC detection, custom-made polymer deposition systems were developed. A spray coating system and a drop coating system were designed and constructed. Thin and uniform polymer coatings were possible with both systems. The SMR devices were functionalised with the polymer solutions using the developed systems.

- An automated VOC test station was developed, capable of delivering VOC mixtures in air at controlled low ppm concentrations (ppb levels also possible). The station was assembled using state-of-the-art equipment and a user-friendly interface was developed (LabVIEW) to control the testing station.

- Polymer coated SMR devices were characterised for the detection of two VOCs (acetone and toluene) to demonstrate their suitability to detect these organic vapours in concentration levels below the safe exposure limits, required for air quality monitoring applications.

- A novel CMOS based SMR device with integrated heater was designed. A 3D finite element model was developed to perform electro-thermal simulations of the microheater. From the simulations, the time constant and maximum temperature of the microheater were determined as 4.3 ms and 550 °C, respectively.

- The CMOS acoustic mirror was simulated using the 1D Mason model. The maximum reflectivity of the acoustic mirror, formed from the selected CMOS process, was determined from the simulations to be approximately -50 dB at frequencies between 2 and 3 GHz. This was used to determine the operating frequency of the device.

- The CMOS devices were fabricated and post-process steps performed. These devices were initially characterised for the detection of fine particles. The characterisation demonstrated the potential of this device to be integrated in a low-cost air quality monitor (reduced post-fabrication steps, enhanced sensitivity and a self-cleaning method).

8.9 FURTHER WORK

The work completed in this thesis focused on the development of the sensing component of a portable air quality monitor. It was demonstrated that the SMR devices were able to detect particulate matter and the target VOCs to within the safe exposure limits currently enforced, but improvements are needed in terms of selectivity, sensitivity, life-time and performance (e.g. stability, TCF) of the sensors. A novel SMR device was designed to address these limitations. Further work involves characterisation of the novel CMOS based SMRs for VOC detection and their monolithic integration with the active CMOS circuitry.

8.9.1 HARDWARE

The integrated heater was proposed for the implementation of a temperature modulation technique. The SMR sensors exhibit higher sensitivity to an individual

compound at a specific temperature. The heater could be used to adjust the temperature of individual device to target a specific analyte. This could be extended to modulating the temperature of a device, thereby allowing several VOCs to be targeted.

The relationship between SMR temperature and sensitivity to a particular VOC is not well understood. Initial experiments to characterise the heaters would be required. These experiments would allow the heater temperatures to be tuned to increase the sensitivity to the VOCs of interest. Additionally, the in-built heater can be used to investigate temperature effect on the response and recovery times of the sensor and potentially reduce the signal to noise ratio.

To reach the target of a low-cost device suitable for volume production, the SMR and circuitry must be monolithically integrated onto a single substrate. The first step towards this monolithic integration requires interfacing the SMR device to an ASIC chip. In Chapter 5 a first-generation ASIC chip was interfaced to the SMR device, via wire-bonding in a hybrid system. However, initial characterisation found the internal mixer was becoming saturated from the oscillator circuit. This caused instability, which prevented usable data from being obtained. The problem could not be rectified without modification of the ASIC, thus a second generation is being redesigned. This new ASIC is being designed based on the equivalent circuit of the fabricated CMOS based SMR device (1.9 GHz).

This first generation of CMOS based SMR did not include features such as a diode temperature sensor. Furthermore, a three-metal process was used which prevented a metal heater from being used. It is proposed a five-metal layer process would allow a metal heater to be included in the design.

The current work was limited to testing a single organic compound at a time. Further work involves developing a system to identify the presence of individual VOCs from a mixture of compounds. This can be achieved through using an array of CMOS based SMR sensors using different coatings. Different coated devices will produce a unique response to a given VOC. These responses can be processed using techniques such as principal component analysis (PCA) to recognise patterns of the sensor array, which can be used to identify the VOCs present.

An array of SMR sensors could be further extended to create the target air quality monitor. The unit would include polymer coated SMRs for VOCs and bare SMR devices for particle detection, temperature and humidity sensing. This unit will help meet the goal of a portable air quality monitor. The miniature footprint of the SMR sensors potentially enable an array of sensors in a unit of 5×5 mm.

8.9.2 EXPERIMENTAL

Initial testing of the SMR devices was performed in dry conditions at constant temperature. Further testing in conditions of various levels of humidity and temperature is required, to replicate the environments experienced in real world application (e.g. 10 % RH to 90 % RH and 15 °C to 40 °C). This will help to analyse the effect of these ambient variations on the sensitivity of the SMR.

SMR sensor results were presented from devices coated with two different polymers. These results were adequate for the detection of toluene and acetone. Further characterisation is required to investigate the ability of the SMR sensors to detect other VOCs (e.g. benzene, ethyl acetate). The performance of the SMRs could be analysed when coated with a wide range of polymer layers, to extend the detectable VOCs with the sensor system. Furthermore, other deposition methods (e.g. ink-jet printing) could be trialled to enable thinner coatings to be deposited. The thinner coatings would help reduce the response time of the SMR devices and enable higher frequency devices to be used.

Further characterisation of the SMR particle sensor is required to analyse the performance of the system integrated with the virtual impactor. The SMR particle sensor in this work was targeted to detect PM2.5. Further testing of the SMR sensor can be performed to analyse the suitability of the device to detect the finest particles (<100 nm). The virtual impactor itself can be improved by incorporating a series of cascaded impactors to separate particles of different sizes (e.g. differentiate between PM10, PM2.5 and UFPs) in a single system. It is proposed the integrated microheater on the CMOS based SMR could be used to clean the sensor surface. Without a method of cleaning the sensor surface, the sensor can become saturated (when overloaded with

particles). The ability of the microheater to clean the surface of the SMR needs to be characterised (i.e. when the temperature of the device is increased).

The SMR devices have not been tested for extended use periods (> 30 hours). The longevity of the devices has not been assessed, in terms of sensitivity and reliability over time. Experiments need to be performed with devices running for periods of several days (or weeks) to assess the sensing performance of the SMRs.

8.9.3 SOFTWARE

As discussed before the integrated heater allows the SMR to be tailored to specific VOCs through temperature modulation. Software is required to control and monitor the temperature of the heater. Software would allow patterns (temperature steps) to be applied, which could be used to investigate the sensitivity and response time of the sensor.

During this work, high level programming languages were used to acquire the data from the SMR sensors and to control the VOC test station. This provided a reliable but inefficient (i.e. processing and hardware requirements) means to collect sensor data. To miniaturise the system for use in a portable air quality monitor, a microcontroller could be used to perform the data acquisition and processing functions. The inefficient software would need to be rewritten, to be able to function with the lower processing power available on a microcontroller. The redeveloped algorithms would allow the software to operate in real-time, without any post-processing.

To provide an accessible means of monitoring air quality, the sensor data must be displayed in an easy to use format. The ubiquitous use of smartphones has enabled their use as a platform for connected devices (e.g. smart homes). Due to their small size and low power consumption, these SMR devices have the potential to be integrated internally into a smartphone or as an add-on module for air quality monitoring. This integration would be possible by the development of a microcontroller system for communication with a smartphone app for real-time, localized air quality monitoring.

8.10 REFERENCES

[1]   Royal College of Physicians. (2016). "Every breath we take: the lifelong impact of air pollution". Report of a working party. London: RCP

[2]   Bowers, W. D. and Chuan, R. L. (1989). "Surface acoustic-wave piezoelectric crystal aerosol mass microbalance", *Review of Scientific Instruments*. **60**(7): 1297-1302.

[3]   Bowers, W. D., Chuan, R. L. and Duong, T. M. (1991). "A 200 MHz surface acoustic wave resonator mass microbalance", *Review of Scientific Instruments*. **62**(6): 1624-1629.

[4]   Thomas, S., Cole, M., Villa-López, F. H. and Gardner, J. W. (2016). "High frequency surface acoustic wave resonator-based sensor for particulate matter detection", *Sensors and Actuators A: Physical*. **244**: 138-145.

[5]   Harrington, B. P., Abdolvand, R., Hajjam, A., Wilson, J. C. and Pourkamali, S. (2010). "Thin-film piezoelectric-on-silicon particle mass sensors", *IEEE International Frequency Control Symposium (FCS)*. Newport Beach, CApp. 238-241.

[6]   Qiu, X., Tang, R., Zhu, J., Yu, H., Oiler, J. and Wang, Z. (2010). "Acetone sensor based on Film Bulk Acoustic Resonator", *2010 IEEE Sensors*. pp. 1546-1549.

[7]   Wang, J. and Chen, D. (2013). "Investigation of polymer-coated film bulk acoustic wave resonator for acetone vapor detection", *2013 IEEE International Conference on Green Computing and Communications and IEEE Internet of Things and IEEE Cyber, Physical and Social Computing*. pp. 1680-1684.

[8]   Iwaki, T. (2007). "Ultra-low power single crystal silicon SOI-CMOS micro-hotplate with novel temperature-modulation principle for chemical sensing", PhD Thesis. *School of Engineering,* University of Warwick,

APPENDICES

APPENDIX A

MATLAB SCRIPT FOR THE ONE-DIMENSIONAL MASON MODEL

```matlab
% University of Warwick - School of Engineering
% PhD in Engineering - Research project by Farah Helue Villa López

% CMOS COMPATIBLE SOLIDLY MOUNTED RESONATOR FOR AIR QUALITY MONITORING

% ------------------------------------------------------------------------
% Matlab code for the implementation of the one-dimensional Mason Model.
% Simulation of frequency response and acoustic mirror transmittance.
% Example shown for SMR working at 870 MHz, 3 pairs of Mo/SiO2 for
% acoustic reflector and Aluminium Electrodes.
% ------------------------------------------------------------------------

clear all;
clc;

% Active area of the Solidly Mounted Resonator
Area = 200e-6*200e-6;            % Square active area (m^2)

% Angular frequency
syms ('f')
omega = 2*pi*f;

% MATERIAL PROPERTIES OF THE SUBSTRATE
rho_Si = 2330;                   % Density of Silicon (kg/m^3)
v_Si = 8320;                     % Acoustic velocity of Silicon (m/s)
d_Si = 500e-6;                   % Thickness of Silicon substrate (m)
Z_Si = Area*rho_Si*v_Si;
k_Si = omega/v_Si;
theta_Si = k_Si*d_Si;

% MATERIAL PROPERTIES FOR THERMAL OXIDE
rho_Oxide = 2070;                % Density of silicon dioxide (kg/m^3)
v_Oxide = 5710;                  % Acoustic velocity of silicon dioxide
 (m/s)
d_Oxide = 200e-9;                % Thickness of the thermal oxide
Z_Oxide = Area*rho_Oxide*v_Oxide;
k_Oxide = omega/v_Oxide;
theta_Oxide = k_Oxide*d_Oxide;

% MATERIAL PROPERTIES OF THE REFLECTOR LAYERS

% High Acoustic Impedance Material (Molybdenum)

rho_Mo = 10200;           % Density of Molybdenum (kg/m^3)
v_Mo = 6340;              % Acoustic velocity of Molybdenum (m/s)
d_Mo = 1.82e-6;           % Thickness of the Molybdenum reflector layer
Z_Mo = Area*rho_Mo*v_Mo;    for 870 MHz SMR Design (m)
k_Mo = omega/v_Mo;
theta_Mo = k_Mo*d_Mo;

% Low acoustic impedance material (Silicon dioxide)

rho_SiO2 = 2070;          % Density of silicon dioxide (kg/m^3)
v_SiO2 = 5710;            % Acoustic velocity of silicon dioxide (m/s)
d_SiO2 = 1.65e-6;         % Thickness of the silicon dioxide reflector
Z_SiO2 = Area*rho_SiO2*v_SiO2;  layer for 870 MHz SMR Design (m)
k_SiO2 = omega/v_SiO2;
theta_SiO2 = k_SiO2*d_SiO2;

% MATERIAL PROPERTIES OF THE ELECTRODES (Aluminium)

rho_Al = 2700;            % Density of Aluminium (kg/m^3)
v_Al = 6450;              % Acoustic velocity of Aluminium (m/s)
```

```matlab
d_Al = 200e-9;              % Thickness of the Aluminium electrode (m)
Z_Al = Area*rho_Al*v_Al;
k_Al = omega/v_Al;
theta_Al = k_Al*d_Al;

% MATERIAL PROPERTIES OF THE PIEZOELECTRIC

rho_ZnO = 5680;            % Density of Zinc Oxide (kg/m^3)
v_ZnO = 6345;              % Acoustic velocity of Zinc Oxide (m/s)
d_ZnO = 3.32e-6;           % Thickness of the Zinc oxide layer
Z_ZnO = Area*rho_ZnO*v_ZnO;
z_ZnO = rho_ZnO*v_ZnO;
k_ZnO = omega/v_ZnO;
phi = (k_ZnO*d_ZnO)/2;

e33 = 1.32;                % ZnO strain constant (C/m^2)
Er = 10.2;                 % Relative permittivity of Zinc oxide
E0 = 8.8541878176e-12;     % Vacuum permittivity (F/m)
E33 = Er*E0;               % Permittivity of Zinc oxide (F/m)
c33 = 209.714e09;
Co = (E33*Area)/d_ZnO;
k2 = (e33^2/(E33*c33))/(1+(e33^2/(E33*c33)));

% ABCD MATRIX FOR THE LAYERS

% Bottom Electrode

ZT_Al = 1i*Z_Al*tan(theta_Al/2);
ZS_Al = (-1i*Z_Al)/(sin(theta_Al));
M_Al = [1+(ZT_Al/ZS_Al), 2*ZT_Al+((ZT_Al)^2/ZS_Al); 1/ZS_Al,
1+(ZT_Al/ZS_Al)];

% Acoustic Mirror

ZT_SiO2 = 1i*Z_SiO2*tan((theta_SiO2)/2);
ZS_SiO2 = (-1i*Z_SiO2)/(sin(theta_SiO2));
M_SiO2 = [1+(ZT_SiO2/ZS_SiO2), 2*ZT_SiO2+((ZT_SiO2)^2/ZS_SiO2);
1/ZS_SiO2, 1+(ZT_SiO2/ZS_SiO2)];

ZT_Mo = 1i*Z_Mo*tan((theta_Mo)/2);
ZS_Mo = (-1i*Z_Mo)/(sin(theta_Mo));
M_Mo = [1+(ZT_Mo/ZS_Mo), 2*ZT_Mo+((ZT_Mo)^2/ZS_Mo); 1/ZS_Mo,
1+(ZT_Mo/ZS_Mo)];

% Thermal Oxide

ZT_Oxide = 1i*Z_Oxide*tan((theta_Oxide)/2);
ZS_Oxide = (-1i*Z_Oxide)/(sin(theta_Oxide));
M_Oxide = [1+(ZT_Oxide/ZS_Oxide), 2*ZT_Oxide+((ZT_Oxide)^2/ZS_Oxide);
1/ZS_Oxide, 1+(ZT_Oxide/ZS_Oxide)];

% Silicon substrate

M_Si = [1,0;1/Z_Si,1];

% CASCADED MATRIX

M_Cascade = M_Al*M_SiO2*M_Mo*M_SiO2*M_Mo*M_SiO2*M_Mo*M_Oxide*M_Si;

% SIMULATION PARAMETERS

Zo = 50;                   % Characteristic Impedance
fi = 500e6;                % Initial Frequency
```

```matlab
fs = 1e6;                % Frequency steps
ff = 2e9;                % Final Frequency
frequency = fi:fs:ff;    % Frequency range

MA = M_Cascade(1,1);
MB = M_Cascade(1,2);
MC = M_Cascade(2,1);
MD = M_Cascade(2,2);

size = length(frequency);

A = zeros(size,1);
B = zeros(size,1);
C = zeros(size,1);
D = zeros(size,1);

theta_AL = zeros(size,1);
OMEGA = zeros(size,1);
PHI = zeros(size,1);

for a=1:size

A(a,1)= subs(MA,'f',frequency(:,a));
    B(a,1)= subs(MB,'f',frequency(:,a));
    C(a,1)= subs(MC,'f',frequency(:,a));
    D(a,1)= subs(MD,'f',frequency(:,a));
    theta_AL(a,1) = subs(theta_Al,'f',frequency(:,a));
    OMEGA(a,1) = subs(omega,'f',frequency(:,a));
    PHI(a,1) = subs(phi,'f',frequency(:,a));

end

% Impedance at the bottom of the piezoelectric layer
Z_Bottom = A./C;

% Impedance at the top of the piezoelectric layer
Z_Top = 1i*Z_Al.*tan(theta_AL);

% Normalised acoustic impedances at the boundaries of piezoelectric
layer
z_Bottom = Z_Bottom/Z_ZnO;
z_Top = Z_Top/Z_ZnO;


Zin = (1./(1i.*OMEGA*Co)).*(1-
(k2.*((tan(PHI))./PHI).*(((z_Bottom+z_Top).*(cos(PHI)).^2+1i.*sin(2*PHI)
)./((z_Bottom+z_Top).*cos(2*PHI)+1i*(z_Bottom.*z_Top+1).*sin(2*PHI)))));

R = (Z_ZnO - Z_Bottom)./(Z_ZnO + Z_Bottom);
T = 10*log10(1-(abs(R)).^2);

figure(1)
plot(frequency,T)

figure(2)
plot(frequency,log10(abs(Zin)))
```

APPENDIX B

FINITE ELEMENT MODELLING

The designed SMRs were evaluated using FEM with COMSOL Multiphysics® software version 4.4. The *Piezoelectric Devices* interface within the Acoustics module was used to this aim. A frequency response analysis was performed. The FEM model in this work was developed based on a COMSOL model for a thin film BAW composite resonator [1].

TWO-DIMENSIONAL MODEL

The 2D model of the SMR was developed using the plane strain assumption, where x, y and z are the lateral, vertical and out-of-plane dimension, respectively. The geometry of the model was drawn using the CAD tool within the software using blocks for the layers. Dimensions of such geometries were set in the parameters section.

Mechanical and electrical boundary conditions were applied to the model as shown in the figure below. An electric potential of 1.0 V was applied between the top and bottom electrode. To do so, the *electric potential* condition was applied to the top electrode and the *ground* boundary condition (V = 0) was applied to the bottom electrode.
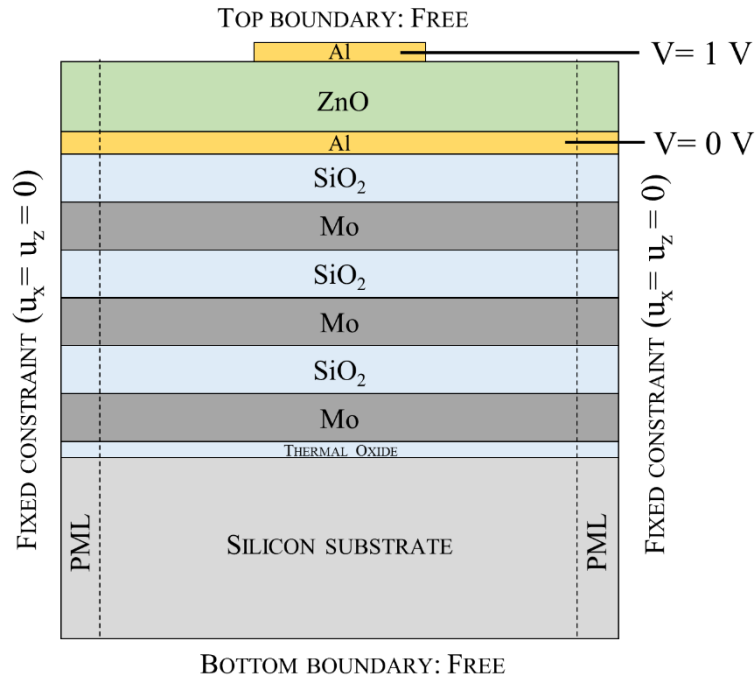
Figure B.1 Mechanical and electrical boundary conditions for the 2D finite element model.

The edges of the structure were set to a *fixed constraint* condition (zero displacement in all directions) while all other boundaries were left set to *free*. In order to avoid cavity modes, perfectly matched layers (PMLs) are used at the two sides of the geometry. These are artificial absorbing boundaries that account for the absorption of the outgoing elastic waves, avoiding the reflection back of the waves at the interfaces and contributing to the damping of the structure. Mechanical losses were also taken into account in the model by adding the structural and dielectric loss factor in the damping loss section of the piezoelectric material.

Each layer of the model was assigned with the corresponding material from the MEMS materials library and material properties were modified if required. The properties of these materials are those provided in Chapter 3. The material parameters needed in COMSOL® (Young's modulus, Poisson's ratio and density) differ to those

used for the one-dimensional model (acoustic velocity and density). However, these properties can be related by:

$$v = \sqrt{\frac{Y(1 - \sigma)}{\rho(1 + \sigma)(1 - 2\sigma)}} \tag{B.1}$$

where v is the acoustic velocity for longitudinal waves, Y is the Young's modulus, σ is the Poisson's ratio and ρ is the density of the material.

For the piezoelectric material, the acoustic velocity for the longitudinal acoustic wave propagation can be calculated as [2]:

$$v = \sqrt{\frac{c_{33} + \frac{e^2{}_{33}}{\varepsilon_{33}}}{\rho}} \tag{B.2}$$

where c_{33}, e_{33} and ε_{33} are the elastic constant, piezoelectric constant and permittivity of the piezoelectric material, respectively.

For meshing of the 2D model, a mapped mesh with several distributions was used generating rectangular elements. When modelling a wave propagation problem with FEM, especial attention should be given to the mesh of the structure as it must provide sufficient resolution to accurately represent the wave. Ten nodes per wavelength is used as a rule of thumb for choosing an appropriate mesh [3]; therefore the maximum mesh element size was set accordingly. Likewise, meshing of the PMLs is important so that the outgoing waves are optimally dampened [4]. A minimum of 8 elements is recommended for a 2D model.

A frequency domain study was performed in order to obtain the plots of electrical impedance against frequency of the SMRs. By considering the resonator as a parallel plate capacitor, the impedance was obtained by computing the following expression:

$$Z = \frac{V}{j\omega Q} \qquad (B.3)$$

where Z is the electrical impedance, V is the voltage applied across the electrodes, ω is the angular frequency and Q is the total charge on the surface of the top electrode. Q was obtained by integrating the charge density over the top electrode boundary using an integration component coupling. The admittance of the device can be directly obtained from the computation if a *Terminal* boundary condition is used instead. In this work, *electric voltage* was used rather than *Terminal* as this last one was not available within the used licensed module.

The standing wave amplitude as a function of depth [5] in the SMR was obtained by defining a new data set at the middle cross section of the device and plotting the *y*-component of the displacement field against the *y*-coordinate. The geometry of the 2D model can be simplified by considering only half of the structure and adding a *symmetry* boundary condition at the symmetry plane of the geometry.

THREE-DIMENSIONAL MODEL

Computation time for 3D models typically takes considerably longer than solving for a 2D model. This is because a greater number of finite elements are created for the 3D geometry. If possible, the 3D geometry should be simplified in order to speed the computation time and avoid running into computer memory limitations.

To this aim, the developed 3D model of the SMR consisted of only one quarter of the complete structure. This was achieved by taking advantage of the symmetry of the device and applying the *symmetry* condition at the appropriate boundaries as shown in Figure B.2. The electrical and mechanical boundary conditions were defined in a very similar way as previously explained for the 2D model.

As the 3D geometry is formed by very thin layers compared to the lateral dimensions, triangular elements and a swept mesh function were used for meshing the model as this significantly reduces the number of elements generated. A minimum of

5 elements is recommended for meshing the PML in the 3D model. A finer mesh was used for the electrodes area as this is where the acoustic wave mainly propagates.
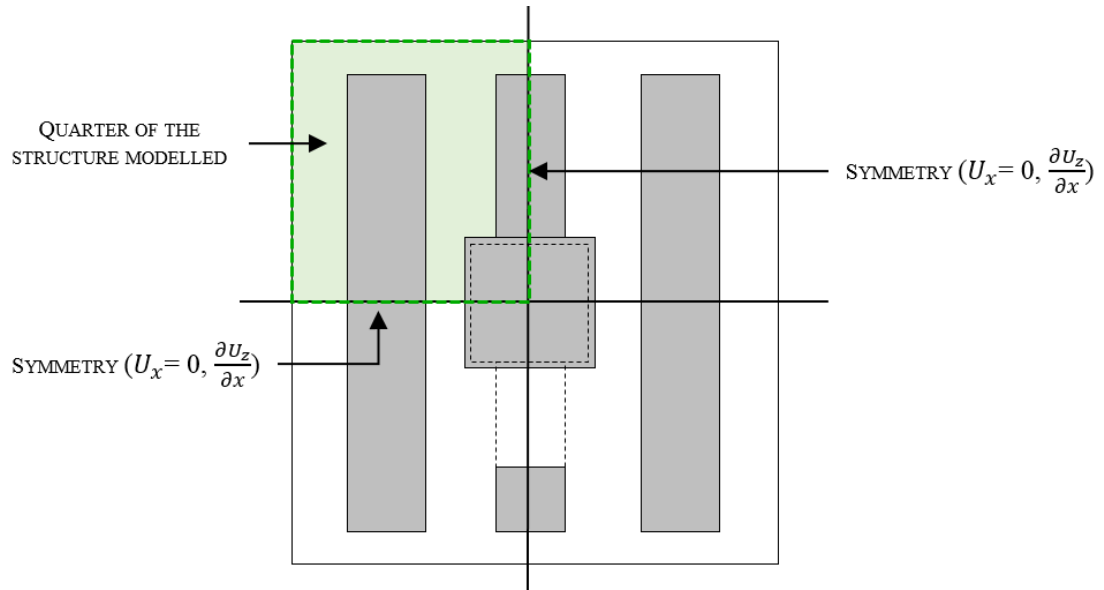
Figure B.2 Section of the structure used for the 3D model of the SMR.

In order to display the results of the computation for the entire geometry, two data sets *Mirror 3D* where created at the corresponding symmetry planes. Figure B.3 shows the mechanical deformation distribution at the resonance frequency of 869 MHz. A uniform distribution of the mechanical displacement can be observed in the centre area of the SMR structure where the electrodes are located.
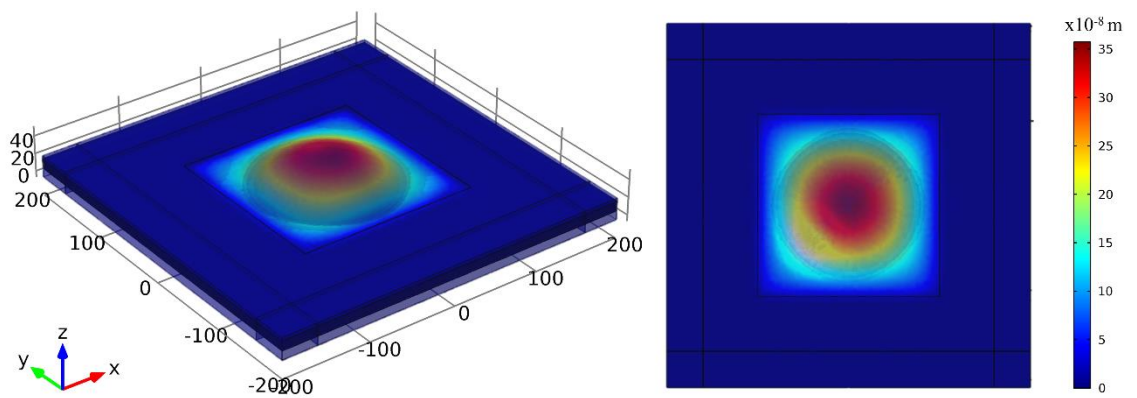
Figure B.3 Mechanical deformation of the fundamental resonant mode in the SMR resonating at 869 MHz obtained with the 3D model.

In the case of the 3D model, a factor of four was considered when computing the impedance of the device as only a quarter of the structure was simulated.

Table B.1 shows a comparison of the total time required to solve the finite element models in COMSOL® and the one-dimensional model implemented in the Matlab script for the same number of frequency points. All models were computed using a workstation with 128 GB of RAM and 2 processors.

Table B.1 Summary on the computation time required to solve the FEM model and the one-dimensional Mason model.

MODEL	MESH ELEMENTS	FREQUENCY POINTS	COMPUTATION TIME
1D	-	500	10 minutes
2D	6400	500	2 hours
3D	50600	500	48 hours

Computation times shown above are for a frequency response analysis with no parametric solutions. Solving for a parametric sweep such as the one computed to evaluate the temperature stability of the devices usually takes about 8 hours using the half 2D model.

Even though the computation of the Mason model in Appendix A is about 12 times faster than solving the 2D FEM model, this is in fact rather slow. If no symbolic variables are used in the script, the computation time of the same problem can be resolved in a matter of seconds.

REFERENCES

[1]   "Thin-Film BAW Composite Resonator". COMSOL application example. Available from: https://www.comsol.com/model/thin-film-baw-composite-resonator-5784

[2]   Rosenbaum, J. (1988). "Bulk acoustic wave theory and devices". Norwood, MA: Artech House.

[3]   Thalhammer, R. K. and Larson, J. D. (2016). "Finite-Element Analysis of Bulk-Acoustic-Wave Devices: A Review of Model Setup and Applications", *IEEE Transactions on Ultrasonics, Ferroelectrics, and Frequency Control*. **63**(10): 1624-1635.

[4]   (2013). "Acoustic scattering of and ellipsoid". COMSOL application example.

[5]   Lakin, K. M. B., J.; McDonald, J. F.; McCarron, K.T. (2001). "Improved bulk wave resonator coupling coefficient for wide bandwidth filters", *IEEE Ultrasonics Symposium*. pp. 827-831

APPENDIX C

6-MASK FABRICATION PROCESS

For the fabrication of the SMR devices, described in Chapter 3, an original 6-mask fabrication process was developed, for which all six photolithography masks were designed and manufactured. This process was optimised to a three-mask process, as described in Chapter 3. However, the original 6-mask process can offer the following advantages:

(1) The reflector layers are patterned. Therefore, devices in the same substrate are isolated from each other. Performing this step of the process would help avoiding any cross talk between devices. This will result particularly advantageous for their use in sensing arrays, where the devices share the same substrate.

(2) Die separation of the wafer is accomplished by a backside deep reactive ion etching (DRIE) process. This process would avoid contamination and possible scratches caused when alternative method is used (e.g. saw dicing).

(3) A mask was included to open windows on the passivation layer to the contact pads and the sensing area of the device. In this way, the devices could be passivated (protected from contamination) while still be possible to access their connections and the sensing area.

The complete six-mask fabrication process is described below and depicted in Figure C.1 and C.2.

1. SUBSTRATE CLEANING. Double-side polished, 4- inch, 525 µm thick (+/- 25µm), p-type silicon wafers with crystallographic orientation (100) and 200 nm thermal oxide on both sides were purchased from Si-Mat (Germany). Cleaning of the substrate to remove any contaminants comprised soaking the wafer in acetone followed by isopropanol (IPA) and then flushing with deionized (DI) water. Finally, the wafer is dried with nitrogen and baked at 125 °C for 3 minutes.

2. DEPOSITION OF THE REFLECTOR LAYERS. A total of three layers of Mo and two layers of SiO_2 are alternately sputtered on the silicon substrate using a high target utilisation sputtering (HiTUS S500) system. As the system can accommodate several targets at a time, deposition of the reflector layers can be performed without breaking the vacuum in the system or removing the sample, resulting in better adhesion between the layers.

3. PATTERNING OF THE ACOUSTIC MIRROR. The acoustic mirror is patterned in order to provide electrical isolation between devices in the same substrate, avoiding crosstalk and reducing capacitive coupling [1]. Mo and SiO_2 layers are sequentially etched. For Mo layers, a dry process is employed with $CF4/O_2$ plasma in reactive ion etching (etching rate of ~200 nm/min). In the case of SiO_2 layers a wet etching using BHF is utilised at an etching rate of ~900 nm/min. During photoresist stripping ultrasound is avoided to prevent delamination thus wafer is soaked in acetone, IPA and DI water. For patterning of the reflector layers, a thick photoresist is used (AZ4562 with a thickness of ~8 µm). This is a positive photoresist and thus a clearfield mask was required.

4. SPUTTERING OF TOP SiO$_2$ LAYER OF ACOUSTIC MIRROR. The top SiO2 layer of the acoustic mirror is deposited using the HiTUS system after patterning the previous reflector layers. This top layer should help encapsulating the reflector stack, preventing delamination and isolating the metal layers of the individual devices.

5. DEPOSITION AND PATTERNING OF BOTTOM ELECTRODE. The bottom electrode (200nm Al or 100/10 Au/Cr) is deposited on top of the acoustic mirror and patterned using a standard lift-off photolithography process. The aluminium layer is sputtered while the chrome/gold layers are thermally evaporated.

6. DEPOSITION OF PIEZOELECTRIC LAYER. The ZnO layer is reactively sputtered at room temperature from a zinc target using an Ar/O$_2$ mixture in the HiTUS system [2] resulting in high quality ZnO films with excellent c-axis orientation, smooth surface and low stress [3] to obtain high quality resonators.

7. DEPOSITION AND PATTERNING OF TOP ELECTRODE. The top electrode is patterned in a second lift-off process in a similar way as the bottom electrode using the same materials, thicknesses and deposition methods.

8. PATTERNING OF PIEZOELECTRIC LAYER. In order to provide electrical contact to the bottom electrode, the ZnO film is patterned and via holes etched through it in a wet etching process using a 2% glacial acetic acid and phosphoric acid solution at room temperature with at etching rate of ~1.2 µm/min.

9. DEPOSITION OF PASSIVATION LAYER. In order to protect devices from environmental factors and scratching during dicing, a passivation layers is deposited on the top with opening windows through it in order to make contact with the electrodes.

10. WAFER DICING. A backside DRIE process is used to create dicing trenches on the wafer. Al$_2$O$_3$ is deposited on the backside to act as a hard mask for this process. The alumina is deposited in the HiTUS system with a deposition rate of ~6 nm/min.
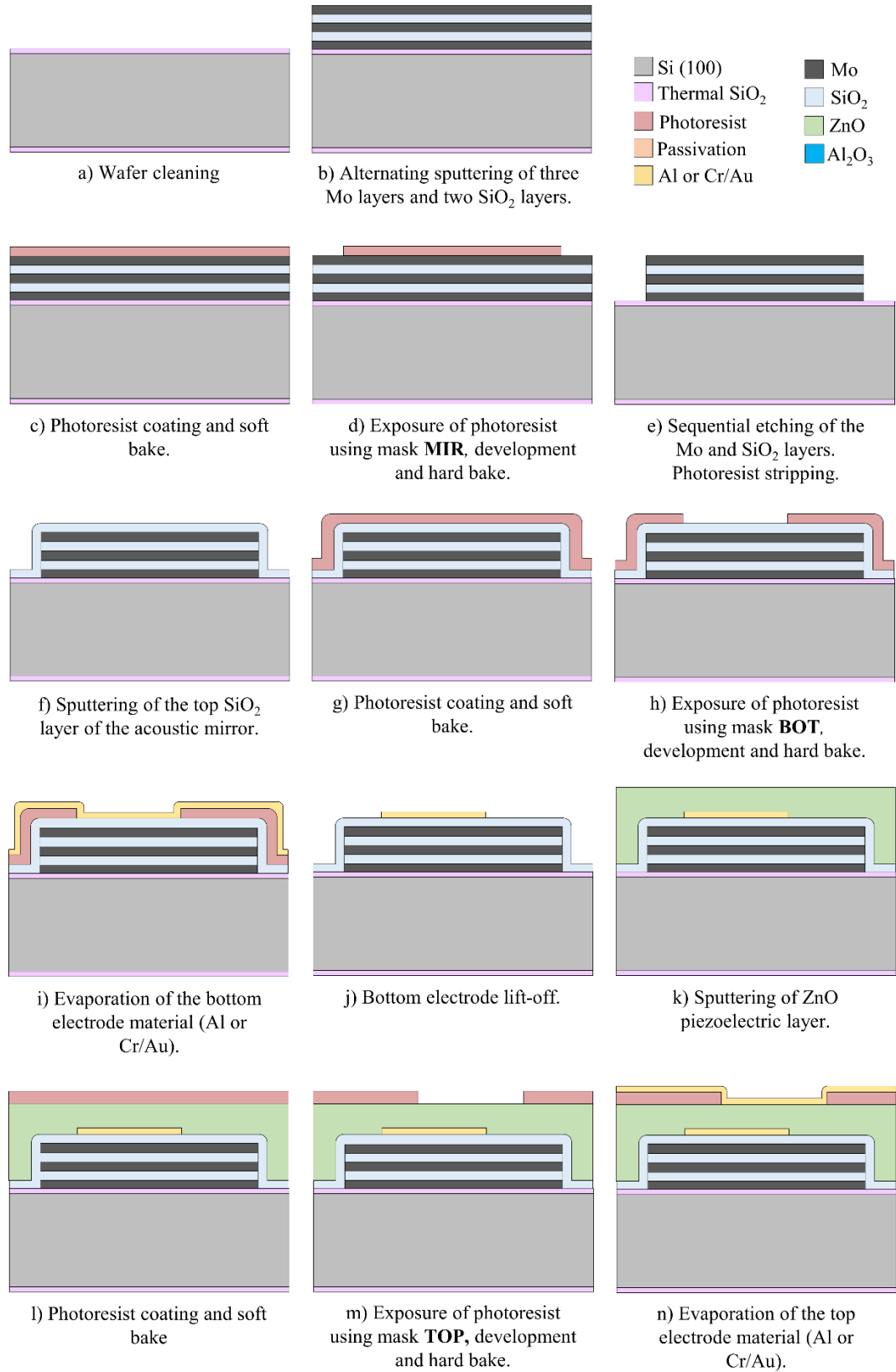
Figure C.1 Original 6-mask fabrication process flow: (a) Wafer cleaning; (b) to (e) deposition and patterning of acoustic mirror; (f) Deposition of encapsulating SiO$_2$ layer; (g) to (j) patterning of bottom electrode; (k) deposition of piezoelectric layer; (l) to (o) patterning of top electrode. Process continues in Figure .

o) Top Electrode Lift-off

p) Photoresist coating and soft bake

q) Exposure of photoresist using mask **PIE**, development and hard bake.

r) Etching of piezoelectric ZnO and photoresist removal.

s) Deposition of passivation layer.

t) Photoresist coating and soft bake.

u) Exposure of photoresist using mask **PAS**, development and hard bake.

v) Opening contact windows to the pads and the active area: etching of the passivation layer and photoresist removal.

w) Deposition of 150 nm of Al_2O_3 on the backside of the wafer.

x) Coating of photoresist on the backside of the wafer and soft bake. Exposure of photoresist using mask **DIC**, development and hard bake.

y) Patterning of the hard mask for the DRIE process: etching of the Al_2O_3 layer and photoresist removal.

z) Separation of dies: deep reactive ion etching (500 um) of the silicon substrate.

Figure C.2 Continuation of 6-mask fabrication process flow in Figure . (p) to (r) patterning of the piezoelectric layer and opening via contact to the bottom electrode; (s) deposition of passivation layer; (t) to (v) patterning of passivation layer to open contact windows to the pads and the active area; (w) to (z) deep reactive ion etching of the silicon substrate for wafer dicing.

Table C.1 summarised the specifications for all six masks, including the polarity and view side.

Table C.1 Specifications of all six photolithography masks for the original fabrication process.

MASK ID	POLARITY	VIEW SIDE	TYPE OF RESIST	DESCRIPTION
MIR	Clearfield	Right Read Chrome down	Positive	Patterning of the Mo and SiO_2 layers to define the acoustic mirror and alternating wet etching of Mo/SiO_2
BOT	Darkfield	Right Read Chrome down	Positive	Patterning of the bottom electrode and lift-off process
TOP	Darkfield	Right Read Chrome down	Positive	Patterning of the top electrode and lift-off process
PIE	Darkfield	Right Read Chrome down	Negative	Patterning the piezoelectric material and opening via access to the bottom electrode, etching of the piezoelectric layer.
PAS	Darkfield	Right Read Chrome down	Positive	Opening Windows on the passivation layer to the contact pads. (Etching)
DIC	Darkfield	Right Read Chrome up	Positive	Backside patterning of the dicing marks for the DRIE process

[1]   Ellael (2002). "Solidly Mounted Multiresonator Bulk Acoustic Wave Filter with a patterned acoustic mirror", *US Patent*.

[2]   García-Gancedo, L., Pedrós, J., Zhu, Z., Flewitt, A. J., Milne, W. I., Luo, J. K. and Ford, C. J. B. (2012). "Room-temperature remote-plasma sputtering of c-axis oriented zinc oxide thin films", *Journal of Applied Physics*. **112**(1): 014907.

[3]   García-Gancedo, L., Ashley, G. M., Zhao, X. B., Pedrós, J., Flewitt, A. J. and Milne, W. I. (2011). "Deposition and characterisation of ultralow-stress ZnO thin films for application in FBAR-based gravimetric biosensors ", *Int. J. Nanomanufacturing*. **7**(3/4): 371-382.

APPENDIX D

POLYMER-VAPOUR PARTITION COEFFICIENTS

In Chapter 6, the calculation of polymer-vapour partition coefficients though the use of linear solvation energy relationships (LSER) was detailed. LSER solvation parameters for a range of polymers were collected from published data [1-5]. In Table D.1 and D.2, a complete list of calculated partition coefficients is presented for VOCs of interest in air quality monitoring.

Table D.1 Partition coefficient values of polymer-vapour pairs.

POLYMER	ACETONE	AMMONIA	BENZENE	ETHANOL	FORMALDEHYDE	TOLUENE	ACETALDEHYDE	n-OCTANE
C28	13.879	2.709	75.955	9.799	3.222	171.741	6.808	223.934
C32	13.617	2.640	75.440	9.657	3.164	170.518	6.677	214.842
C36	12.990	2.580	72.987	9.393	3.064	163.668	6.424	201.855
CSVAL	88.257	19.118	400.498	271.238	9.211	1148.947	27.353	1406.048
FPOL	1325.959	315.915	92.164	894.396	39.683	255.376	287.700	58.993
HPMB	9.759	1.913	54.664	7.186	2.359	120.782	4.857	127.809
OV202	149.053	11.243	223.491	55.510	17.378	616.836	49.769	389.762
OV25	65.418	3.768	277.895	28.925	7.589	825.239	21.485	244.568
P4V	40303.244	6258.064	226.986	11338.615	469.462	716.077	5901.739	95.940
PBF	3412.628	1500.579	205.594	3037.358	94.295	573.338	760.673	446.478
PBMA	21.537	3.411	62.041	24.987	5.035	130.479	9.409	64.863
PCL	24.666	3.697	64.529	30.471	6.337	127.790	10.992	36.874
PCLP	10.507	1.566	48.070	6.783	2.737	101.207	5.204	49.363
PCPMS	234.929	28.274	387.609	300.318	34.338	891.614	81.219	166.848
PDMS	67.809	10.432	410.147	82.718	9.166	1164.528	24.462	1867.239
PMCPS	358.344	36.718	644.644	679.548	49.023	1574.780	111.240	338.532
PEA	25.431	3.981	54.810	30.091	7.068	103.703	11.711	29.914
PECH	166.909	11.015	371.860	117.233	17.914	1039.561	50.501	201.558
PEE	10.309	2.115	55.066	7.205	2.599	119.358	5.271	136.044
PEI	14.402	3.361	45.136	831.362	1.425	116.182	3.072	17.931
PEM	54.369	2.255	37.629	128.431	4.825	113.167	11.178	35.612

Table D.2 Partition coefficient values of polymer-vapour pairs.

POLYMER	ACETONE	AMMONIA	BENZENE	ETHANOL	FORMALDEHYDE	TOLUENE	ACETALDEHYDE	n-OCTANE
PEO	30.522	4.448	62.919	46.514	8.358	117.413	13.427	20.978
PIB	16.285	1.167	164.180	8.852	1.644	583.203	5.198	962.942
PLF	8918.155	3692.589	170.787	4284.045	279.995	403.821	2150.463	152.869
PMA	21.441	3.082	42.517	24.130	6.557	76.256	10.161	13.521
PMAPS	170.887	19.468	501.280	265.993	20.114	1410.977	52.597	1107.643
PMHS	21.676	2.763	253.890	28.372	3.618	723.417	8.269	1087.126
PMiPCAS	155.554	25.814	424.248	374.533	20.059	1106.853	50.017	919.602
PMPS	106.069	8.660	496.661	86.262	13.589	1445.007	35.193	922.147
PMTFPS	235.604	21.618	138.113	61.666	27.850	343.295	82.724	211.485
PP1	9.935	1.890	52.881	6.625	2.413	116.979	4.971	131.692
PP2	19.243	5.052	103.697	23.722	4.468	227.677	9.271	323.952
PTHF	23.744	4.276	75.553	34.601	5.574	157.414	10.388	76.899
PVA	23.335	3.074	42.482	28.332	6.642	78.211	10.463	13.292
PVE	14.451	2.510	64.411	9.534	3.598	139.235	7.149	123.208
PVPR	88.461	18.065	263.281	218.534	10.566	634.556	29.824	120.116
PVTD	48.994	5.886	237.969	123.163	4.654	745.727	13.559	624.597
SXCN	44.455	2.743	59.377	69.462	5.008	154.401	11.987	15.981
SXFA	3948.571	1968.883	377.329	2734.513	149.865	930.208	1078.301	371.193
SXPHB	68.024	3.828	296.306	29.932	7.718	890.902	22.102	266.195
SXPYR	52.615	3.337	110.718	1129.692	2.863	394.194	7.879	65.103
ZDOL	729.138	379.359	72.704	852.020	31.725	178.238	193.865	132.678

REFERENCES

[1] McGill, R. A., Mlsna, T. E., Chung, R., Nguyen, V. K. and Stepnowski, J. (2000). "The design of functionalized silicone polymers for chemical sensor detection of nitroaromatic compounds", *Sensors and Actuators B: Chemical*. **65**(1–3): 5-9.

[2] Santiuste, J. M. a. and García-Domínguez, J. A. (2000). "Study of retention interactions of solute and stationary phase in the light of the solvation model theory", *Analytica Chimica Acta*. **405**(1–2): 335-346.

[3] Matatagui, D., Martí, J., Fernández, M. J., Fontecha, J. L., Gutiérrez, J., Gràcia, I., Cané, C. and Horrillo, M. C. (2011). "Chemical warfare agents simulants detection with an optimized SAW sensor array", *Sensors and Actuators B: Chemical*. **154**(2): 199-205.

[4] Demathieu, C., Chehimi, M. M. and Lipskier, J.-F. (2000). "Inverse gas chromatographic characterization of functionalized polysiloxanes. Relevance to sensors technology", *Sensors and Actuators B: Chemical*. **62**(1): 1-7.

[5] Hierlemann, A., Zellers, E. T. and Ricco, A. J. (2001). "Use of linear solvation energy relationships for modeling responses from polymer-coated acoustic-wave vapor sensors", *Analytical Chemistry*. **73**(14): 3458-3466.

APPENDIX E

CIRCUIT DIAGRAMS

SMR Pierce Oscillator Board
F.H Villa Lopez
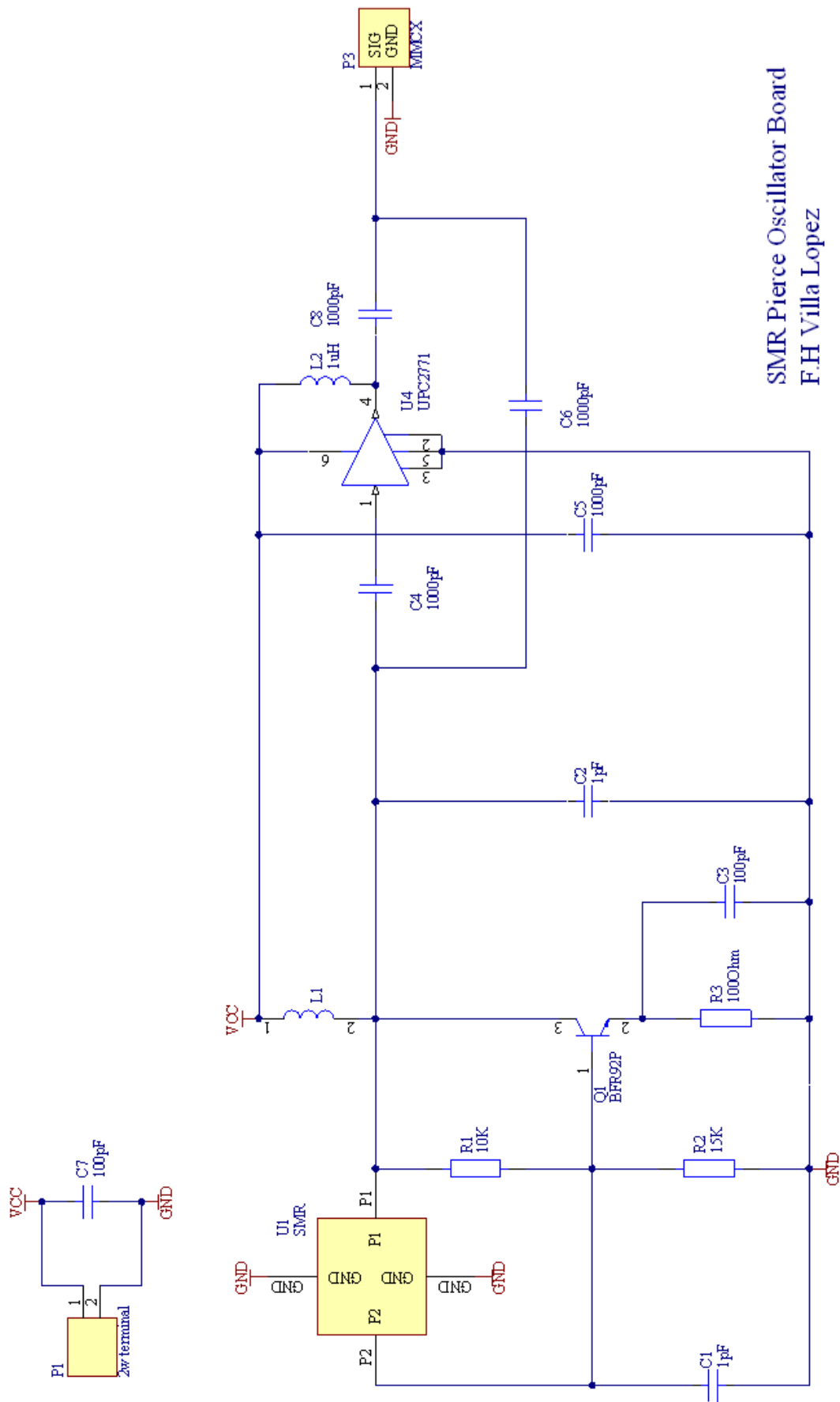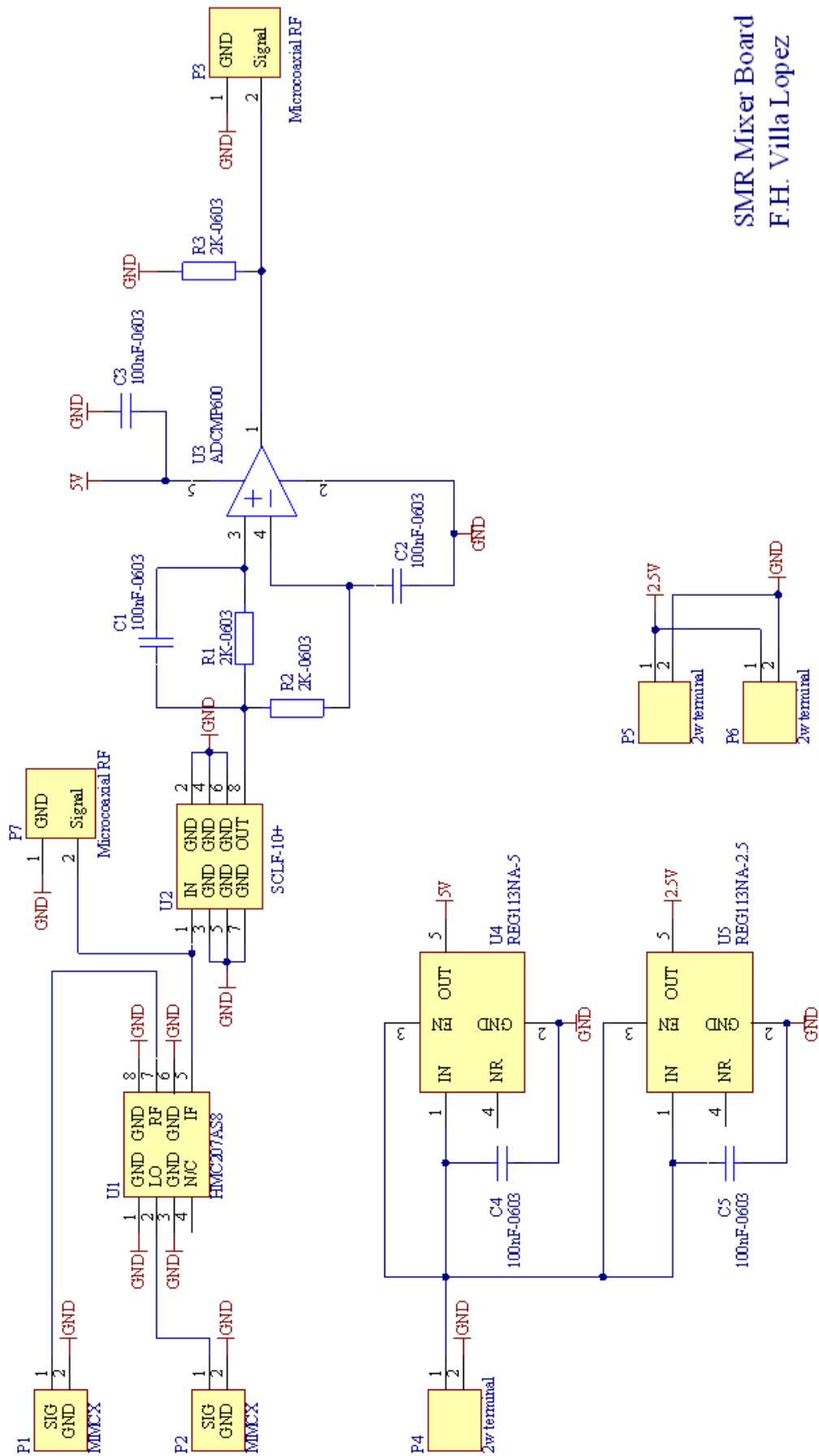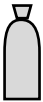
SMR Mixer Board
F.H. Villa Lopez

APPENDIX F

VOC STATION HARDWARE COMPONENTS

The development of an automated VOC test rig was presented in Chapter 6. The Table below details the hardware components used for its development. The symbols presented in the first column refer to those used in the schematic diagram of the VOC rig, presented in Figure 6.16.

SYMBOL	PART	PHOTOGRAPH	SUPPLIER
	Compressed gas cylinder		BOC Group Limited – Gas cylinders usually AK size. (Mixture of 200 ppm of acetone in air and 100 ppm of toluene in air)
	Manual Valve		Swagelok – Stainless steel 1-piece 40 series ball valve, 1/8 inch. Part No. SS-2F-05.
	Solenoid Valve		Bürkert Fluid Control systems – Stainless steel, normally closed, 12 VDC voltage. Type 6012 and plug connection type 2506.
	Regulator with gauge.		BOC Group Limited – HP1700 Series two stage regulators for the VOC lines.
	Zero air generator		Parker Balston – Model number HPZA-3500.
	Particulate Filter		Swagelok – Stainless steel in-line particulate filter, 1/8 inch, 0.5 micron pore size. Part No. SS-2F-05
	Check valve		Swagelok – Stainless steel poppet check valve. Part No. SS-2C-1/3.
	Bubbler		250 ml Dreschel bottle (Scientific Laboratory Supplies) with head and grade 1 sinter.

	Mass flow controller	Alicat Scientific – Ranged 2.5 – 500 sccm. Product code MC-500SCCM-D/5M,5IN
	Temperature and Humidity Sensor	Rotronic – Hygroclip 2, HC2-S placed inside a in-house made stainless steel chamber
	Mixing chamber and block heater 1.	IKA Werke GmbH –Single dry block heater. Product number 4025100. In house made mixing chamber
	Sensor chamber and block heater 2.	Techne Ltd- dual block Dri-block heater DB-2D.
	Mass flow meter	Alicat Scientific – Ranged 2.5 – 500 sccm. Product code M-500SCCM-D/5M
	T-Junction	Swagelok – Stainless steel Tube fitting, Union Tee, 1/8 in Tube OD. Part Number: SS-200-3
	Stainless steel tubing	Swagelok – 316/316L Stainless steel seamless tubing, 1/8 in OD x 0.028 in wall. Product Number: SS-T2-S-028-6ME

APPENDIX G

VIRTUAL INSTRUMENTATION

Virtual instrumentation was developed in LabVIEW v2015 for the automated control of the VOC test station and data acquisition. This virtual instrumentation performs three main functions:

(1) HARDWARE CONTROL. Control of the gas flow equipment including the mass flow controllers, the mass flow meter and the electronic valves.

(2) VOC STATION DATA ACQUISITION. Acquisition of the temperature and humidity sensor readings within the rig as well as the mass flow values of the mass flow controllers (MFCs). The acquired data is shown on screen in real time and can be saved to a .tdms file.

(3) SENSOR DATA ACQUISITION. This virtual instrument (VI) allows real time monitoring (on-screen view) of the sensor data which can also be saved for post-processing analysis.

The front panel of the VI for controlling of the VOC station is shown in Figure G.1. The station can operate in two modes: manual and automatic. These two modes can be selected from the tabs at the left-hand side of the front panel (orange or blue tabs). The manual operation tab is currently showed in the figure while the automatic operation tab is shown in Figure G.2.
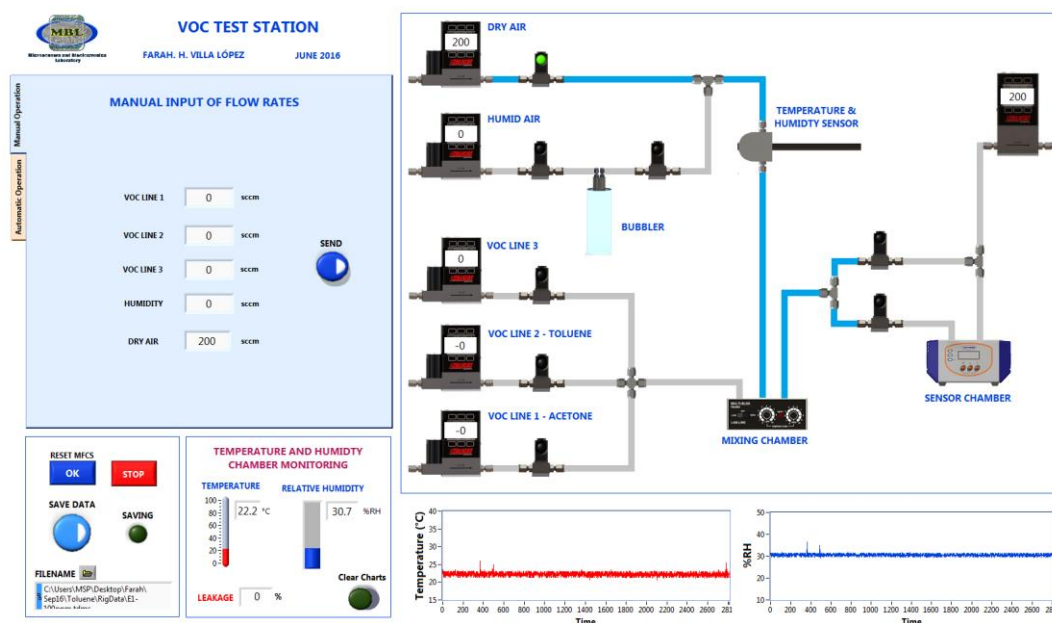

Figure G.1 Front panel for controlling VOC test station.

The manual operation mode allows writing to the mass flow controllers by manually entering the desired values and opening/closing the valves as needed. The former is achieved by clicking the *send* button while the latter is accomplished by clicking on the corresponding valve graphic indicator. As the name suggests, this mode is used in the case that complete manual operation of the rig is required, and is usually employed at the start of each experiment to test any leakage within the system.

Figure G.2 Automatic operation mode of the virtual instrument.

The automatic mode allows complete automated control of the rig, in which the user is only required to load a file containing the testing steps. An example of this file is shown in Figure G.3. Each line (row) corresponds to one exposure step in which the desired concentration of the selected VOC is given along with humidity levels (if desired) and the total duration time of the exposure step. The file can be created in Microsoft Excel but should be saved and uploaded as a .csv file. In the case of dry air needed for the baseline, the values that need to input are all zero such as in the second line of the sample file.

	A	B	C	D	E
1	VOC LINE 1 (ppm)	VOC LINE 2 (ppm)	VOC LINE 3 (ppm)	RELATIVE HUMIDITY (%RH)	TIME (min)
2	0	0	0	0	30
3	200	0	0	0	10
4	0	0	0	0	10
5	100	0	0	0	10
6	0	0	0	0	10
7	50	0	0	0	10
8	0	0	0	0	10
9	100	0	0	0	10
10	0	0	0	0	10
11	200	0	0	0	10
12	0	0	0	0	10
13					

Figure G.3 Sample of the testing file that should be uploaded.

Before loading the file, two important actions are required:

(1) The VOC to be tested needs to be selected the drop-down menu (Acetone 200 ppm is selected in the case shown above). The drop-down menu lists the VOC cylinders available in the laboratory. If VOC mixtures are used, two or more VOC lines should be defined. It is important to select the correct VOCs in the designed lines, as this will determine the maximum concentration of the cylinder and the program will perform the flow rate calculations based on this.

(2) The total flow rate should be introduced in the corresponding box, shown to the left of the *Load file* button. This is the total flow rate that will go into the exposure chamber and this value is again needed for the calculations of the concentrations.

Once these two steps have been completed, the *Load File* button can be pressed which will open a dialogue window to browse to the location of the .csv file, previously created. Once uploaded, the VI will use this information to calculate the required flow rates of each MFC which will be displayed in the table of the front panel.

To start the VOC test, the *start* button is pressed. Once done, the flow rates for the first step (first row of the table) will be written to the MFCs and will remain during the specified time for that step. The elapsed time and remaining time are displayed for the current step as well as for the complete experiment. Once the time for the current step has elapsed, the calculated mass flow values for the next step will be sent to the

MFCs during the specified time and this process will be repeated until the last step is completed. A blue contour highlights the current step (row of the table) being performed. Once completed, the program will pop up a notification confirming that all testing steps were successfully completed.

In the lower left corner of the front panel, three buttons are available. The emergency *stop* and *reset all* buttons are used to abort execution of the virtual instrument and reset all the equipment to default values, respectively. The third button is used to save the station data (mass flow rates, temperature and humidity) to a. tdms file. The file path can be selected in the same section.

Two indicators are used to display temperature and humidity readings from the sensor placed after the dry air and wet air lines and two graphs show these readings in real time plots for easy visualization. Block diagrams of the main parts of this virtual instrument are shown below.
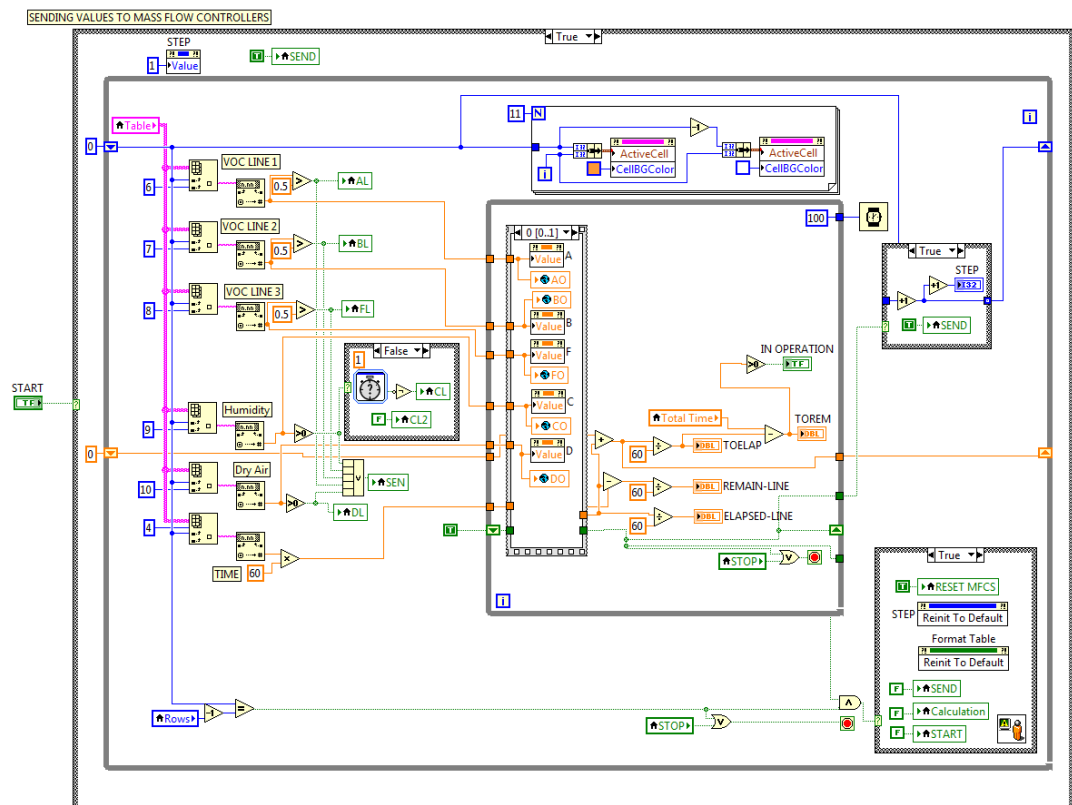

Figure G.4 Part of the block diagram for the automatic mode operation.

Figure G.5 Part of the block diagram to write/read values to the mass flow controllers.

Figure G.6 Part of the block diagram for the control of the electronic valves and acquisition of temperature and humidity readings.
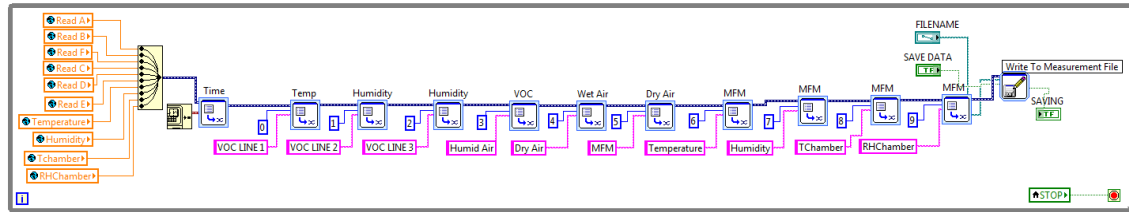
Figure G.7 Part of the block diagram to save the VOC station data (MFCs values, temperature and humidity).

Sensor data acquisition was accomplished by a separate virtual instrument in which the data is acquired via serial port communication with the microcontroller (Teensy 3.2). The COM port assigned to the microcontroller should be selected in the corresponding field.

The front panel of the acquisition for one sensing signal is shown in Figure G.8. Block diagram for this implementation is shown in Figure G.9. The front panel consists of a graphical indicator where the sensor readings are plotted in real time at a sampling rate of 10 Hz. Interactive buttons are included to clear the chart and auto scale the data as required. As in the previous VI, the sensor data can be saved to a separate specified file (.tdms).
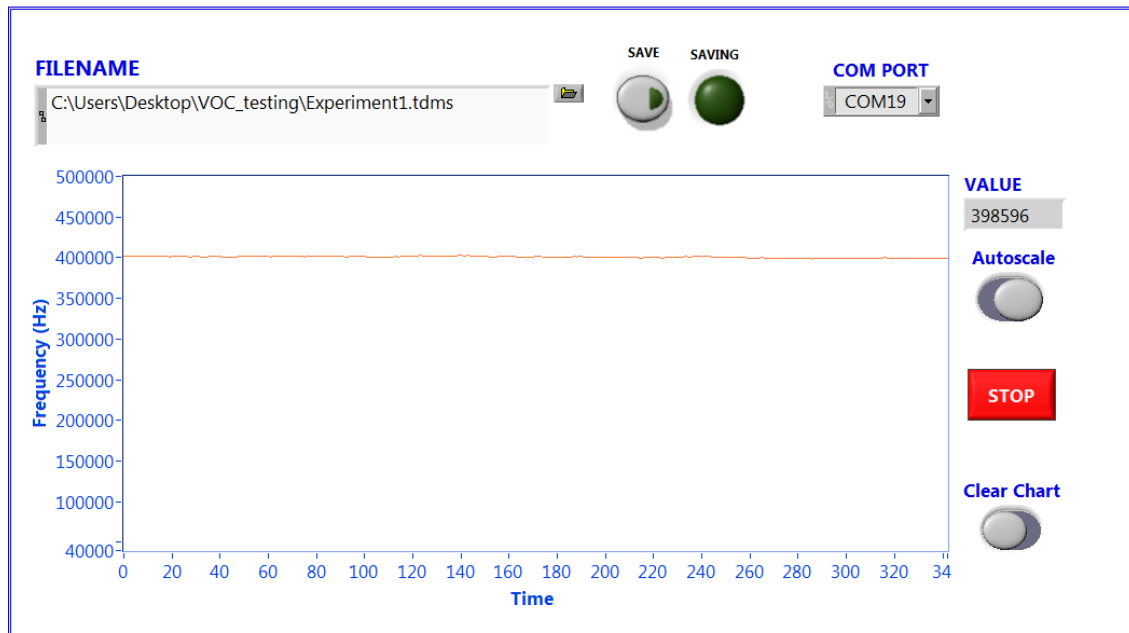

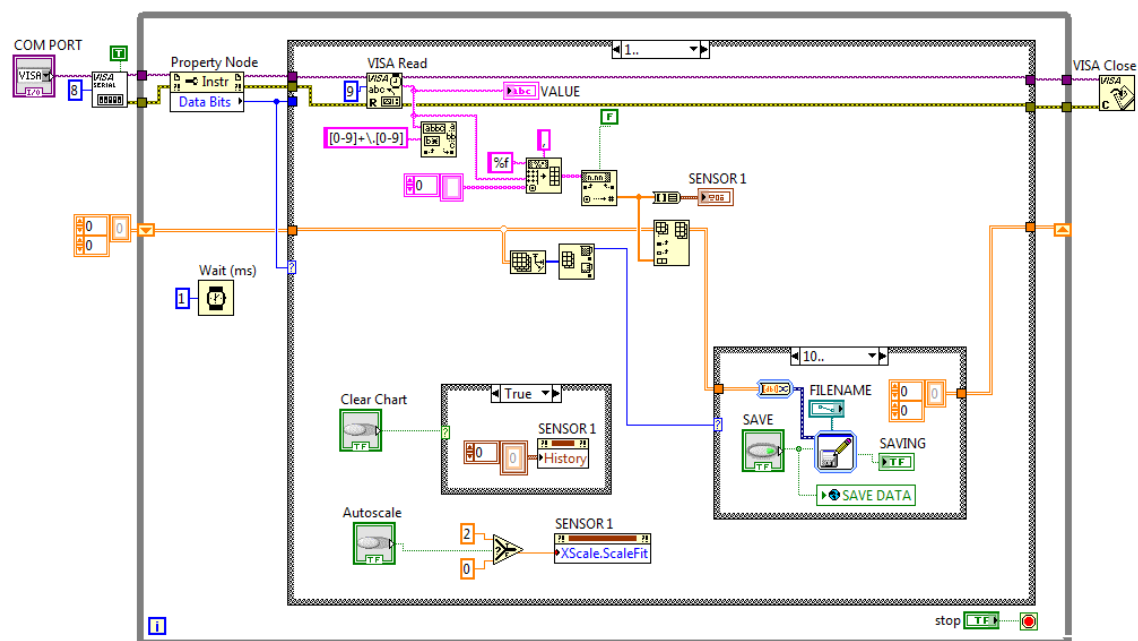**Figure G.8** Front panel of virtual instrument used for sensor data acquisition.

Figure G.9 Block diagram for sensor data acquisition.

APPENDIX H

ZnO BASED CMOS SMR DEVICES

In Chapter 7, post-processing of the CMOS fabricated devices was detailed for AlN based SMR devices. ZnO based devices were also fabricated. The performance of the AlN devices was superior compared to the ZnO devices. The post-fabrication of these devices took place at the Centre for Advanced Photonics and Electronics (CAPE), University of Cambridge UK in collaboration with Dr Mario De Miguel Ramos and Dr Andrew Flewitt. Fabrication and characterisation of these devices is presented in this appendix.

The post-fabrication steps consisted on the deposition of the bottom electrode, piezoelectric layer and top electrode. In this first attempt for the post-fabrication process, a one-mask photolithography process was used, in which only the top electrode was patterned using capacitive coupling to excite the resonator. Only one

mask was used to facilitate alignment during the photolithography process. Thicknesses and materials used for these layers are summarised in Table H.1 below. For these designed layers, the devices are expected to resonate at a frequency of ~2.1 GHz.

Table H.1 Layers deposited during the post-processing steps for the CMOS based SMR.

THICKNESSES	
Bottom Electrode (Mo)	200 nm
Piezoelectric (ZnO)	800 nm
Top Electrode (Mo)	200 nm

The molybdenum layers for the electrodes were sputtered from a Mo target (99.95% purity) at a deposition rate of 6.5 nm/min. The ZnO piezoelectric layer was deposited in the HiTUS system (previously detailed in Chapter 4) with a deposition rate of ~92.5 nm/min. Patterning of the top electrode was performed in s standard photolithography process and the Mo layer was etched with Al etchant at room temperature. Photographs of the device before and after completing the post-processing steps are presented in Figure H.1.
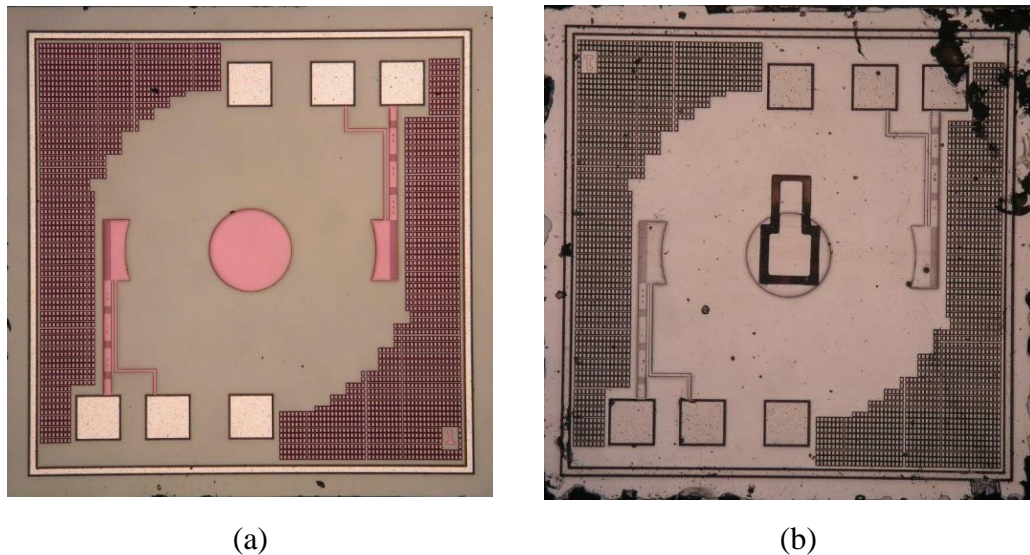

(a)   (b)

Figure H.1. Photographs of the top view of the CMOS based SMR devices: (a) Fabricated CMOS device before post-processing and (b) ZnO based SMR (after completion of the post-processing steps).

After completion of the post-CMOS fabrication steps, the device was characterised using the Network Analyser. The measured impedance for one device is shown in Figure H.2 below. Devices were found to resonate at a frequency of ~1.9 GHz (suggesting that a thicker layer of ZnO was deposited, compared to the designed thickness). The quality factors of these devices were measured at 126 and 160 for the series and parallel frequencies, respectively, and an electromechanical coupling coefficient k_{eff}^2 of ~4% was found. Even though the performance metrics of these devices could be improved, the results obtained from this first batch of ZnO based CMOS devices are promising for their implementation in sensing applications.
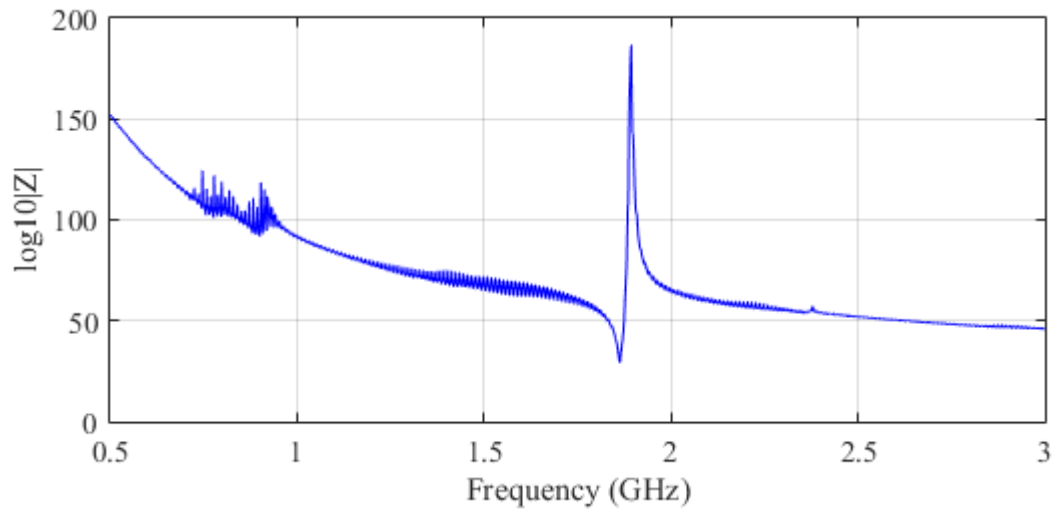

Figure H.2 Frequency response of the CMOS based SMR with ZnO as the piezoelectric layers and Mo electrode